SUSTAINABLE HARD MACHINING USING MECHANICAL MICRO-TEXTURED CUTTING TOOLS WITH MINIMUM QUANTITY NANO-GREEN CUTTING FLUIDS

A thesis submitted in
partial fulfillment of the requirements
for the degree of

DOCTOR OF PHILOSOPHY

By

Kishor Kumar Gajrani

(136103020)

Department of Mechanical Engineering
Indian Institute of Technology Guwahati
December – 2018

DEDICATED

TO

MY PARENTS AND FAMILY

DEPARTMENT OF MECHANICAL ENGINEERING

INDIAN INSTITUTE OF TECHNOLOGY GUWAHATI

GUWAHATI-781039, ASSAM

INDIA

DECLARATION

I declare that,

a. The work contained in this thesis is original and has been done by me under the guidance of my supervisor.
b. The work has not been submitted to any other institute for any degree or diploma.
c. I have followed the guidelines provided by the institute in preparing this thesis.
d. I have confirmed to the norms and guidelines given in the ethical code of conduct of the institute.
e. Whenever I used materials (data, theoretical analysis, figures and text) from other sources, I have given their detail in references.

Kishor Kumar Gajrani

DEPARTMENT OF MECHANICAL ENGINEERING
INDIAN INSTITUTE OF TECHNOLOGY GUWAHATI
GUWAHATI-781039, ASSAM
INDIA

CERTIFICATE

It is certified that the work contained in the thesis entitled "**Sustainable Hard Machining Using Mechanical Micro-Textured Cutting Tools with Minimum Quantity Nano-Green Cutting Fluids**" submitted by **Mr. Kishor Kumar Gajrani** to the Indian Institute of Technology Guwahati for the award of the degree of Doctor of Philosophy has been carried out under my supervision in the Department of Mechanical Engineering, Indian Institute of Technology Guwahati. This work has not been submitted elsewhere for the award of any other degree or diploma.

(Dr. Mamilla Ravi Sankar)
Assistant Professor
Department of Mechanical Engineering,
Indian Institute of Technology Guwahati,
Guwahati-781039, India

December, 2018

ACKNOWLEDGEMENT

"Starting something can be easy; it is finishing that is the highest hurdle". The journey of doctoral study is always a difficult and challenging task. Throughout this long journey, I have gained a lot by learning to persevere despite hardship. I would never have successfully completed this thesis without the assistance of numerous people who I am indebted to. Their direction, advice, support and contributions have proved invariable along the way.

First and foremost, I would like to express my special appreciation and respect to my supervisor, Dr. M. Ravi Sankar, who has been a tremendous mentor for me. I appreciate all his contributions of time, ideas and funding to make my PhD experience productive and stimulating. I am also thankful to him for the excellent example he has provided as a successful research scientist and professor. The joy and enthusiasm he has for his research were contagious and motivational for me, even during the tough times in my PhD pursuit. A very special gratitude goes to him for encouraging my research. Thank you very much, sir, for your advice on my research, my career, as well as my personal life, has always been priceless.

I offer my sincere thanks to my doctoral committee members, Professor P. S. Robi, Professor Uday Shanker Dixit, Dr. Sachin D. Kore and Dr. Ashwini Sharma for their insightful comments and encouragement, and also for the hard questions which incented me to widen my research from various perspectives.

I am also fortunate and grateful to receive guidance from Professor Uday Shanker Dixit, Professor Satish Vasu Kailas (IISC Bangalore) and Mr. P.S. Suvin (IISC Banglore). It was fantastic to have the opportunity to work with them through various collaborations and their valuable suggestions and concise comments have always been a source of inspiration to me. With their expertise and in-depth knowledge in my field of research, they had given various suggestions which brought my thesis work in good shape.

My sincere gratefulness to past and present departmental heads Professor A. K. Dass and Professor S. K. Dwivedy for their kind permission for enrollment, registration and several important supports at IIT Guwahati. I am also grateful to Dr. Pankaj Biswas and all the faculty members of Mechanical Engineering Department for giving me a comfortable and friendly environment for pursuing my research.

Next, I would like to express my special sense of gratitude to Mr. Nandan Kanan Das, assistant workshop superintendent and all the staffs of the workshop specially Mr. Dhaneswar

Khaklary, Mr. Mrinal Sarma, Mr. Dilip Chetri, Mr. Chandan Banikya, Mr. Ali, Mr. Bijoy Kumar Choudhury, Mr. Upen Gohain and Mr. Minesh Ch. Medhi for extending their help in fabrication of experimental setups and various other experimental work. I sincerely acknowledge the assistance received from Mr. Saiffuddin Ahmed, Mr. Sanjib Sarma, Mr. Jiten Basumatary, Mr. Pranjol Paual and Dr. Dhruba Jyoti Bordoloi in various experimental proceedings. I also wise to express my gratitude to the Central Instruments Facility, IIT Guwahati for providing technical support.

"A good friend is like a four leaf clover hard to find and lucky to have", I have been fortunate to be surrounded myself by some amazing friends, Rasmi, Sachin, Abhishek, Siddesh, Sarita, Sumit, Purnendu, Anupam Alok, Shuvayan, Mukul, Shivesh, Shyam, Shatrughan, Rajendra, Arun, Johnney, Muthuraja, Arbind, Woldaytinsay and Ketema. Thank you all for your support and encouragement. I am also thanks to internship students for their support. Special thanks are also due to Swapnali mam and Professor S.N. Bora for giving me warmth in their home. Also, special thanks to Neha, Smrati, Ankur, Swalpa, Snehil, Vinay, Rakhee, Mitali, Abhradip and Geetimukta who made my PhD journey a memorable one. Also, I am grateful to few amazing talented friends Nilotpal, Biswajit, Subrat, Anand, Shaym, Basant, Pankaj, and all other group members of Badminton Freaks for the beautiful evenings and keeping me healthy and physically fit.

It is my pleasure to acknowledge the help provided by my seniors, juniors and internship students, especially, Pavan, Dhannaram, Suresh, Charan, Bishal, Dilli Babu, Radha, Mahesh, Vignesh, Venkateshu, Arnab and Monami and all other lab members from our lab.

"The love of a family is life's greatest blessings". In this precious moment of my life, I would like to express my deep sense of gratitude to my parents, Mr. Dilip Kumar Gajrani and Mrs. Sunita Gajrani for their love, blessings and constant encouragement throughout my life. I would like to thanks my brother Krishna Kumar Gajrani and sisters Neha Poptani, Nisha Katariya for their love and best wishes. I want to offer my sincere gratitude to all extended members of my family. You have always been inspiring, supporting and teaching me to understand the true value of human life.

Kishor Kumar Gajrani

ABSTRACT

In metal cutting with continuous chips, severe friction exists over the cutting tool rake surface. High normal load of chip increases the real contact area and thus creating intimate contact with tool rake surface. Relative motion between the surfaces generates frictional heating to the cutting tool, resulting in high temperature at the tool-chip interface. As a result, crater wear develops on the tool rake surface. Thus, gradual tool wear (crater as well as flank wear) is commonly observed in metal cutting and the same is very difficult to eliminate.

Cutting fluids are often applied in machining to alleviate the severe friction and wear conditions. The two primary functions of cutting fluids are lubrication and cooling. Lubrication is effective when cutting fluid is introduced to the tool-chip interface through either penetration or diffusion, which is more likely to happen at low cutting speeds. Also, petroleum-based cutting fluids have various detrimental effects due to harmful chemical constituents, causing harm to the system (operator) and surroundings (environment). Researchers are trying to develop alternate methodologies to reduce or eliminate cutting fluids during machining. Apart from conventional cutting fluids, surface textures on cutting tool surface, coating of cutting tools, application solid lubricants and minimum quantity lubrication (MQL) are probable techniques for smooth machining.

The existing techniques should be improved as well as hybridised (combining two or more lubrication techniques) for more effective machining experience. The effectiveness of cooling and lubrication increases by providing micro-textures (dimple, grooves, and channels) on the cutting tool rake surface. Hybridisation of mechanical micro-textures on the cutting tools and minimum quantity nano-green cutting fluids enhances tribological performance between tool-chip interface, reduces machining forces, cutting temperature, workpiece surface roughness, tool-chip contact length and tool wear.

In this study, mechanical micro-textures are fabricated on the rake face of the cutting tool. Initially, tribological studies of mechanical micro-textured plasma nitrided high-speed steel (PN-HSS) pins having varying area density textures were conducted. Experiments were performed with both uncoated as well as MoS_2 coated pins. The coefficient of friction, wear, weight loss and wear rate of pins were investigated. The best results were obtained with MoS_2 filled micro-textures having 10% texture area density. Afterwards, machining experiments with un-textured (UT), mechanical micro-textured (MµT) and MoS_2 coated mechanical micro-textured (C-MµT) PN-HSS cutting tools were carried out. Performance of

C-MµT cutting tool is improved by mechanical micro textures due to the reduction in actual contact area between tool-chip interfaces and proper lubrication across the tool-chip contact area. C-MµT experiences 23.75 % lower tool-chip interface temperature, 41.06 % reduction in cutting force, and produces 14.37 % less workpiece surface roughness compared to UT cutting tool.

A comparative study of hard machining with different mechanical micro-textured (micro-dimple, parallel micro-groove and perpendicular micro-groove) and MoS_2 coated mechanical micro-textured tungsten carbide cutting tools are carried out. Six different uncoated and MoS_2 coated MµT are fabricated on the tungsten carbide cutting tool rake face, and their hard machining performance is compared with UT tool, during machining of AISI H-13 steel. MoS_2 coated cutting tool having MµTs perpendicular to the main cutting edge showed least machining forces, tool-chip interface coefficient of friction, workpiece surface roughness and less redundant plastic deformation work (lesser chip thickness) among all tested cutting tools.

Environmental friendly green cutting fluid (GCF) was developed using mixtures of various vegetable oils and emulsifiers. Afterwards, biodegradation, thermal, rheological, storage stability and anti-corrosion properties of in-house developed GCF are compared with commercial bio-cutting fluid (BCF) and mineral oil (MO). GCF was found to be highly biodegradable, more thermally stable with higher viscosity, better storage stability as well as anti-corrosion properties. For minimising the cutting fluid quantity during machining experiments, an economic minimum quantity cutting fluid (MQCF) setup was fabricated. The MQCF input parameters such as emulsion composition, stand-off distance between the nozzle and machining zone as well as nozzle spraying angle are optimised experimentally. Afterwards using experimental optimised input parameters, hard machining performance of MO, BCF and GCF with MQCF technique were compared. Machining performance with BCF is best among three followed by GCF, MO and then dry machining (DM), respectively.

Nano-green cutting fluids with varying concentration (0.1−0.5 %) of MoS_2 and CaF_2 based are prepared. The effect of the nano-solid lubricant (MoS_2 nanoplatelet and CaF_2 nanoparticles) enhanced cutting fluids are studied by conducting absorbance tests, dynamic viscosity tests, thermal conductivity tests, volumetric specific heat test and wettability test. Afterwards, hard machining experiments are carried out to evaluate the performance of nano-solid lubricant enhanced GCF using MQCF technique and it is found that 0.3 % MoS_2 based nano-green cutting fluids showed least wettability (lower contact angle), less machining forces, minimum coefficient of friction and workpiece surface roughness.

After experimentally optimising the above conditions, hybridisation of the above four individual sustainable machining processes is carried out to make machining more sustainable and environmentally friendly process. During hard machining, a combination of MμT tungsten carbide cutting tool with minimum quantity MoS_2 based nano-GCF is used. Experimental results show that the hybridisation of above four individual sustainable machining techniques results in the reduction of cutting forces in the range of 38−59.5%, feed forces in the range of 15.9−39.2% and workpiece surface roughness in the range of 15.9−61% compared to an untextured conventional tool (dry machining). Also, tool wear enormously reduces after hybridisation of all four sustainable techniques compared to untextured conventional cutting tool.

TABLE OF CONTENTS

LIST OF FIGURES

LIST OF TABLES

ABBREVATIONS

ANN	Artificial neural network
ANOVA	Analysis of variance
ASTM	American society for testing materials
A2	2% texture area density pin
A4	4% texture area density pin
A6	6% texture area density pin
A8	8% texture area density pin
A10	10% texture area density pin
A12	12% texture area density pin
A14	14% texture area density pin
A2-M	2% MoS_2 filled texture area density pin
A4-M	4% MoS_2 filled texture area density pin
A6-M	6% MoS_2 filled texture area density pin
A8-M	8% MoS_2 filled texture area density pin
A10-M	10% MoS_2 filled texture area density pin
A12-M	12% MoS_2 filled texture area density pin
A14-M	14% MoS_2 filled texture area density pin
BCF	Bio-cutting fluid
BOD	Biological oxygen demand
CaF_2	Calcium fluoride
CCD	Central composite design
CCRD	Central composite rotatable design
COD	Chemical oxygen demand
COF	Coefficient of friction
C-MµT	Coated-mechanical micro-texture
CryoMQL	hybrid cryogenic and MQL
CTAB	Cetyltrimethylammonium bromide
DLC	Diamond like coating
DM	Dry machining
DOE	Design of experiment

EDM	Electrical discharge machining
EOoW	External oil-on-water
EDS	Energy dispersive spectroscopy
FC	Flood cooling
FEA	Finite element analysis
FEM	Finite element method
FESEM	Field emission scanning electron microscope
GCF	Green cutting fluid
GCF-0.3C	0.3 % concentration calcium fluoride based nano-green cutting fluid
GCF-0.3M	0.3 % concentration molybdenum disulphide based nano-green cutting fluid
GRA	Grey relation analysis
HSS	High speed steel
LAM	Laser assisted machining
LVDT	Linear variable differential transducer
Micro-EDM	Micro-electrical discharge machining
MO	Mineral oil
MoS_2	Molybdenum disulphide
MQCF	Minimum quantity cutting fluid
MQL	Minimum quantity lubrication
MRR	Material removal rate
MµT	Mechanical micro-texture
MWCNT	Multi-walled carbon nano tube
Nano-GCF	Nano-green cutting fluid
NDM	Near-dry machining
PCBN	Polycrystalline cubic boron nitride
PN-HSS	Plasma-nitrided high speed steel
PDT	Perpendicular texture
PDT-M	Molybdenum disulphide coated perpendicular texture
PDT-NGCF	Perpendicular texture cutting tool with nano-green cutting fluid
PT	Parallel texture
PT-M	Molybdenum disulphide coated parallel texture
RSM	Response surface methodology
TEA	Triethanolamine

UV	Ultraviolet
UT	Untextured tool/pin (Conventional tool/pin)
VT	Vickers texture
VT-M	Molybdenum disulphide coated Vickers texture
xGnP	Exfoliated graphite nano-powder
XRD	X-ray diffractometry
WC	Tungsten carbide
WS_2	Tungsten disulphide

Notations

α	Rake angle
β	Friction angle
φ	Shear angle
ψ	Sphericity
ξ	Chip reduction ratio
A_w	Area of tool-chip contact
K_r	Angle of approach
λ_s	Inclination angle
α_o	Clearance angle
r_ε	Nose radius
τ_c	Shear strength at tool-chip interface
c_p	Specific heat
c_{bf}	Specific heat of base fluid
c_{pnf}	Specific heat of nanofluids
f	Feed
k	Number of input parameters
k	Thermal conductivity
k_{eff}	Effective thermal conductivity
k_{bf}	Thermal conductivity of base fluid
k_p	Thermal conductivity of nanoparticles
ν	Poisson's ratio
v	Cutting speed
d	Depth of cut
d_f	Degree of freedom
q	Heat flux
ω	Nanoparticles mass fraction
A_c	Shearing area
A_d	Texture area density
C_I	Confidence interval for any individual population parameter
E	Young's modulus

E'	Hertz elastic modulus
E_a	Activation energy
F_c	Cutting force
F_f	Feed force
F	Load
F_r	Resultant force
F_s	Shear force
F_y	Thrust force
F_z	Main cutting force
L	Sliding distance
l_r	Real tool-chip contact length
l_a	Apparent tool-chip contact length
$\bar{P}_c$	Critical load for a single-asperity contact
R	Real gas constant
R^2	Coefficient of determination
R_a	Surface roughness
S_y	Yield strength
T	Temperature
$t(d_f;\alpha)$	Critical value of *t*-test
W	Wear rate
$\bar{y}$	mean value

Chapter 1

INTRODUCTION AND LITERATURE REVIEW

1.1 Introduction

Machining is one of the oldest fundamental manufacturing processes. Before the industrial revolution in the 18th century, hand tools were used for machining. Ever since the advent of steam power, power-driven machine tools became common in industries. Some of the conventional machining processes are turning, milling, drilling and grinding. Among these, turning is the most widely used machining process. In view of its importance, the present thesis investigates the turning process from the viewpoint of sustainability in a green manufacturing environment. This chapter covers introduction about turning process, cutting tool, cutting fluid, environmental aspects in turning process. Also, relevant literature review about hard machining, sustainable machining, dry machining, near-dry machining, environmental friendly cutting fluids and cutting tool performance evaluation.

1.2 Turning process

Turning is a traditional machining process for obtaining cylindrical, conical or tapered parts. In this process a single point turning tool of relatively harder material compared to the workpiece and having a sharp cutting edge is fed to the rotating workpiece. The cutting action takes place due to fracture of the workpiece material at the shear zone to remove the unwanted part for producing the desired geometry. However, it is observed that under normal machining conditions at moderate and high speeds, the thickness of the shear zone is minimal and it can be idealised as a plane. The plane where the shear occurs is known as the shear plane, and its inclination with the machined surface is called the shear angle. Figure 1.1 shows the schematic of the orthogonal turning operation.

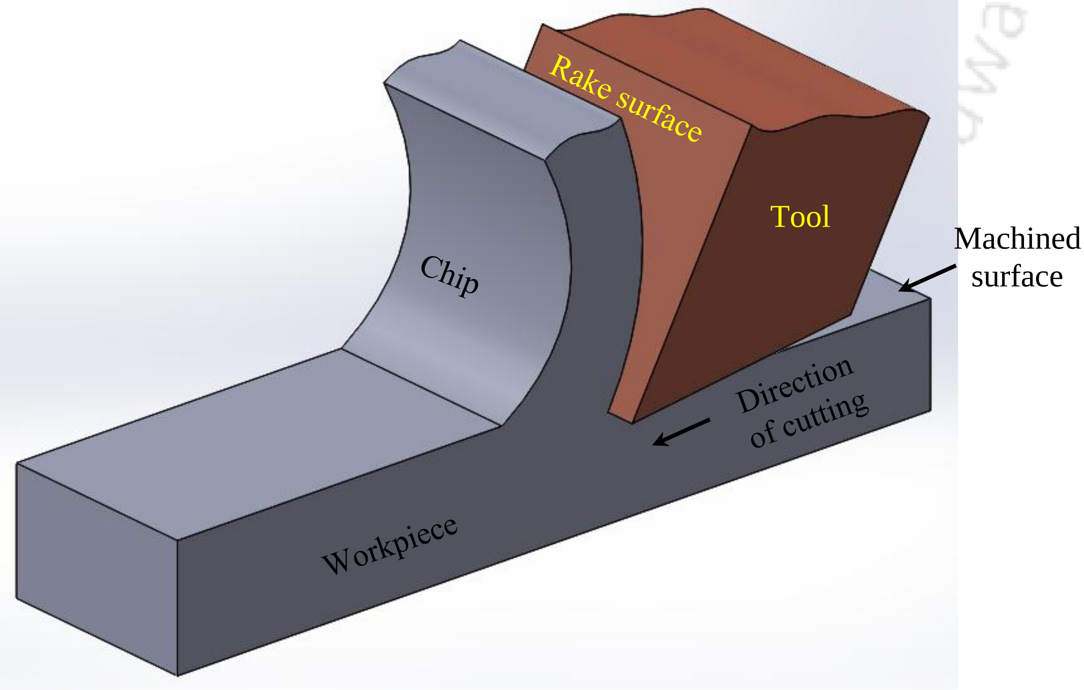

Figure 1.1. Geometry of the orthogonal turning

Often, large amounts of data from experiments are needed for evaluation of machining performance. In the turning operation, the primary process parameters are cutting speed, feed and depth of cut, whose optimum value depends upon the cutting tool and workpiece material. The significant performance parameters are tool-chip interface temperature, cutting force, feed force, coefficient of friction, workpiece surface roughness and tool wear. Other relevant parameters are cutting fluid, cutting fluid application technique, cutting tool material, work material, tool geometry, workpiece dimension, machine stability, etc. that have the direct influence on the turning process. Tool geometry affects chip formation, tool strength, cutting force, feed force and workpiece surface roughness. The cutting force, feed force, cutting fluid and cutting fluid application technique has a direct influence towards the workpiece surface roughness and tool wear. It is always important to work with optimum process parameters to obtain better surface finish, minimise tool wear and to make machining more sustainable.

1.3 Basics of turning

In turning operation, there are three zones of deformation. Figure 1.2 shows the shear, friction and tertiary zones that influence the cutting response. In shear (primary deformation) zone, work material plastically deforms along the shear plane in continuous or discontinuous manner. In friction (secondary deformation) zone, chip moves over the rake surface of the cutting tool, which causes severe friction between sliding surfaces. Therefore, a high amount of heat is generated, which results in the high tool-chip interface temperature. Friction and temperature results in tool thermal softening and tool wear. In the tertiary zone, flank surface of the cutting tool comes in contact with the workpiece. In this zone, the deformation is mostly elastic. The maximum temperature in the secondary deformation zone can be up to 1000°C depending on the workpiece and cutting tool materials as well as cutting conditions. Therefore, the tool-chip interface temperature must be moderated and controlled. The forces experienced in the friction and shear zones can also be quite significant, influencing the cutting process and chip formation.

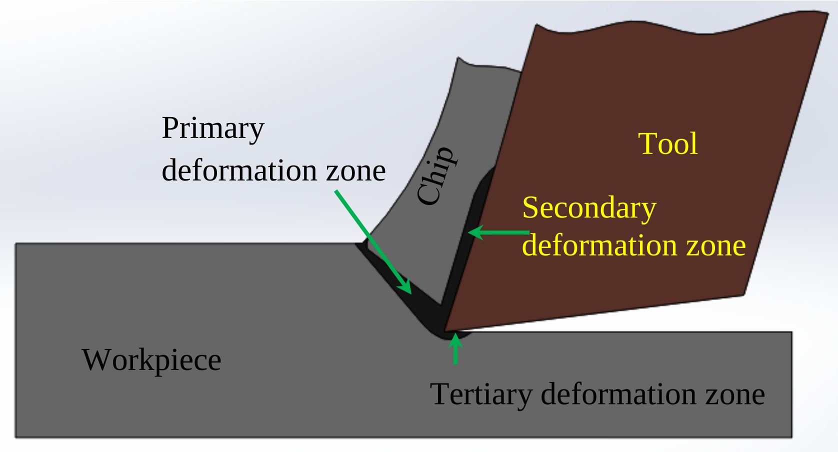

Figure 1.2. Deformation zones in cutting

The friction in the secondary deformation zone further influences the chip formation at the shear zone. Two models are generally accepted in showing the influence of the friction on the shear zone: the Lee and Shafer Shear Angle relation and Merchants Shear Angle relation. If φ is the shear angle, β is the friction angle, and α is the tool rake angle, the following shear angle solutions show the relationship between friction and shear angle.

Merchants Shear Angle relation

$$2\varphi + \beta - \alpha = 90° \tag{1.1}$$

Lee and Shaffer Shear Angle relation

$$\varphi + \beta - \alpha = 45° \tag{1.2}$$

With the change in the friction angle (β) at a constant rake angle (α), the direct influence on cutting speed can be seen. The shear angle influences the force required to shear the chip as seen in the following equation, where F_s, F_f and F_c is the shear, feed as well as cutting force. τ is the shear strength of the workpiece material, t is the thickness of the material being cut and, b is the width of the cut.

$$F_s = \frac{\tau bt}{sin\varphi} \tag{1.3}$$

A decrease in β causes an increase in φ and a corresponding decrease in the shear force required to form the chip.

$$\tan(\beta - \alpha) = F_f / F_c \tag{1.4}$$

Reduction in the tool-chip interface coefficient of friction leads to a decrease in the energy required for chip formation, thus improving the process efficiency.

1.4 Hard turning

The vast majority of components used in the automotive industry are machined to final geometrical form after hardening. Currently, grinding is the predominant method for finishing these parts, which include shafts, gears, pinions and bearing, due to its features like easy to operate and control. Grinding has some inherent problems like the use of fixed shape of bonded wheels taking the longer time to finish, which increases the cost of operation. Although, shaped wheels can be used to address the first problem, still, this alternative is quite expensive as for each product type it needs one shaped wheel. These problems gave rise to the efforts to develop a cost-effective and environmentally safe process to finish the hardened parts to the similar levels as grinding. The improvement in machine tools and tooling technology proved to be a shot in the arm of the solution seekers.

Nowadays, due to improvement in machine tool rigidity and the development of advanced tool materials like coated tungsten carbide, polycrystalline cubic boron nitride (PCBN) cutting tools, hard turning gained ground as a cost-effective alternative to grinding.

Hard turning is performed on the materials within the 45 to 68 HRC, using a variety of solid or tipped cutting inserts. Ever since its introduction in the mid-eighties, the process has dramatically gained popularity. More and more manufacturers are now recognising the advantages of hard turning over grinding.

Although grinding is known to produce good surface finish at relatively high or low feed rates, hard turning can produce as good or better surface finish at significantly higher material removal rates. Even though the process is performed within the small depth of cut and feed rates, the estimate of reduced machining is as high as 60% for conventional hard turning [1].

1.5 Friction in turning

Friction is the resistance force that opposes the sliding motion of surfaces that are in contact. Classical friction theory gives the coefficient of friction as the ratio of the tangential force and normal force between the surfaces in contact. In classical friction applications, due to the moderate normal forces, contact occurs only at very few asperities between the opposing surfaces, and as such the real area of contact is far less than the apparent surface area. Thus the apparent area of contact does not affect the coefficient of friction. Figure 1.3 shows a representation of two surfaces in contact under similar conditions.

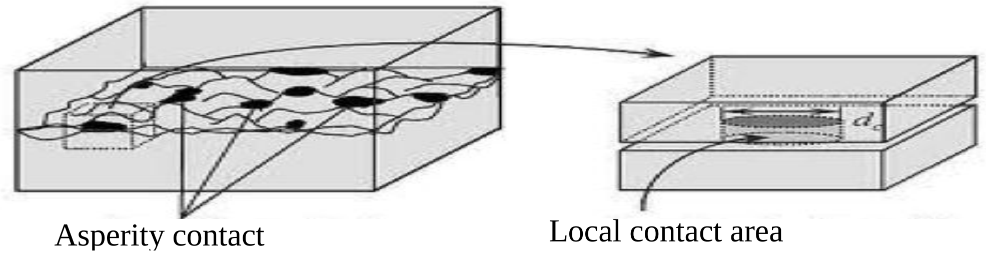

Figure 1.3. Localized contacts of the asperities

In the turning process, frictional force opposes the motion of the chip on the tool rake surface, accounting for approximately 25% of the specific cutting energy [2]. It leads to high tool temperatures that limit process productivity. High temperatures encountered due to friction causes several types of tool wear. Crater wear is experienced on the rake surface of the cutting tool. It can cause catastrophic failure on the cutting tool as it can lead to fracture of the tooltip if much material is worn away. Adhesion also occurs at the tool-chip interface due to the high pressure and temperature at junctions of the asperities in contact. Furthermore, asperities in contact may adhere to the cutting tool and subsequently fracture removing bits of the cutting tool and hardened chip. These hard pieces of metal can cause abrasive wear on the tool as they are embedded in the chip and moved along the rake surface that can cause cutting tool wear. Diffusion occurs between the cutting tool and chip, which increases exponentially with temperature. Diffusion refers to atoms moving from high concentration to low concentration from the tool to chip and chip to tool, causing a change in tool composition and reduction in hardness [2]. Therefore, friction reduction would improve tool life, and it also results in savings tool costs.

1.6 Friction reduction

Surfaces in sliding contact can be tailored to reduce friction with several methods. A popular method is to use coatings (non-stick coatings used on frying pans or coatings with low shear strength used) on tool surfaces that promote sliding between surfaces in contact by reducing adhesion. Another popular method is by using liquid (oil, emulsions, cutting fluids) and solid lubricants (molybdenum disulphide (MoS_2), calcium fluoride (CaF_2), graphite, etc.).

1.6.1 Coatings

Cutting tool coatings help for reduce adhesion at the tool-chip interface and chemical interactions between chip and cutting tool, improving tool life and reducing friction, tool-chip interface temperature and machining forces. Also, the temperature at which the tool starts to disintegrate can be increased through the use of coatings. It is estimated that approximately

20% of the heat generated during cutting is transported into the tool [3]. Therefore, improving the thermal properties of the tool can also improve tool life. Furthermore, coatings also result in the reduction of workpiece adhesion to the cutting tool surface. These coatings influence the chip flow and formation, allowing the cutting tool for cutting at higher speeds.

1.6.2 Cutting fluids

Cutting fluids are generally used for friction reduction, cooling and chip evacuation in machining. Cutting fluids are classified as lubricants and coolants. Lubricants are primarily used for friction reduction at low cutting speeds with minimal cooling capacity whereas coolants are used at higher cutting speeds for heat dissipation with minimal friction reducing properties.

In conventional turning, friction cannot be significantly reduced by the application of coolants. However, the heat generated between the tool and workpiece being machined by friction can be reduced by a lubricant. Coolants work primarily at higher speeds to cool the tool and workpiece that increases tool life. Dimensional accuracy of the workpiece and tool hardness is maintained by the removal of the heat generated during the process. Coolants are sufficiently stable to avoid its chemical breakdown due to the high temperatures.

Lubricants work by chemically reacting with the fresh surface of the chip created during turning, forming a film of low shear stress separating the tool and the chip. Lubricants are primarily effective at low speeds for friction reduction and tend to break down during high-speed operations due to heat generation. Lubricants can reduce the forces experienced thus allowing work on less powerful machine tools with less energy used and less tool failure. Temperature has a substantial effect on the effectiveness of the lubricant being used. Lubricants can provide solid film protection until the temperature increases sufficiently such that the film melts and breakdowns completely decreasing the effect of the lubricant.

Oils adhere better and react to high pressures than water-based lubricants and therefore offer better lubricity. However, water-based coolants have better capability to dissipate heat from the tool-chip interface region.

1.7 Environmental aspects in turning

Environmental concerns call for the reduction of cutting fluid in metal cutting practice and nowadays it has become an essential objective in industry. Efficient utilisation of cutting tool in machining is an essential focus of researchers. The performance of cutting tool depends on the process parameters and the cutting environment. Many times, cutting fluid is used to enhance the tool life and to improve the surface integrity. The fluids that are used to lubricate in machining contains environmentally harmful or potentially damaging chemicals constituents. The airborne particle of cutting fluids can be inhaled by operators that cause respiratory irritation, asthma, pneumonia, dermatitis and several types of cancers (oesophagus, skin, lung, pancreas, colon etc.) [4, 5]. Figure 1.4 illustrates various diseases caused due to prolonged exposure to petroleum-based cutting fluids.

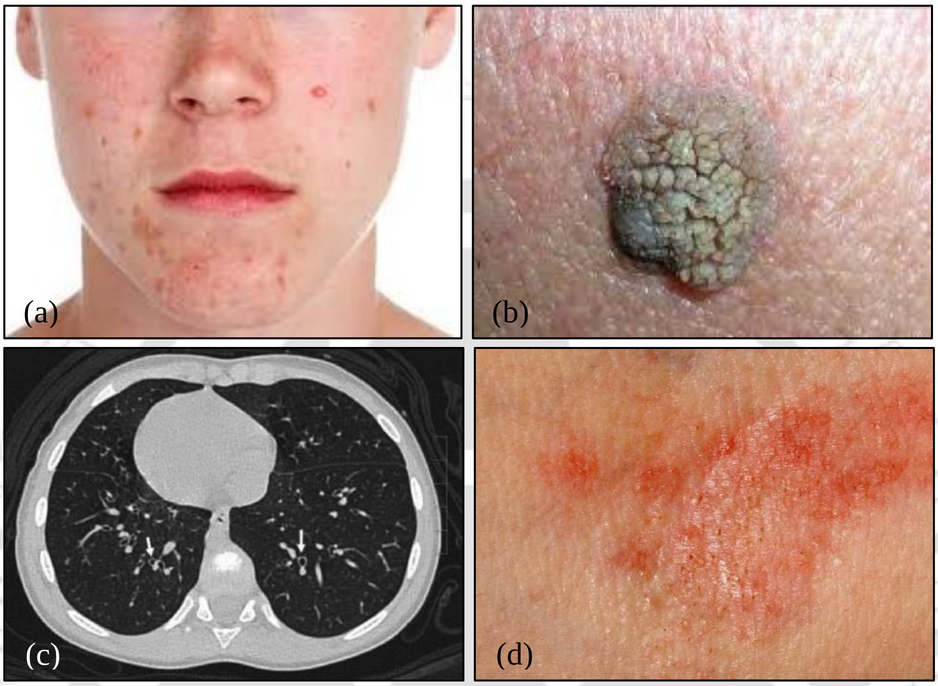

Figure 1.4. Various diseases caused due to prolonged exposure of the petroleum-based cutting fluids: (a) oil acne [9], (b) skin cancer [10], (c) mild bronchiectasis [11] and (d) dermatitis [12]

The concept of dry machining has the advantages of non-pollution of the atmosphere and water, no residue on the swarf resulting in the reduction of the disposal and cleaning cost, and no danger to health such as skin rupture and allergy etc. As such, dry machining has become popular with regards to the safety of the environment as well as low production cost. However, sometimes the surface integrity of the finished product in dry turning is not superior as compared to wet turning. The concept of surface textures, minimal quantity fluid, green and nanofluids in turning seems to be a better alternative to conventional dry and wet turning [6−8]. Moreover, the combination of the above processes makes machining much more sustainable by reducing adverse environmental effects, associated costs and enhancing operators safety. Furthermore, it also enhances machining performance and final workpiece surface finish.

1.8 Literature review

Nowadays "sustainable machining" has become very popular. Sustainable machining considers environmental, economic and social aspects. The sustainable machining aims to develop technologies for transforming machining with the objectives of reducing the emission of greenhouse gases, avoiding the use of nonrenewable or toxic materials and avoiding generation waste.

Nowadays, there has been an increasing concern about environmental consideration in machining. Sustainable machining, in particular, and green machining, in general, has become popular in industries. Sustainable machining is crucial for the twenty-first century, integrating all the issues of machining with its ultimate aim of reducing and minimising environmental impact and resource consumption during a product life cycle. Sustainable machining is a method for minimising wastes and pollutions. These goals can be achieved by a proper strategy, which focuses on tool surface modification, coatings, minimal cutting fluid, as well as green and nanofluids.

1.8.1 Dry machining

Dry machining is ecologically desirable, and it will be considered as a necessity for manufacturing enterprises in the near future. Industries will be compelled to consider dry machining to enforce environmental protection laws for occupational safety and health regulations. The advantages of dry machining include non-pollution of the atmosphere (or water); no residue on the swarf which will be reflected in reduced disposal and cleaning costs; no danger to health; and it is non-injurious to skin and is allergy free. Moreover, it offers cost reduction in machining.

The various possible routes to achieve clean machining processes were analysed and discussed by Byrne and Scholta [13]. Elimination of the use of cutting fluids, if possible, can be a significant incentive. The costs connected with the use of cutting fluids are estimated to be many more times than the labour and overhead cost [14]. Hence the implementation of dry machining will reduce manufacturing costs. In the manufacturing industry, cutting fluids help: to remove the heat generated due to friction during cutting; to achieve better tool life, surface finish and dimensional tolerances; to prevent the formation of built-up edge and to facilitate the transportation of chips. Coolants are essential in the machining of materials such as aluminium alloys and most steels, which tend to adhere to the tool and cause a built-up edge. At the same time, the coolants produce problems in the working environment and also create problems in waste disposal. It creates a large number of ecological problems, but which in turn result in more economical overheads for manufacturing industries [15, 16].

If industries were to practice dry machining, then all of the problems as mentioned above should be addressed satisfactorily. The cutting fluid industries are reformulating new composites that are more environmentally friendly and which do not contain lead, sulphur or chlorine compounds. The use of cutting fluids will be increasingly more expensive as stricter enforcement of new regulation and standards are imposed. It leaves no alternative, but to consider dry machining [17].

In dry machining, there will be more friction and adhesion between the tool and the workpiece, since they will be subjected to higher temperatures. It will result in increased tool wear and hence the reduction in tool life. Higher machining temperatures will produce ribbon-like chips, and this will affect the form and dimensional accuracy of the machined surface [18]. However, recent developments in dry machining can overcome the issues mentioned above and are capable of reducing friction, which ultimately reduces temperature and enhances overall machining performance. Some of these developments are applying coatings of solid lubricants or addition of solid lubricants with tool materials, tool geometry modifications, under cooling system, use of heat pipe, cryogenic cooling, etc. [6, 18−21]. Surface texturing is one such novel sustainable manufacturing methodology that can allow environmental friendly machining by altering the surface topography.

1.8.2.1 Surface textures

Surface texturing refers to the modification in the topography of surface to improve tribological performance between sliding pairs. It has been reported that friction and wear results in an economic cost of 5% of GDP of developed countries [22−25]. Researchers have found that surface texturing can help to improve load carrying capacity and better lubrication [26−28]. Moreover, the surface modifications have been found to decrease wear and friction in piston rings, piston pins and hydrodynamic bearings [29−31]. Recently, surface texturing has also been used in cutting tools. To provide lubrication to the inaccessible area of the tool-chip contact zone and to decrease contact length of the chip on the tool, the research has been focused on the development of micro and nano textured cutting inserts to have a cleaner production with fewer carbon footprints [32−35].

Electric discharge machining [36, 37], mechanical grinding [38], electron beam lithography [39], abrasive jet machining [40] and laser beam machining [41, 42] have been used to produce textures on the surface. Figure 1.5 illustrates few micro-textured cutting tools fabricated using different techniques. Researchers [43−46] have reported that the modified surface of the cutting tool improves anti-adhesion, wear resistance, cutting forces, cutting temperature and friction coefficient [47−49]. The following section highlights a comparative analysis between conventional plane cutting tools and textured cutting tools.

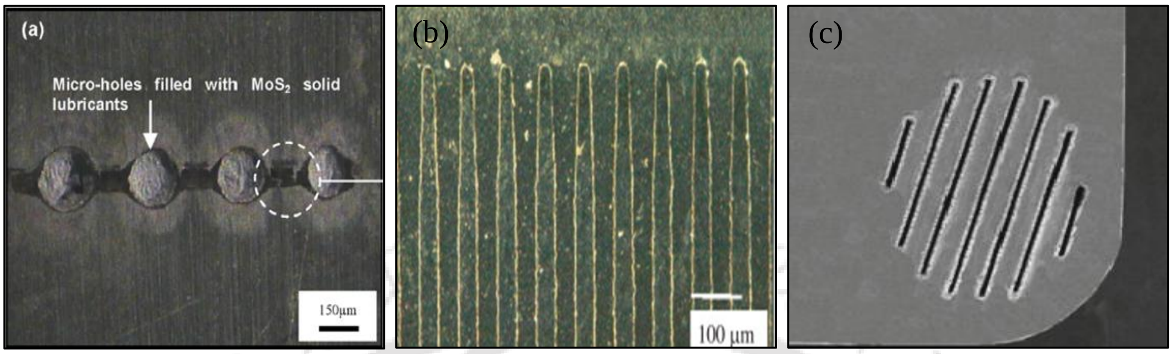

Figure 1.5. Various micro-textured cutting tools fabricated using (a) micro-electric discharge machining [36], (b) electron beam lithography [39] and (c) Ti-sapphire laser [42]

1.8.1.1.1 Machining forces

The effectiveness of a cutting process is governed by cutting forces, which are affected by cutting conditions (cutting velocity (*v*), feed (*f*) and depth of cut (*d*)), cutting tool geometry and workpiece material properties. Any method for the reduction of cutting force would result in an extension of the life of the tool and a better surface finish of the machined product. The cutting forces could be reduced with the use of textured tools in machining as discussed below.

During the cutting process, the average frictional force (F_f) between chip and tool rake surface has been related as per the following equation [50, 51]:

$$F_f = A_w \tau_c \tag{1.5}$$

where A_w represents the area of tool-chip contact and τ_c denotes shear strength at tool-chip interface. The cutting force components (for Coulomb friction) in turning are related to frictional force as follows [51]:

$$F_r = \frac{F_f}{sin\beta} \tag{1.6}$$

$$F_y = F_r cos(\beta - \alpha) \tag{1.7}$$

$$F_z = F_r \sin(\beta - \alpha) \tag{1.8}$$

where F_r denotes resultant force, F_y is thrust force, F_z is the main cutting force, β denotes friction angle, α is rake angle. Thus, it can be deduced that cutting forces have a direct relation with shear strength at the interface and contact area.

Xie at al. [52] found a reduction of 32.7% in cutting forces for the micro-grooved tool in comparison to a conventional plane tool for different material removal rates while machining titanium alloy. They reported that the depth of micro-grooves significantly affected the force reduction. A deep groove resulted in more contact area between chip and rake surface of the tool and hence resulted in high cutting forces. However, Obikawa et al. [39] found that lubrication effectiveness of texture increased with small patterns having more depth while machining aluminium alloy A6061-T6. This trend could be accounted for the fact that pattern having shallow depth would quickly fill up with debris as chip flow over textured rake surface. However, if the depth of the groove is more, not only the lubricant storage capacity would increase, but it would also provide more space for debris entrapment. Therefore, shallow depth pattern when filled with debris would result in more frictional force between the tool-chip interface and hence would account for high cutting forces as compared to the pattern having more depth.

Lian et al. [53] and Xing et al. [54] related force reduction during metal cutting with shear strength and tool-chip contact length. The micro-grooves filled with MoS_2 (having lower shear strength) reduced the cutting forces during turning of hardened steel. They reasoned the formation of a thin lubricating film between chip back and tool rake surface for the reduction in frictional forces. Moreover, micro-grooves were found to decrease the effective contact area between chip and tool, which also resulted in the force reduction.

Kawasegi et al. [55] showed nano-textured rake surface to be effective than the micro-textured tool for force reduction while machining aluminium alloy. It was found that material adherence to tool surface was more in micro-textured pattern as compared to nano-textures. They reported that grooves oriented in a perpendicular direction performed better than parallel grooves. It can be accounted for the reason that because of the plastic deformation of work material in parallel grooves, there occurred severe adhesion and hence higher cutting forces. However, for grooves oriented at 90° phase difference to chip flow direction provided more restricted contact area and hence resulted in a reduction in frictional forces.

Few research works have also been focused on studying the effect of texturing on the flank surface. Researchers found that high cutting speed resulted in an ineffective performance of textured tool [37, 54]. It could be accounted for the reason that lubrication effectiveness decreases with a rise in cutting speed while machining hardened steel. It was because the distance to which lubricant penetrated into the machining region was inversely proportional to cutting speed.

Texturing has also been found to decrease the variability of cutting forces during turning of hardened steel [37]. It is because of the textured cutting insert maintained more consistent tool-chip contact length as compared to the plane tool. They also reported 100% textured surface known as areal texture to be more beneficial in force reduction as compared to the linear grooves.

Similar to the findings of Jianxin et al. [46], another study reported the micro holes filled with solid lubricant on rake surface to be more effective in comparison to flank surface and un-textured tool while machining hardened steel [56]. Wenlong et al. [57] compared the effect of MoS_2, CaF_2 and graphite filled in micro holes. For cutting speed up to 100 m/min, MoS_2 was found to be superior for force reduction while machining hardened steel. However, above 100 m/min, CaF_2 was found to perform better. It may be because at the temperature above 450 °C, MoS_2 began to get oxidised to form MoO_3, which enhances the friction and hence high cutting forces were developed.

Thus, it can be inferred from the above literature that textured cutting tools can effectively help in reduction of cutting forces. However, the researchers have followed trial and discovery approach in the development of textured pattern, but the effectiveness of such pattern may be increased by ensuring less contact area between chip and tool rake surface. However, texturing should also ensure that strength of cutting edge is not reduced due to changes made on rake surface of cutting insert to prevent catastrophic tool failure.

1.8.1.1.2 Cutting temperature

The primary purpose of cutting fluid during the machining process is to provide lubrication and cooling. However, because of environmental obligations, there has been an evolution of new techniques for temperature control in machining. Due to the better effectiveness in temperature control, the surface textured tools have also been reported by several researchers. The average temperature of the chip near the cutting tip (θ_t) can be calculated using the following formula [58]:

$$\theta_t = \theta_0 + \frac{R_1 v_s \tau_s}{c_1 \rho_1 V} \sin\phi + 0.752 R_2 \tau_c \sqrt{\frac{a_2 l_f V}{\psi}} / \lambda_2 \tag{1.9}$$

where θ_0 is ambient temperature, R_1 represents ratio of heat flowing into chip to total heat generated by shear, R_2 denotes ratio of heat flowing into chip to total heat generated by tool-chip friction, V is cutting speed, v_s denotes shear velocity, ϕ is shear angle, τ_c represents shear strength at the tool-chip interface, τ_s is shear strength of workpiece. c_1, ρ_1, λ_2, a_2 represents the chip-specific heat, chip density, thermal conductivity and thermal diffusivity of the workpiece at temperature $(\theta_s+\theta_0)/2$, respectively. θ_s is the average shear plane temperature, l_f represents contact length of chip-tool interface and Ψ is the deformation coefficient of the chip.

From Eq. 1.9, it can be inferred that ambient temperature depends upon l_f, which decreases due to the presence of textures and using solid lubricant in texturing further reduces the shear strength (τ_c) of the tool-chip interface. Thus, micro-textured cutting inserts were found to reduce the cutting temperature of the tool-chip interface during machining hard to cut materials. In case of the micro-textured tool without lubrication, the texturing provided aerodynamic lubrication and a decrease in the tool-chip contact length; whereas, for the lubricated textured tool, the smearing of solid lubricant on rake surface was found to decrease the cutting temperature effectively. Hence, self-lubricating tool helped to effectively control the temperature in the processing zone while machining hard to cut materials.

In another study, it was found that the temperature at cutting tip in micro-grooved cutting tool was less than a conventional plane tool [52]. The authors reasoned the grooves to provide the site for heat to be dissipated from rake surface when the chip travelled over the tool and prevented the temperature not to rise above 500 °C during machining titanium-based alloy. It resulted in better convective heat transfer and provided aerodynamic lubrication in case of textured cutting inserts.

Similar to the previous study, another study has also reported a rise in the temperature with rising cutting speed while turning carbon steel [51]. They reported that the elliptical grooves were able to reduce more temperature as compared to linear and inclined grooves. It was because the elliptical grooves provided more surface area on rake surface for heat dissipation. It is due to the air pockets created between textured rake surface and chip back surface resulted in aerodynamic lubrication, which helped to lower the machining temperature.

Ze et al. [56] found texturing on rake surface to result in lowest temperature rise when compared to texturing provided on the flank surface during machining of the Ti6-Al-4V alloy. It was because the chip carrying 80% of the heat generated during metal cutting travelled over the rake surface of the cutting tool. Thus, the grooves on rake surface decreased tool-chip contact length, which in turn decreased heat conduction between tool and chip.

Research has also been carried out for studying the effect of soft coatings (MoS_2, CaF_2 and WS_2) on textured surfaces. In this regard, it found that WS_2 soft coated tool helped in more effective control of the tool-chip interface temperature as compared to textured and conventional plane tool [54]. A 10–20% reduction in the temperature was observed by the use of WS_2 soft coated tool during machining of steel. It was due to the ultra-low friction coefficient and a high-temperature resistance of WS_2 coating.

From the above discussion regarding machining zone temperature using textured cutting tools, it can be observed that temperature reduction occurs near the tool cutting edge. The lubrication regime developed between the sliding surfaces ensures a better temperature reduction, which helps to maintain the tool edge integrity and ensures less tool wear and chip adhesion as has been discussed in the following section.

1.8.1.1.3 Friction

It has been reported that 30% of the world's energy is used to overcome friction. In various automotive applications, the use of a highly smooth surface is required for reducing friction, which accounts for 40% of energy consumption in an engine [58]. However, due to material properties and machining constraints, the surface finish that can be achieved on a surface is limited. Another possible alternative used for reducing the coefficient of friction is texturing. The textured pattern has been extensively used not only in sliding contact but also in metal machining for storage of lubrication, which not only reduces friction; but, also prevents the excessive temperature rise in contact zone [40].

A study reported banded grooves (having polished surface in between micro and nano texturing) provide lesser friction coefficient than parallel and perpendicular direction oriented grooves while machining medium carbon steel. It may be because the tool surface lubricity was enhanced by the creation of banded grooves [59].

Another study reported a decreasing trend for friction coefficient with a rise in cutting speed during turning of Ti6Al4V. The texturing on rake surface was found to be more beneficial than on the flank surface. It might be due to the formation of the MoS_2 lubricant layer which resulted in less friction as chip slide over tool rake surface [56].

Surface texturing has also been found to shift the Stribeck curve, which results in less coefficient of friction between the contact of two solids [40, 60]. It may be because surface texturing provided micro pool lubrication regime (in case of boundary and mixed lubrication), which decreased friction. The authors also reported a decrease in coefficient of friction with a decrease in groove aspect ratio. Thus, use of the textured tool in turning helps to provide better lubrication regime with less coefficient of friction by using appropriate lubricant.

1.8.1.1.4 Workpiece surface roughness

The poor thermal conductivity of advanced materials results in high temperature in the process zone, which affects tool wear and hence surface finish. The result of poor surface finish affects post-finishing operations, which ultimately increases the manufacturing cost of the product. The following section highlights the use of micro textured cutting inserts for reducing the surface roughness of the machined workpiece.

Micro-textured cutting inserts increased the surface roughness of titanium and steel parts, respectively as reported in [61, 62]. However, the deviation in surface roughness (E_R) was decreased using textured cutting insert. The deviation (E_R) in surface roughness (R_a) has been defined as the maximum fluctuation in surface roughness reading from the mean value of five points reading taken over the cylindrical workpiece. Xie et al. [61] used this term to signify that although conventional plane tool results in better surface quality than the grooved tool, it produced more uneven surface. It was accounted because of more chattering in the plane tool as compared to the textured tool.

However, contradictory to findings of [61, 62], Jiang [63] found that bio mimicked cutting inserts improved surface finish as compared to highly polished PCBN insert while turning 4340 hardened steel. The better surface finish of the machined workpiece can be accounted for the better anti-wear ability of textured tool. Such a phenomenon helped to maintain the integrity of cutting edge for an extended period [64].

1.8.1.1.5 Anti-adhesion and tool wear

The production rate of any industry is highly dependent upon tool life and the number of parts that can be manufactured from a given tool. During metal cutting, the adhesion of work material with tool results in a decrease in the repeatability of the tool and hence leads to wear either at rake or flank surface. The following section highlights a comparative analysis of tool wear between the conventional plane and textured cutting inserts.

After machining of hardened steel, Jianxin et al. [51] performed elemental analysis of textured tool to confirm the fact that solid lubricant filled in elliptical grooves, having lower shear strength was smeared on the tool surface. It prevented adhesion of work material on rake surface and hence resulted in lesser tool wear. However, in the conventional plane tool;

the iron (Fe) particles (from workpiece material) could be located on WC insert, which indicated severe adhesion and tool wear with the progression of the cutting process.

Xie et al. [52] investigated the surface micrograph of worn rake surface of the conventional and grooved tool during turning of titanium alloy. The wear pattern on the grooved tool was found to be less, which could be accounted for rapid heat removal that occurred in the textured tool. However, wider grooves (123 µm) were found to result in more wear. It was because the wider grooves (with no lubrication) resulted in more friction between the tool-chip interface.

Sugihara and Enomoto [56] inspected the anti-adhesion properties generated by the textured tool while turning steel. The dry cutting was found to result in more adhesion and hence a large concentration of work material on rake surface. Moreover, the pockets provided by grooves for storage of lubrication resulted in less temperature rise and hence lesser adhesion for the developed tool. The banded nano textures were found to reduce the adhesion by 50% as compared to nano grooves on rake surface.

Lei et al. [65] found 28% reduction in contact area for micro pool lubricated cutting insert as compared to dry cutting during machining of mild steel. Due to micro pool lubrication, the direct tool-chip contact area is reduced from 1.8 mm to 1.3 mm. The decreased direct contact area resulted in less friction force. Moreover, due to high interface temperature during machining, the thermal expansion of solid lubricant stored in micro-holes make lubricant rise above the pattern and forms a thin lubricating layer at the tool-chip interface. Hence, due to the combined effect of less friction force and lubrication, tool wear is found to be reduced as compared to the un-textured tool.

Texturing on flank surface prevented the flank wear by 10–30% as compared to rake surface textured and conventional tool during turning of steel [56]. Also, it was found that the tool life decreased with a rise in cutting speed. It can be accounted for the reason that at higher cutting speed, an increase in temperature near the tool-chip interface resulted in localised welding of work material to the cutting tool. Thus, tool life of textured tool was found to be comparable with the conventional tool at cutting speed over 150 m/min.

Another study observes the effect of orientation of grooves during the turning process while performing the machining of titanium alloy. They reported that grooves oriented in the direction of chip flow helped in the fast removal of heat from the tool-chip interface and hence resulted in 6.7% lesser tool wear than textured orthogonal tool surface [61].

1.8.2 Environmental friendly cutting fluids

Over the past 200 years, cutting fluids are extensively used in metalworking operation [66]. Survey estimation says that the United States uses 100 million gallons of metalworking oil each year [67]. In ancient times, cutting fluids constituted of only water which was used on grindstones. About 100 years ago, tallow (animal fat rendered form) was applied as lubricating wax. Then, cutting fluids were comprised of simple oils which were applied with brushes for lubricating the cutting tool. Later, lard oil was used, but it became rancid. Sometimes, directly whale oil or animal fat was included to enhance the cutting fluid lubricating properties. In the initial years of the 20th century, soap was mixed in water [68]. Straight cutting fluids were the popular choice for specific machining operations in the past. Soluble oils were introduced in 1936 and cutting fluids made of chemicals came into metalworking operation in 1944 [69]. Gradually, compositions of the cutting fluids became more complicated, as the cutting actions became more difficult. These days to fulfill the required performance demands of the manufacturing industries, cutting fluids are an enhanced combination of oil, water, emulsifiers and chemical additives [70]. Therefore, environmental friendly cutting fluid is the viable alternative for solving above issues. The environmental friendly cutting fluid generally comprises of vegetable oils, bio-cutting fluid and some chemically synthesised fluids as esters including phosphate esters, polyalkene glycols, polyalphaolefins (PAOs), alkylated aromatics and polybutenes that dominates the market among for the same. However, vegetable oils are highly biodegradable and sustainable.

1.8.2.1 Vegetable oils

In due course of time, the conventional mineral oil based cutting fluids started causing problems for the manufacturers as the substances present in them caused severe health effects on the workers and the surrounding environment [71]. Along with the economic and technical aspects of the manufacturing processes, the environmental safety of the products has also become an essential area of concern, and it is triggered by the fact that environmental agencies and government have imposed strict measures when it comes to protecting the employees' health and environment [72, 73]. Subsequently, there is a need to analyse the measures that can be taken to reduce the harmful effects of cutting fluids as much as possible.

Availability of mineral-based oils is limited as they are the finite source and decreasing steadily, whereas vegetable based cutting fluids are sustainable. Literature studies about machining using vegetable based cutting fluids are limited. Vegetable oils are evolving as metal cutting fluids due to its higher biodegradability and ability to minimise the waste treatment costs. It also reduces the health risks to operators, which are quite familiar with petroleum-based mineral oils due to their lower toxicity [74]. Cleaner and healthier work environment having less mist in the air is the primary point. For the reasons mentioned above, vegetable oils as cutting fluids are environmentally friendly. Furthermore, they are also better lubricants as compared to others [75]. Above all, they are extracted from renewable sources and thus unlimited and sustainable.

All these factors have pushed the industries, research centres and universities for studying the process in detail and come up with the better optimal solution. Several of them have proposed various methods for reducing the exposures of cutting fluids while some have advised in changing its composition [76]. Vast quantities of cutting fluids are still in use in the industries releasing harmful gases into the atmosphere, causing numerous skin and respiratory diseases to the workers and increasing disposal costs [77]. Thus, a research study has been conducted to analyse the vegetable oils that act as an eco-friendly cutting fluid, so that the industries can find alternative answers and use protective measures.

1.8.2.2 Physico-chemical and rheological properties of vegetable oils

Vegetable oils mostly consist of triglycerides, which are long chain fatty acids having the number of unsaturated double bonds [78, 79]. Most vegetable oils have a minimum four to maximum 12 different fatty acids. Weather and geo-climate mostly affect the proportion of individual fatty acids.

Cutting at high speed and feed leads to high temperature. Use of cutting fluid at high temperature has possibilities of smoke formation and fire hazard. Vegetable oils have a higher flash point compared to mineral oils which reduce the smoke formation and fire hazard [80, 81]. Vegetable oils have a high viscosity index. The viscosity of oil also affects machining productivity [80]. As the viscosity index of vegetable oil increases, viscosity drops more slowly than that of mineral oils with the increase in temperature. Therefore, with a fall in temperature, vegetable oils remain more viscous than mineral oils, which lead to early drainage from workpiece and chips. Vegetable oils higher viscosity ensures more stable lubricity across the operating temperature range [81]. Molecule sizes of mineral oils are varying, but vegetable oil molecules sizes are quite homogeneous resulting in less variation of its properties concerning physical parameters [80]. Vegetable oil has higher molecular weight and higher boiling point, and this reduces misting and vaporisation [82]. They are much better substitutes for the petroleum-based cutting fluids which make them the probable candidate for industrial use.

Apart from the properties as mentioned above, oxidation stability of vegetable oils depends on the amount of unsaturated products present. For high melting point and even better oxidation stability, the presence of unsaturated product should be low. To reduce friction and wear, long and polar fatty acid carbon chains perform better to interact with metallic surfaces actively.

Micro-organisms have the ability to metabolised and ingest vegetable oils base stock which creates problems toxic mists environment affecting operators health. Various researchers are investigating and exploring oils from vegetables and seeds such as canola, rapeseed, palm, jatropha, olive, neem and coconut to use for metal cutting fluids as the base stock. Table 1.1 shows the physicochemical and rheological properties of various vegetable oils [83].

Table 1.1 Physico-chemical and rheological properties of vegetable oils [83]

Properties	Soybean [84]	High oleic soyabean [85]	Sunflower [86]	Rapeseed [87]	Jojoba [88]	Pongammiapinnata [89]	Jatrophacurcass [87, 90]	Neem [91]	Castor [87, 90]
Kinematic viscosity@ 40 ºC (cSt)	32.93	41.34	40.05	45.60	24.9	43.0	47.48	68.03	220.60
Kinematic viscosity@ 100 ºC (cSt)	8.08	9.02	8.65	10.07	6.43	8.30	8.04	10.14	19.72
Viscosity index	219	-	206	216	233	172	208	135	220
Saponofication value(mgKOH g^{-1})	189	-	-	180	94.69	179	196.80	166	180

Total acid value(mgKOH g^{-1})	0.61	0.12	-	1.40	1.10	22	3.20	23	1.40
Iodine value(mg I g^{-1})	144	85.9	-	104	98	78	97	66	87
Pour point(0 ºC)	−9.0	-	−12.0	−12.0	9.0	−9.0	0	9.0	-27.0
Flash point(0 ºC)	240	-	252	240	-	-	240	-	250

1.8.2.3 Merits and applications of vegetable oils

Vegetable oils have numerous advantages over petroleum-based mineral oils apart from being sustainable. Table 1.2 shows the merits and demerits of vegetable oils over mineral oil properties. Demerits of vegetable oils can be tackled using chemical and genetic modification as well as the reformulation of base stock.

Table 1.2 Merits and demerits of vegetable oils over mineral oils [84, 92−94]

Merits	Demerits
• Sustainable and highly biodegradable • Least toxic compare to mineral oils • High viscosity and viscosity index • Environmental friendly • High flash point • Additives compatible • Less volatile	• Low thermal and oxidative stability • High pour point • More corrosive behaviour

1.8.2.4 Vegetable oils as cutting fluids during turning applications

Vegetable based cutting fluids associated with machining literature are presented in this section. Most of the researchers have used vegetable oils as cutting fluid with minimum quantity lubrication (MQL) technique. In a study, during turning of AISI 1060 steel, authors found that the tool wear, surface roughness and cutting temperature were reduced in comparison to dry machining. On an average of 5-12% reduction of cutting temperature was observed while using MQL with vegetable oil as compared to dry machining. Cutting forces were also reduced by using MQL with vegetable oil [82, 95].

In another study, the experimental performance of sunflower oil, canola oil, semisynthetic and mineral based cutting fluids including different concentration (8 and 12%) of extreme pressure additives were compared during turning of AISI 304L stainless steel. Machining forces, tool life and surface roughness with all four types of cutting fluids were measured and found that vegetable oils have shown better machining performance. It is due to the presence of the long chain fatty acid content in vegetable oils. Canola-based cutting fluids are found to be best as compared to all three including sunflower oil-based cutting fluids. It is attributed to the fact that canola oil has three more carbons in its fatty acid chain, which can perform better at higher cutting temperature. Moreover, canola oil has the high viscosity which provides more effective lubrication at the tool-chip interface, reducing cutting temperature and removing heat efficiently. Higher concentration of pressure additives in vegetable oils results in higher surface roughness values. Canola-based cutting fluid with 8 % of extreme pressure additive has shown better performance than others [96].

Furthermore, another study compared machining performance of four different vegetable based cutting fluids (coconut oil, palm kernel oil, groundnut oil and shear butter oil) during turning of copper, mild steel and aluminium. Cutting forces were measured and compared with four different cutting fluids during cutting of various materials. It was found that the effects of vegetable-based cutting fluid are material dependent. Out of the four, groundnut oil showed the best machining performance [97].

Moreover, tool wear and surface roughness were analysed during turning of AISI 304 stainless steel using bio-based cutting fluid as well as neat cutting oil emulsion. Reduction in tool wear and better surface finish was observed with bio-based cutting fluid compared to other oils due to its high viscosity and better lubricating properties [98].

From the broader prospect of cutting fluids literature, it was found that, in the fifties, correct viscosity was the most crucial requirement of cutting fluids. In the sixties, specific additives were mixed to enhance properties of lubricants while in seventies few synthetic fluids stated challenging mineral oil for performing even better, but former was challenged due to its high cost. In the eighties, hydrocracked quasi-synthetic oils made by British Petroleum, Shell, Fuchs was economical and also enhanced working performance. In the nineties, criteria for cutting fluids took the significant shift towards the environment and eco-friendly fluids. In the 21st century, more compatible working fluids with greater performance trend is in continuation with much more development to come in the future to make it more environmentally friendly and economical.

1.8.3 Near-dry machining

Hard machining of difficult-to-cut material generates significant heat, which results in high temperatures. In manufacturing processes using conventional fluid application methods, 15−17% of product cost is associated with cutting fluid cost [99]. Research has shown that the costs associated with cutting fluids are frequently higher than those for cutting tools [13]. Therefore, the elimination or minimisation of cutting fluids is desirable from both economic and environmental perspectives. Therefore, for these applications, the concept of near-dry machining came into existence [100].

Near-dry machining (NDM) or MQL or micro-lubrication, also known as minimum quantity cutting fluid (MQCF), is an alternative solution for reducing detrimental environmental effects and improving machining performance [101−103]. In MQCF applications, a minute amount of cutting fluid is used at a flow rate of 5–600 mL/h. A cutting fluid with a high convective heat transfer coefficient is mixed with compressed air to form a uniform atomised mist. This generated mist is injected directly into the chip-tool interface in the machining region [104, 105]. MQCF reduces occupational hazards, addresses environmental issues, and produces economic benefits by reducing cutting fluid costs. MQCF is an accepted eco-friendly machining method that can improve workpiece surface finish, and reduce tool wear and cutting forces relative to dry machining [106, 107]. Gunter and Sutherland [108] concluded that a mist generated by mixing soluble oil and air showed better machining performance than flood cooling (FC). Sohrabpoor et al. [109] used soluble oil as the cutting fluid in wet and MQL turning while comparing four different cooling conditions (dry, air cooling, wet and MQL technique) during turning of AISI 4340 stainless steel. They observed that MQL outperformed others concerning the cutting tool flank wear and workpiece surface roughness. Dhar et al. [110] confirmed similar results during machining for both AISI 1040 and AISI 4340 steel. Heat reduction at the tool-chip interface because of MQL mist is considered as one of the main reason to reduce the growth of the flank wear as MQL mist penetration ability in between tool-chip interface is higher as compared to wet cooling. MQL machining studies related to difficult-to-machine materials have also shown great potential to reduce generated heat, tool wear and to improve the surface finish of the workpiece. Park et al. [111, 112] compared electric power consumption by dry machining (DM), FC, cryogenic machining (liquid nitrogen), MQL machining and laser-assisted machining (LAM) during surface milling operation of Ti-6Al-4V. Results showed that FC consumes the maximum electrical power of 2.75 kW, whereas it was followed by LAM, cryogenic, DM and MQL machining technique (only 1.53 kW). In the case of MQL, lower tool wear was the primary factor that leads to the least electrical power consumption among all.

Beatrice et al. [113] predicted the surface roughness using an artificial neural network (ANN) technique during the machining of AISI H13 steel using minimal cutting fluid. The surface roughness predicted by the ANN model matched the experimental results reasonably well. Sarikaya and Gullu [114] investigated the flank wear, notch wear, and surface roughness of a cobalt-based superalloy (Haynes 25) during turning with MQL. A Taguchi-based grey relational analysis (GRA) was used to simultaneously optimise cutting fluids, fluid flow rates, and cutting speed. The results showed that flank wear, notch wear, and surface roughness were enhanced during the turning of Haynes 25 using the Taguchi-based GRA. Another study showed that feed was the most effective parameter concerning surface roughness and that MQL successfully improved surface finishes during the machining of AISI 1050 steel [115]. Sharma and Sidhu [116] compared dry machining and NDM using vegetable oil on AISI D2 steel. The results showed that work–tool interface temperatures and surface roughnesses reduced with NDM. Further surface roughness was reduced even more at higher speeds.

Heinemann et al. [117] compared the performance of synthetic ester with and without alcohol as well as the mixture of oil-free synthetic lubricant and water concerning tool life during deep-hole drilling. The result showed that the oil-free synthetic lubricant and water mixture performed better as compared with others due to its low viscosity and high cooling ability. In end milling, lower cutting forces were observed due to improved cooling and better lubricating properties of a new oil film on water type lubrication [118, 119]. Furthermore, storage stability, oxidation, biodegradability and cutting performance was improved for synthetic polyesters as compared to vegetable oil [120, 121].

MQCF provides several benefits during machining. MQCF techniques have existed since the past decade; however, the effectiveness of its input parameters has not been discussed. The efficiency of an MQCF system depends upon mist (the mixture of pressurised air and cutting fluid) formation and quality, which are controlled by the MQCF input parameters, namely, emulsion composition, stand-off distance between the nozzle and machining zone, nozzle spraying angle, and air pressure. No clear guidelines have been created by researchers for selecting or optimising these parameters.

1.8.4 Minimum quantity nano-cutting fluids

Minimum quantity cutting fluids (MQCF) is an alternative for dry machining and flood cooling. However, use of MQCF is limited to mild machining conditions due to high heat generation during machining of hard materials. The applicability of MQCF can be extended in aggressive machining conditions by using vegetable-based cutting fluids with nanoparticles as potential additives. A colloidal mixture of nanometer-sized metallic and non-metallic particles in the conventional cutting fluid is called nanofluid. Nanofluids are considered to be potential heat transfer fluids because of their superior thermal and tribological properties.

A new class of cutting fluids can be synthesised by mixing metallic, non-metallic, ceramics, or carbon nanoparticles in a conventional cutting fluid because as compared with suspended milli-sized or micro-sized particles, nanofluids show better stability, rheological properties, excellent thermal conductivity, and no adverse effect on pressure drop [122]. Saidur et al. [123] and Kakac and Pramuanjaroenkij [124] reviewed the work of many researchers and found that nanofluids may possess outstanding heat extraction capabilities (thermal conductivity) over conventional cutting fluids. They concluded that this enhanced thermal conductivity might be an essential factor for better performance in various applications. The inclusion of nanoparticles of metal oxides into any base fluid enhances its thermal conductivity [125]. Chen and Ding [126] reviewed the literature regarding the improvement in thermal conductivity of metallic, carbon, inorganic and carbide materials and concluded that thermal conductivity of nanofluids increases with an increase of nanoparticle concentration. Srikant et al. [127] found that the addition of nanoparticles in cutting fluids improved their coolant properties. Further, Eastman et al. [128] noticed an increment of up to 40% in thermal conductivity of ethylene glycol by mixing Cu nanoparticles into it. Liu et al. [129] noticed 23.8% improvement in thermal conductivity at 0.1 vol% Cu nanoparticles in cutting fluid due to the increased surface area. Yoo et al. [130] concluded in his investigation that ratio of surface area and volume of nanoparticles might be the primary factor that the affects thermal conductivity of nanofluids. It is well understood that this ratio will always be increased by the addition of smaller size nanoparticles into base fluid. Chon et al. [131] also observed an enhancement of thermal conductivity of nanofluids at higher temperatures due to the Brownian motion of nanoparticles. Choi et al. [132] found that nanoparticles increase the rate of heat transfer without an increase in pumping power. Vajjha and Das [133] observed that 6% Al_2O_3 in base fluid increases the thermal conductivity by 22.4% at room temperature. Qiang and Yimin [134] found that nanofluid with 2 vol %, Cu nanoparticles have 60% more convective heat transfer coefficient compared with the base fluid. He et al. [135] discovered that the addition of nanoparticles into base fluid improves the thermal conduction. It was also found that the thermal conduction improved with the increasing particle concentration and decreasing particle size. Choi et al. [136] reported an unusually high improvement in thermal conductivity of nanofluid by adding multi-walled carbon nanotube (MWCNT) up to 150% as compared to base fluid.

Besides thermal conductivity, the friction between tool and workpiece may also be an important factor responsible for the high-temperature generation at the cutting zone that affects the workpiece dimensional accuracy, surface quality, and, more importantly, the tool life during machining. Lee et al. [137] found that the addition of graphite nanoparticles improves the lubricating property of conventional lubricants due to the reduction in the friction coefficient. Because of their low friction behaviour, the graphite and MoS_2 solid lubricants may contribute to the reduction of cutting force and reduce the surface roughness in machining [138]. Also, the addition of nanoparticles into base fluid can enhance their convective heat transfer coefficient, lubricating properties, and wettability. On the other hand, it can reduce tool wear, surface roughness, cutting force, and chip thickness compared with dry machining and conventional fluid machining [105, 139–151]. Various nanofluids and their effect on different machining processes are listed in Table 1.3.

Table 1.3 Nanofluids and their effect on machining parameters during different machining processes

S. No.	Refer-ences	Types of nanoparticles	Base fluid	Size (nm)	Process	Remarks
1	[105]	Al_2O_3	Servo-Cut-S	––	Turning	Nanofluid reduced cutting force, crater wear and surface roughness and also produced tiny segmented chips of low thickness
2	[139]	CNT	––	––	Turning	Up to 2% CNT inclusion, nodal temp was decreased, but beyond 2%, the change was minimal. High CNT % lowered the flank wear
3	[140]	Nanoboric acid	SAE-40 oil	50	Turning	0.5% nano boric acid in

			and coconut oil			coconut oil performed better concerning cutting temperature, tool wear, and surface roughness.
4	[141]	MoS_2 GF Cu CuO	Grease	1000 150 200 48	Turning	Copper nanoparticle (10%) mixed in grease generated surface with lowest roughness and yielded minimum tool wear.
5	[142]	SiO_2	Mineral oil	5–15	Turning	0.5 wt% SiO_2 with 2 bar air pressure and 60 nozzle angle recorded minimum tool wear and with low air pressure and 30 nozzle angle produced best surface
6	[143]	Nano graphite	Water soluble oil	80	Turning	% inclusion of nano graphite decreased the cutting force, surface roughness, tool wear, and temperature. 0.3% graphite at 15 mL=min flow rate showed best performance
7	[144]	ND	Paraffin oil and vegetable oil	30	Drilling	Paraffin with 1% ND and vegetable oil with 2% ND recorded the lower torque and thrust force. Nanofluid enhanced the tool life and drilled good quality holes.
8	[145]	Al_2O_3	Deionized water	40	Grinding	Reduction in grinding temperature, grinding force, and surface roughness
9	[146]	CNT	SAE-	10–20	Grindin	Increased the flash and the

			20W40 oil		g	fire point of fluid. Improved surface roughness
10	[147]	MWCNT	SAE-20W40 oil	10–20	Grinding	Surface quality improved from micro level to nano level.
11	[148]	xGnP	IPA, TRIM SC200	5–10	Grinding	Large size platelets were found to be more effective than small ones. 1 wt% graphite platelets produced best surface finish
12	[149]	xGnP	Vegetable oil	10	Milling	0.1 wt% xGnP with 1 mm dia. and 10 nm thickness showed lowest friction coefficient
13	[150]	Carbon onions	Alumicut oil	5–20	Milling	Highest carbon onion concentration (1.5 wt%) yielded minimum cutting force and surface roughness
14	[151]	MoS_2	ECOCUT HSG 905S oil	20–60	Milling	0.5 wt% MoS_2 produced the best surface and surface quality deteriorated as MoS_2 concentration increased to 1 wt%

Nanofluids provide several benefits during machining. Nanofluids have existed since the past decade; however, most of the research is carried out with metallic or ceramic nanoparticles, which are too costly. Solid lubricants based nano cutting fluids such as MoS_2, CaF_2, WS_2, can enhance thermal conductivity, specific heat and lubricating properties of cutting fluid. Also, solid lubricant nanoparticles are economical as compared to metal and ceramic-based nanoparticles. Furthermore, the concentrations of nanoparticles in cutting fluids are also vital in machining. No clear guidelines have been created by researchers for selecting or optimising these parameters.

1.8.5 Gaps in the literature

Based on the literature survey on dry machining, environmental friendly cutting fluids, minimum quantity cutting fluids and nano-cutting fluids in various fields, major gaps are:

1. Almost in all previous studies, surface textures are fabricated using thermal based texturing methods. However, thermal-based texturing methods have various drawbacks such as heat affected zone of textures, recast layers, inferior qualities of textures that causes more abrasive wear.
2. Not much attention is paid to optimizing area density of textures (number of textures per unit area) between sliding surfaces.
3. The researchers have followed trial and discovery approach in the development of textured pattern, but the effectiveness of such pattern may be increased by ensuring less contact area between chip and tool rake surface. The detailed comparison between micro-indent and micro-channel textures needs to be studied in depth.
4. The focus on cutting fluids has shifted from only machining performance to environmental friendliness and its biodegradability over the years to protect our precious environment. Extensive comparative analysis of thermal, rheological, biodegradation, storage stability and anti-corrosion property of mineral oil, bio-cutting fluid and vegetable-based green cutting fluids still needs to be done.
5. MQCF techniques have existed since the past decade; however, the effectiveness of its input parameters has not been discussed. The efficiency of an MQCF system depends upon mist (the mixture of pressurised air and cutting fluid) formation and quality, which are controlled by the MQCF input parameters namely, emulsion composition, stand-off distance between the nozzle and machining zone, nozzle spraying angle, and air pressure. No clear guidelines have been proposed by researchers for selecting or optimising these parameters.
6. Nanofluids have existed since the past decade; however, most of the research is carried out with metallic or ceramic nanoparticles, which are too costly. Solid lubricants based nano cutting fluids are not given much attention. Due to the low cost and outstanding properties of solid lubricants, they have enormous potential to be an innovative, effective alternative to metallic or ceramic nanoparticles for nano cutting fluid applications.
7. Hybridization of surface textured cutting tool, environmental friendly cutting fluid and minimum quantity nano cutting fluid has not been attempted until now.

1.9 Objectives of the present work

As discussed in the literature above, mineral oil based cutting fluids have various disadvantages. The overall objective of this thesis is to make machining more sustainable for the environment, economic and social benefits. It can be achieved by elimination or minimization of cutting fluid usage, shifting towards highly biodegradable and environmental friendly cutting fluids and optimized use of nano cutting fluids. Furthermore, hybridisation of all above process makes machining more sustainable.

The research tasks of the current work are as follows:

1. Fabrication of micro-textured cutting tools using the conventional mechanical method such as Vickers hardness tester and scratch tester to avoid various disadvantages of thermal based surface texturing.
2. Optimization of the of texture area density (number of textures per unit area).
3. Comparative machining performance of micro-indent and micro-groove based textured cutting tool.
4. Comparison of thermal, rheological, biodegradation, storage stability and anti-corrosion property of mineral oil, bio-cutting fluid and in-house developed vegetable based green cutting fluids.
5. Optimization of the MQCF input parameters such as emulsion composition, stand-off distance between the nozzle and machining zone, nozzle spraying angle as well as to compare hard machining performance using MO, BCF and GCF.
6. Development of solid lubricant based nano cutting fluids and to investigate its dispersion, dynamic viscosity, thermal conductivity, volumetric specific heat, wettability and hard machining performance.
7. Combination of four different individual sustainable machining techniques to create hybrid and advanced sustainable process for making machining more sustainable:

- Textured tools (economic and conserve energy)
- Green cutting fluids (minimise adverse environmental impact and ensure safety to employees and consumers)
- Minimum quantity cutting fluids (minimise cutting fluid usage and minimise adverse environmental impact)
- Nano cutting fluids (to enhance hard machining performance and conserve energy)

1.10 Organization of the thesis

Current thesis is organised into nine chapters with references and appendices at the end. Figure 1.6 shows the plan of work carried out in this thesis.

- **Chapter 1** discusses the need for elimination or minimisation of conventional cutting fluids in machining processes. A brief literature review of the dry machining, environmental friendly cutting fluids, near dry machining and nano cutting fluids are also discussed. Finally, gaps in the literature, different challenging issues, scope and detailed objectives of the present thesis are described.
- **Chapter 2** includes discussion about the fabrication of mechanical micro-textures on the surface of the high-speed steel pin with different area density. Tribological performance of MoS_2 coated mechanical micro-textured cutting tools during the dry sliding test are investigated. The area densities of textures (number of textures per unit area) between the sliding surfaces are also optimised.
- **Chapter 3** presents preliminary experimentation to find the area for texturing on the rake surface of the tool. Afterwards, mechanical micro-textures are fabricated on the rake surface of the tool. In order to check the effect of micro-textures on the strength of the tool, static structural finite element analysis is done in the Ansys® workbench. Later, comparative study of machining performance with un-textured, mechanical micro-textured and MoS_2 coated mechanical micro-textured high-speed steel cutting tools are carried out.
- **Chapter 4** deals with the comparative study of hard machining with various mechanical micro-textured and MoS_2 coated mechanical micro-textured tungsten carbide cutting tools. Six different uncoated and MoS_2 coated mechanical micro-textures are fabricated, and their hard machining performance is compared. For comparison, machining is also carried out using the conventional cutting tool.
- In **Chapter 5,** environmentally friendly green cutting fluid was developed using the mixture of various vegetable oils and emulsifiers. Afterwards, biodegradation, thermal, rheological, storage stability and anti-corrosion properties of in-house developed green cutting fluids are compared with commercial bio cutting fluid and mineral oil.
- **Chapter 6** discusses the development of minimum quantity cutting fluid setup. The MQCF input parameters such as emulsion composition, stand-off distance between the nozzle and machining zone as well as nozzle spraying angle are optimised experimentally. Afterwards, using optimised input parameters, hard machining performance of MO, BCF and GCF with MQCF technique are compared.

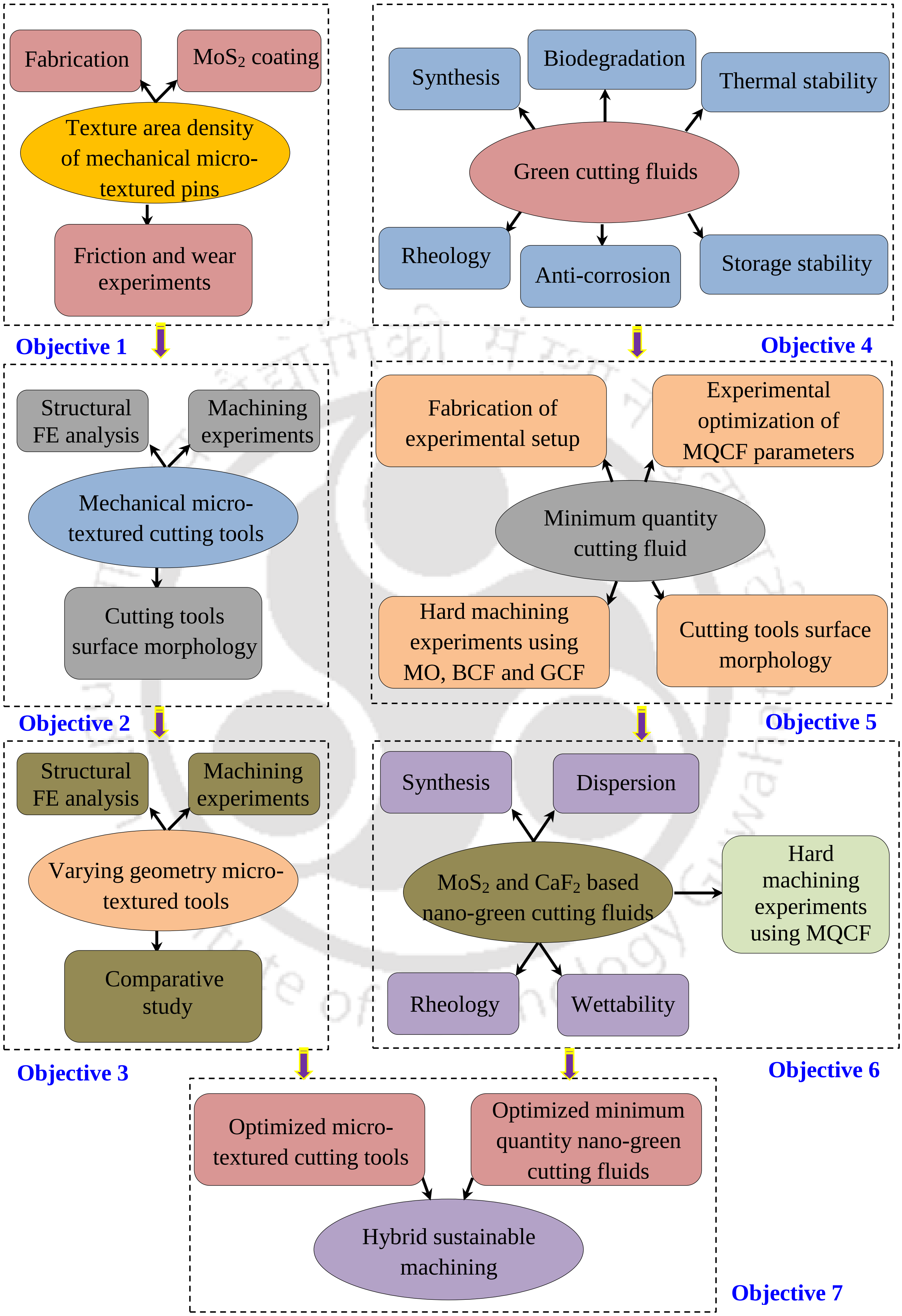

Figure 1.6. Plan of work carried out in this thesis

- In **Chapter 7**, MoS_2 and CaF_2 based nano-green cutting fluids with varying concentration are developed. The effect of the nano-solid lubricant (MoS_2 nanoplatelet and CaF_2 nanoparticles) enhanced cutting fluids are studied by conducting absorbance tests, dynamic viscosity test, thermal conductivity test, volumetric specific heat test and wettability test. Afterwards, hard machining experiments are carried out to evaluate the performance of nano-solid lubricant enhanced GCF using MQCF technique.
- **Chapter 8** deals with the hybridisation of the above four individual sustainable machining processes. For hard machining, the combination of the mechanical-micro-textured cutting tool with in-house fabricated minimum quantity cutting fluid using in-house developed nano-green cutting fluid is used.
- **Chapter 9** represents the main findings of the present work, important conclusions and future scope in the field of sustainable machining. The outcome of the present work in the form of various journal papers, book chapter and conferences is reported.

References and appendices are included at last.

Chapter 2

TRIBOLOGICAL PERFORMANCE OF MECHANICAL MICRO-TEXTURED PINS

2.1 Introduction to the tribological aspects of micro-textured cutting tools in machining

2.2 Experimental details

- 2.2.1 Fabrication of mechanical micro-textured pins and coating with solid lubricant
- 2.2.2 Sliding friction and wear test

2.3 Results and discussion

- 2.3.1 Friction coefficient of the test material
- 2.3.2 Surface temperature of the test material
- 2.3.3 Wear, weight loss and wear rate of the test material
- 2.3.4 Wear morphology and elemental composition of the test material

2.4 Findings from the research work

Chapter 2 contains the fabrication of mechanical micro-textures on the surface of the high-speed steel pin with different area density. Also, the tribological performance of MoS_2 coated mechanical micro-textured cutting tools during the dry sliding test are investigated. The area density of textures (number of textures per unit area) between sliding surfaces are also experimentally optimised in this Chapter.

2.1 Introduction to the tribological aspects of micro-textured cutting tools in machining

As found out from the literature survey (Chapter 1), surface texturing is an established method for enhancing the tribological properties. Researchers used a wide range of processes to fabricate surface textures such as laser-based texturing [152−155], focused ion beam [156], electrical discharge machining [157], photolithography and photochemical texturing [158]. Most of these processes are thermal energy and chemical based texturing methods. These processes produce recast layer, heat affected zone, residual stresses, chemically affected layers and cracks. Texturing can also be fabricated by inexpensive mechanical methods, avoiding the defects as mentioned above.

In self-lubricating composites, solid lubricants are applied either as fillers or as surface coatings [159]. Filling of solid lubricants is easy, and they do not alter characteristics of the parent material. MoS_2 has various advantages such as low volatility, non-toxic, nonradioactive, chemical inertness, strong adhering ability, good load bearing capacity and resistance against wear [160].

It is crucial to correlate machining with tribology of sliding interface for the better understanding of friction and wear at tool-chip interfaces. In this study, a mechanical texturing process was used to create micro-indents on the surface of the plasma nitrided high-speed steel (PN-HSS) workpiece by indenting using Vickers hardness tester. Micro-indents were filled with MoS_2 in a grease base. The objective of this study is to study the effect of texture area density (2 to 14%) on the COF, pin surface temperature, wear, weight loss of the pin and wear rate. Friction and wear tests were carried out using pin-on-disc tribometer on both types of pins (with and without MoS_2 filled pins). For comparison purpose, experiments were also carried out on un-textured (UT) pin.

2.2 Experimental details

Plasma nitrided HSS was chosen as work material in the form of pins for this study due to its number of application in sliding interfaces of many cutting tools viz drill bit, milling cutters, taps, saw blades, gear cutters, etc. HSS material had a hardness of 65−67 HRC, density of 8.16 g/cm^3, Young's modulus (E) of 210 GPa, yield strength (S_y) of 2750 MPa, Poisson's ratio (ν) of 0.27 and thermal conductivity of 54.6 W/m.°C. MoS_2 is having an average particle size of 0.3 μm manufactured by Loba Chemie, Mumbai, India was used as a solid lubricant.

2.2.1 Fabrication of mechanical micro-textured pins and coating with solid lubricant

Pins for friction and wear test were fabricated using wire cut electrical discharge machining from plasma nitride HSS cutting tool blank as shown in Figure (2.1). An array of mechanical micro-indents were fabricated on the pin surface using Vickers hardness tester (Make: Fuel Instruments & Engineering Private Limited, India, Figure 2.2 (a-c)) with texture area density of 2 to 14%. Pins having 2%, 4%, 6%, 8%, 10%, 12% and 14% texture area density are named as A2, A4, A6, A8, A10, A12 and A14, respectively (Figure 2.3). The MoS_2 solid lubricant of average particle size of 0.5 μm was mixed with graphite-based grease such that the concentration of MoS_2 is 70% by volume. Micro-indents were smeared with this mixture and then compacted. Uniformity of MoS_2 burnishing was cross-checked using dial gauge. The MoS_2 filled textured pins were dried for 2 hours before starting the friction and wear test. Pins filled with MoS_2 having 2%, 4%, 6%, 8%, 10%, 12% and 14% texture area density are named as A2-M, A4-M, A6-M, A8-M, A10-M, A12-M and A14-M, respectively.

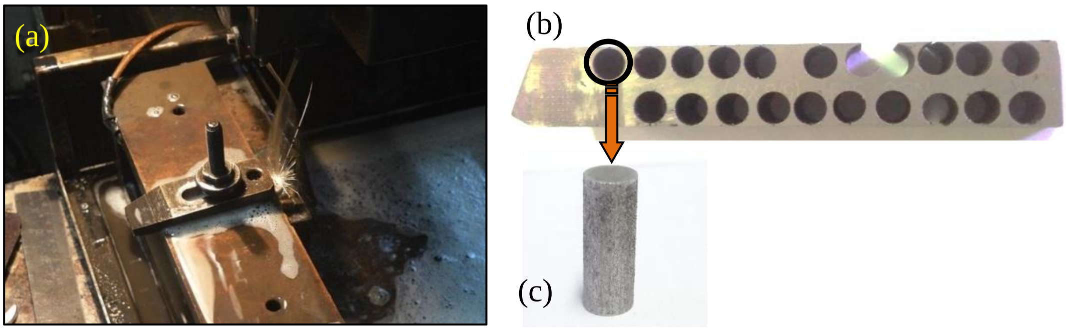

Figure 2.1. (a) Fabrication of pins using a wire-cut electrical discharge machine, (b) plasma nitride high-speed steel cutting tool blank and (c) fabricated pin

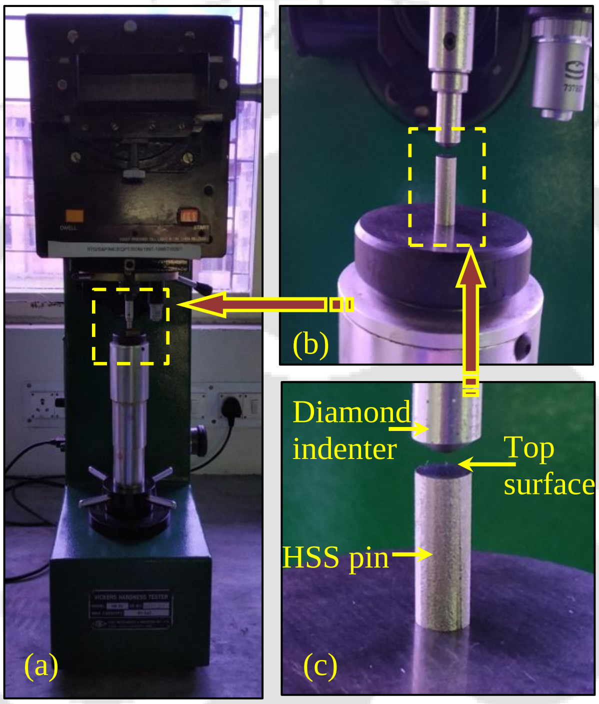

Figure 2.2. (a) Overview of Vickers hardness tester, (b) close up view of Vickers hardness tester and (c) diamond indenter and high speed steel pin

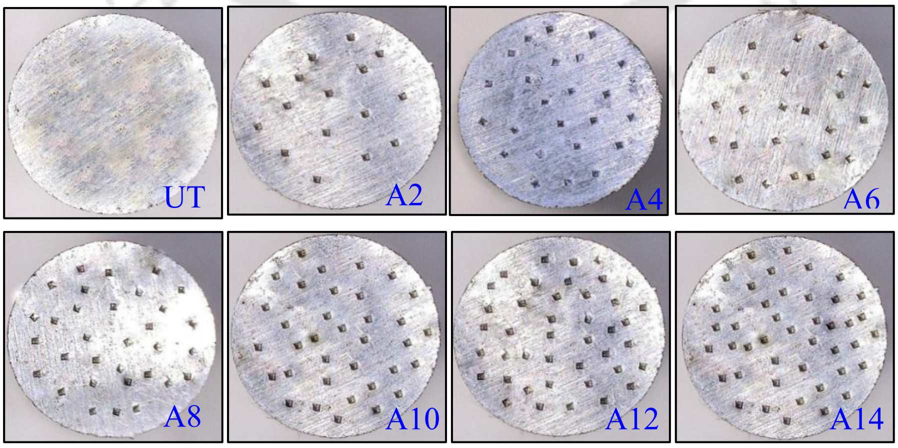

Figure 2.3. Fabricated mechanical micro-textured high-speed steel pins with varying textures area density

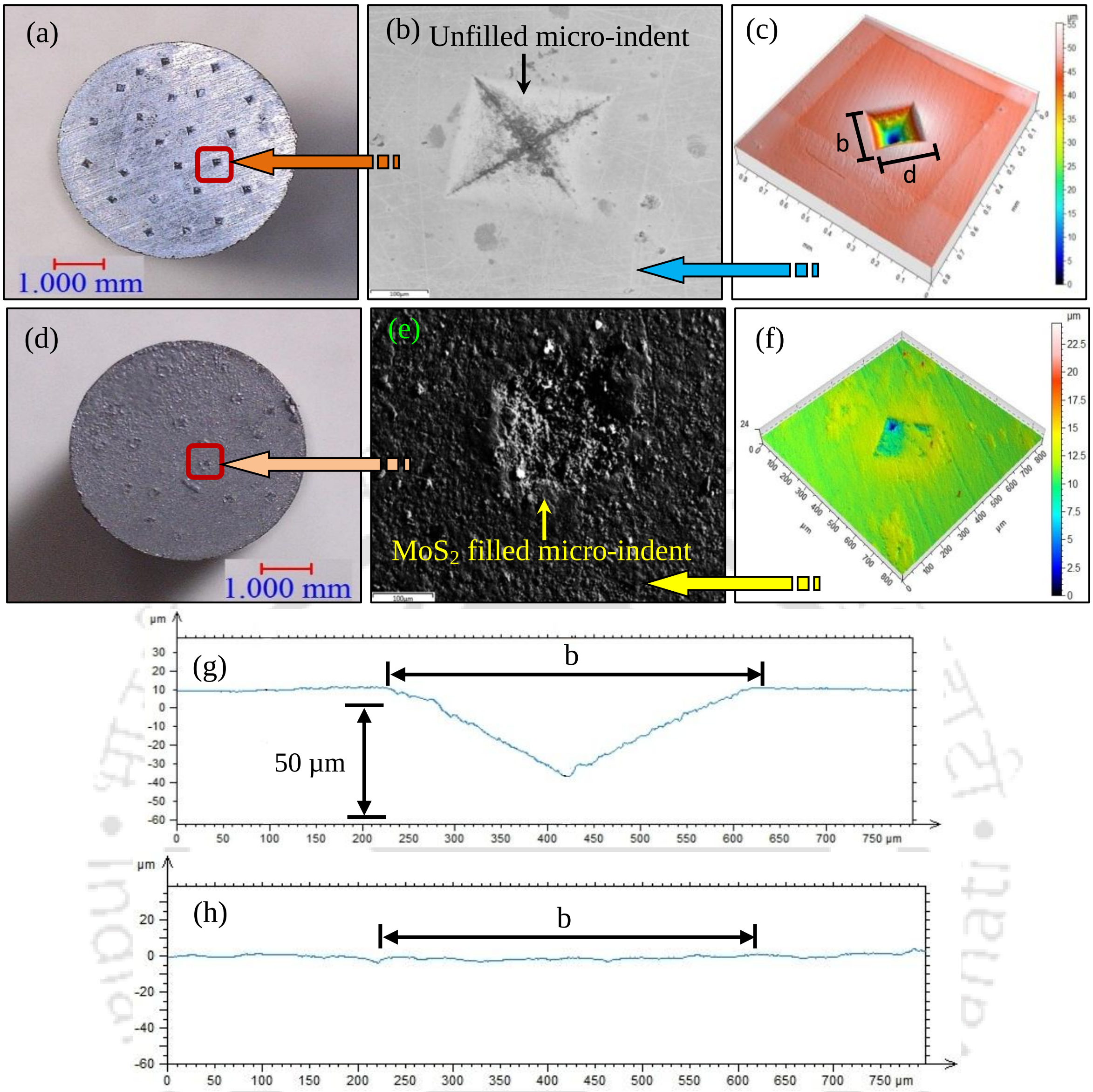

Figure 2.4. Unfilled and MoS_2 filled textured surfaces of HSS pins: (a) macroscopic view of unfilled texture, (b) surface micrograph of unfilled texture, (c) 3-D profile of unfilled texture, (d) macroscopic view of MoS_2 filled textured pin, (e) MoS_2 filled texture surface micrograph, (f) 3-D profile of MoS_2 filled texture, (g) 2-D profile of an unfilled texture and (h) 2-D profile of MoS_2 filled texture

2.2.2 Sliding friction and wear test

Friction and wear performance of mechanical textured pins were carried out using pin-on-disc tribometer (Make: DUCOM, Model: TR-201) under the dry sliding condition as per ASTM G99 standard. MoS_2 filled and unfilled textured pin specimens of 20×6×6 mm having an initial surface roughness (R_a) of 0.65±0.05 µm were prepared. The silicon carbide abrasive sheet having 220 grit size was fixed on the tribometer steel disc. In general, sliding interfaces experience abrasive, adhesive and diffusive wears. Abrasive wear is the most common in HSS tools. Friction and wear tests were carried out at elastic and plastic loading condition with the normal load of 19.6 N (elastic loading of asperities) and 49 N (plastic loading of asperities) with sliding speed of 30 m/min. All tests were carried out for 30 minutes at dry conditions.

A rough estimate of the type of loading was made as follows. Considering von Mises yield criterion, the critical load ($\bar{P}_c$) for a single-asperity contact is given by [161]

$$\bar{P}_c = \frac{4}{3}\left(\frac{R}{E'}\right)^2\left(\frac{C}{2}\pi S_y\right)^3, \tag{2.2}$$

where R is the radius of asperity and C is the critical yield stress coefficient given by $1.295\times e^{(0.736\,\nu)}$. E' is the Hertz elastic modulus defined as

$$\frac{1}{E'} = \frac{1-\nu_1^{\,2}}{E_1} + \frac{1-\nu_2^{\,2}}{E_2}, \tag{2.3}$$

where E_1, E_2 are Young's moduli of two contacting materials and ν_1, ν_2 are corresponding Poisson's ratios. Taking E_2 as 410 GPa and ν_2 as 0.14 for silicon carbide, E' came out to be 164 GPa. From the measurement by a non-contact profilometer, the number of asperities on the pin surface was obtained as 3.39×10^5 and R as 0.67 μm. From a code developed on the basis of the multi-asperity friction model of Mao et al. [162], the asperities under contact were estimated as 5.085×10^4 and 1.271×10^5 for 19.6 N and 49 N normal load, respectively. It was assumed that all contacting asperities equally share the total load. Using this methodology, with 19.6 N normal load, the load on an asperity came out to be 3.85×10^{-4} N, which is less than the critical load of 9.39×10^{-4} N. With 49 N normal load, the load on an asperity came out to be 9.6×10^{-4} N, which is more than the critical load. Hence, the light load is considered to cause elastic deformation, and high load is considered to cause plastic deformation of asperities.

Friction force and wear were recorded continuously using strain gauge based load cell and linear variable differential transducer (LVDT), respectively. Pin surface temperature of each specimen was measured using infrared thermography camera (Make: InfraTec hr Head, Model: VarioCam 480SL). The weight of pins were measured before and after tests using weighing balance (0.1 mg accuracy). Figure 2.5 shows an experimental setup with pin specimen, abrasive sheet and thermal infrared camera. Wear rate (W) of specimens were calculated using the following formula:

$$W = \frac{V}{FL}, \tag{2.4}$$

where W denotes the wear rate (mm^3/N.m), V denotes the volume loss due to wear (mm^3), F is the normal load (N), and L is the sliding distance (m). More precisely, W is called the specific wear rate coefficient.

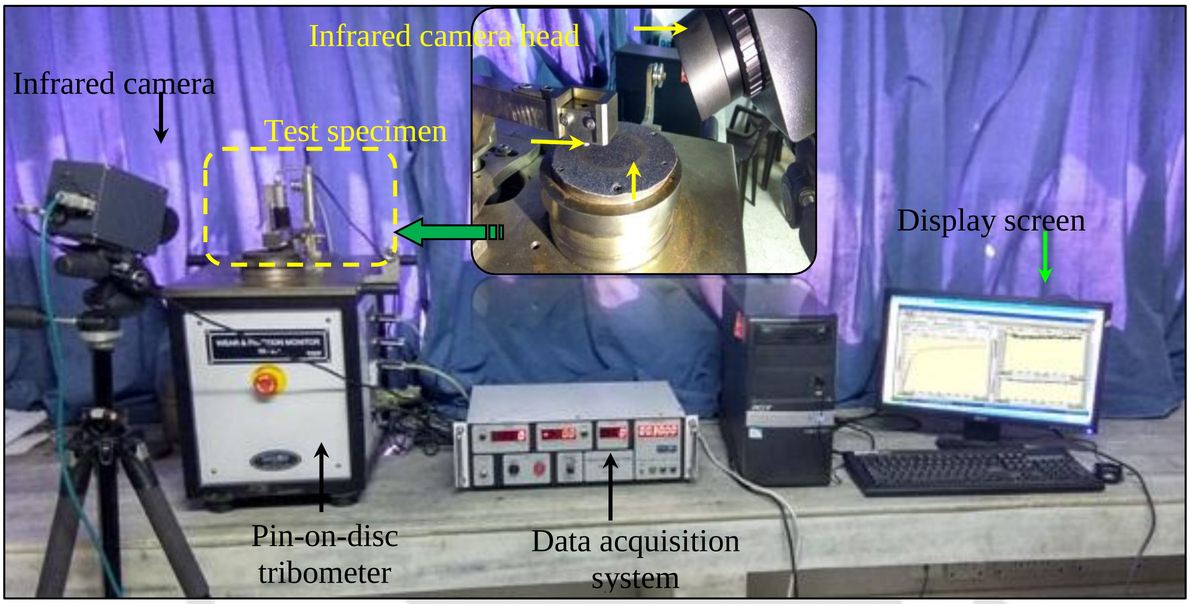

Figure 2.5. Experimental setup of pin-on-disc tribometer along with thermal imaging camera

2.3 Results and discussion

Sliding tests were conducted without lubrication following ASTM G99 standard. Each sliding test was carried out against the new abrasive sheet. All tests were repeated thrice, and the average (mean) result is reported.

2.3.1 Friction coefficient of the test material

There are various measures of friction, e.g., friction (or shear) factor and Coulomb's coefficient of friction. In this section, equivalent Coulomb's coefficient of friction is denoted by COF. It is the ratio of friction force to normal load. Figure 2.6 shows the variation of COF with respect to sliding time. It is observed that initially, COF for all pins increases gradually and after certain sliding time period a steady state is reached. The observed behaviour is due to increase in sliding contact area till uneven and weak surface asperities of an abrasive sheet as well as pin surface are worn-out. COF during the sliding time from 200 to 1800 s is considered as a representative COF. UT pin specimen exhibited a COF in the range of

0.44−0.51, whereas the A10 pin had COF in the range of 0.31−0.39, which was the least among all unfilled textured pins (Figure 2.6 a).

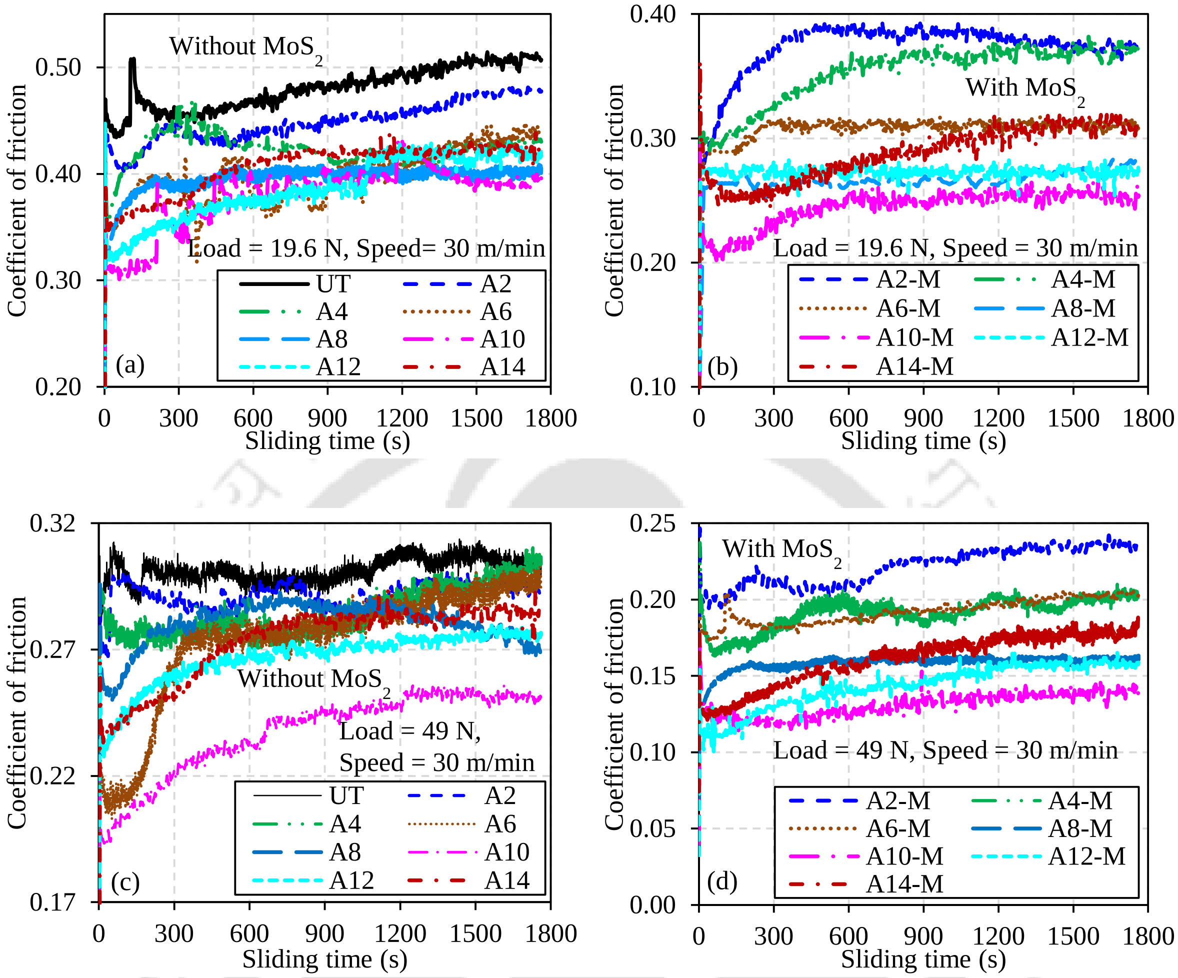

Figure 2.6. Variation of coefficient of friction of the HSS pin with sliding time at constant speed of 30 m/min for loads of (a) 19.6 N (without MoS_2), (b) 19.6 N (with MoS_2), (c) 49 N (without MoS_2) and (d) 49 N (with MoS_2)

During sliding test, MoS_2 burnished 10% texture area density (A-10M) pins shows least coefficient of friction (COF). With the increase in texture area density from 0% to 10%, COF decreased. This is due to the number of abrasive particles taking part in friction and wear reduces because of presence of increasing number of micro-textures in contact with abrasive sheet, which is the reason for decreasing COF. However, with further increase in texture area density from 10% to 14%, a slight increase in COF is observed. It is due to the accumulation of number of abrasive particles in-between sliding surface in contact because of increasing number of micro-indents, which form a slight bulge near its vicinity that leads to increased penetration of the abrasive particles leading towards higher coefficient of friction.

COF of A2-M pin was in the range of 0.35−0.37, which is even less than A10 pins (Figure 2.6 b). With further increase in texture area density from 2% to 10% of MoS_2 filled textured pins, COF further decreased. A10-M pin exhibited the minimum COF amongst all. As per the test, the 10% texture area density samples provided the minimum COF in unfilled as well as MoS_2 filled pins.

A similar trend is observed for COF at the higher load of 49 N as shown in Figure 2.6 (c) and (d). However, the magnitude of COF reduces with increase in load. An asperity based model predicts the same behaviour [162]. A10-M pin shows COF around 0.12−0.14, the least among all (Figure 2.6 d).

2.3.2 Surface temperature of the test material

Figure 2.7 shows the variation of the pin surface temperature of all specimens with respect to sliding time. Upto 200 s sliding time, the interaction of silicon carbide particles with pin surface causes an increase in COF. Therefore, the surface temperature of the pin increases rapidly initially.

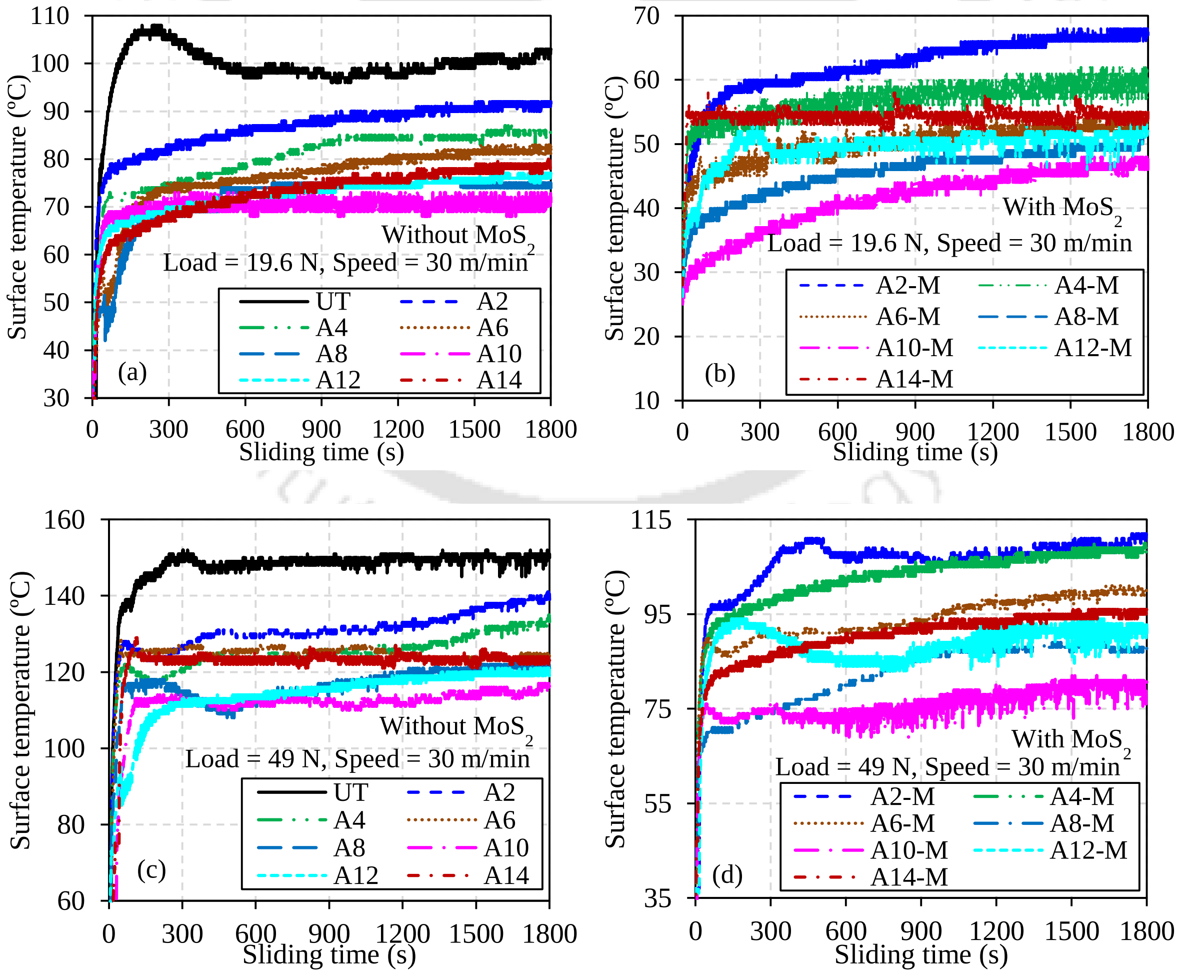

Figure 2.7. Variation of HSS pin surface temperature with sliding time at constant speed of 30 m/min for the normal load of (a) 19.6 N (without MoS_2), (b) 19.6 N (with MoS_2), (c) 49 N (without MoS_2) and (d) 49 N (with MoS_2)

After 200 s of sliding time, a steady-state value of COF is achieved. It also provides the constant surface temperature of pins. Wu et al. [163] also observed similar behaviour for cemented carbide material. UT pin exhibits the maximum surface temperature of around 103 ºC during steady state with the normal load of 19.6 N (Figure 2.7 a). Surface temperature with unfilled textured pins was less than that for UT pins. With the increase in texture area density of micro-indents from 2% to 10%, surface temperature decreased. A10 pin showed the minimum surface temperature of 74 ºC among all unfilled textured pins (Figure 2.7 a). With MoS_2 filled textured pins, surface temperature further decreased and reached the minimum of 50 ºC for the A10-M pin (Figure 2.7 b). However, similar to COF increase in texture area density beyond 10% resulted in an increase in pin surface temperature.

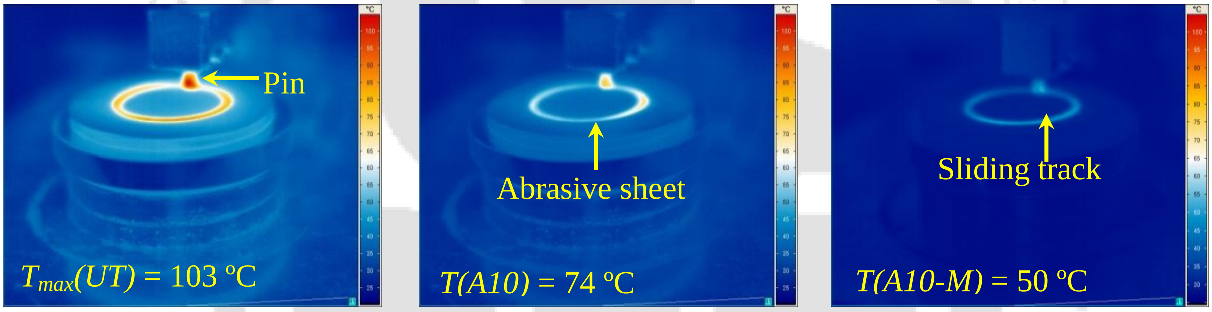

(a) Load = 19.6 N

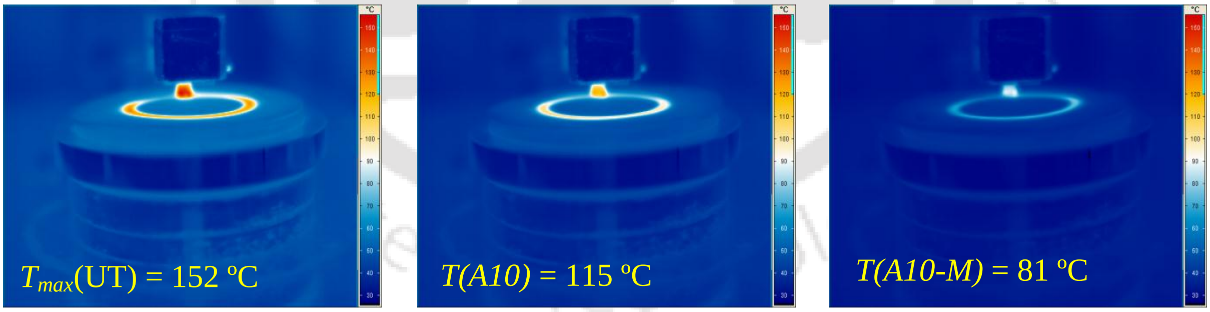

(b) Load = 49 N

Figure 2.8. Thermal images of pin surface temperature of UT, A10, A10-M pins during the sliding test with sliding speed of 30 m/min for the normal load of (a) 19.6 N and (b) 49 N

The similar trend was observed for pin surface temperature at a higher load of 49 N as shown in Figure 2.7 (c) and (d). However, the magnitude of the pin surface temperature is more with the load of 49 N. A10-M pin showed the pin surface temperature of around 81 ºC, the least among all (Figure 2.7 d). This behaviour is expected because although the COF is less for 49 N load as compared to 19.6 N load, the overall frictional stress is more for 49 N load. Thermal images of the pin surface temperature of UT, A10 and A10-M pins with normal loads of 19.6 N and 49 N are shown in Figure 2.8 (a) and (b), respectively.

2.3.3 Wear, weight loss and wear rate of the test material

Figure 2.9 shows the variation of wear of pins with respect to sliding time at normal loads of 19.6 N and 49 N. During the test, change in the position of a pin is continuously measured using LVDT sensor; the deflection from initial position gives wear. Initial and final weights of the pins are measured using weighing balance.

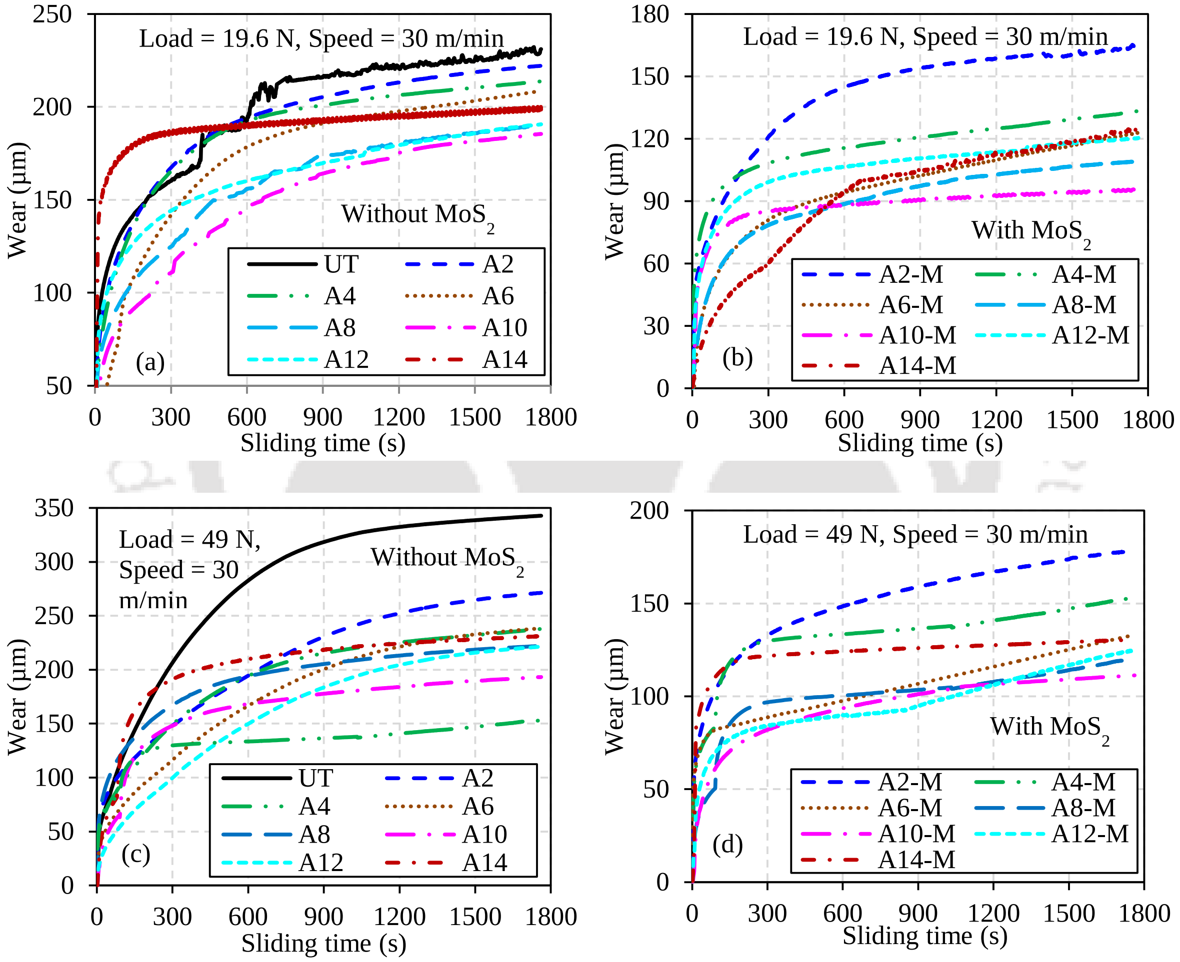

Figure 2.9. Variation of wear of the HSS pin with sliding time at constant speed of 30 m/min for the load of (a) 19.6 N (without MoS_2), (b) 19.6 N (with MoS_2), (c) 49 N (without MoS_2) and (d) 49 N (with MoS_2)

Figure 2.10 shows the average weight loss of the unfilled and filled MoS_2 pins having varying texture area density after friction and wear tests at the normal load of 19.6 N. Figure

2.11 shows the wear rates of tested pins, which are calculated using Eq. (2.4). UT pin specimen shows the maximum wear, weight loss and wear rate, whereas A10-M pin shows the least among all. Actual contact area reduction with textured pins and formation of MoS_2 self-lubricating film between sliding interfaces are two main reasons for minimum wear, weight loss as well as wear rate. At 49 N load, pin wear and weight loss were more as compared to 19.6 N load as expected.

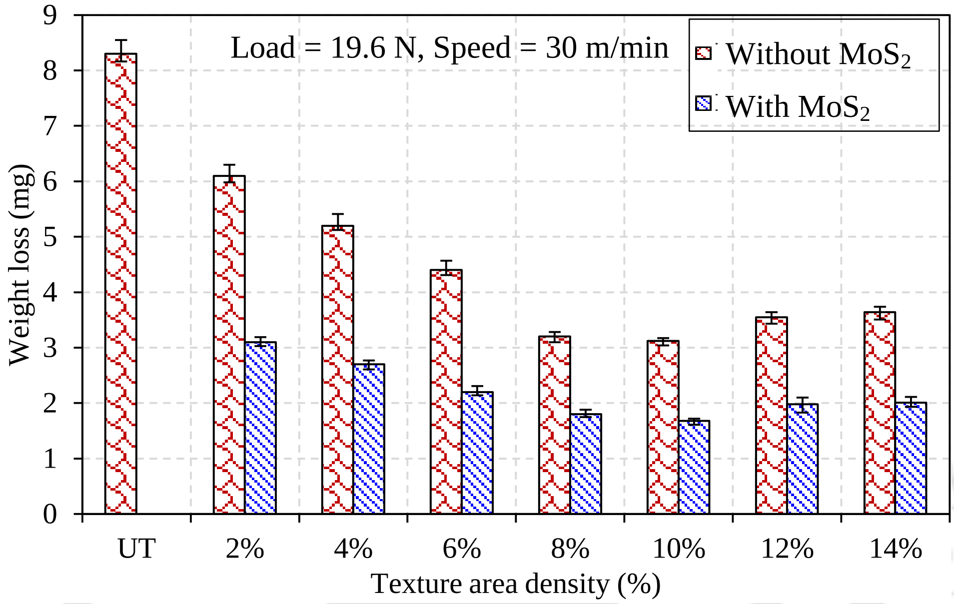

Figure 2.10. Variation of weight loss of the HSS pin with respect to texture area density

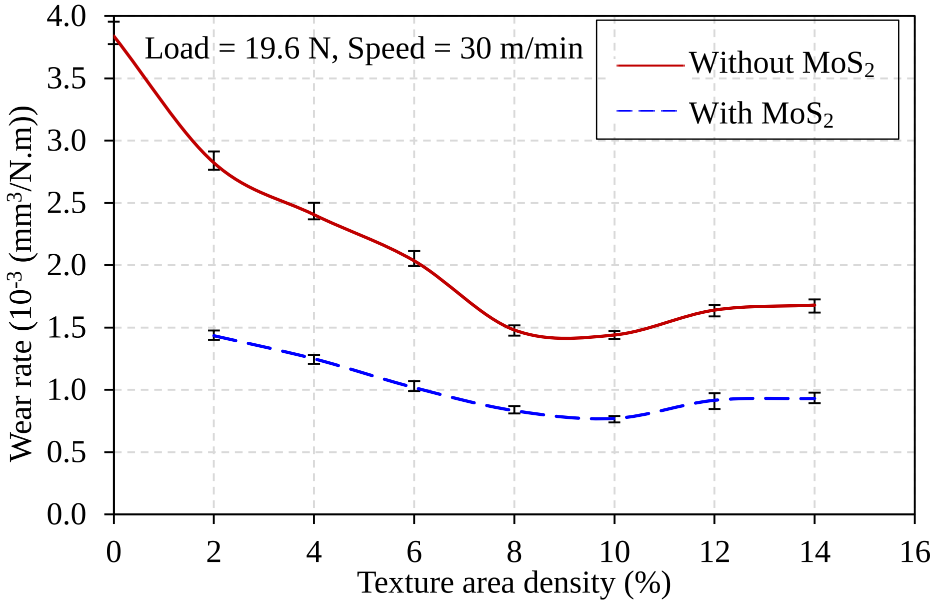

Figure 2.11. Variation of wear rate of the HSS pin with respect to texture area density

For the observed mean values of the small sample, a confidence interval (C_I) may be estimated using the following formula based on *t*-distribution [164]:

$$C_I = \left[\bar{y} \pm t(d_f;\alpha)\frac{s}{\sqrt{n}}\right], \tag{2.5}$$

where C_I represents the confidence interval for any individual population parameter, $\bar{y}$ is the mean value, n is the sample size, d_f is the degree of freedom (n–1), s is the standard deviation of sample and $t(d_f;\alpha)$ is the critical value of t-test, which is obtained from a statistical table for a given d_f and level of significance (α). In this work, for n=3, 95% confidence intervals (α=5%) were estimated. For a typical case, the results are presented in Table 2.1. It is seen that due to the good repeatability of the data, confidence intervals are small and all the estimates can be considered to have an accuracy of the order of 5 to 10%.

Table 2.1. Confidence intervals of coefficient of friction, pin surface temperature and wear for a typical case

Pin	UT (COF)	UT (T in °C)	UT (W in µm)	A10-M (COF)	A10-M (T in °C)	A10-M (W in µm)
$\bar{y}$	0.48	103	232	0.26	45	96
s	0.011	1.2	1.24	0.007	1.32	1.29
C_I	0.45-0.50	106-100	229-235	0.24-0.28	42-48	92-99

2.3.4 Wear morphology and elemental composition of the test material

A mechanism for the formation of the self-lubricating film between sliding interfaces is hypothesised. Figure 2.12 (a) shows a schematic of UT pin and abrasive sheet sliding interface. Figure 2.12 (b) shows MoS_2 filled textured pin, which releases MoS_2 from micro-indents during sliding test. With the increase in temperature and sliding velocity, MoS_2 particles smear in-between sliding interfaces and create a self-lubricating film as shown in Figure 2.12 (c). Due to this, reduction of COF is observed with the MoS_2 filled textured pin.

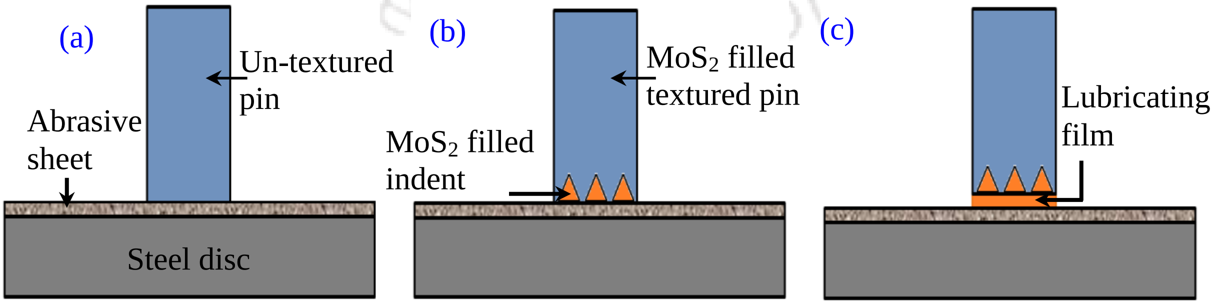

Figure 2.12. (a) Un-textured pin (b) MoS_2 filled textured pin and (c) formation of the lubricating film between sliding interfaces

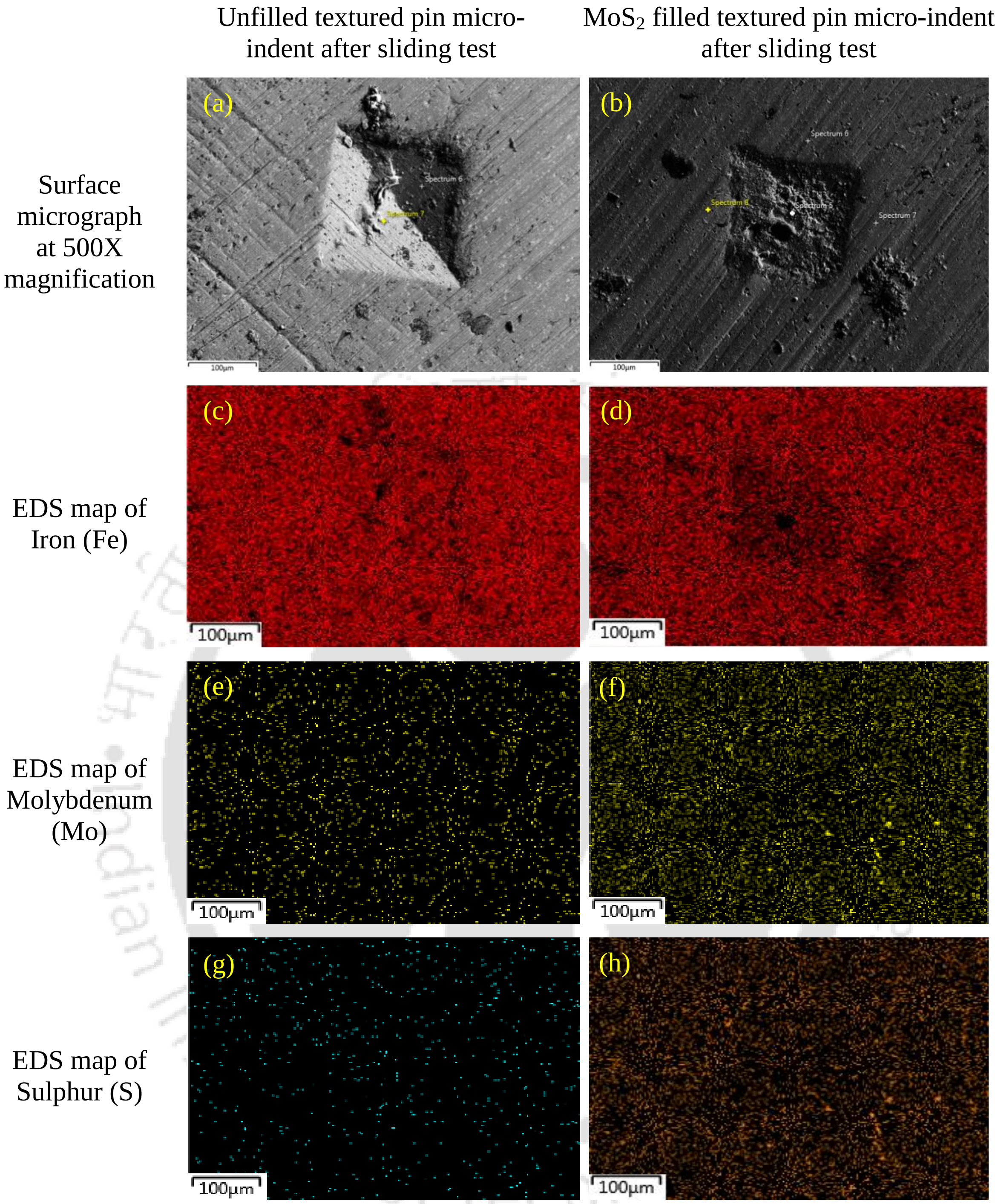

Figure 2.13. Surface micrograph of (a) tested unfilled textured pin micro-indent, (b) tested MoS_2 filled textured pin micro-indent, (c) EDS map of iron for tested unfilled textured pin micro-indent, (d) EDS map of iron for tested MoS_2 filled textured pin micro-indent, (e) EDS map of molybdenum for tested unfilled textured pin micro-indent, (f) EDS map of molybdenum for tested MoS_2 filled textured pin micro-indent, (g) EDS map of sulphur for tested unfilled textured pin micro-indent and (h) EDS map of sulphur for tested MoS_2 filled textured pin micro-indent at 500X magnification

Figure 2.13 (a-b) shows surface micrograph of a micro-indent on the tested A8 and A8-M pins at 500X magnification, respectively after five minutes of sliding test with a load of 19.6 N. Figure 2.13 (c-h) shows energy-dispersive X-ray spectroscopy (EDS) mapping of iron (Fe), molybdenum (Mo) and sulphur (S) on the tested unfilled and MoS_2 filled pins, respectively. From EDS mapping, it is observed that Fe is everywhere in the mapped area of tested unfilled and the MoS_2 filled pins because HSS contains 85 % of it. However, it is clearly visible that Mo and S are much more in the mapped area of MoS_2 filled pin as compared to unfilled pin. Therefore, it is confirmed that MoS_2 solid lubricant is able to get released and smeared on the sliding surface and create a self-lubricating film as shown in Figure 2.12.

To properly understand the wear morphology, tested pin surfaces are observed under FESEM and EDS. Figure 2.14 (a-f) shows the surface morphology and elemental composition analysis of UT, A8 as well as A8-M pins, respectively. Figure 2.14 (a) shows the abrasion wear and pits formation due to ploughing effect. Hard abrasive silicon carbide grits and less hardness of test material cause high friction. Therefore, abrasion wear is dominant on the surface of UT pin. Harder silicon carbide asperities are also able to cause the formation of pits, which are clearly visible. Figure 2.14 (b) shows elemental composition analysis of highlighted area on UT pin after sliding test.

Figure 2.14 (c) shows the surface morphology of unfilled textured pin after sliding test. The presence of micro-indents on the surface of pin reduced the number of abrasive particles taking part in friction. Therefore, only mild abrasion wear was observed. No pit-formation was observed in case of unfilled textured pins. Micro-indents also entrap wear debris. The small amount of entrapped wear debris does not come in contact between sliding interfaces. Therefore, they are not able to take part in enhancing the wear. This is another reason due to which COF and wear of unfilled textured pins reduce. Figure 2.14 (d) shows elemental composition analysis of highlighted area on the unfilled textured pins after the sliding test. Figure 2.14 (e) shows the surface morphology of MoS_2 filled textured pin after the sliding test. Surface morphology of MoS_2 filled textured pin showed very less damage due to the release of MoS_2 particles and formation of the lubricating film further reduces COF. Very mild abrasion wear was seen on the surface of MoS_2 filled textured pin as compared to unfilled textured pin and UT pins. No pit-formation was observed. Figure 2.14 (f) shows elemental composition analysis of highlighted area on MoS_2 filled textured pins after sliding test. Areas A, B and C are selected on the sliding side of micro-indent of UT, unfilled textured and MoS_2 filled textured pins. Elemental composition analysis provides weight percentage of iron (Fe), cobalt (Co), molybdenum (Mo), tungsten (W) and sulphur (S) at three different areas.

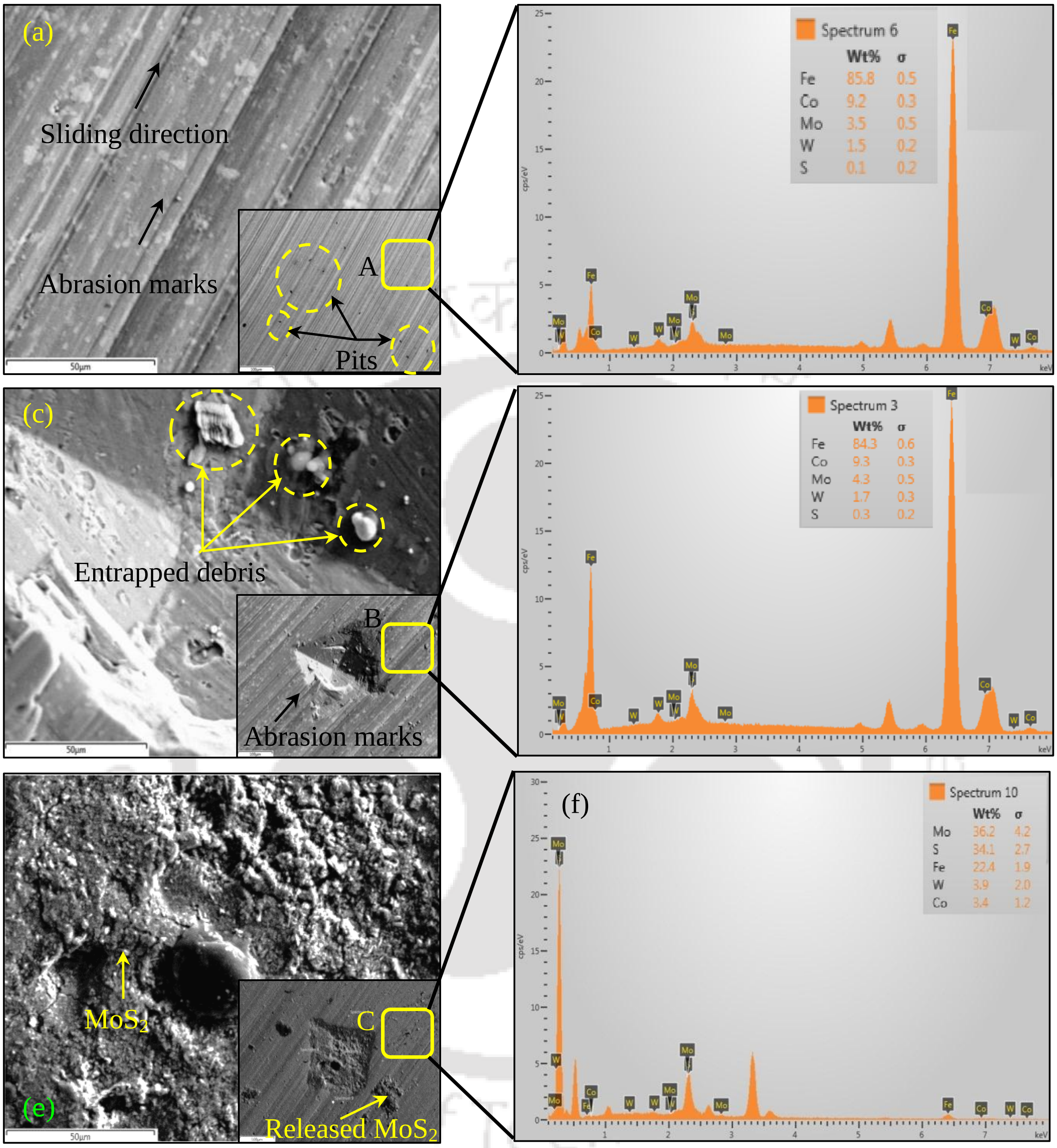

Figure 2.14. (a) Surface morphology of un-textured pin, (b) elemental composition of un-textured pin at corresponding area A, (c) surface morphology of unfilled textured pin micro-indent, (d) elemental composition of unfilled textured pin micro-indent at corresponding area B, (e) surface morphology of MoS_2 filled textured pin micro-indent and (f) elemental composition of MoS_2 filled textured pin micro-indent at corresponding area C after sliding test

2.4 Findings from the research work

The mechanical texture was fabricated on the sliding surface of the plasma nitrided HSS cutting tool with Vickers hardness tester. MoS_2 solid lubricant with graphite-based grease was filled in the micro-indents. Friction and wear tests were carried out with un-textured, unfilled textured and MoS_2 filled textured pins having varying texture area density. The salient findings are as follows:

- Coefficient of friction between MoS_2 filled textured A10-M pin was reduced by 51.37% and 53.33% as compared to UT pins under 19.6 N and 49 N loads, respectively.
- MoS_2 filling of textured tools reduced the pin surface temperature, wear, weight loss of pin and wear rate.
- MoS_2 filled pins with 10% texture area density showed the best tribological performance amongst all investigated samples.
- Surface morphology and elemental mapping analysis confirmed the formation of the self-lubricating film between sliding surfaces for MoS_2 filled micro-textured pin.

Chapter 3

MACHINING PERFORMANCE OF MECHANICAL MICRO-TEXTURED CUTTING TOOLS

Chapter 3 presents preliminary experimentation to find the area for texturing on the rake surface of the tool. Afterwards, 10 % area density mechanical micro-textures (experimentally optimised in Chapter 2) are fabricated on the rake surface of the cutting tool. In order to check the effect of micro-textures on the strength of the tool, static structural FE analysis is done in the Ansys$^{®}$ workbench. Later, comparative study of machining performance with un-textured, mechanical micro-textured and MoS_2 coated mechanical micro-textured high-speed steel cutting tools are carried out.

3.1 Introduction to machining with micro-textured cutting tools

As discussed in the literature, nowadays, dry machining is preferred due to hazardous health and environmental concerns. Researchers have tried to improve the tribological properties of tools in dry machining through the use of a variety of methods. Researchers have used coated Ni-P (h), Ti+Nb or diamond-like coating on to substrates to enhance its tribological properties [165−167]. Self-lubricating tool, which has low friction between the tool and workpiece were also developed to enhance tribological properties by in-situ film formation [168]. Deng et al. [169] added CaF_2 solid lubricants to ceramic cutting tool inserts to improve its machining performance.

Surface texturing over cutting tool surface have emerged for sustainable machining for further improvement in last decade. Surface texturing is a reliable technique to enhance tribological properties and to reduce tool wear of lubricated surfaces. Various physical mechanisms, such as reduction in the real contact area of tool-chip, wear debris entrapment, increase in the supply of lubricants by the creation of fluid reservoir and hydrodynamic effect are responsible for the improvement in load carrying capacity and better performance [170].

Various techniques such as laser [55, 171], micro-EDM [172], wet etching, photolithography and spattering [39] are used for creating micro-texture over the surface of the cutting tool. Micro-textures were fabricated over rake surface of the cutting tool using a femtosecond laser by irradiating the DLC coated tool surface. Results indicate that adhesion of work surface to the tool material and friction coefficient between tool-chip interfaces reduces [55, 171]. Deng et al. [172] used micro-EDM to create micro holes on the flank as well as the rake surface of carbide tools, and micro holes were filled by molybdenum disulphide solid lubricants. Results indicate that these kinds of self-lubricating tools reduce maximum cutting force up to 35% and tool-chip interface friction up to 29 % when compared to the un-textured (UT) tool insert. Obikawa et al. [39] developed four different micro-textures at the cemented carbide tool face through wet etching, photolithography, and spattering. They found that micro-textures were more successful in enhancing lubricating conditions when texture pattern became smaller and more in-depth. However, mechanical texturing has not been employed until recently, despite having various merits.

Mechanical micro-texturing has some when compared to thermal-based processes such as electric discharge machining (EDM), and laser beam surface texturing. Thermal-based texturing methods have various disadvantages such as heat affected zone formation, recast layer formation, crack formation and thermal stress development. Moreover, thermal-based texturing cannot assure relative precision (same size) with the same input parameter. However, mechanical texturing is easy, repeatable and much more accurate when compared to other thermal-based texturing.

In this study, an alternative approach is used to fabricate textures over the cutting tool surface through mechanical indentation using a Vickers hardness tester rather than texturing by thermal based advanced machining processes. In this work, structural analysis was conducted on the cutting tool using an ANSYS® workbench to evaluate the micro-textures effect on stress generation at the tool cutting edge. Tool-chip interface temperature, cutting force, feed force, coefficient of friction and workpiece surface roughness are the evaluating responses of machining. The purpose of this research is to investigate the mechanical texturing technique potential during machining for industrial applications.

3.2 Experimental details

3.2.1 Materials

In order to achieve mechanical micro-texturing, plasma-nitrided high-speed steel (PN-HSS) grade M2 tools were selected. Plasma nitriding is a surface treatment process which can enhance tribological properties such as wear and friction coefficient and also improve fatigue and corrosion resistance by diffusing nitrogen using thermo-chemical treatment. AISI 1040 steel was used as the workpiece material. The cylindrical bars of the diameter 50 mm and length 250 mm were selected to have L/D ratio less than 10 (ISO 3685 standards). The length of cut was 200 mm. Table 3.1 shows the properties of tool and workpiece material.

Table 3.1. Properties of plasma nitrided M2 high-speed steel tool material and AISI 1040 steel as workpiece material

Material	Density (g/cm^3)	Young's modulus E (GPa)	Hardness (HRC)	Poisson's ratio	Thermal conductivity (W/m°C)	Thermal expansion co-efficient(μm/m°C)
PN-HSS M2	8.16	210	62−65	0.27	54.6	12.2
AISI 1040 steel	7.18	200	15−18	0.3	47.7	11

3.2.2 Preliminary experimentation

Preliminary experimentation was carried out to find out wear zone on the UT cutting tool and to select proper input cutting parameters. Tool-chip contact region on the rake surface of the UT cutting tool (Figure 3.1 a−b) was identified using an optical microscope (Make: Zeiss®, Model: AxioCam MRc) and non-contact 3-D surface profilometer (Make: Taylor Hobson®, Model: Talysurf CCI 600). 10% area density mechanical micro-textures were fabricated on the new cutting tools in an area that can encompass the probable tool-chip contact region with sufficient margin. Area for texturing was kept constant for all the cutting tools.

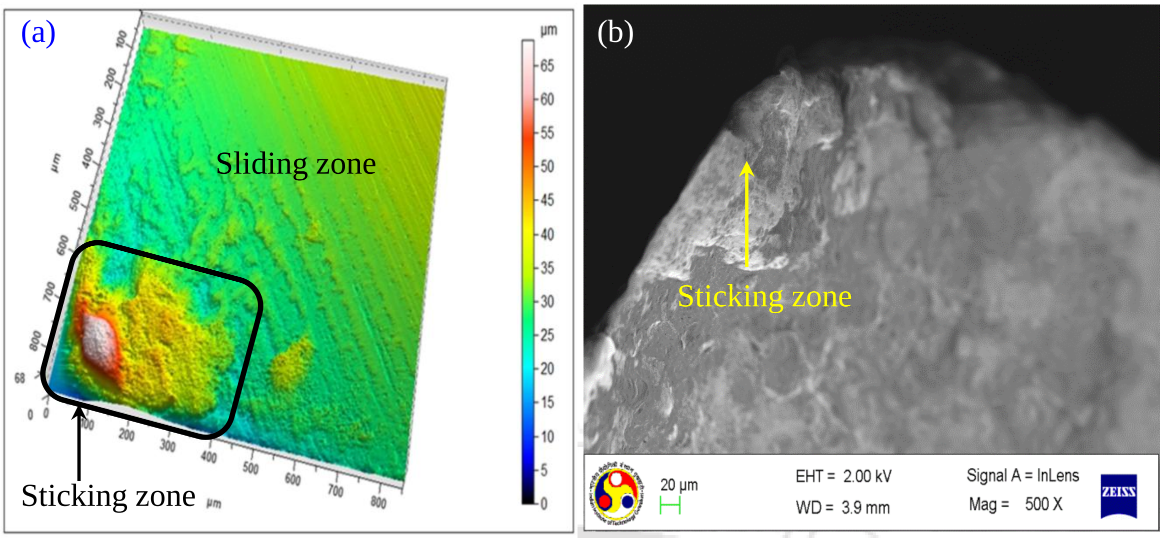

Figure 3.1. Sticking and sliding zone over rake surface of the un-textured tool after machining (a) 3D surface and (b) surface micrograph showing the sticking zone

3.2.3 Fabrication of mechanical micro-textures on the rake surface of the cutting tools

Mechanical micro-textures were created using a Vickers hardness tester (Make: Fuel Instruments & Engineering Private Limited, India; Experimental setup is shown in Chapter 2) on the rake surface of the PN-HSS cutting tool in three different zones. The surface topography of texture generated on the cutting tool rake surface is illustrated in Figure 3.2. Figure 3.2 (a) shows the rake surface of mechanical micro-textured (MµT) cutting tool. Figure 3.2 (b) shows the parent tool material, whereas Figure 3.2 (c) shows field emission scanned electron micrograph of the MµT cutting tool. Figure 3.2 (d) illustrates a 3-D surface profile of the mechanical micro-texture, having an average width of 200 µm and a depth of 50 µm. Figure 3.2 (e−f) shows a field emission scanning electron micrograph of the MµT tool and MoS_2 coated mechanical micro-textured (C-MµT) cutting tools, respectively. Width and depth of mechanical micro-textures are measured using the optical microscope and non-contact 3-D surface profilometer. The MoS_2 solid lubricant of the average particle size of 0.5 µm was mixed with graphite-based grease such that the concentration of MoS_2 was 70 % volume. The micro-textures were filled and compacted with this mixture. The filled textured tools were dried at room temperature for 2 hours before starting the machining.

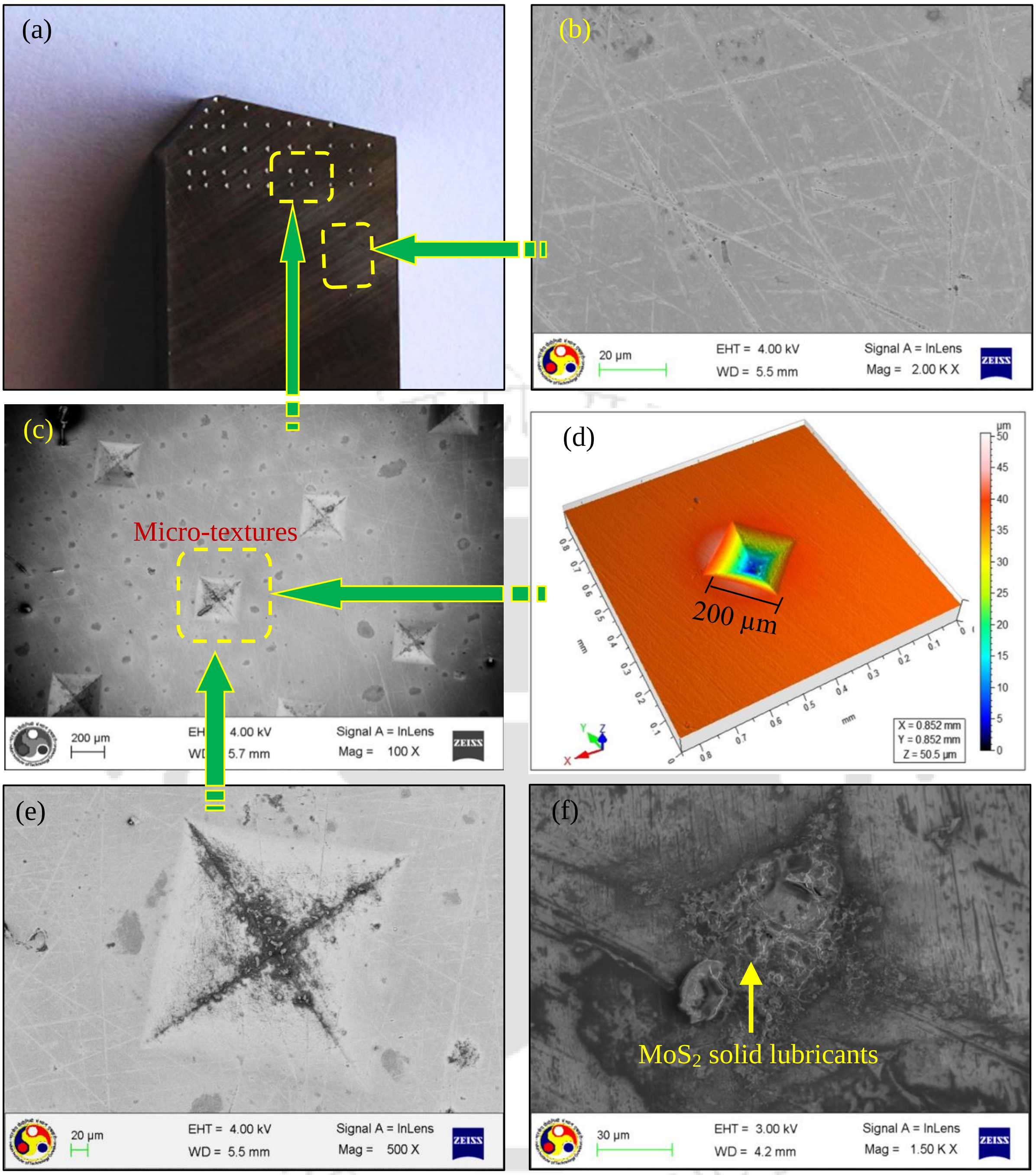

Figure 3.2. Mechanical micro-textured cutting tool (a) overview of mechanical micro-textures on the rake surface of cutting tool (b) surface morphology of un-textured tool rake surface, (c) array of mechanical micro-textures on tool rake surface, (d) 3-D surface profile of single mechanical micro-texture along with dimension, (e) surface morphology of a single uncoated mechanical micro-texture, and (f) surface morphology of a single MoS_2 solid lubricant filled mechanical micro-texture

3.2.4 Experimental design

Expected conclusions have been drawn by using a design of experiments (DOE), an analytical tool which ensures that a minimum number of experiments are planned and performed.

3.2.4.1 Design of experiments

Design of experiments (DOE) is used to evaluate the impact of input process parameters on the output response. Applied statistical techniques ensure a proper output response. If the response (output) is nominated as ‘Y’ and the experimental process input variables as ‘x’, then it may be written as:

$$Y_j = \Phi(x_{1j}, x_{2j}, \ldots x_{Nj}) + e_j \qquad (3.1)$$

where, j = 1,2,3…N represents N observations in the factorial experiment ϕ is the function, which is known as the response surface. The experimental error of the j^{th} observation is measured by e_j [173].

3.2.4.2 Quadratic response surface

The function Φ has to be approximated in the range of the experimental parameters, using polynomial functions in ‘x’ as its mathematical form is not known. In general, first or second order functions are used. Appropriate statistical methods are applied for fitting the function to the experimentally obtained results. The basic form of the quadratic equation (second-degree polynomial) is

$$Y_j = \beta_0 + \sum_{i=1}^{k} \beta_i x_{ij} + \sum_{i=1}^{k} \beta_{ii} x_{ij}^2 + \sum_{i<j}^{k} \beta_{ij} x_{ij} x_{ij} \qquad (3.2)$$

where k = Number of variables.

x_{ij} represents the i^{th} factor in the j^{th} observation. The surface contains linear terms in (x_{ij}), square terms (x_{ij}^2) and the cross product terms ($x_{ij}.x_{jj}$).

3.2.4.3 Central composite rotatable design (CCRD)

CCRD is a modified version of the 2*k* factorial design. A factor is assigned two values (levels), one lower and other higher (coded as +1 and -1, respectively) in a factorial design of experiment. Therefore, this design is known as 2*k* design. This design consists of experiments with the combination of the input parameters at these two levels. The design also includes extra levels (star or axial levels) to ensure that the system is rotatable, i.e., the standard error is equal to all points composite design. A central composite design possesses double star points then factors (i.e., 2*k) in design [173]. As per CCRD technique, experiments number = $2^k + 2k$ + central runs. In this study, input variables are two (cutting speed and feed) i.e., $k = 2$. As per CCRD technique [173], experiments required for two input parameter are (4+4+5), i.e., 13. Preliminary experiments were carried out to find the proper range of input parameters: feed is varied in the range of 0.04-0.20 mm/rev and cutting speed 7−44 m/min at the constant depth of cut 0.3 mm. Coded and the original value of input parameter as per CCRD are listed in Table 3.2. Analysis of variance (ANOVA) is carried out for obtaining estimations of various output responses for a particular model. A significance test was also carried out to check the fitness model and to determine the coefficient of determination (R^2), which provides the measure of goodness of fitted model.

Table 3.2. Coded and the original values of input parameters as per central composite rotatable design

Coded values	**−1.414**	**−1.000**	**0.000**	**1.000**	**1.414**
Cuting speed (m/min)	7	9	15	26	44
Feed (mm/rev)	0.04	0.06	0.12	0.16	0.20

3.2.5 Machining experiments

The turning experiments were performed on a lathe (Make: HMT®, Model: NH 26) equipped with UT, MµT and C-MµT tool having 0° rake angle, 6° clearance angle, 0° inclination angle, 75° cutting edge angle, and 0.8 mm nose radius. A piezoelectric dynamometer (Make: Kistler®, Model: 9272B) connected with charge amplifier was used to measure machining forces, and infrared thermography camera (Make: Infratech®, Model: VARIOCAM hr-400) was used for measuring tool temperature. The cutting zone temperature was measured at the tool-chip interface. The cutting tools rake surface regions after machining was examined using field emission scanning electron microscopy (FESEM; Make: Zeiss®, Model: Sigma). For each test, averages of three experiments were undertaken. An overview and magnified view of the experimental setup is detailed in Figure 3.3 (a-b), respectively.

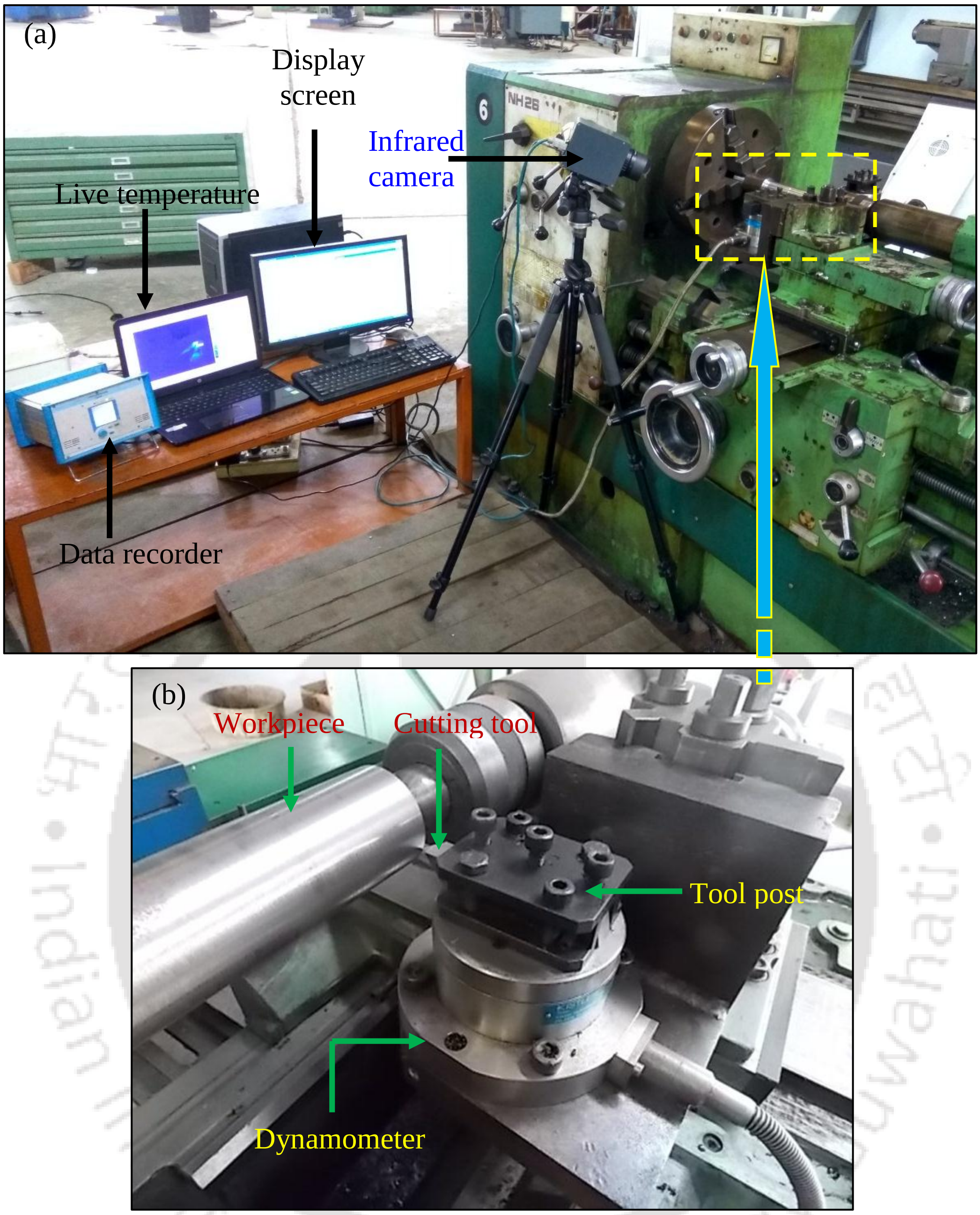

Figure 3.3. (a) Overview of the experimental machining setup and (b) closeup view of the machining region along the dynamometer, tool post and tool-workpiece interaction

3.3 Results and discussion

In this section, the results of finite element simulations for assessing the strength of the tools are reported. Afterwards, the experimental results on the performance during dry machining are presented. All experiments are repeated at least thrice, and average values are reported.

3.3.1 Effect of mechanical micro-textures on the cutting tool strength

Finite element analysis (FEA) was undertaken using ANSYS® 14.0 Workbench to determine the effect of mechanical micro-texture on the strength of tools, under the influence of respective cutting forces. A simplified version of the cutting tool was modelled as cuboid, and 10-noded tetrahedral elements were used. Cutting force and feed force components from experiments were applied on the tool-chip contact area (1 mm × 1mm) as average normal pressure with the assumption that the forces are uniformly distributed to the cutting edge. The cutting tool was kept constrained in all direction to restrict its movement. Table 3.1 shows the properties of the cutting tool material. Figure 3.4 shows the von Mises stress distributions under respective cutting and feed force for UT and MμT cutting tools. The stresses and strains experienced by both the tools are in safe limit. However, Figure 3.4 (a–b) suggest that the MμT tool has less generated von Mises stress when compared to the UT tool, due to the reduction of machining forces in the later. Therefore, it can be considered that the mechanical strength of the tools does not have as much influence as expected due to the presence of the mechanical micro-textures on the rake surface of the tool.

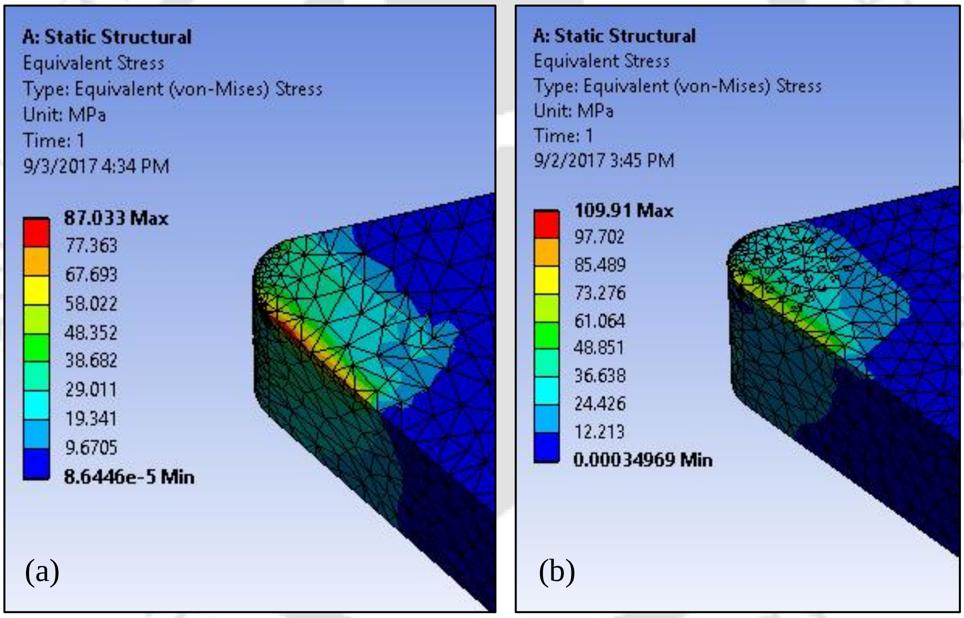

Figure 3.4. von Mises stress field distribution in (a) un-textured cutting tool, and (b) mechanical micro-textured cutting tool

3.3.2 Tool-chip interface temperature

Table 3.3 shows the plan of experiments and obtained results for the C-MμT cutting tool. All measurements were taken thrice for the length of cut of 200 mm and average values are reported. With the regression analysis, the response surface models for $T_{c\text{-}M\mu T}$, $F_{c\text{-}C\text{-}M\mu T}$, $F_{f\text{-}C\text{-}M\mu T}$, $\mu_{C\text{-}M\mu t}$, and $R_{C\text{-}M\mu T}$ are obtained and are given in Eq. (3.5), (3.9), (3.12), (3.16) and (3.19) are in terms of actual factor values (Table 3.2).

Table 3.3. Plan of experiments and summary of responses for coated mechanical micro-textured cutting tool

S.No	**Cutting velocity (m/min)**	**Feed (mm/rev)**	**Cutting force (N)**	**Feed force (N)**	**Friction coefficient**	**Surface roughness (µm)**	**Cutting temperature (ºC)**
1	7	0.12	102.4	42.69	0.43	3.07	63.97
2	9	0.06	60.24	31.75	0.41	3.12	79.06
3	44	0.12	84.78	35.52	0.24	5.43	174.13
4	15	0.04	40.00	14.11	0.35	4.00	91.29
5	9	0.16	146.65	69.37	0.42	3.56	89.14
6	15	0.20	179.3	78.76	0.41	4.43	105.41
7	15	0.12	90.11	37.12	0.40	4.28	111.56
8	15	0.12	90.11	37.12	0.40	4.28	111.56
9	15	0.12	90.11	37.12	0.40	4.28	111.56
10	15	0.12	90.11	37.12	0.40	4.28	111.56
11	26	0.06	58.67	29.56	0.33	4.46	121.56
12	26	0.16	125.6	55.98	0.36	5.05	194.58
13	15	0.12	90.11	37.12	0.40	4.28	111.56

Equation models for tool-chip interface temperature as per CCRD are given below (Eq.3.3–3.5).

$$T_{UT} = 45.9 + 0.684v + 215.69f + 4.04vf - 0.002057v^2 - 1276.1f^2 \tag{3.3}$$

$$T_{M\mu T} = 79.718 + 0.281v - 244.37f + 6.071vf - 0.001399v^2 - 244.814f^2 \tag{3.4}$$

$$T_{C\text{-}M\mu T} = 38.139 + 0.645v - 4.336f + 7.012vf - 0.003271v^2 - 1878.955f^2 \tag{3.5}$$

where f, v represents the feed and cutting speed respectively, and T_{UT}, $T_{M\mu T}$, and $T_{C\text{-}M\mu T}$ are the tool-chip interface temperatures of the tool-chip interface for UT, MµT, and C-MµT.

Table 3.4 shows ANOVA analysis for the tool-chip interface temperature of UT cutting tool. It has been found that among the cutting speed (B and B^2 terms from ANOVA) has the highest contribution (68.97 %) followed by feed (A and A^2 terms from ANOVA) has 30.93 % contribution for tool-chip interface temperature of the UT cutting tool. The R^2 value was found to be 0.9712, whereas the adjusted R^2 value was 0.9591. The CCRD terms are considered in the regression models to improve its predictive accuracy. R^2 value for UT and MµT cutting tools was found to be more than 0.95 for all output results.

Table 3.4. ANOVA for cutting temperature of the coated mechanical micro-textured cutting tool

Source	F Value	p-value Prob>F	Contribution (%)
Model	7.11	0.0007	
A-Feed	18.61	0.0041	18.74
B-Speed	31.89	0.0064	32.10
AB	0.08	0.8137	0.08
A^2	12.10	0.0046	12.19
B^2	36.62	0.0002	36.87
Lack of Fit	1.12	0.5321	

Figure 3.5 illustrates the variation distribution of cutting tool temperature of the UT, MµT, and C-MµT cutting tools with respect to varying feed and cutting speed respectively. It is observed that as the feed and cutting speed increases, the tool-chip interface temperature increases. With an increase in cutting speed, the tool surface feed increases resulting in more friction, which in turn causes an increase in tool-chip interface temperature (Figure 3.5 a).

At the cutting speed of 15 m/min, feed of 0.12 mm/rev and depth of cut of 0.3 mm, tool-chip interface temperature is 140 ºC using UT cutting tool. However, the tool-chip interface temperature is reduced up to 125 ºC and 116 ºC using MµT and C-MµT cutting tools. Reductions in tool-chip interface temperatures by micro-texturing of the tool rake surface might be possible, due to the reduction of the contact area between tool-chip interfaces over the rake surface of mechanical micro-textured tools. Reduction in tool rake surface and chip direct contact area leads to less friction force which results in lower tool-chip interface temperature with MµT cutting tool. In C-MµT cutting tool, lubricant entrapped within mechanical micro-textures starts flowing along the chip flow direction. The presence of lubricant reduces the friction between the tool-chip interfaces.

$$l'_f = l_f - n.d \tag{3.6}$$

where l'_f is real tool-chip length in contact, l_f is apparent tool-chip contact length, n is a number of mechanical micro-textures in contact area and d is the average length of texture.

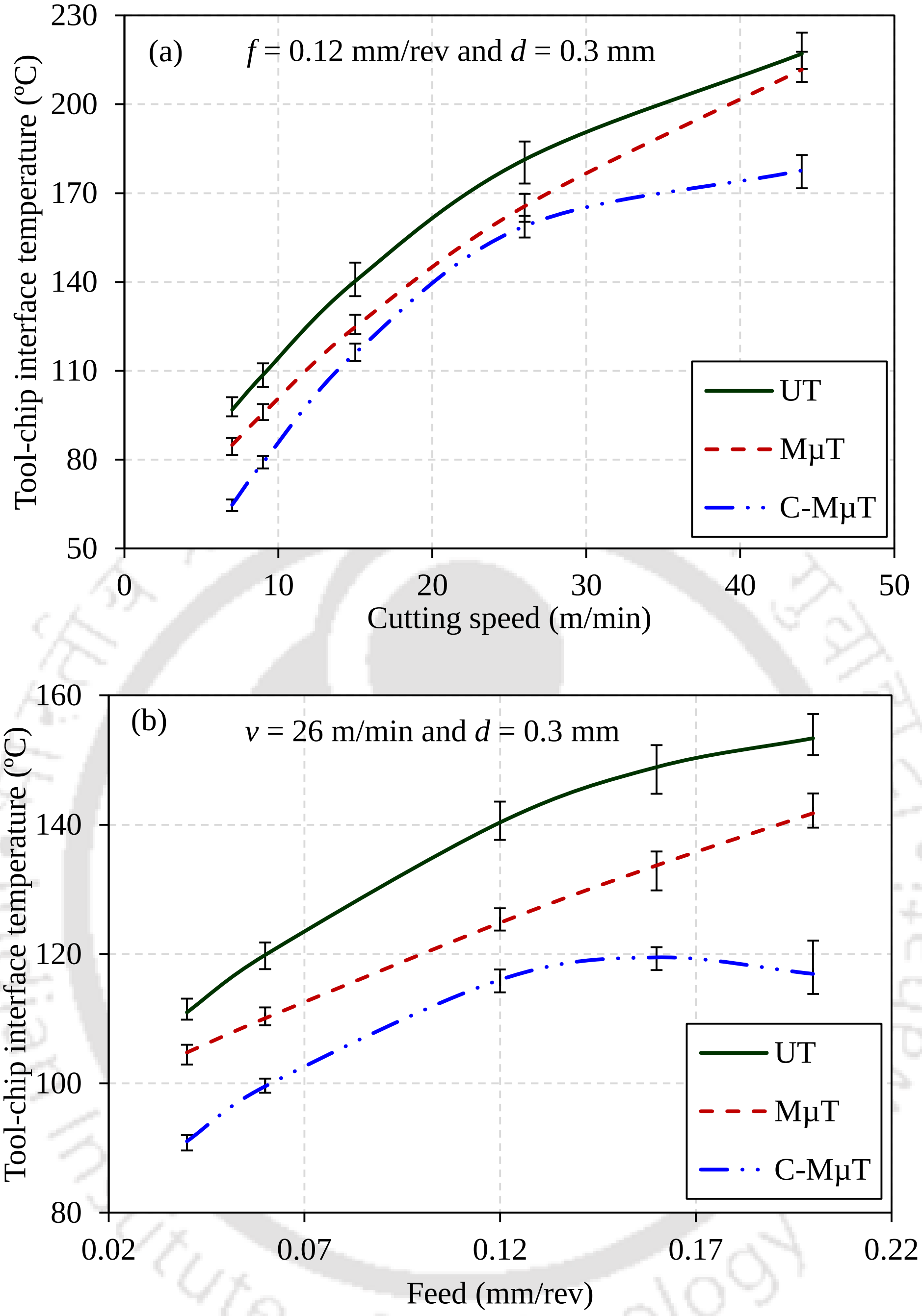

Figure 3.5. Tool-chip interface temperature variation with respect to (a) cutting speed, and (b) feed

As the feed increases, the tool advancement per revolution increases which means contact between tool and workpiece per unit time increases. More amount of material removal per unit time leads to higher temperature generation on the rake surface (Figure 3.5 b). Figure 3.6 (a–c) illustrates thermographic images captured during machining using UT, MμT, and C-MμT cutting tools.

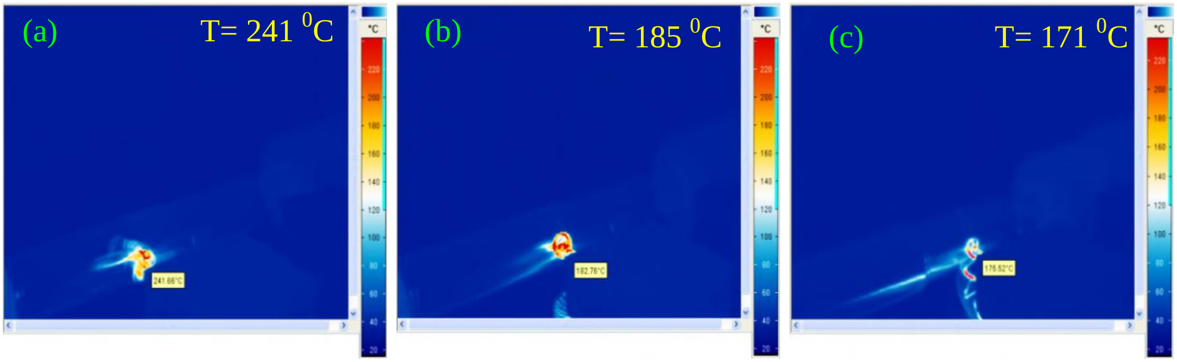

Figure 3.6. Thermal micrographs during machining with (a) un-textured cutting tool, (b) mechanical micro-textured cutting tool and (c) coated mechanical micro-textured cutting tool

3.3.3 Cutting forces

Equation models for cutting force as per CCRD are given below (Eq. 3.7-3.9).

$$F_{c-UT} = 18.556 + 0.0836v + 1153.253f - 1.7998vf - 0.0000248v^2 - 441.492f^2 \quad (3.7)$$

$$F_{c-M\mu T} = 42.875 - 0.05814v + 581.527f - 2.825vf + 0.0009046v^2 + 1976.70f^2 \quad (3.8)$$

$$F_{c-C-M\mu T} = 36.447 - 0.057v + 238.005f - 2.158vf + 0.0008367v^2 + 3370.317f^2 \quad (3.9)$$

where f, v represents the feed and cutting speed respectively, and $F_{c\text{-}UT}$, $F_{c\text{-}M\mu T}$, and $F_{c\text{-}C\text{-}M\mu T}$ are the cutting forces for UT, MµT, and C-MµT cutting tools.

The temperature in primary as well as secondary shear zones increases as the cutting speed increases. Flow stress of workpiece material decreases with a rise in secondary shear zone temperature. Therefore, with an increase in cutting speed reduction of cutting forces are observed (Figure 3.7 a). At the cutting speed of 15 m/min, feed of 0.12 mm/rev and depth of cut of 0.3 mm, cutting force is 137 N using UT cutting tool. However, cutting force is reduced up to 113 N and 92 N using MµT and C-MµT cutting tools. With an increase in cutting speed, the effective tool-chip interface friction reduces. The thickness of chips also decreases with an increase in cutting speed, which in turn leads to an increase in shear plane angle resulting in friction reduction. The effective friction is higher in case of UT and minimum with C-MµT cutting tool. Thus the cutting forces are maximum in UT and minimum in C-MµT (Figure 3.7 a). Shear angle decreases and the chip thickness increases corresponding to feed due to increase in chip thickness, chip load increases which lead to more friction on the tool rake surface. Therefore, the cutting force increases with feed (Figure 3.7 b). Since the mechanical micro-textures and mechanical micro-textures with the coating are provided to decrease the friction on the rake surface, the cutting force will reduce.

Therefore, cutting force observed in C-MμT cutting tool is lower when compared to MμT and UT cutting tool (Figure 3.7b).

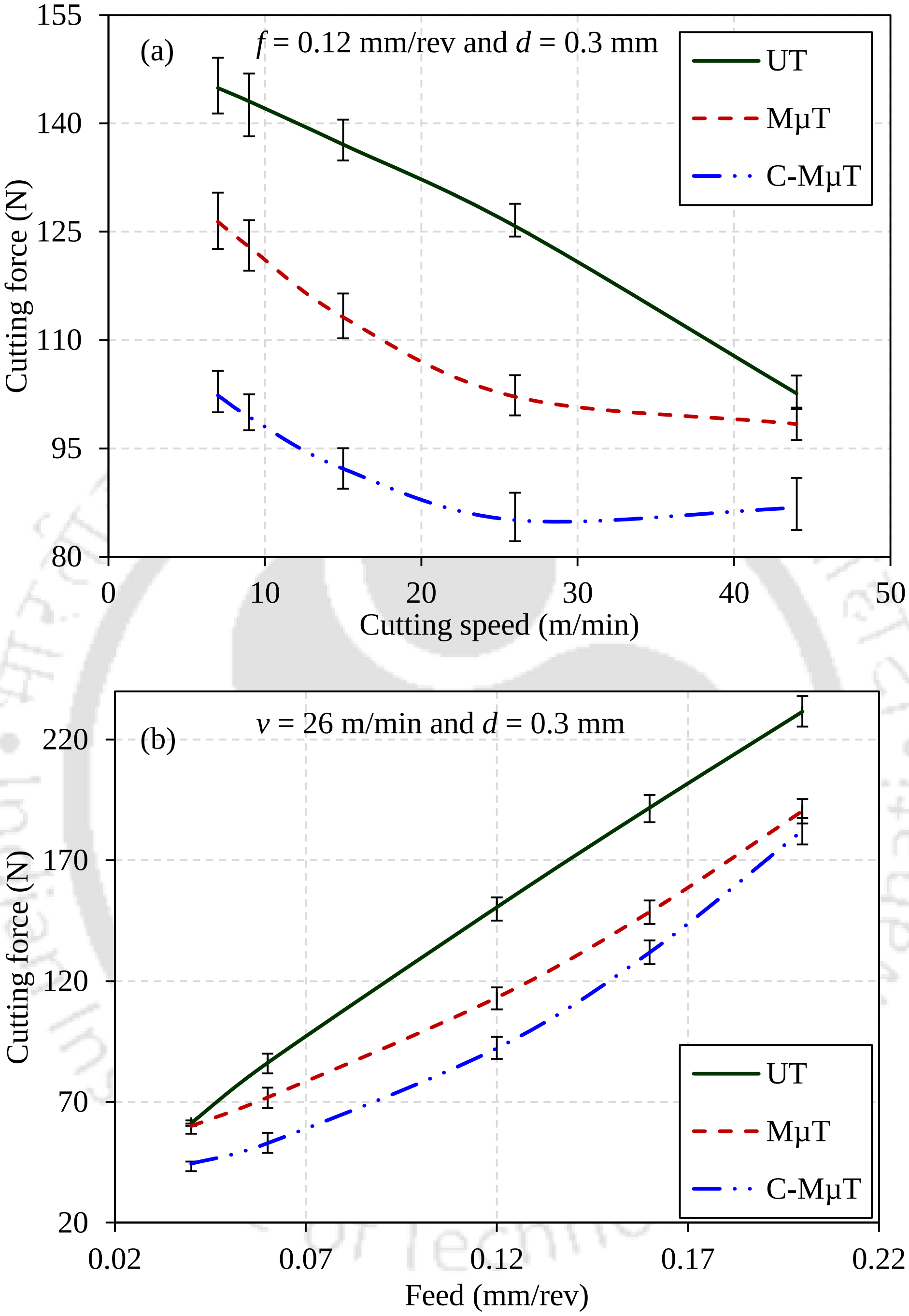

Figure 3.7. Cutting force variation with respect to (a) cutting speed, and (b) feed

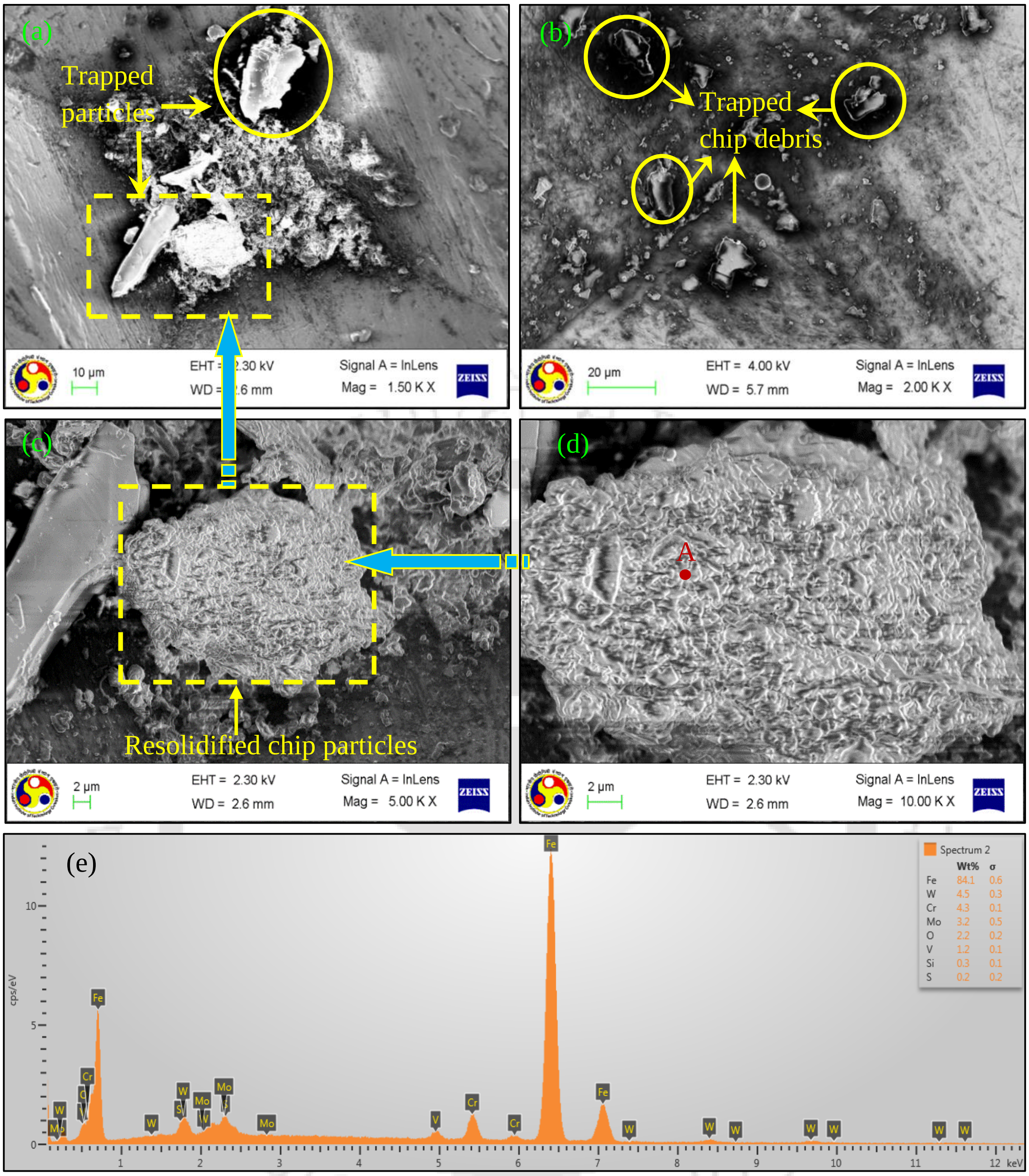

Figure 3.8. Surface morphology and metallurgical characterization, (a) trapped chip particles in mechanical micro-textured cutting tool, (b) other trapped chip particles in mechanical micro-textured cutting tool, (c) resolidified entrapped chip particles, (d) point at resolidified chip particle for energy dispersive x-ray spectroscopy, and (e) elemental analysis of resolidified chip particle

Lower cutting forces were also observed in case of MμT and C-MμT cutting tools due to micro-wear debris from chips entrapped within these micro-textures which were created by welding and rupture phenomena during dry cutting operations, as shown in Figure 3.8 (a−b). Figure 3.8 (c) illustrates resolidified chip particles entrapped inside micro-textures. Figure 3.8

(d) shows a magnified resolidified chip particle at which energy dispersive x-ray spectroscopy (EDX) point analysis of point ‘A’ is carried out. EDX analysis (Figure 3.8 e) shows the presence of Fe at point A, which confirms the fact that micro-debris and resolidified particles from the workpiece are entrapped in micro-textures.

3.3.4 Feed forces

Equation models for feed force as per CCRD are given below (Eq. 310−3.12).

$$F_{f-UT} = -5.683 - 0.081v + 978.16f - 0.928vf + 0.000405v^2 - 1462.412f^2 \tag{3.10}$$

$$F_{f-M\mu T} = 18.089 - 0.123v + 382.019f - 1.157vf + 0.000550121v^2 + 816.997f^2 \tag{3.11}$$

$$F_{f-C\text{-}M\mu T} = 20.752 - 0.041v + 26.047f - 1.289vf + 0.00055251v^2 + 1949.539f^2 \tag{3.12}$$

where f, v represents the feed and cutting speed respectively, and $F_{f\text{-}UT}$, $F_{f\text{-}M\mu T}$ and $F_{f\text{-}C\text{-}M\mu T}$ are the feed forces for UT, MµT, and C-MµT cutting tools.

With an increase in cutting speed, feed force increases (Figure 3.9 a). At the cutting speed of 15 m/min, feed of 0.12 mm/rev and depth of cut of 0.3 mm, feed force is 77 N using UT cutting tools. However, feed force is reduced up to 57 N and 39 N using MµT and C-MµT cutting tools. Increase in cutting speed leads to an increase in tool-chip interface temperature, which results in crater wear and built up edge (BUE) formation as shown in Figure 3.10 (a). Figure 3.10 (b) illustrates the magnified area of built-up edge and Figure 3.10 (c) confirms the brittle fracture of the BUE and adhering from workpiece material over the tool rake surface due to high tool-chip interface temperature. Micro-cracks present in the BUE are shown in Figure 3.10 (d). Therefore, the feed motion of the tool as opposed to increasing the size of the BUE, i.e., increases the feed force. When compared to UT cutting tool, feed force is lower in case of MµT tool because some portion of BUE is accommodated in mechanical micro-textures which are confirmed by the 2-d surface profile of indent having 9.78 µm differences before and after machining (Figure 3.11). Prior to machining, air is trapped inside mechanical micro-textures which improve convection when compared to the UT cutting tool. Therefore, the observed increase in the feed force is minimal in MµT cutting tool.

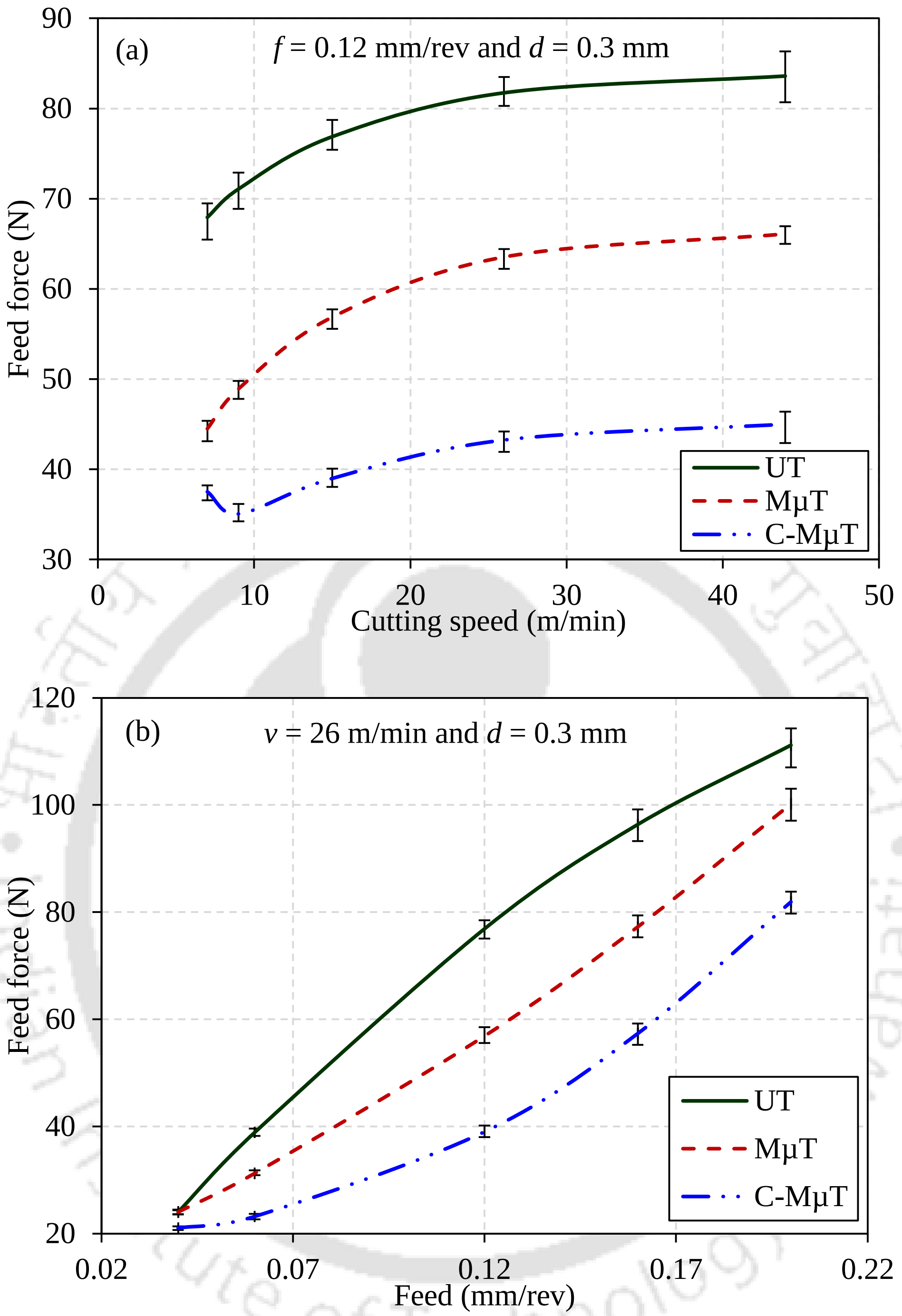

Figure 3.9. Feed force variation with respect to (a) cutting speed and (b) feed

In C-MμT cutting tool, due to proper lubrication of MoS_2, feed force reduces. Therefore, feed force is 31.5% and 49.3% lower in C-MμT when compared to MμT and UT cutting tools (cutting speed = 15 m/min, feed = 0.12 mm/rev and depth of cut = 0.3 mm). As the feed increases, the tool advancement per revolution increases which means contact between tool and workpiece per unit time increases. An increase in the amount of material removal per unit time leads to higher temperature generation on the rake surface (Figure 3.9

b). With the UT cutting tool, the complete rake surface is in contact with the chips. Therefore, due to the high tool-chip contact length, friction will be high, which in turn results in higher temperature and forces. In case of MμT cutting tool, the contact area between tool rake surface and chip decreases. However, for C-MμT cutting tools, the contact of the chip surface is with MoS_2. Therefore, there is no restriction to the flow of chip. Entrapped MoS_2 solid lubricant enhances the lubrication effect, and the tool-chip interface temperature as well as forces reduce significantly (Figure 3.9 b).

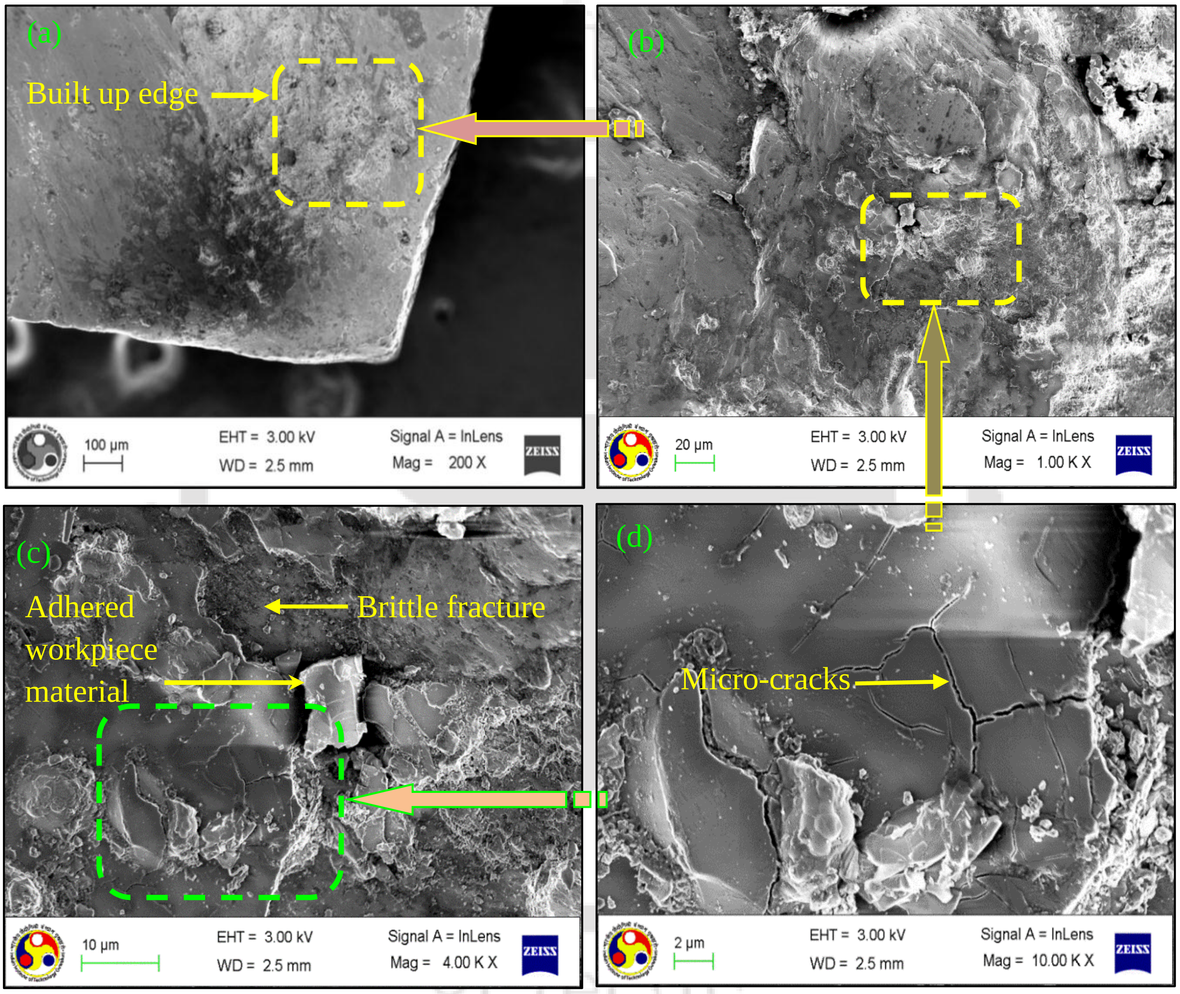

Figure 3.10. Surface morphology of (a) un-textured tool having built up edge on the rake surface, (b) magnified view of build-up edge, (c) brittle fracture and adhered workpiece material on the rake surface and (d) micro-cracks present on the rake surface of the cutting tool

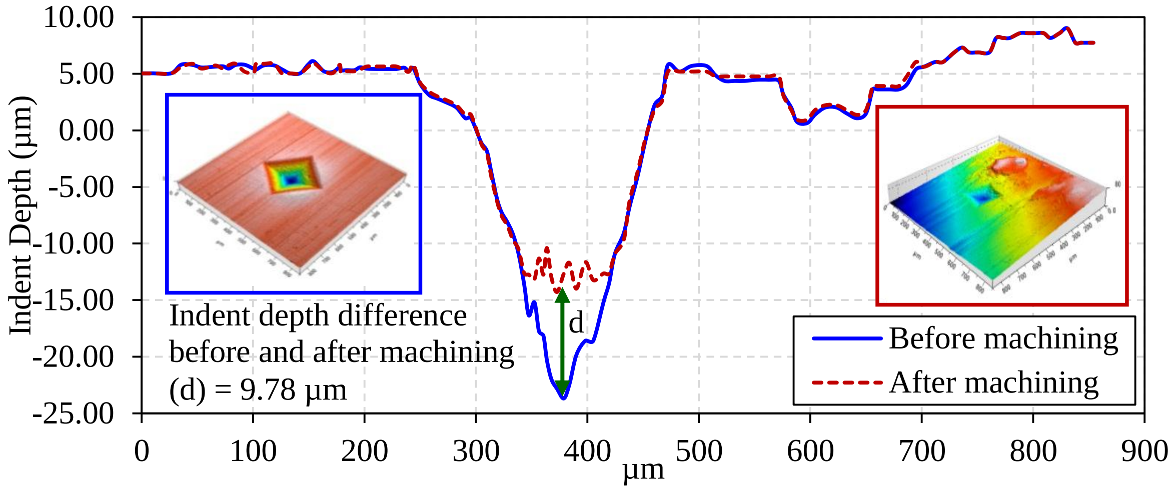

Figure 3.11. 2-D surface profile of mechanical micro-texture before and after machining and corresponding 3-D views

3.3.5 Tool-chip interface coefficient of friction

Friction angle can be related to feed force and cutting force by Merchant's circle diagram. The average coefficient of friction (μ) can be evaluated using the following formula [174]:

$$\mu = \tan(\beta) = \tan(\alpha + \arctan(F_f / F_c)) \qquad (3.13)$$

where α is the rake angle and β is the angle of friction. During this study, when creating mechanical micro-textures flat cutting tools are used (α = 0°). F_c denotes cutting force and F_f illustrates feed force. The decrease in tool-chip interface friction leads to reduce the energy required for formation of the chip, which improves the efficiency of the machining process. Equation models for the coefficient of friction as per CCRD are given below (Eq. 3.14–3.16).

$$\mu_{UT} = 0.583 - 0.000646v + 0.782f + 0.00101vf - 0.0000028v^2 - 2.829f^2 \qquad (3.14)$$

$$\mu_{M\mu T} = 0.476 - 0.0005385v + 0.862f + 0.0014958vf - 0.000003219v^2 - 1.573f^2 \qquad (3.15)$$

$$\mu_{C-M\mu T} = 0.411 - 0.0006868v + 0.548f + 0.00227508vf - 0.00000166456v^2 - 1.978f^2 \qquad (3.16)$$

where f, v represents the feed and cutting speed respectively, and μ_{UT}, $\mu_{M\mu T}$ and $\mu_{C\text{-}M\mu T}$ represent the friction coefficient of UT, MμT, and C-MμT cutting tools.

At the cutting speed of 15 m/min, feed of 0.12 mm/rev and depth of cut of 0.3 mm, coefficient of friction between tool-chip interface is 0.56 using UT cutting tool. However, it is reduced up to 0.502 and 0.422 using MμT and C-MμT cutting tools. At the tool-chip interface, the frictional force is linearly proportional to average shear stress and tool-chip length of contact [175]. Mechanical micro-textures can reduce the tool-chip length of contact for MμT and C-MμT tools. In the case of MμT cutting tool, real contact area reduction results in the lesser coefficient of friction and solid lubricants presence in C-MμT reduces the magnitude of the coefficient of friction even more (Figure 3.12).

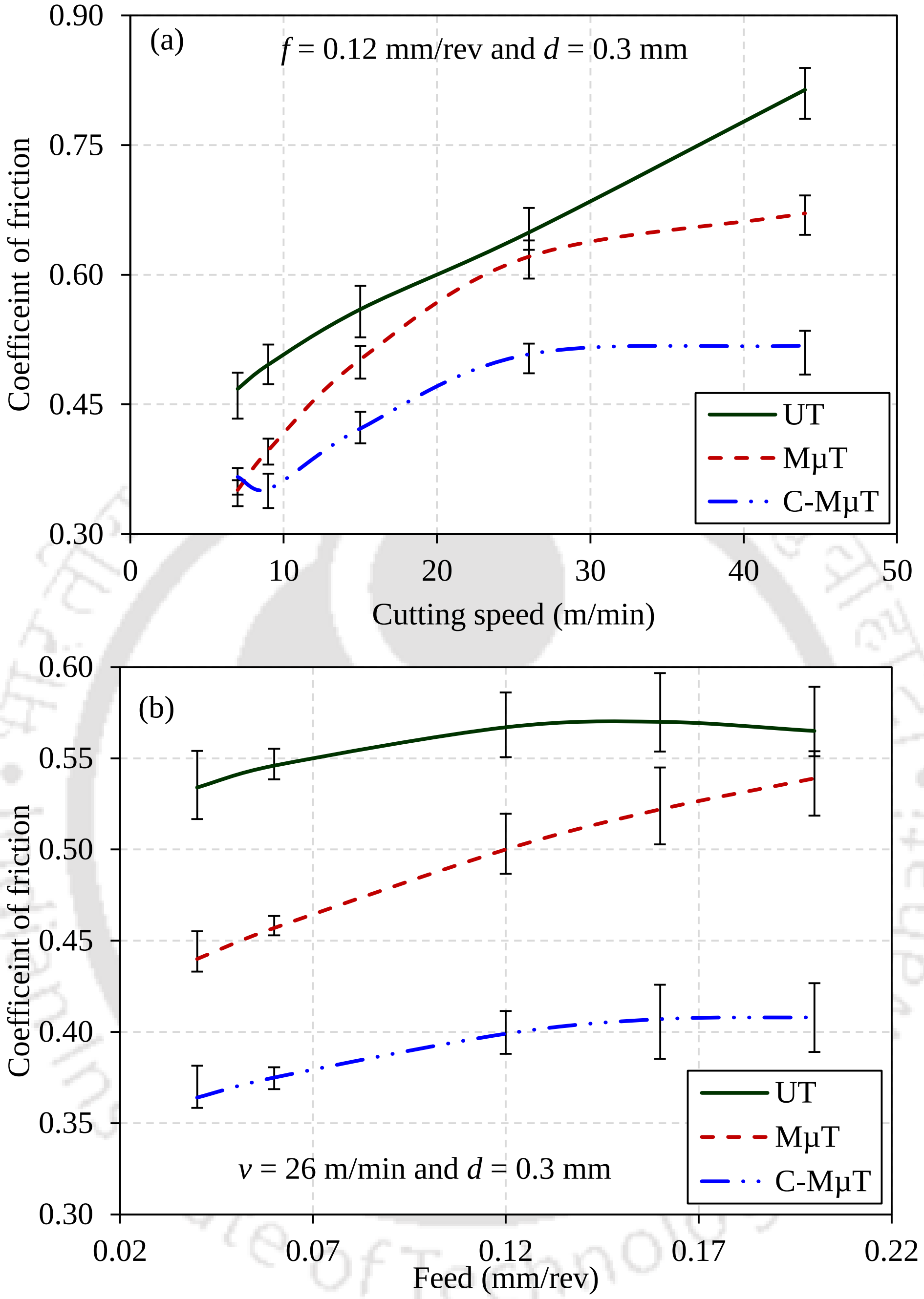

Figure 3.12. Variation of coefficient of friction with (a) cutting speed and (b) feed

Mechanical micro-textures act as a lubricant reservoir for the C-MμT cutting tool. With an increase in the cutting speed, tool-chip interface temperature increases. The trapped lubricant starts to flow in chip flow direction, which results in the creation of a self-lubricant film due to the higher temperature during machining. The presence of lubricant reduces the friction between the tool-chip interfaces (Figure 3.12 a). As the feed force is less compared to cutting force when varying the feed, the friction coefficient is less in magnitude when compared to its variation against cutting speed (Figure 3.12 b).

Figure 3.13 (a–b) shows the micrograph of C-MµT after machining at feed (*f*) = 0.12 and 0.2 mm/rev respectively with a cutting speed (*v*) = 15 m/min and depth of cut (*d*) = 0.3 mm. Dense and deep wear tracks were observed in the vicinity of mechanical micro-textures at high feed as shown in Figure 3.13 (b). It is due to less interaction time between the chip and mechanical micro-textures, only a fraction of solid lubricant was able to smear and create a lubricating film at a higher feed when compared to lower feed (Figure 3.13 a), which leads to higher friction coefficient.

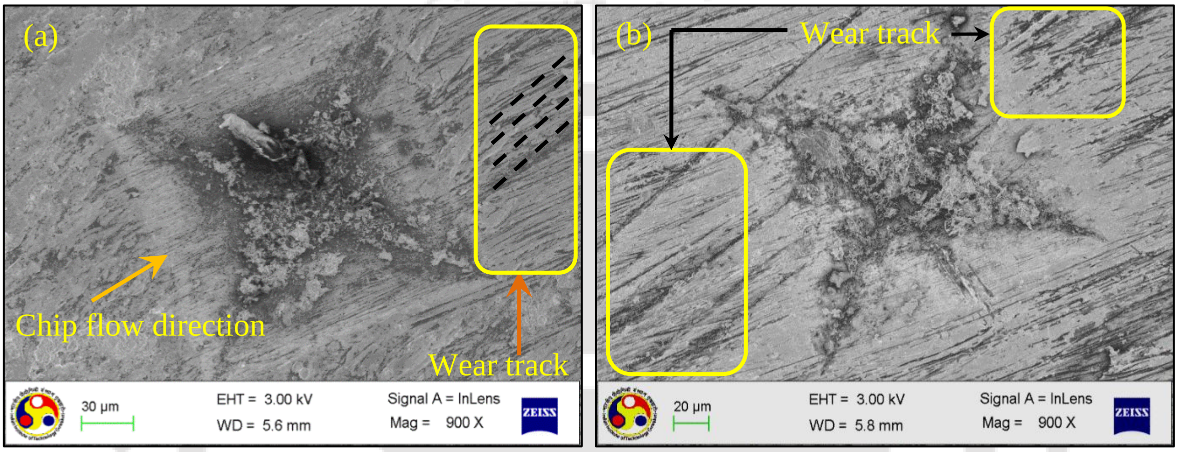

Figure 3.13. Morphology of tribological mechanical micro-textured rake surface filled with MoS_2 after machining at different feeds, (a) feed = 0.12 mm/rev, and (b) *f* = 0.2 mm/rev (At constant *v*=15 m/min, d = 0.3 mm)

3.3.6 Workpiece surface roughness

Equation models for surface roughness (R_a) as per CCRD are given below (Eq. 3.17−3.19):

$$R_{UT} = 3.063 + 0.004875v + 9.069f - 0.013vf - 0.00000082v^2 - 1.384f^2 \quad (3.17)$$

$$R_{M\mu T} = 2.008 + 0.03v - 6.7f + 0.04vf - 0.0000793203v^2 + 24.799f^2 \quad (3.18)$$

$$R_{C\text{-}M\mu T} = 1.716 + 0.026v + 5.538f + 0.027vf - 0.00006644v^2 - 17.699f^2 \quad (3.19)$$

where *f*, *v* represents the feed and cutting speed respectively, and R_{UT}, $R_{M\mu T}$ and $R_{C\text{-}M\mu T}$ are the R_a for UT, MµT, and C-MµT. Figure 3.14 (a–b) shows the R_a of the workpiece machined with UT, MµT, and C-MµT cutting tools with respect to feed and cutting speed.

It was observed that workpiece R_a increases with increasing feed irrespective of the type of cutting tool (Figure 3.14 b). At the cutting speed of 15 m/min, feed of 0.12 mm/rev and depth of cut of 0.3 mm, R_a of the workpiece is 4.35 µm using UT cutting tool. However, it is reduced up to 4.21 µm and 4.01 µm using MµT and C-MµT cutting tools. Due to the higher temperature during machining with UT when compared to MµT and C-MµT cutting tools, the magnitude of adhesion of tool material on the workpiece is dominant. Also, friction between the tool-chip interface is higher, which results in greater R_a of the workpiece in the UT. However, during machining with C-MμT cutting tool, due to lesser cutting and feed force comparatively less cutting tool vibration occur leading towards the better surface finish.

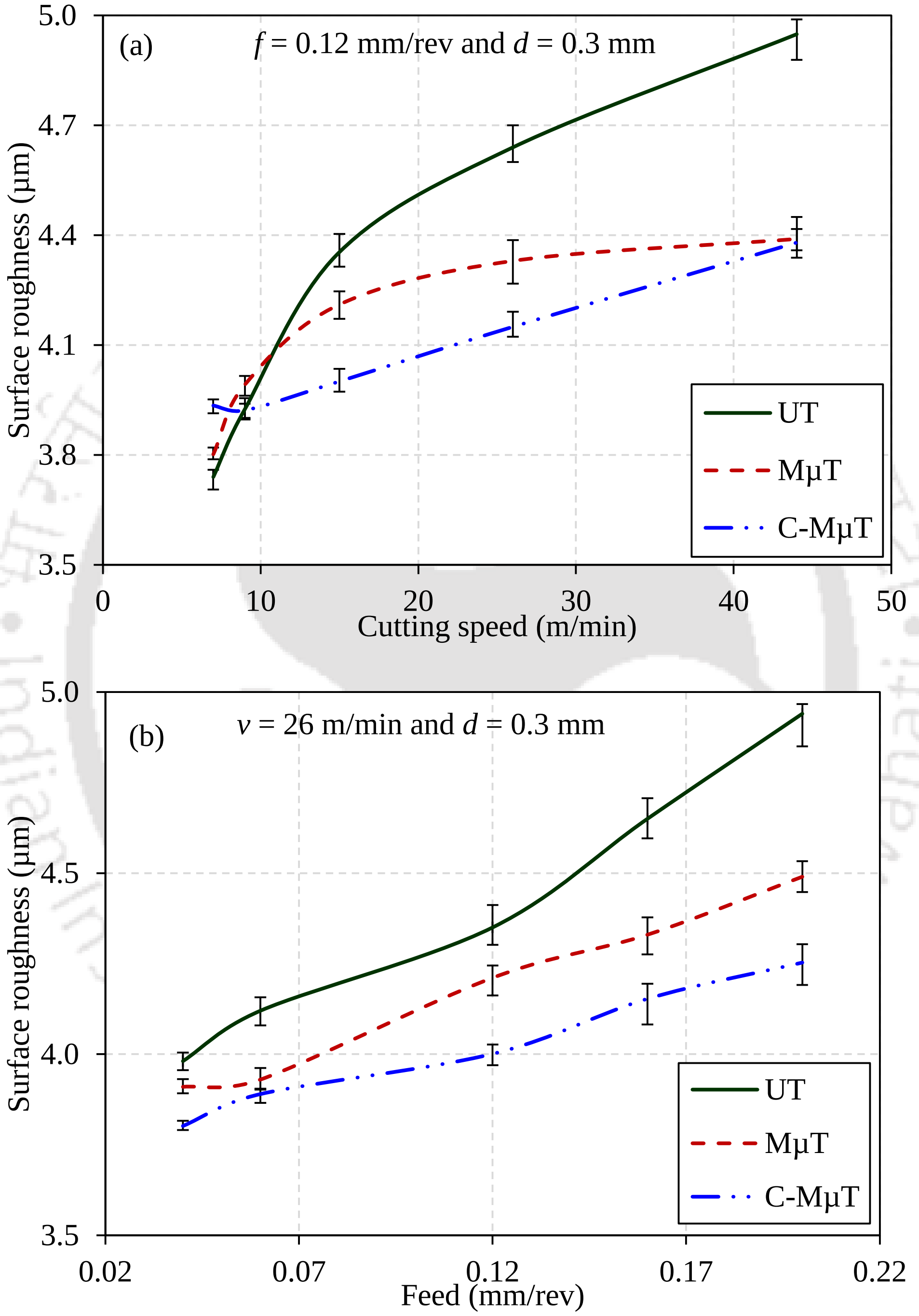

Figure 3.14. Centre line average surface roughness of workpiece variation with respect to (a) cutting speed, and (b) feed

3.4 Findings from the research work

The mechanical micro-texturing method was used to fabricate mechanical micro-textures (10% area density) over the rake surface of PN-HSS cutting tools, and molybdenum disulphide solid lubricant was coated over mechanical micro-textures. Cutting tests were performed using UT, MµT, and C-MµT and the obtained conclusions are detailed as follows:

- Finite element analysis shows that von-Mises stress generation at the cutting edge of UT and MµT cutting tools are in safe limits. Also, the presence of the mechanical micro-textures on the tool rake surface had very less influence on the mechanical strength of the cutting tool.
- Tool-chip interface temperature, machining forces and tool-chip interface coefficient of friction were reduced significantly for MµT and C-MµT as compared to UT cutting tools.
- Workpiece surface roughness decreases with MµT and C-MµT cutting tools as compared to UT cutting tool.
- In C-MµT cutting tool, the formation of the self-lubricating film during machining reduces friction, which is the prime reason for the improvement in its cutting performance.

Chapter 4

COMPARATIVE HARD MACHINING PERFORMANCE OF VARIOUS MECHANICAL MICRO-TEXTURED CUTTING TOOLS

4.1 Introduction

4.2 Experimental details

- 4.2.1 Materials
- 4.2.2 Selection of texturing area
- 4.2.3 Fabrication of various mechanical micro-textures on the rake surface of the tungsten carbide cutting tools
- 4.2.4 Experimental design
- 4.2.5 Machining experiments

4.3 Results and discussion

- 4.3.1 Effect of various mechanical micro-textures on the cutting tool strength
- 4.3.2 Tool-chip interface temperature
- 4.3.3 Machining forces
- 4.3.4 Tool-chip interface coefficient of friction
- 4.3.5 Surface morphology of cutting tool rake surface
- 4.3.6 Chip morphology

4.4 Findings from the research work

In **Chapter 4**, a comparative study of hard machining with various mechanical micro-textured and MoS_2 coated mechanical micro-textured tungsten carbide cutting tools are carried out. Six different uncoated and MoS_2 coated mechanical micro-textures were fabricated, and their hard machining performance is compared. For comparison, machining is also carried out using the conventional un-textured cutting tool.

4.1 Introduction

In Chapter 3, machining experiments are conducted using PN-HSS cutting tools. However, for hard machining applications, PN-HSS cutting tools are not suitable. Particularly for hard machining, cutting tool inserts made of tungsten carbide (WC) are the viable option. Therefore, for hard machining applications, WC inserts are used.

As investigated in Chapter 3, micro-textures have the ability to reduce tool-chip interface friction and tool wear. Although surface texturing has several merits, however, it is also reported that textures fabricated using thermal based methods have some problems. Heat affected zone of textures was obvious one of the main problem. Inferior quality of textures fabricated using focused energy beam causes more abrasive wear [54].

Fabricating micro-textures using conventional mechanical method is an effective way to solve the above mention problem. Traditional methods such as Vickers hardness tester and scratch tester can fabricate micro-textures. These mechanical methods are free of harmful gases and are environment-friendly. Figure 4.1 (a-d) shows surface morphology, and 3-d surface profile of a micro-texture fabricated using thermal based CO_2 laser and scratch tester. These textures are given the name as mechanical micro-textures (MμTs). Micro-textures are free from heat affected zone, thermal stresses, or poor surface finish (Figure 4.1 a-b). MμTs are also precise, repetitive and easy to fabricate.

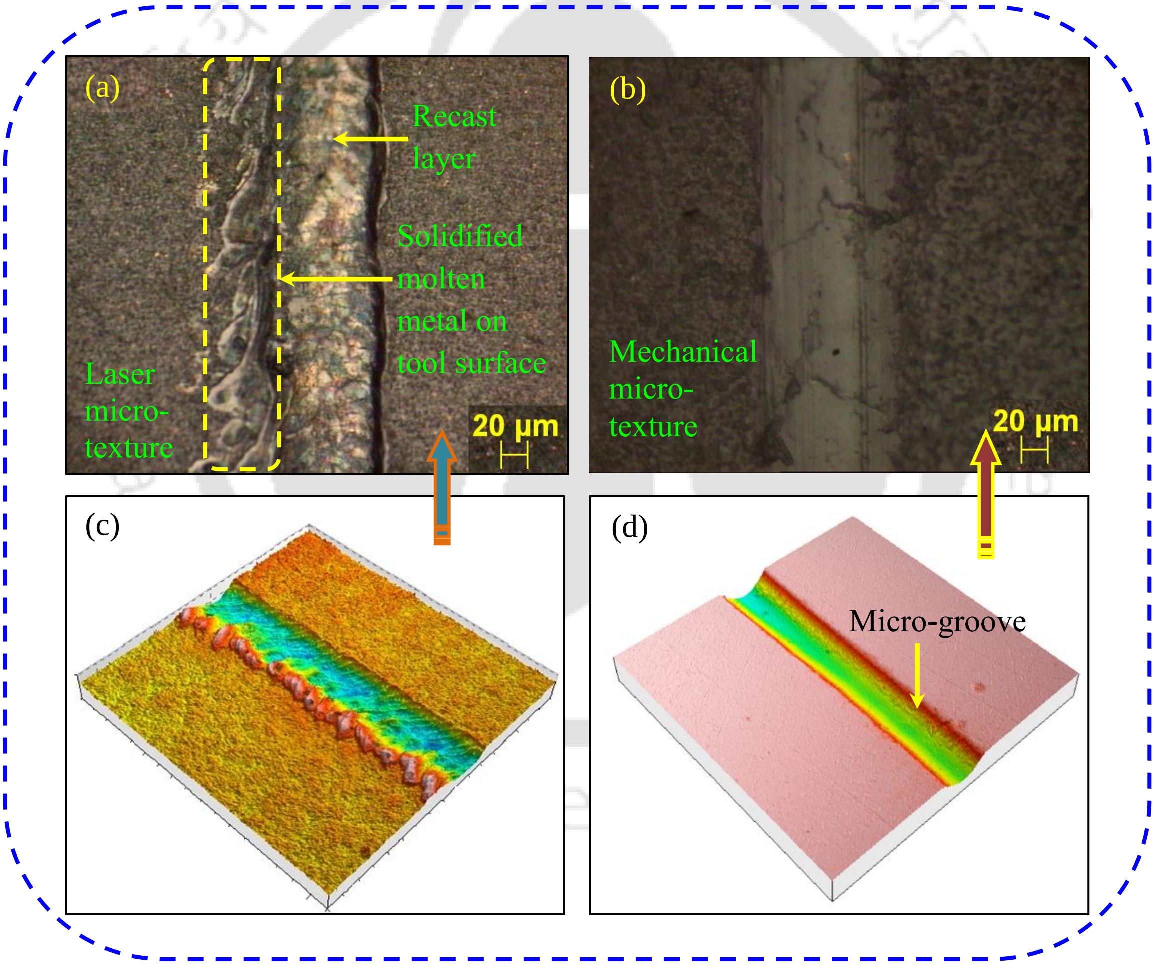

Figure 4.1. Surface morphology of (a) laser micro-texture, (b) mechanical micro-texture, (c) 3-d surface profile of laser micro-texture and (d) 3-d surface profile of mechanical micro-texture

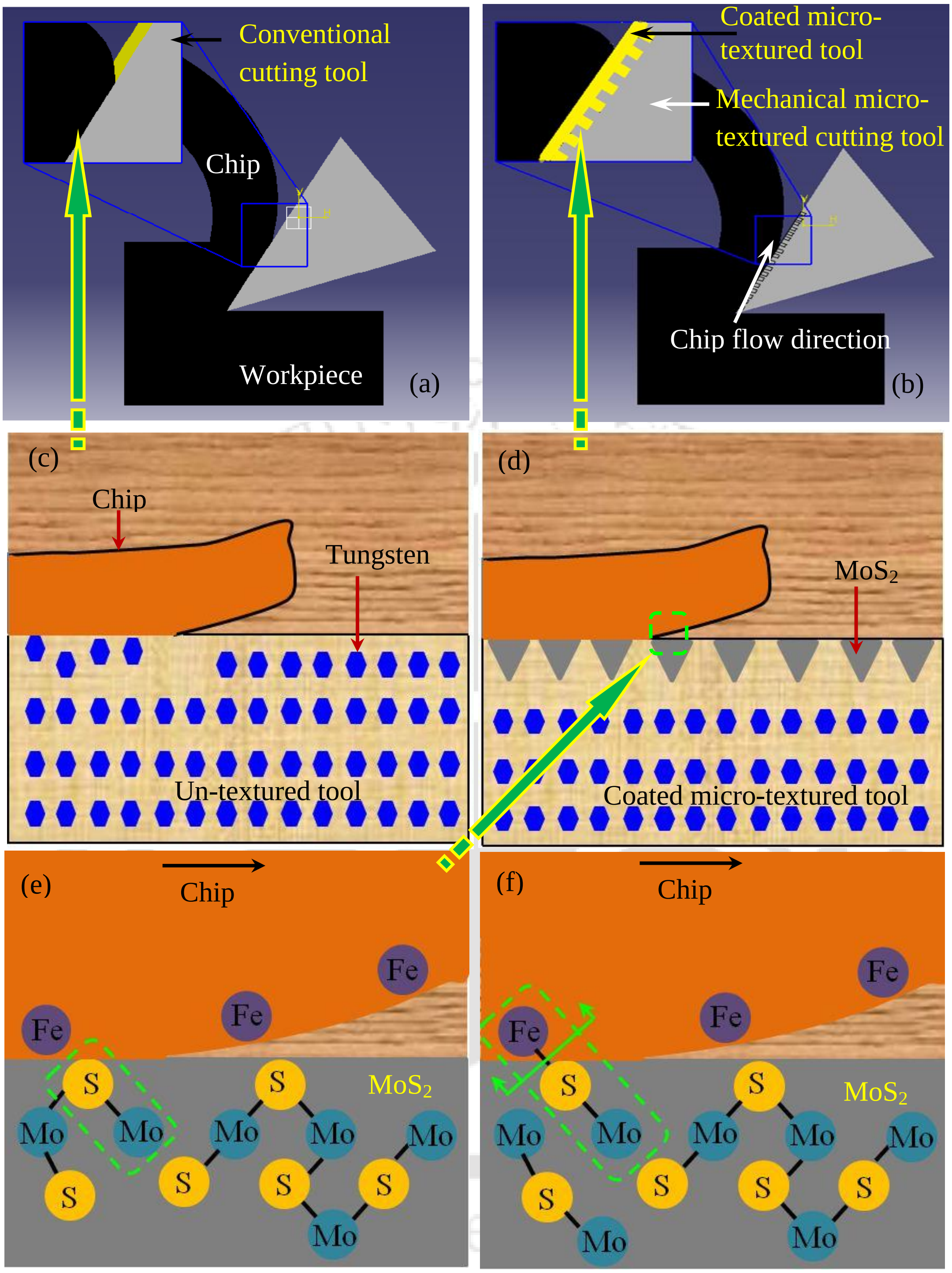

Figure 4.2. Schematic diagram of the tool-chip interface in (a) un-textured cutting tool, (b) coated micro-textured cutting tool, (c) Worn out tool (tungsten grains are plucked out), (d) MoS_2 lubricated micro-textured cutting tool, (e) formation of MoS^{2-} and (f) formation of iron-molybdenum sulphide-bridge

In this study, MμTs are fabricated on the rake surface of the tungsten carbide cutting tool insert using a Vickers hardness tester and scratch tester. MoS_2 solid lubricants are coated in textures. Figure 4.2 explains the hypothesis of MoS_2 coated MμT cutting tools. Figure 4.2 (a-b) shows schematic of the tool-chip interface of the un-textured cutting tool and MoS_2

coated micro-textured cutting tool. Figure 4.2 (c) shows that chips sliding over rake surface of the un-textured cutting tool can pluck out tungsten grains and break the bond with cobalt binder due to high temperature and pressure during machining. Thus, un-textured tool rake surface worn out, which results in crater wear. Figure 4.2 (d) shows that chips sliding over the rake surface of MoS_2 coated micro-textured cutting tool can pluck out MoS_2 lubricant. MoS_2 released from textures have a low shear strength (30−35 MPa), whereas the shear strength of tungsten carbide is about 700−800 MPa. Figure 4.2 (e) shows the formation of MoS^{2-} due to interaction with Fe^{2+} ions that lead to the formation of iron-molybdenum sulphur-bridge (Figure 4.2 f) in-between the tool-workpiece interface, which reduces the friction. Due to the lubricating properties of MoS_2 than tungsten carbide, the tool-chip interface temperature, cutting force and feed force will be lower.

In this Chapter, machining experiments are performed using MoS_2 coated and uncoated MμT cutting tool. Experiments are also carried out using un-textured cutting tool for comparison purpose. Tool-chip interface temperature, cutting force, feed force, the coefficient of friction (COF) and workpiece surface roughness is measured. After experiments, surface morphology, elemental composition analysis and elemental mapping of the cutting tool are analysed using scanning electron microscope and energy dispersive spectroscopy. The purpose of this research work is to compare the performance of various mechanical texturing processes for improving the machining performance. It is a step towards green manufacturing.

4.2 Experimental details

4.2.1 Materials

For this study, uncoated rake surface and coated flank surface tungsten carbide (WC/Co) cutting tool inserts were selected. Coated flank surface inserts were chosen to reduce flank wear, as mechanical micro-textures were not fabricated on the flank surface. Sandvik Coromant® make ISO TNMA220412 insert was chosen for the machining of hardened AISI H-13 steel having an average hardness of 56 HRC. The cylindrical bars of the diameter 50 mm and length 250 mm were selected to have L/D ratio less than 10 (ISO 3685 standards). The length of cut was 200 mm. Its main composition is C 0.32–0.4%, Cr 5.13–5.25%, Mo 1.33–1.4%, V 1%, Si 1 %, Fe remaining. Table 4.1 shows the properties of the cutting tool and workpiece material.

Table 4.1. Properties of tungsten carbide tool and hardened AISI H-13 steel workpiece

Material	**Density (g/cm^3)**	**Young's modulus (GPa)**	**Flexural strength (MPa)**	**Hardness (HRC)**	**Poisson's Ratio**	**Co-efficient of thermal expansion µm/(m. °C)**
WC+CO	14.5	550	2000	89±3	0.23	4.51
H-13 steel	7.8	210	950	56±2	0.30	7.42

4.2.2 Selection of texturing area

Initially turning experiments were conducted with the un-textured cutting tool. Machining was carried out for 900 seconds with a cutting speed of 125 m/min and feed of 0.28 mm/rev to get maximum affected rake surface area as shown in Figure 4.3 (a). Figure 4.3 (b-d) shows worn out rake surface of the cutting tool. Adhesion and abrasion wear region on the rake surface of the un-textured cutting tool is identified (Figure 4.4 a). MµTs were fabricated on the new cutting tools in an area that can encompass the probable wear zone with sufficient margin (Figure 4.4 b). Textures are fabricated 250 µm away from cutting edge and 400 µm from the nose of the insert such that the strength of the tool is not affected that much (Figure 4.4 b).

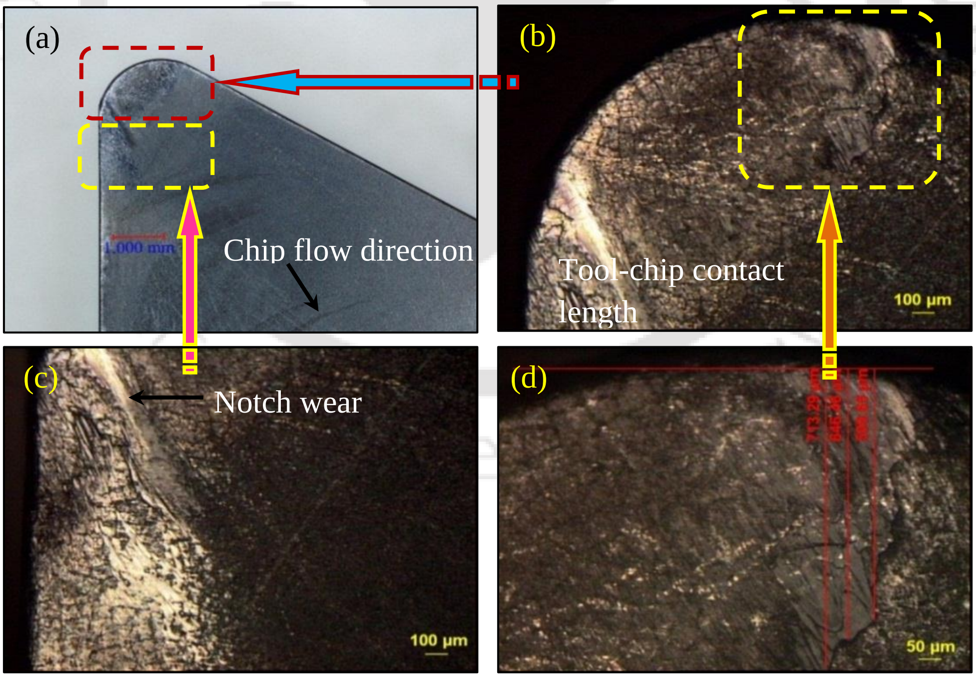

Figure 4.3. Surface morphology of rake surface of un-textured cutting tool showing (a) adhesion and abrasion wear region, (b) tool-chip contact length region, (c) formation of notch wear and (d) tool-chip contact length measurement after 900 seconds of machining

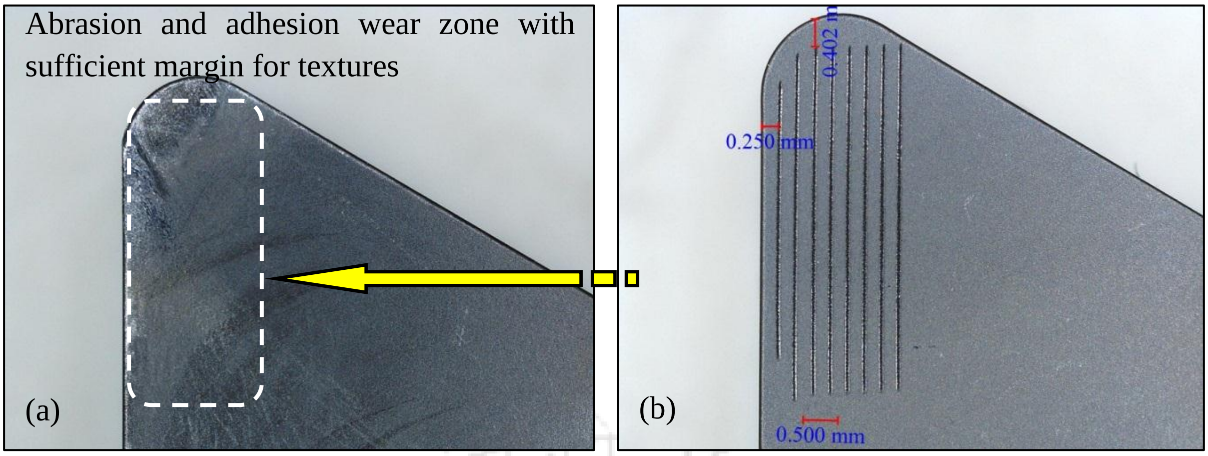

Figure 4.4. (a) Rake surface region for mechanical micro-texturing and (b) fabricated rake surface mechanical micro-textured cutting tool

4.2.3 Fabrication of various mechanical micro-textures on the rake surface of the tungsten carbide cutting tool

The MμTs are fabricated using Vickers hardness tester (Make: Fuel Instruments & Engineering Private Limited®, India; Experimental setup is shown in Chapter 2) and scratch tester (Make: DUCOM®, Model: TR-101). Figure 4.5 (a-b) illustrates the overview and magnified view of the scratch tester (Make: DUCOM®, Model: TR-101).

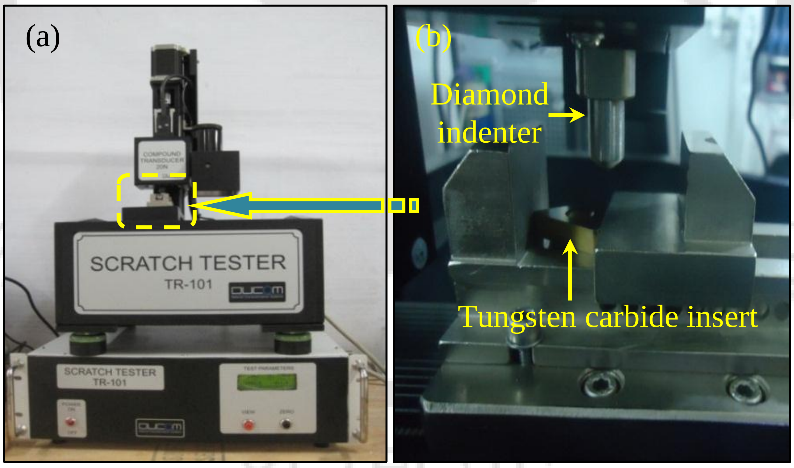

Figure 4.5. (a) Overview of the scratch tester and (b) magnified view of tungsten carbide insert and diamond indenter

The MμT cutting tool with micro-dimples on its rake surface is given the name as VT (Figure 4.6 a). Cutting tool having MμTs parallel to the main cutting edge is given the name as PT (Figure 4.6 b). Cutting tool having MμTs perpendicular to the main cutting edge is given the title as PDT (Figure 4.6 c). The MoS_2 solid lubricant average particle size of 0.3 μm are smeared in the MμT cutting tool as well as then compacted and are named as VT-M, PT-M and PDT-M, respectively (Figure 4.6 d–f, respectively). An un-textured cutting tool named UT is used for comparison purpose. Figure 4.7 (a–b) shows the surface morphology of the PT and PT-M cutting tools, respectively. Figure 4.7 (c–d) shows the 3D surface profile of uncoated and MoS_2 coated MµTs, respectively.

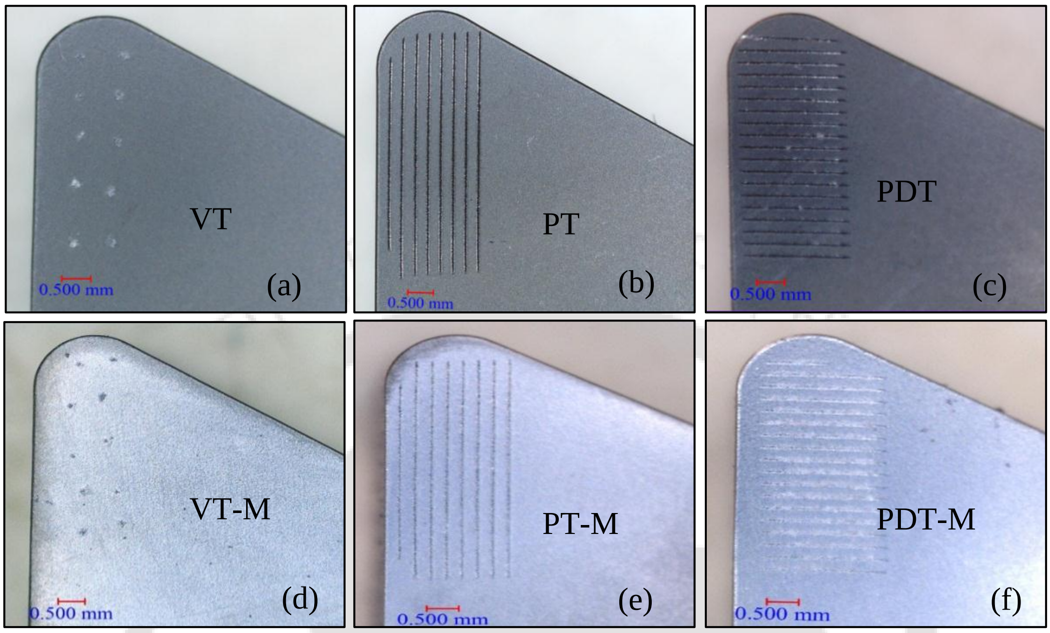

Figure 4.6. Rake surface of mechanical micro-textured tools: (a) uncoated micro-dimple textured cutting tool, (b) uncoated parallel micro-textured cutting tool, (c) uncoated perpendicular micro-textured, (d) MoS_2 coated micro-dimple textured cutting tool, (e) MoS_2 parallel micro-textured cutting tool and (f) MoS_2 coated perpendicular micro-textured

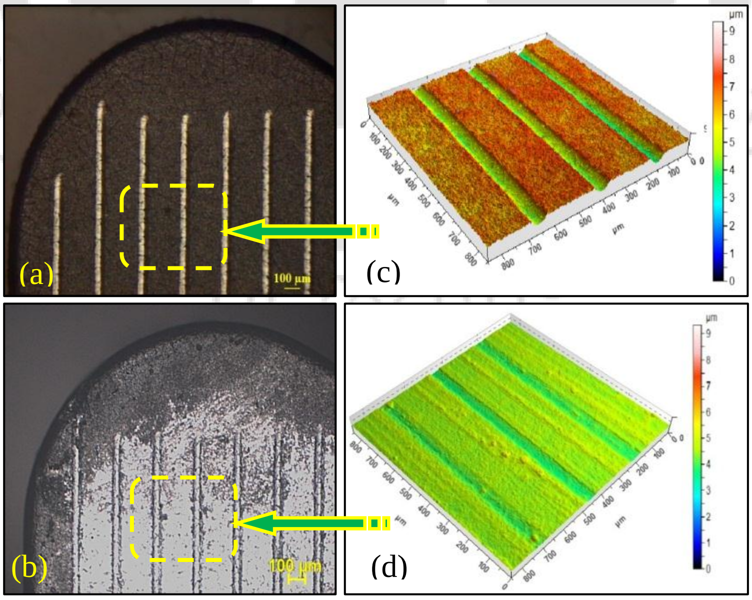

Figure 4.7. Surface morphology of (a) uncoated parallel micro-textured cutting tool, (b) MoS_2 coated parallel micro-textured cutting tool, (c) 3-D surface profile of uncoated parallel micro-textures and (d) 3-D surface profile of MoS_2 coated parallel micro-textures

4.2.4 Experimental design

Experiments are planned in such a way that useful inferences could be obtained by performing the minimum number of experiments using the central composite rotatable design (CCRD). Based on preliminary experiments, cutting speed is varied in the range of 55–125 m/min and feed are in the range of 0.04–0.28 mm/rev with a constant depth of cut of 0.5 mm. All these experiments are carried out with VT, PT, PDT, VT-M, PT-M, PDT-M and UT cutting tools (Total experiments = 91). The coded and original value of the input parameter as per CCRD for the single tool is listed in Table 4.2. All experiments were repeated thrice, and the average value is reported. Influence of control variables on the output response is also determined.

Table 4.2. CCRD coded and actual values of input parameters for the machining process

CCRD coded values	**−1.414**	**−1.000**	**0.000**	**1.000**	**1.414**
Cutting speed (m/min)	55	65	90	115	125
Feed (mm/rev)	0.04	0.08	0.16	0.24	0.28

4.2.5 Machining experiments

Machining experiments are conducted on a lathe (Make: HMT®, Model: NH 26) fitted with a PTGNR 2525 M 22 (Make: Sandvik Coromant®) commercial tool holder. Tool holder has rake angle (γ_o) of −6°, clearance angle (α_o) of 0°, inclination angle (λ_s) of −6°, angle of approach (K_r) of 91° and nose radius (r_ε) of 1.2 mm. VT, PT, PDT, VT-M, PT-M and PDT-M MμT cutting tools were used. For comparison, UT (un-textured) cutting tool is also used. Cutting force and feed force are measured using a piezoelectric quartz dynamometer (Make: KISTLER®, Model: 9272 B). After machining, surface morphologies of the cutting tools are observed using field emission scanning electron microscopy (FESEM) and optical microscope (Make: Zeiss®, Model: AxioCam MRc). Elemental mapping and composition analysis of the tool rake surface is done using energy dispersive spectroscopy (EDS). Figure 4.8 shows the experimental setup of machining.

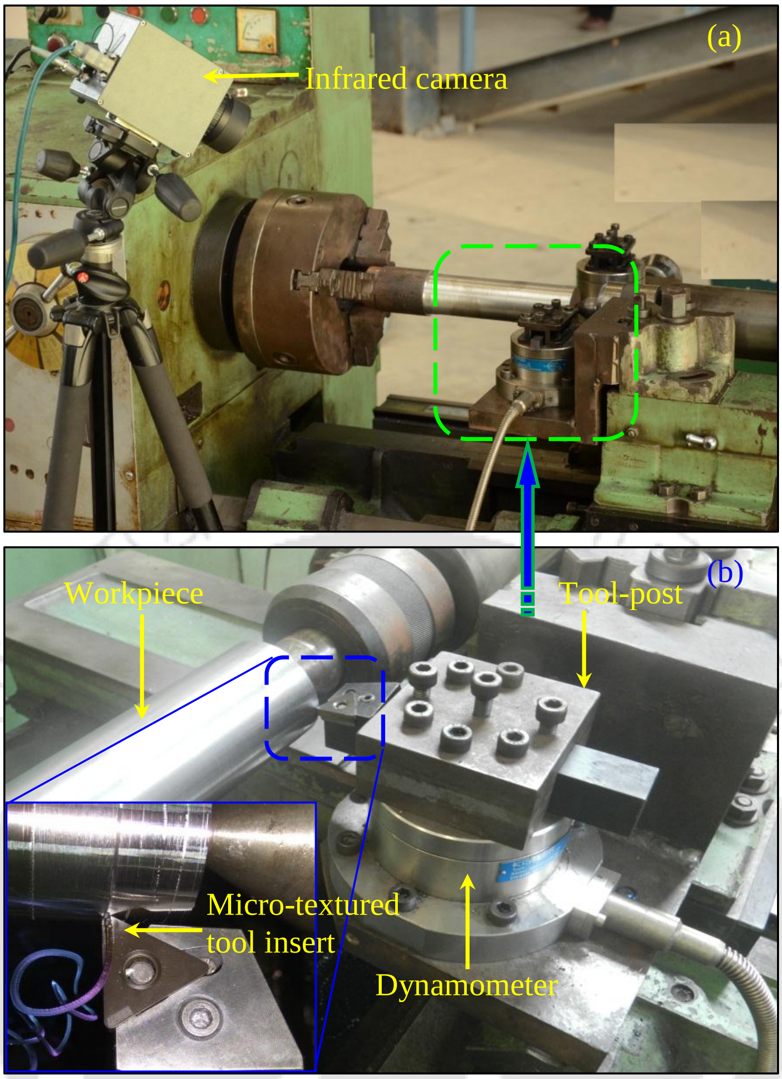

Figure 4.8. (a) Overview of experimental machining setup and (b) magnified view of dynamometer, tool-post and workpiece

4.3 Result and discussion

In this section, the results of finite element simulations for assessing the strength of the tools are reported. Afterwards, the experimental results on the performance during dry machining are presented. Explanations are provided for the observed behaviour.

4.3.1 Effect of various mechanical textures on the cutting tool strength

Rake surface micro-texturing influences the stresses and their distribution. Finite element method (FEM) based ANSYS 14.0® Workbench is used to estimate stresses and strain distribution under the action of respective cutting and feed forces. 10322 Solid 92 (10-noded tetrahedral) elements are used for cutting tool gridding model. The bottom face of the cutting tool is constrained for movement in all directions. Experimentally obtained maximum cutting force and feed force at cutting speed of 55 m/min and feed of 0.28 mm/rev for UT cutting tools are used for stress analysis. Force components are applied to the contact area of 1 mm × 1mm as average normal pressure. The static analysis method is used. Few assumptions are made to reduce calculation time. Forces are considered uniformly distributed on the cutting edge. Cutting tool self-weight is neglected. Thermal stresses are not considered. Mechanical properties of the tool materials used for simulations are shown in Table 4.1. Figure 4.9 shows the FEM gridding model for VT, PT, PDT and UT cutting tools.

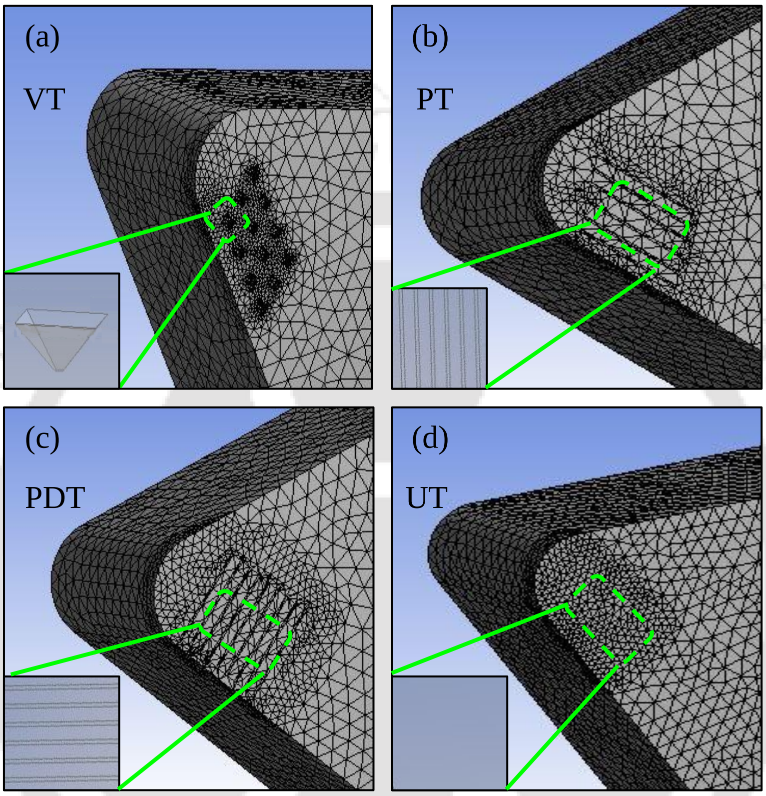

Figure 4.9. FEM gridding model of (a) uncoated micro-dimple textured cutting tool, (b) uncoated parallel micro-textured cutting tool, (c) uncoated perpendicular micro-textured and (d) un-textured cutting tool

Static analyses are done for VT, PT, PDT and UT cutting tools. Figure 4.10 shows the von Mises stress distributions for uncoated MµT and un-textured cutting tools, respectively. It is witnessed that the von Mises stresses experienced by the MµT cutting tool are higher as compared to UT cutting tool. VT cutting tool shows maximum von Mises stress of 188 MPa (Figure 4.10 a), whereas PT and PDT cutting tools show maximum von Mises stress of 183 MPa (Figure 4.10 b) and 149 MPa (Figure 4.10 c), respectively. However, UT cutting tool shows the maximum von Mises stress of 127 MPa (Figure 4.10 d). Maximum von Mises stresses happen close to the MµTs. Due to the presence of MµTs on the cutting tool, stress concentration factor occurs. Thus, more stresses are observed with the MµT cutting tool as compared to UT cutting tool. Thus, static analyses conclude that stresses experienced by micro-textured tools are slightly higher as compared to UT cutting tools. However, the stresses experienced by all the cutting tools are in safe limit. During experiments, no catastrophic failure of the cutting tool is observed, which confirms the static analyses conclusion.

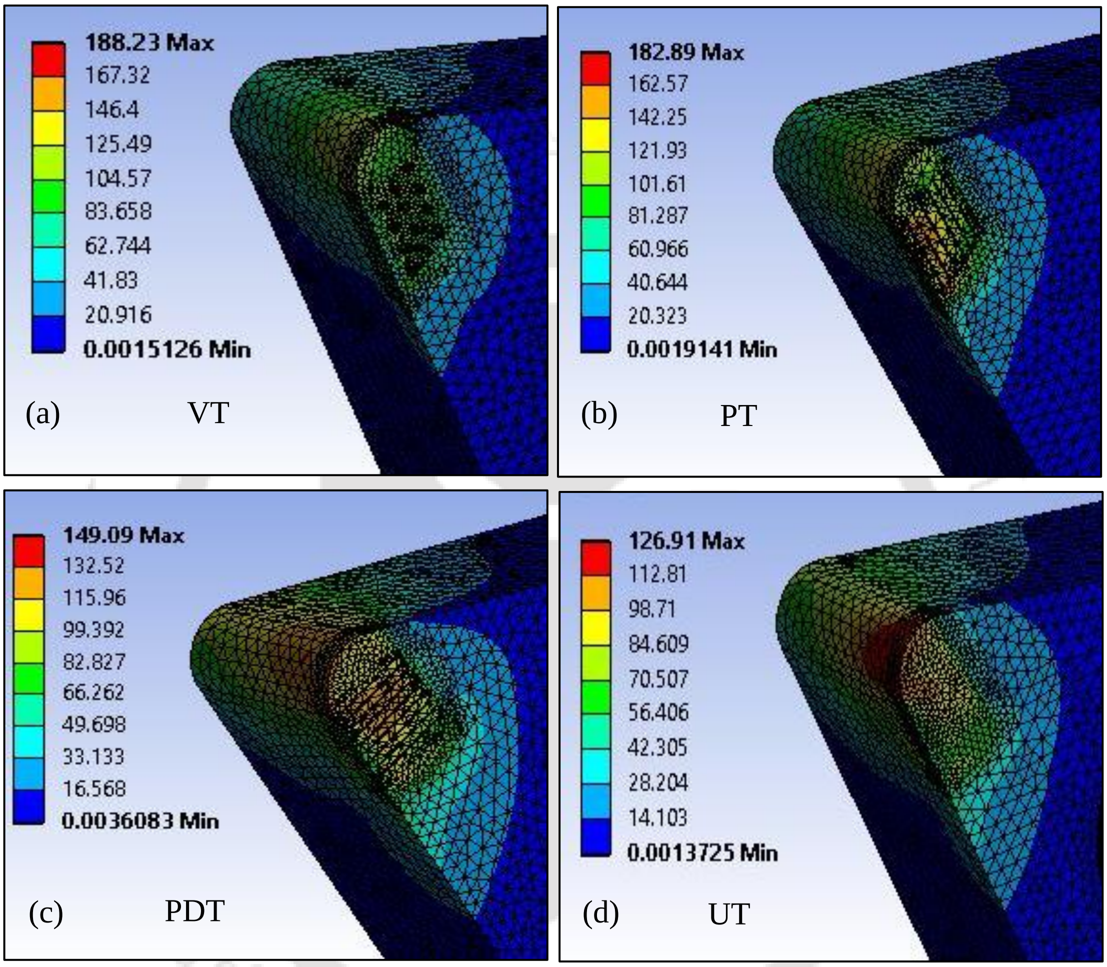

Figure 4.10. von Mises stress field (MPa) of (a) uncoated micro-dimple textured cutting tool, (b) uncoated parallel micro-textured cutting tool, (c) uncoated perpendicular micro-textured and (d) un-textured cutting tool

4.3.2 Tool-chip interface temperature

Tool-chip interface temperature is measured using the thermal infrared camera (Make: Infratech hr-400®, Model: Variocam). Table 4.3 shows the plan of experiments and obtained temperature responses with the different cutting tool. With the regression analysis, the obtained response surfaces models for T_{UT}, T_{VT}, T_{PT}, T_{PDT}, $T_{VT\text{-}M}$, $T_{PT\text{-}M}$, and $T_{PDT\text{-}M}$, are given in Eq. 4.1−4.7.

Table 4.3. Plan of experiments and measured temperature with different cutting tools

S. No.	Cutting speed (m/min)	Feed (mm/rev)	T_{UT} (°C)	T_{VT} (°C)	T_{PT} (°C)	T_{PDT} (°C)	$T_{VT\text{-}M}$ (°C)	$T_{PT\text{-}M}$ (°C)	$T_{PDT\text{-}M}$ (°C)
1	115	0.24	615	590	555	502	488	441	417
2	90	0.16	513	498	466	429	412	377	358
3	90	0.16	509	492	469	424	415	372	357
4	125	0.16	636	612	578	529	504	454	411
5	90	0.28	695	655	619	514	528	470	431
6	115	0.08	342	319	297	260	241	212	199
7	65	0.24	537	490	461	417	390	357	326
8	90	0.16	510	535	472	427	415	378	359
9	90	0.04	159	141	133	149	153	145	133
10	55	0.16	382	358	332	297	271	247	225
11	90	0.16	512	496	466	426	411	375	358
12	65	0.08	232	211	192	184	169	157	144
13	90	0.16	508	494	469	429	413	375	360

The tool-chip interface temperature empirical models are as follows:

$$T_{UT} = -572.39 + 4809.86v + 9.029f - 1.0012vf - 8672.6v^2 - 0.03346f^2 \tag{4.1}$$

$$T_{VT} = -449.96 + 4658.13f + 6.6831v - 4.06752vf - 7058.24v^2 - 0.018f^2 \tag{4.2}$$

$$T_{PT} = -531.119 + 4462.911f + 8.23v - 1.44vf - 7772.55v^2 - 0.0292f^2 \tag{4.3}$$

$$T_{PDT} = -437.045 + 3891.67f + 7.13v + 1.085vf - 7766.81v^2 - 0.026f^2 \tag{4.4}$$

$$T_{VT-M} = -496.375 + 3271.73f + 9.18v + 3.41vf - 6451.13v^2 - 0.0401f^2 \tag{4.5}$$

$$T_{PT-M} = -441.766 + 2952.04f + 8.33v + 3.522vf - 6001.79v^2 - 0.0374f^2 \tag{4.6}$$

$$T_{PDT-M} = -417.81 + 2814.03f + 7.418v + 3.642vf - 5709.36v^2 - 0.03512f^2 \tag{4.7}$$

where v and f represent the cutting speed (m/min) and feed (mm/rev) respectively. The subscript in the temperature (T) denotes the type of cutting tool.

Table 4.4 shows ANOVA for the tool-chip interface temperature of PDT-M cutting tool, and it has been found that the cutting speed terms (B and B^2) have the highest combined contribution (64.72 %) followed by the combined feed terms (A and A^2, 35.1 %) for the tool-chip interface temperature. The coefficient of determination (R^2) is found to be 0.9644, whereas the adjusted R^2 value is 0.9389. All the CCD (central composite design) terms are considered in the regression models to improve its prediction accuracy. R^2 values for the other six cutting tools are found to be more than 0.95 for all output responses.

Table 4.4. ANOVA for tool-chip interface temperature of the MoS_2 coated perpendicular mechanical micro-textured cutting tool

Source	***F*-Value**	***p*-value Prob>*F***	**Percentage contribution**
Model	8.75	0.0004	
A-Feed	18.32	0.0036	18.51
B-Speed	29.41	0.0048	29.72
AB	0.09	0.9412	0.09
A^2	16.41	0.0036	16.59
B^2	34.72	0.0007	35.09
Lack of Fit	1.05	0.5128	

Figure 4.11 (a–b) shows variations of tool-chip interface temperature with respect to varying feed and cutting speed. As per the experimental results, feed has a profound effect on the tool-chip interface temperature. As feed increases, the shear angle decreases and chip thickness increases. The increase in chip thickness increases the chip load and friction on tool rake surface. Therefore, the tool-chip interface temperature rises with feed (Figure 4.11 a). With the increase in cutting speed, the tool-workpiece interaction time during machining is less but the material removal rate (MRR) is high. More amount of MRR per unit time causes a rise in temperature with an increase in cutting speed (Figure 4.11 b).

With the UT cutting tool, tool-chip contact length is more, which leads to high heat generation resulting in higher temperature. In the case of VT-M, PT-M and PDT-M cutting tools, tool-chip contact reduces due to the presence of many micro-channels on the rake surface of the cutting tool causes lesser heat generation. Reduction of tool-chip interface temperature by MµTs of tool rake surface is likely due to decrease in the contact area between tool-chip interfaces on the rake surface of MµT tools. Reduction in tool rake surface and chip direct contact area leads to less COF, which results in lesser temperature with VT, PT and PDT tools.

$$l_r = l_a - n.d \tag{4.8}$$

where l_r is the real tool-chip length in contact, l_a is the apparent tool-chip contact length, n is the number of MµTs in contact length and d is the average width of texture.

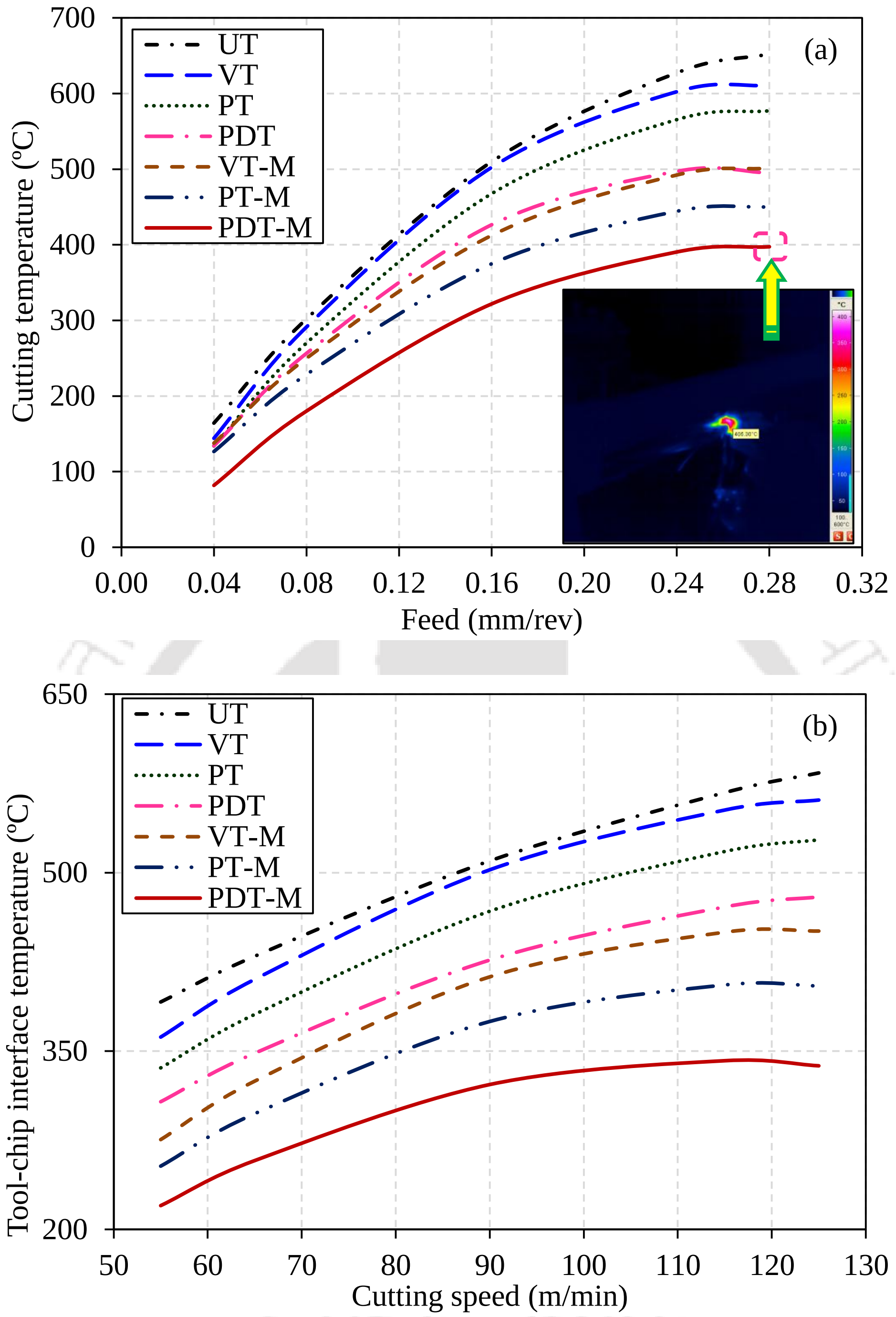

Figure 4.11. Variation of tool-chip interface temperature with (a) feed and (b) cutting speed

In the case of VT-M, PT-M and PDT-M cutting tools, the contact of the chip back surface is with MoS_2. Thus, there is no restriction to the flow of chips due to the low shearing ability of solid lubricant. At higher temperature and pressure, MoS_2 has the ability to come out from the textures and form a thin film having lubricating properties on the rake surface of the tool. Entrapped MoS_2 enhances the lubrication effect, and the temperature reduces significantly. Figure 4.12 (a-c) shows thermo-graphic images with PDT, PDT-M and UT cutting tools captured during machining, respectively.

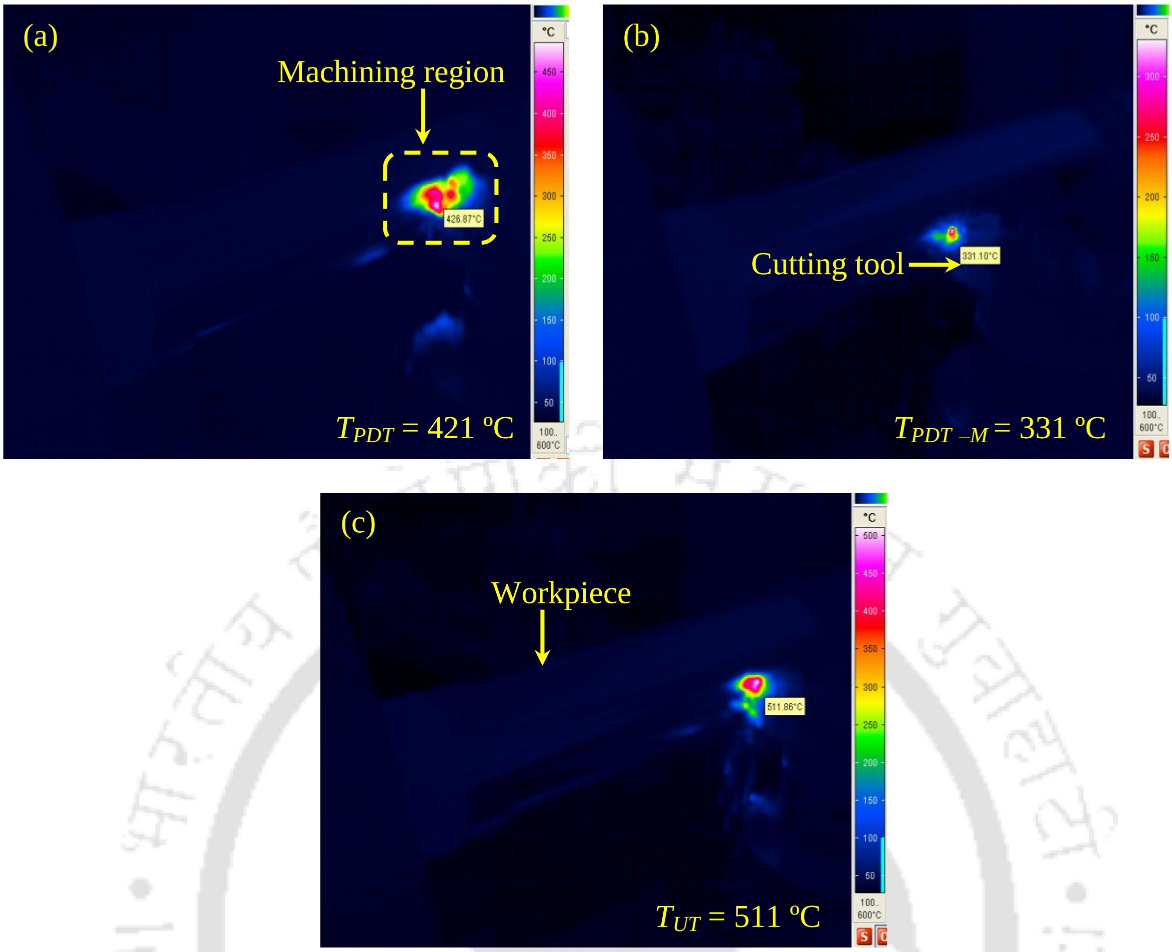

Figure 4.12. Thermal micrographs during machining with (a) uncoated perpendicular micro-textured cutting tool (b) MoS_2 coated perpendicular micro-textured cutting tool and (c) un-textured cutting tool

4.3.3 Machining forces

The empirical relation between the cutting force (F_c) and feed force (F_f) for VT, PT, PDT, VT-M, PT-M, PDT-M and UT cutting tools are as follows:

Equations models for cutting force as per CCRD are as follows (Eq. 4.9–4.15):

$$F_{cVT} = 521.43 + 1436.19f - 7.79v - 1.79vf + 207.5f^2 + 0.05v^2 \tag{4.9}$$

$$F_{cPT} = 502.42 + 1556.00f - 7.72v - 2.97vf + 222.97f^2 + 0.03v^2 \tag{4.10}$$

$$F_{cPDT} = 323.66 + 2220.36f - 5.85v - 7.67vf - 254.61f^2 + 0.03v^2 \tag{4.11}$$

$$F_{cVT-M} = 400.29 + 1918.84f - 6.35v - 3.62vf - 602.4f^2 + 0.03v^2 \tag{4.12}$$

$$F_{cPT-M} = 308.17 + 2284.53f - 6.17v - 9.96vf + 325.61f^2 + 0.03v^2 \tag{4.13}$$

$$F_{cPDT-M} = 264.46 + 2301.38f - 5.65v - 10.295vf + 484.361f^2 + 0.03v^2 \tag{4.14}$$

$$F_{cUT} = 529.18 + 1302.57f - 7.45v - 2.48vf + 644.81f^2 + 0.03v^2 \tag{4.15}$$

where the subscript in the cutting force denotes the type of cutting tool.

Equations model for feed force as per CCRD are as follows (Eq. 4.16–4.22):

$$F_{fVT} = -10.73 + 663.99f + 1.018v - 0.79vf - 699.61f^2 - 0.006v^2 \tag{4.16}$$

$$F_{fPT} = 11.01 + 658.89f + 0.62v - 1.08vf - 665.30f^2 - 0.004v^2 \tag{4.17}$$

$$F_{fPDT} = 35.74 + 649.27f - 0.25v - 1.58vf - 415.84f^2 + 0.0016v^2 \tag{4.18}$$

$$F_{fVT-M} = -4.19 + 608.64f + 0.759v - 1.75vf - 439.64f^2 - 0.003v^2 \tag{4.19}$$

$$F_{fPT-M} = 13.78 + 556.17f + 0.41v - 1.51vf - 406.09f^2 - 0.00226v^2 \tag{4.20}$$

$$F_{fPDT-M} = -9.79 + 471.38f + 0.79v - 1.50vf - 296.95f^2 - 0.0035v^2 \tag{4.21}$$

$$F_{fUT} = 18.61 + 637.72f + 0.55v - 0.695vf - 643.79f^2 - 0.004v^2 \tag{4.22}$$

where the subscript in the feed force denotes the type of cutting tool.

Figure 4.13−4.14 show the effect of cutting speed and feed on the cutting force and feed force using seven different cutting tools. As per the experimental results, feed has an intense influence on the cutting force. As feed increases, the shear angle decreases and chip thickness increases. The increase in chip thickness increases the chip load and tool-chip friction. Therefore, the cutting force increases with feed (Figure 4.13 a).

As cutting speed increases, the tool-workpiece interaction time during machining is less but the material removal rate (MRR) is high. Therefore, the temperature in primary as well as secondary shear zones increases. Due to the good thermal conductivity of workpiece, there is a probability of preheating, which is slightly ahead of the current machining region. Thus, thermal softening of workpiece surface takes place. The temperature rise in the secondary shear zone causes the decrease of flow stress of the workpiece material, thereby reducing the cutting force with increasing cutting speed (Figure 4.13 b).

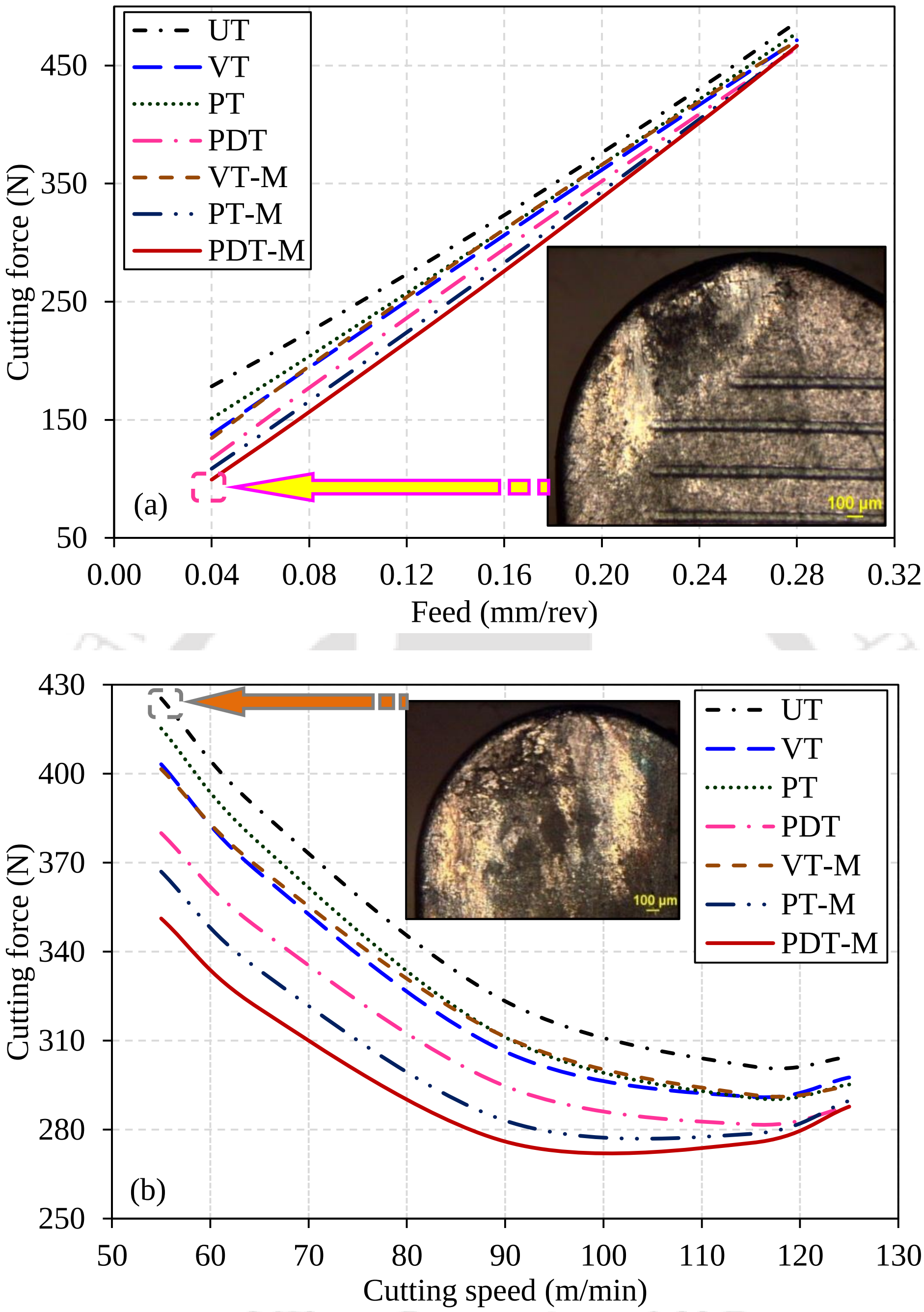

Figure 4.13. Variation of cutting force with (a) feed and (b) cutting speed

Figure 4.14 (a) shows the variation of feed force with respect to feed at a constant depth of cut (0.5 mm) during machining. As the feed increases, the advancement per revolution by the tool increases, i.e., the amount of workpiece material comes in contact with the tool per unit time increases. Therefore, the load on the tool increases. Thus, the feed force increases irrespective of any type of cutting tool. As cutting speed increases feed force reduces due to the rise in MRR (Figure 4.14 b). Increase in MRR leads to the rise in temperature, which results in thermal softening of the workpiece. Thus, feed force reduces.

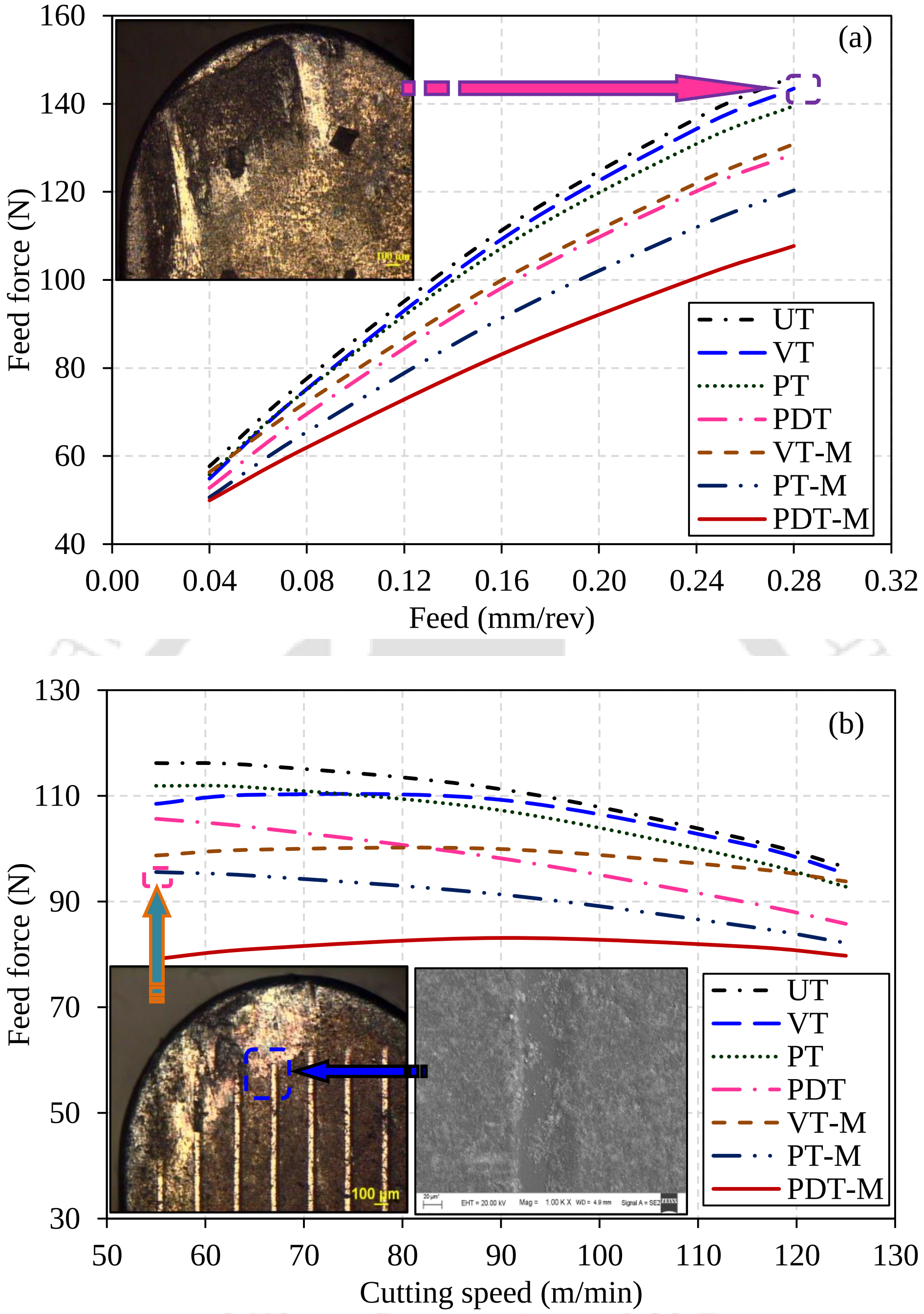

Figure 4.14. Variation of feed force with (a) feed and (b) cutting speed

It is also observed that uncoated and coated MµT cutting tools reduce cutting force as well as feed force. Ernst and Merchant proposed relations between machining force and shearing force as follows [50, 174]:

$$F_s = \frac{\tau_s A_c}{\sin\phi} = \frac{\tau_s a_c a_w}{\sin\phi} \tag{4.23}$$

$$F_r = \frac{F_s}{\cos(\phi + \beta - \gamma_0)} \tag{4.24}$$

$$F_r = \frac{F_{f1}}{\sin\beta} \tag{4.25}$$

$$F_z = F_r \cos(\beta - \gamma_0) \tag{4.26}$$

$$F_y = F_r \sin(\beta - \gamma_0) \tag{4.27}$$

where F_s, F_r, F_{f1}, F_y and F_z represents shearing force, resultant force, tool rake surface frictional force, feed force as well as main cutting force, respectively. τ_s denotes material shear strength, ϕ is the shear angle, A_c represents the shearing area which is mathematically defined as $\alpha_c\alpha_w$, a_c represents undeformed chip thickness, a_w denotes cut width, γ_0 is rake angle and β is friction angle. Figure 4.15 illustrates the force diagram for the shear plane showing various machining forces and machining angles.

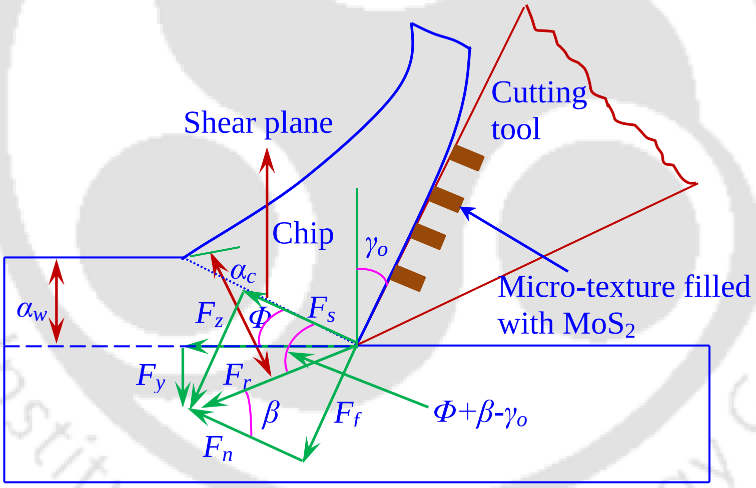

Figure 4.15. Schematic of force diagram for the shear plane

In case of tool coatings or dry lubrication between the tool-chip interface (MμT cutting tools), the frictional force is calculated as [175]:

$$F_{f1} = a_w l_a \tau_c \tag{4.28}$$

where l_a denotes the contact length of the tool-chip and τ_c represents lubricant shear strength at the tool-chip interface

After combining Eq. (4.25−4.28), the machining forces can also be represented as:

$$F_r = \frac{a_w l_a \tau_c}{\sin\beta} \tag{4.29}$$

$$F_z = \frac{a_w l_a \tau_c \cos(\beta - \gamma_0)}{\sin\beta} \tag{4.30}$$

$$F_y = \frac{a_w l_a \tau_c \sin(\beta - \gamma_0)}{\sin\beta} \tag{4.31}$$

From Eq. (4.29–4.31), it is observed that all machining forces (F_r, F_z and F_y) have a linear relationship with the contact length of the tool-chip (l_a) and the shear strength of the material in contact. With the use of MμT cutting tools, the real contact length (1_r) of the tool-chip interface reduces as shown in Eq. 4.32.

$$l_r = l_a - nd \tag{4.32}$$

where l_r is the real chip-tool length in contact, l_a is the apparent tool-chip contact length, n is the number of MμTs in contact length and d is the average width of texture.

For a typical case (v = 90 m/min, f = 0.16mm/rev and d = 0.5mm) as studied with PDT cutting tools, chip flow direction is at 18° from principal cutting edge (Figure 4.16). Therefore, keeping the chip flow direction constant, n depends on the micro-textures type and their position. Figure 4.16 shows chip flow direction over various mechanical micro-textured cutting tools. It was observed that the number of mechanical micro-textures in contact with chip varies are least with VT cutting tools and maximum with PDT cutting tools ($n_{VT} < n_{PT} < n_{PDT}$, where subscript denotes the type of the cutting tool). Therefore, cutting and feed forces are less in case of PDT cutting tools as compared to other uncoated MμT cutting tools.

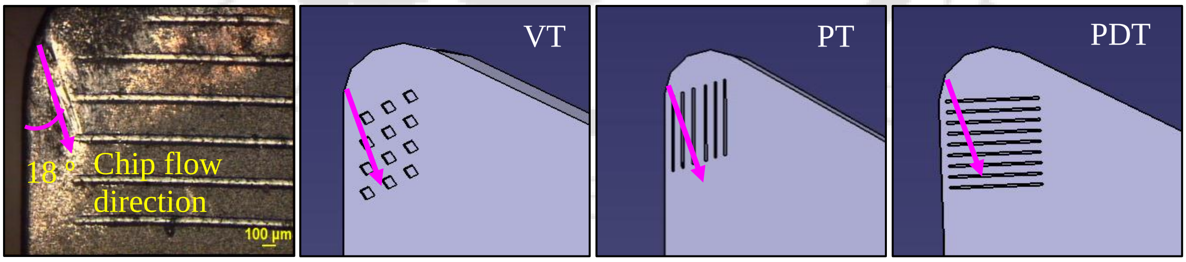

Figure 4.16. Representation of chip flow direction over various mechanical micro-textured cutting tools

In addition, the shear strength of tungsten carbide tool is about 700–800 MPa, however, the shear strength of MoS_2 at the tool-chip interface is in the range of 30–35 MPa [176]. Therefore, with the formation of self-lubricating film in-between tool-chip interface, cutting force and feed force reduces as compared to uncoated MµT cutting tools due to the lower shear strength of MoS_2.

It is also observed that at low cutting speed and feed reduction of machining forces are high using MµT cutting tools as compared to UT cutting tool. However, for the high cutting speed (125 m/min) and feed (0.28 mm/rev) reduction of machining force using MµT tools is less as compared to UT. It is mainly due to two reasons. First, at higher feed and cutting speed flow of chips on the rake surface is at high speed. Therefore, the interaction of chip with micro-textures will be very less per unit time, which results in very less difference in machining force. Another reason is that at high feed and cutting speed, the tool-chip interface temperature is high. MoS_2 solid lubricant oxidised with atmospheric oxygen at 450 °C and converted into MoO_3, which does not have lubrication properties. Therefore, machining force is less affected at higher feed and cutting speed. PDT-M cutting tool shows the best performance among others by reducing 6−18 % of cutting force and 12−43 % feed force as compared to UT cutting tool.

4.3.4 Tool-chip interface coefficient of friction

Tool-chip interface COF is calculated using experimental values of cutting and feed forces. The COF is given as follows [174]:

$$\mu = \frac{F_c \sin\alpha + F_f \cos\alpha}{F_c \cos\alpha - F_f \sin\alpha} \tag{4.33}$$

where F_f is the feed force, F_c is the cutting force, α is the rake angle and μ is the COF.

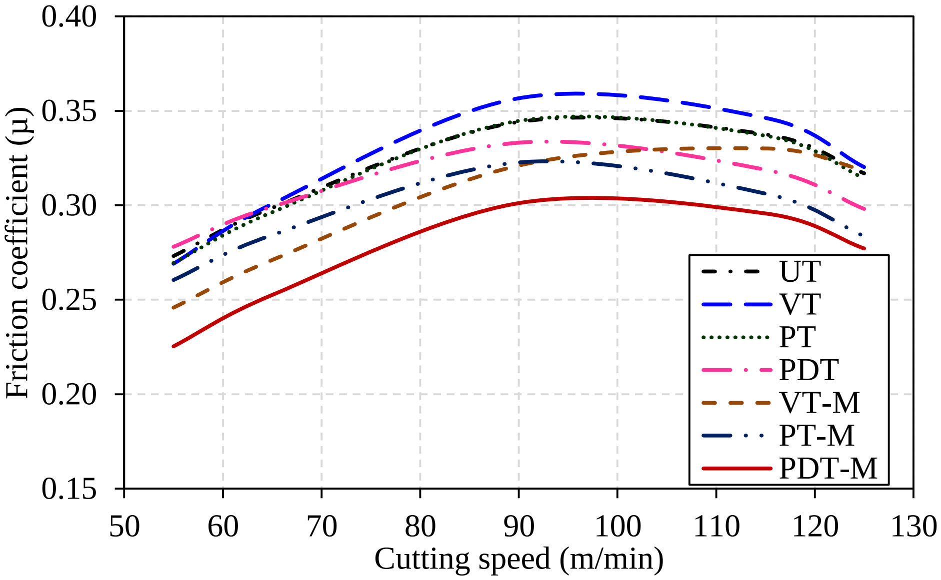

Figure 4.17. Variation of coefficient of friction with cutting speed

Figure 4.17 shows the average COF of different MμT and UT cutting tools with respect to cutting speed. The frictional force at the tool-chip interface depends on the tool-chip contact length. The MμT cutting tools reduce the tool-chip contact length. Therefore, observed COF is lower with MμT cutting tools and with the presence of solid lubricants in VT-M, PT-M and PDT-M the magnitude of COF decreases further (Figure 4.17). In the case of UT cutting tool, the heat generated due to increase in cutting speed is partially injected into tool rake surface by chips. Thus, adhesion is dominant and tool-chip interface COF is high. However, for MoS_2 coated MμT cutting tools, micro-textures act as a lubricant reservoir. As the cutting speed increases, the tool-chip interface temperature rises. Therefore, in high temperature and pressure, the entrapped MoS_2 lubricant starts to flow in chip flow direction and create a self-lubricant film. The presence of lubricant reduces the tool-chip interface COF.

Results also show that the geometry of the MμTs profoundly influences the variation of temperature, cutting force, feed force and COF. The PDT-M cutting tool has shown the best machining performance as compared to others, and the VT-M cutting tool has shown least improvement among all coated MμT cutting tools. It is due to inability to release of MoS_2 lubricant due to its trapezoidal geometry shape. In the case of PT-M tool, the direction of micro-texture is nearly parallel to the chip flowing direction, whereas for the PDT-M tool, the direction of micro-texture is approximately perpendicular to the chip flowing direction. The back side of chip carries MoS_2 particles and creates a lubricating film on the rake surface of the cutting tool. Therefore, MoS_2 is readily released from PDT-M cutting tool as compared to PT-M cutting tool. COF for PDT-M cutting tool is reduced by 13−16 % as compared to CT cutting tool.

4.3.5 Surface morphology of cutting tool rake surface

Figure 4.18 shows the surface morphology of the rake surface of UT cutting tool after 900 seconds of machining at cutting speed of 90 m/min, feed of 0.16 mm/rev and depth of cut of 0.5 mm. In the case of UT cutting tool, abrasion marks are observed on the rake surface (Figure 4.18 a). Due to high-temperature workpiece material sticks to the back side of the chip which slides over the rake surface of the tool. Repetitively severe adhesion of chip and the rake surface of the UT tool cause loss of the tool materials from the rake surface, which is also known as the catastrophic failure as shown in Figure 4.18 (b). Figure 4.18 (c) shows fractured surface on the rake surface of the un-textured cutting tool. Shredding of tungsten carbide particles are observed from the interface of fractured surface and parent tool surface (Figure 4.18 d).

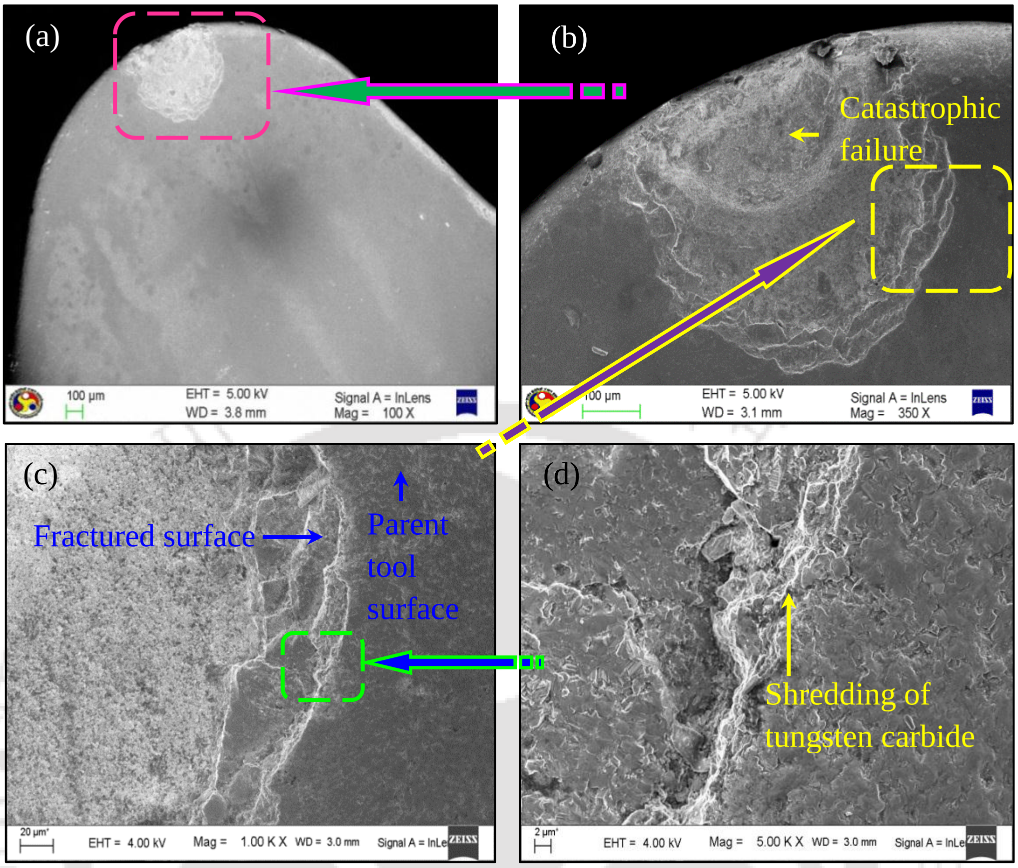

Figure 4.18. Surface morphology of un-textured tool after 900 seconds of machining (a) rake surface morphology, (b) crater wear formation, (c) fractured surface and (d) shredding of tungsten carbide

Figure 4.19−4.22 shows the surface morphology, elemental maps of iron (Fe), molybdenum (Mo) and sulphur (S) as well as composition analysis on the rake surface of VT-M, PT-M and PDT-M cutting tools, respectively after 900 seconds of machining (*v* = 90 m/min, *f* = 0.16 mm/rev and *d* = 0.5 mm). Figure 4.19 (a) shows wear track of rake surface on the VT-M cutting tool. Figure 4.19 (b-d) shows the elemental mapping of Fe, Mo and S on the tested VT-M cutting tool rake surface. From elemental mapping, it is observed that Fe particles are in a few places, which confirms the presence of adhered material from the workpiece. However, it is clearly visible that the presence of Mo and S on the rake surface of VT-M cutting tool is everywhere. Therefore, it can be confirmed that MoS_2 solid lubricant is able to release and create a self-lubricating film on the rake surface of the tool.

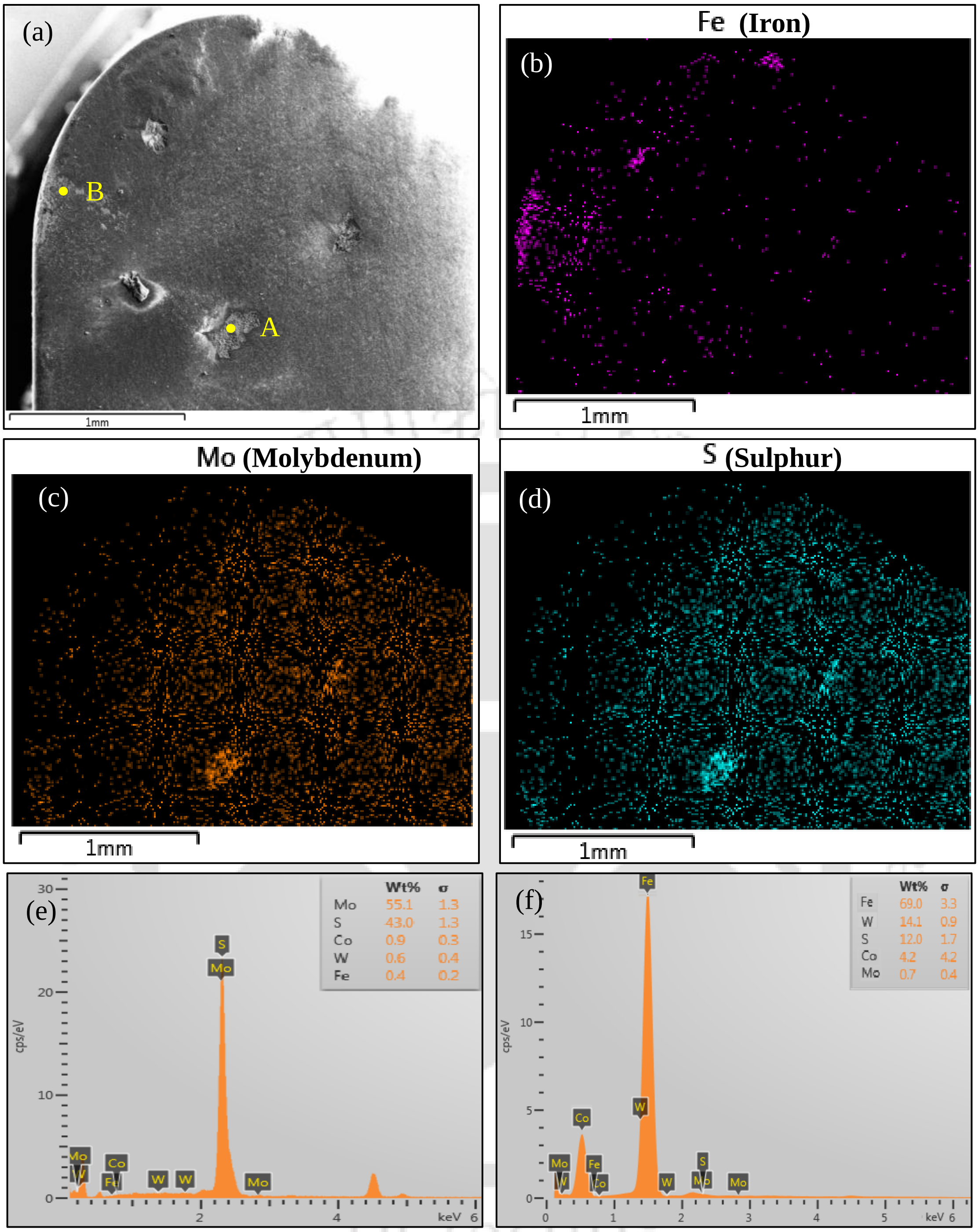

Figure 4.19. MoS$_2$ coated Vickers mechanical micro-textured cutting tool rake surface after 900 second of machining: (a) surface micrograph of the cutting tool, (b) elemental map distribution of Fe, (c) elemental map distribution of Mo, (d) elemental map distribution of S, (e) elemental composition of point A and (f) elemental composition of point B

Figure 4.19 (e-f) shows the elemental composition of highlighted point A and B, respectively (Point A and B in Figure 4.19 a). Point A is selected on the micro-texture, whereas point B is selected near to cutting edge. The weight percentage of Fe is much higher in point B as compared to point A. It confirms that adhesive wear is predominant near cutting edge of the tool.

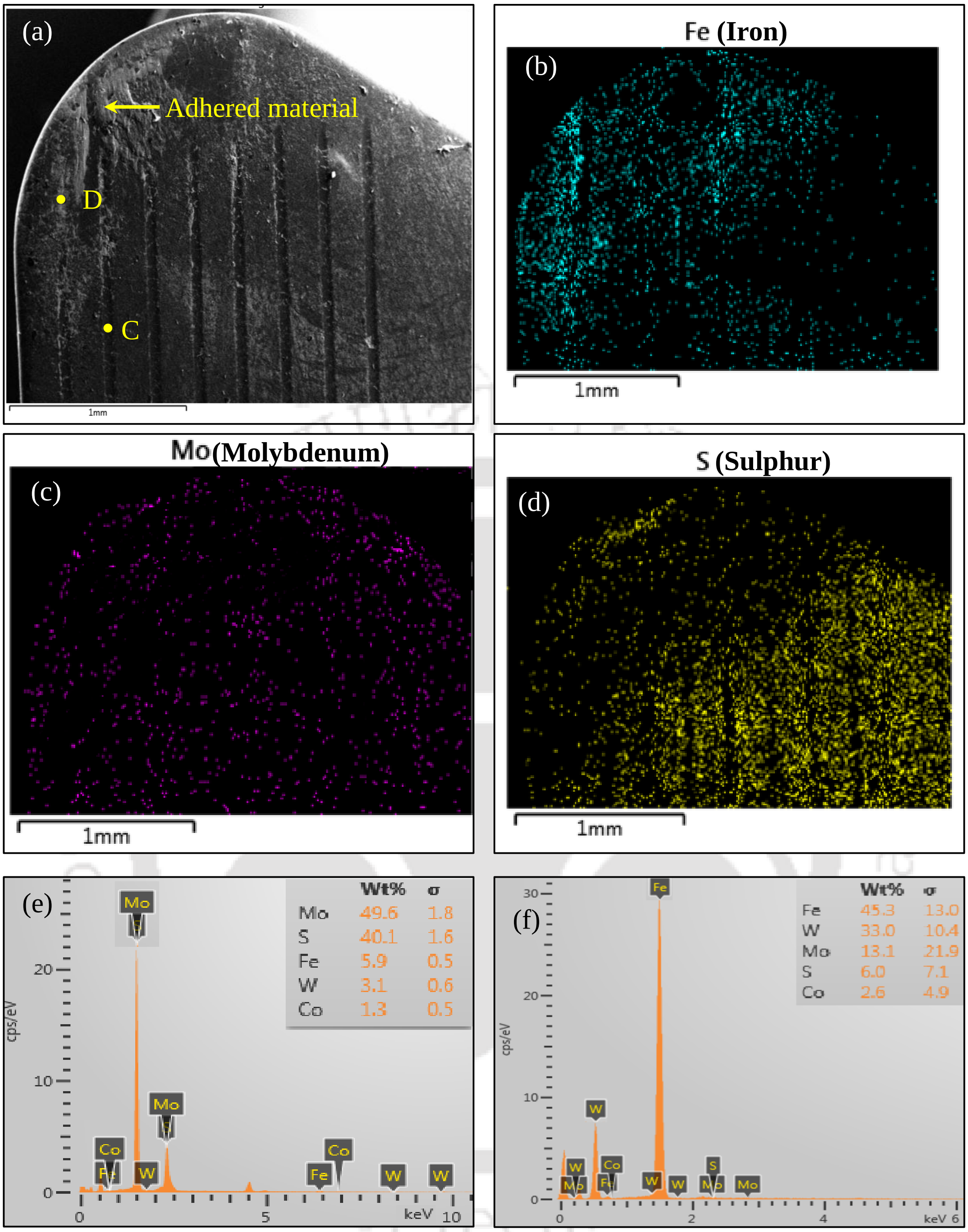

Figure 4.20. MoS_2 coated parallel mechanical micro-textured cutting tool rake surface after 900 second of machining: (a) surface micrograph of the cutting tool, (b) elemental map distribution of Fe, (c) elemental map distribution of Mo, (d) elemental map distribution of S, (e) elemental composition of point C and (f) elemental composition of point D

Figure 4.20 (a) shows wear track of rake surface on the PT-M cutting tool. Figure 4.20 (b-d) shows the elemental mapping of Fe, Mo and S on the tested VT-M cutting tool rake surface. Figure 4.20 (e-f) shows the elemental composition analysis of highlighted point

C and D, respectively (Point C and D are shown in Figure 4.20 a). In this case also, elemental mapping and elemental composition analysis confirm the formation of a thin lubricating film of MoS_2.

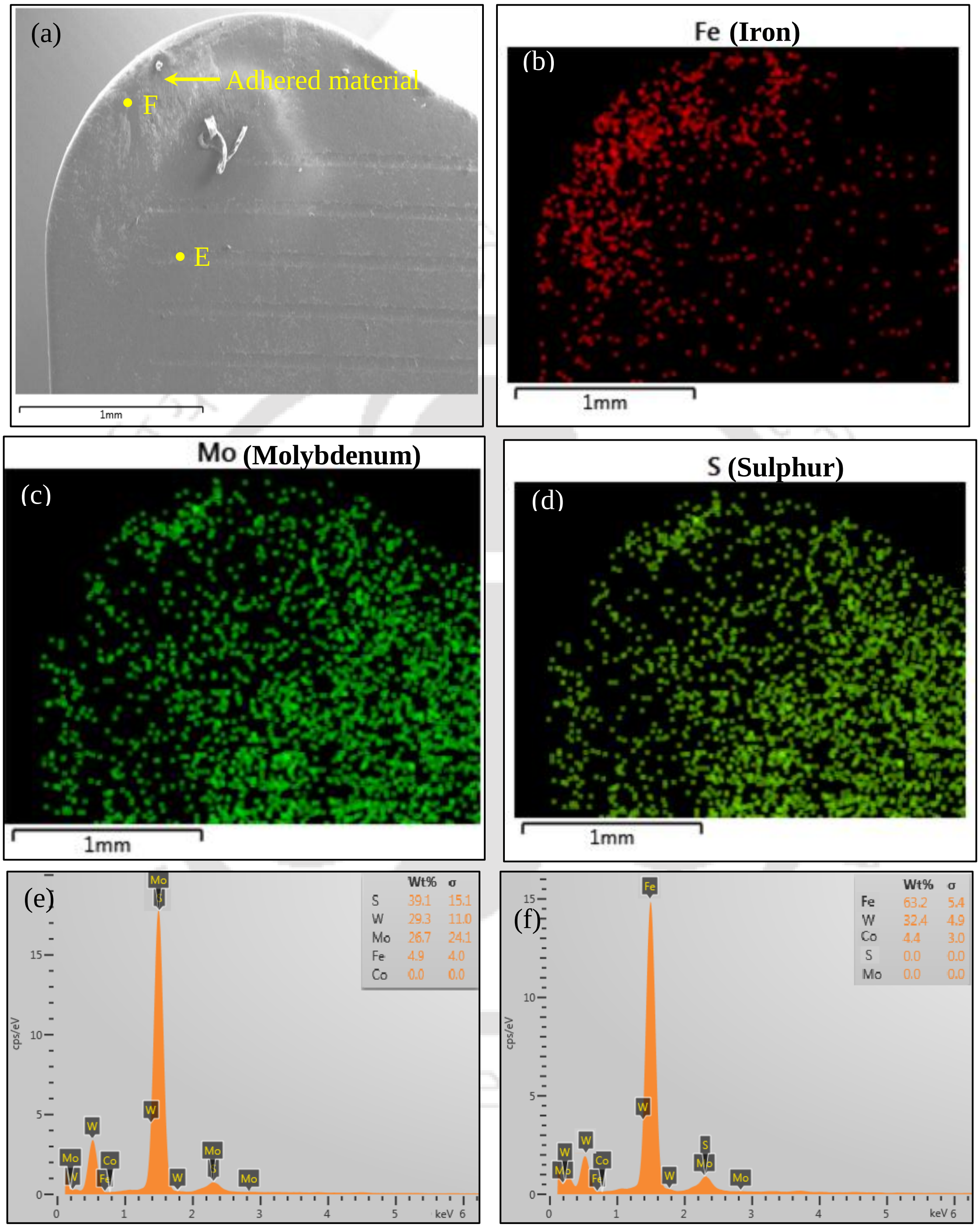

	Wt%	σ
S	39.1	15.1
W	29.3	11.0
Mo	26.7	24.1
Fe	4.9	4.0
Co	0.0	0.0

	Wt%	σ
Fe	63.2	5.4
W	32.4	4.9
Co	4.4	3.0
S	0.0	0.0
Mo	0.0	0.0

Figure 4.21. MoS_2 coated perpendicular mechanical micro-textured cutting tool rake surface after 900 second of machining: (a) surface micrograph of the cutting tool, (b) elemental map distribution of Fe, (c) elemental map distribution of Mo, (d) elemental map distribution of S, (e) elemental composition of point E and (f) elemental composition of point F

Similar analysis is carried out for PDT-M cutting tool as illustrated in Figure 4.21. It is observed that the tool-chip interface contact area on PDT-M cutting tool is slightly different from PT-M cutting tool wear track. PDT-M cutting tool wear track is quite smaller and shows comparatively smooth rake surface than other cutting tools. Also, less adhesion of workpiece material is observed with PDT-M cutting tool as compared to VT-M and PT-M cutting tool (Figure 4.21 a-b). Corresponding elemental maps of Mo and S for PDT-M cutting tools shows more uniform and better formation of the thin-lubricating film as compared to VT-M and PT-M cutting tools as shown in Figure 4.21 (c-d). Figure 4.21 (e-f) shows the elemental composition analysis of highlighted point E and F, respectively (Point E and F are shown in Figure 4.21 a).

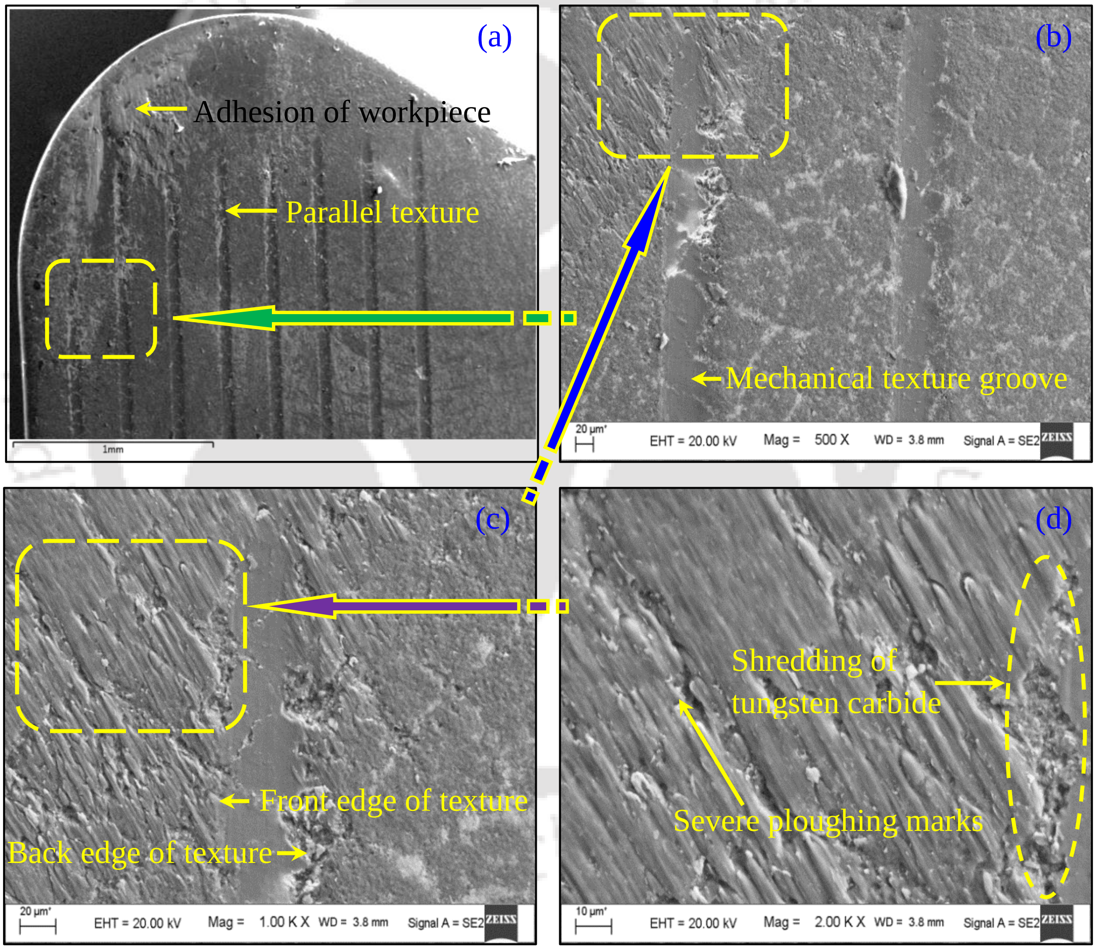

Figure 4.22. (a) Rake surface of the parallel micro-textured cutting tool after 900 seconds of machining, (b) individual mechanical micro-texture groove, (c) front and back edge of texture groove and (d) severe ploughing marks

Figure 4.22 shows surface morphology of rake surface of PT-M cutting tool after 900 seconds of machining (υ = 90 m/min, f = 0.16 mm/rev and d = 0.5 mm). Severe adhesion of workpiece material is observed on the rake surface of PT-M cutting tool as shown in Figure 4.22 (a). Individual MµT groove is shown in Figure 4.22 (b). Figure 4.22 (c) shows the front and back edge of the MµT groove. Severe ploughing marks and shredding of tungsten carbide particles are observed near the front edge of MµT groove due to abrasion of chips on the rake surface of the PT-M cutting tool as shown in Figure 4.22 (d). However, in the case of PDT-M cutting tool ploughing marks and shredding of tungsten carbide particles are not observed.

4.3.6 Chip morphology

After machining, chips produced from all experiments were collected. Surface micrographs of chips were obtained using an optical microscope as well as FESEM, and average chip-thickness was measured. Experimentally obtained average values of chip thickness for various experimental runs are plotted. The average is taken for minimum three readings. Chip reduction ratio (ξ) is also plotted which is defined as the ratio of cut chip thickness to uncut chip thickness. Figure 4.23 shows the schematic of serrated chips formation.

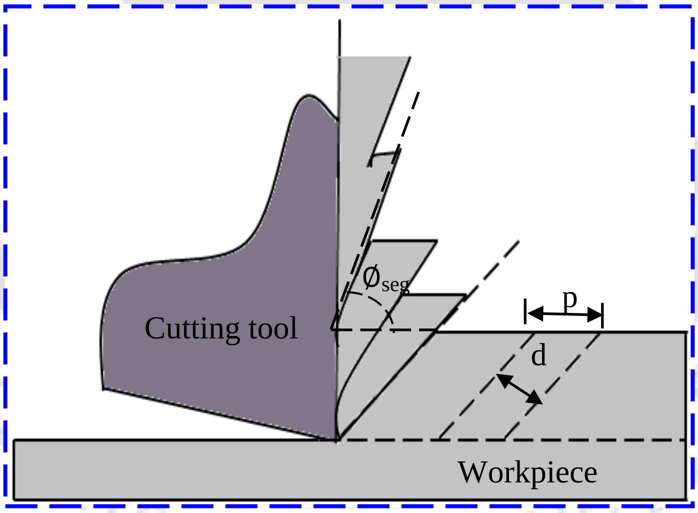

Figure 4.23. Schematic of serrated chips formation

The variation of chip thickness and chip reduction ratio with different feed at constant cutting speed (v = 90 m/min) and depth of cut (d = 0.5 mm) are shown in Figure 4.24 (a-b). It is observed that chip thickness and chip reduction ratio has a significant effect with respect to feed. As the feed increases, chip thickness and chip reduction ratio are also increasing trend irrespective of the type of micro-texture tool inserts whereas it is also observed that at the constant feed, chip thickness and chip reduction ratio are showing a downward trend with the micro-textured tool with and without solid lubricant coating. Out of all PDT-M cutting tool performs best among all.

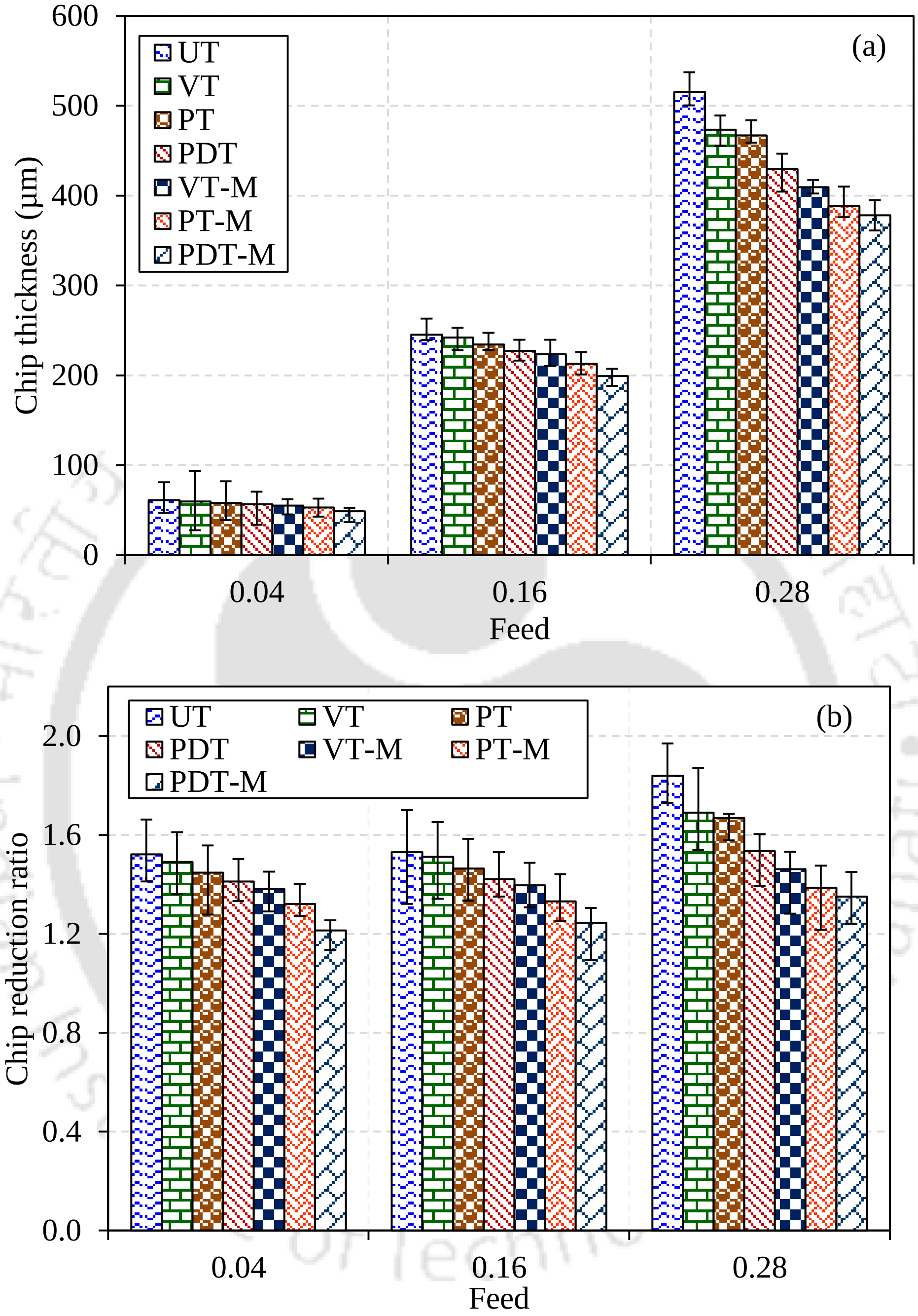

Figure 4.24. Effect of feed on (a) chip thickness and (b) chip reduction ratio

Collected chip micrographs of machined AISI H-13 tool steel at cutting speed v = 90 m/min, depth of cut d = 0.5 mm with two different feeds of 0.04 and 0.28 mm /rev and seven different MμT cutting tool are illustrated in Figure 4.25. For the lower feed, metallic colour continuous chips with small serrations were observed. Chip morphologies with different

MμT cutting tools at lower feed are almost similar to the UT cutting tool chips apart from chip thickness and related parameters.

With the increase in feed, dark blue colour discontinuous chips with large serrations were formed with UT cutting tools. However, uncoated and coated MμT cutting tools chips were light blue in colour having lesser segmentation. With solid lubricant coated MμT, chip thickness and chip reduction ratio were reduced much more that indicates better machinability of high hardiness AISI H-13 tool steel.

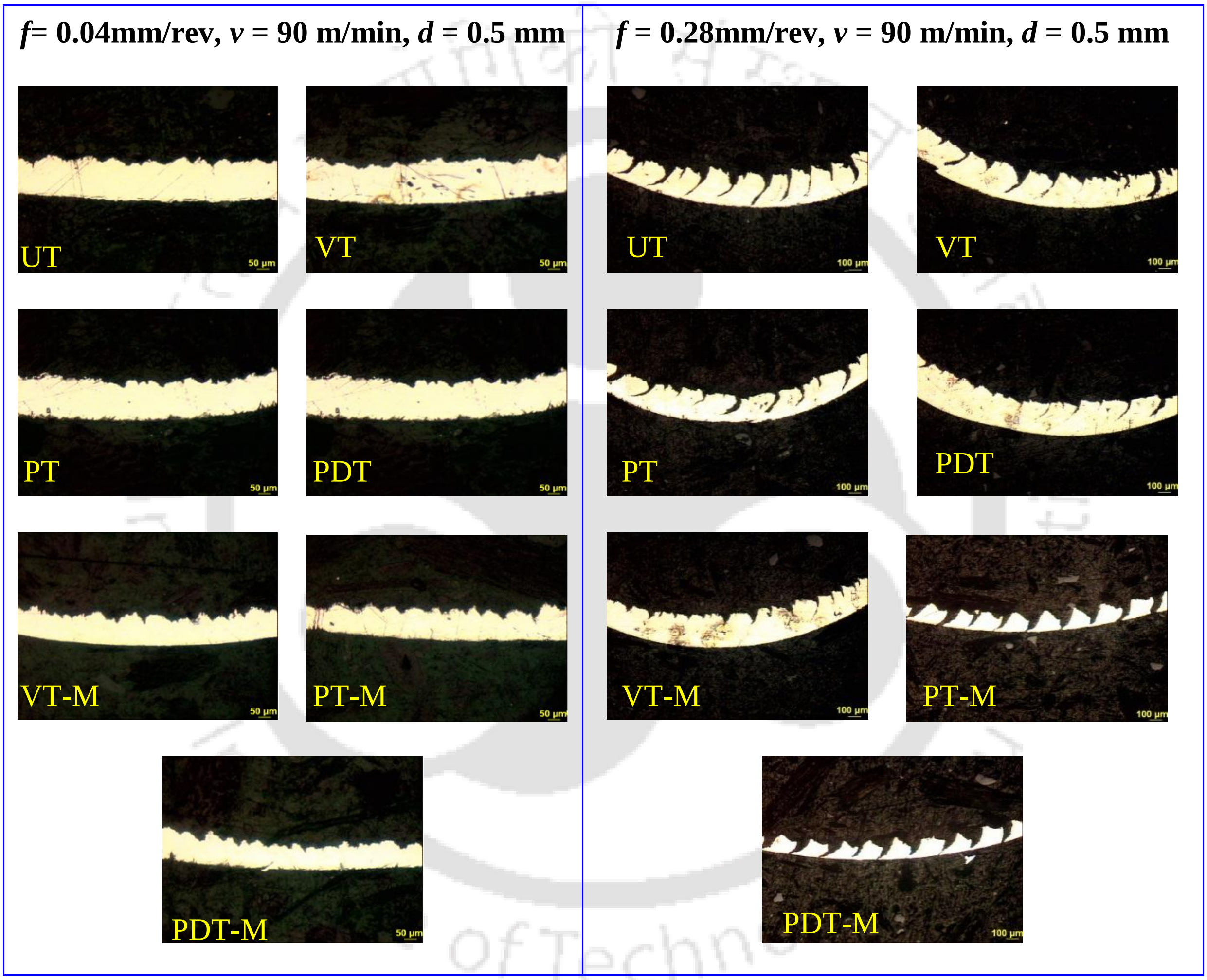

***f*= 0.04mm/rev, *v* = 90 m/min, *d* = 0.5 mm**

***f* = 0.28mm/rev, *v* = 90 m/min, *d* = 0.5 mm**

Figure 4.25. Chip morphologies of AISI H-13 tool steel machined with various cutting tools at cutting speed *v* = 90m/min, depth of cut *d* = 0. 5 mm with two different feed *f* = 0.04 and 0.28 mm/rev

Figure 4.26 illustrates the chip surface morphology for UT, PDT and PDT-M cutting tools. It was observed that severe chip serrations occur in the top (free) surface of the chip, which is caused due to periodic crack propagation and severe plastic deformation of chips. Due to the large angle of the cutting tool, high compressive stresses are experienced, which results in plasticization. Dogra et al, 2010 also observed similar behaviour [177].

In the case of PDT-M cutting tool, the longitudinal strain is low as compared to PDT and UT cutting tools. Cut chip thickness is the least for chip during machining using PDT-M cutting tool as compared to PDT and UT cutting tool. It suggests that less chip thickening occurs and redundant plastic deformation work is the least in the case of machining using PDT-M cutting tool. It is due to the less friction between tool-chip interfaces of PDT-M cutting tools, which provide less resistance to flow to chip in width direction.

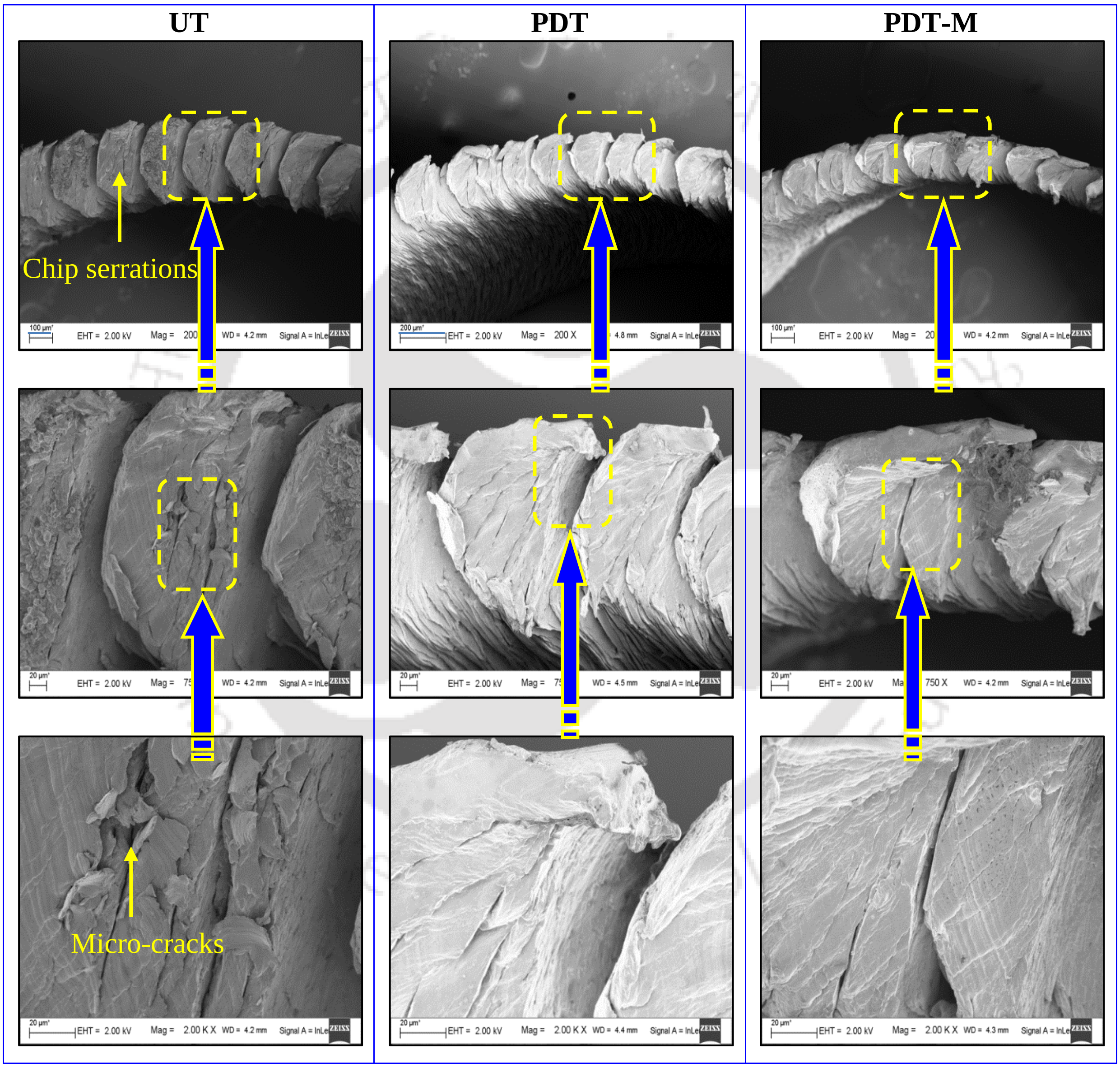

Figure 4.26. Surface micrograph of machined chips top surface using (a) untextured tool, (b) uncoated perpendicular textured tool and (c) coated perpendicular textured tool (cutting speed of 90 m/min, feed of 0.16 mm/rev and depth of cut of 0.5 mm)

4.4 Findings from the research work

Three different environmental friendly mechanical textures were fabricated on the rake surface of tungsten carbide cutting tool with Vickers hardness tester and mechanical scratch tester. MoS_2 solid lubricants were coated in the micro-textures. Dry machining experiments are carried out with VT, PT, PDT, VT-M, PT-M, PDT-M and UT cutting tools. Following observations are made:

- Finite element analysis confirms that MμTs affects the overall stress distribution in the cutting tool. However, the overall stresses on the MμT cutting tool are also well within safe limits.
- Tool-chip interface temperature, machining forces and tool-chip interface COF are reduced significantly for VT, PT, PDT, VT-M, PT-M and PDT-M as compared to UT cutting tools.
- The improvements in machining performance of uncoated MμT cutting tools are due to reduced contact length.
- During machining with MoS_2 coated MμT cutting tools, the formation of a self-lubricating film of MoS_2 reduces friction, thus enhancing its machining performance.
- The cutting force was reduced in the range of 4.23−10.82 % and 7.31−17.41 %, respectively, with PDT and PDT-M as compared to UT cutting tools.
- Amongst all, PDT-M cutting tool machining performance is best in terms of reducing tool-chip interface temperature, machining forces and tool-chip interface COF.
- Less chip thickness and least redundant plastic deformation work were observed in the case of machining using PDT-M cutting tool.

Chapter 5

SYNTHESIS OF GREEN CUTTING FLUID AND ITS COMPARATIVE STUDY WITH COMMERCIAL BIO-CUTTING FLUID AND MINERAL OIL

In **Chapter 5,** environmental friendly green cutting fluid was developed using mixtures of various vegetable oils and surfactants. Afterwards, biodegradation, thermal, rheological, storage stability and anti-corrosion properties of in-house developed green cutting fluids are compared with commercial bio cutting fluid and mineral oil.

5.1 Introduction to environmental friendly cutting fluids

In due course of time, the conventional cutting fluids shown problems for the manufacturers as the chemicals present in them caused severe health effects on the workers and the surrounding environment [71]. Along with the economic and technical aspects of the manufacturing processes, the environmental safety is also an important area of concern, and it is triggered by the fact that environmental agencies and government have imposed strict measures when it comes to protecting the employees' health and environment [72, 73]. Therefore, there is a need to analyse the measures that can be taken to reduce the harmful effects of metalworking fluids as much as possible.

Availability of mineral oil (MO) based cutting fluids is limited as they are the finite source and decreasing, whereas vegetable based cutting fluids are sustainable. Vegetable oils are evolving as metalworking fluids due to its higher biodegradability and ability to minimise the waste treatment costs. It also reduces the health risks to operators ho were quite prone to petroleum-based mineral oils due to their lower toxicity [74]. Cleaner and healthier work environment having less mist in the air is the primary point. For reasons as mentioned above, vegetable oils as metalworking fluids are environmental friendly and are also better lubricant as compared to others [75]. Above all, they are extracted from renewable sources and thus unlimited and sustainable.

All these factors have pushed the industries, research centres and universities for studying the process in detail and come up with the better optimal solution. Several of them have proposed various methods for reducing the exposures of cutting fluids while some have advised in changing its composition [76]. Vast quantities of metalworking fluids are still in use in the industries releasing harmful gases into the atmosphere, causing numerous skin and other diseases in the workers and increasing disposal costs [77]. Thus, a research study has been conducted to analyse the vegetable oils that act as an environmental friendly cutting fluid, so that the industries can find alternative answers and use protective measures.

In this Chapter, vegetable-based green cutting fluid (GCF) is synthesised. Various physical properties of GCF, commercial bio-cutting fluid (BCF) and MO are investigated. Also, biodegradable potential, thermal, rheological, apparent activation energy, anti-corrosion and storage stability characteristics of all cutting fluids are investigated and compared.

5.2 Experimental details

5.2.1 Synthesis of green cutting fluid

Green cutting fluid is synthesised using biodegradable, non-toxic, environmental friendly base materials. Raw coconut oil (without chemical refining) was used as base oil. Three commercially available food grade emulsifiers (Polysorbate 85 (E1), Polysorbate 80 (E2) and Triethanolamine (E3), 99.98 % purity) were also added to stabilise the cutting fluid emulsion.

Two essential environmental friendly additives extracted from *Azadirachta indica* (A1) and *Cymbopogon citratus* (A2), respectively were obtained from Falex International Export and Import, Bangalore, India. Another green additive was extracted from stem and leaf of *Centella asiatica* (A3). Commercially obtained jaggery syrup (A4) was also added to improve anti-corrosion property of GCF. Mass % of various ingredients is as follows:

- Coconut oil base (50%)
- Emulsifiers (E1+E2+ E3; 40%) - [Polysorbate 85 (77%); Polysorbate 80 (20%); Triethanolamine, (3%)]
- Additives - A-1 (1%), A-2 (3%), A-3 (3%), A-4 (3%)

Mixing of various cutting fluid ingredients was carried out at room temperature, i.e., 25±2 °C (above pour point of all ingredients) using a magnetic stirrer. The mixing continued for a stipulated time period until the proper mix was achieved. A proper mix of cutting fluid was ensured by the visual colour inspection and observed no separation among its ingredients. Figure 5.1 shows the flowchart for the synthesis of GCF.

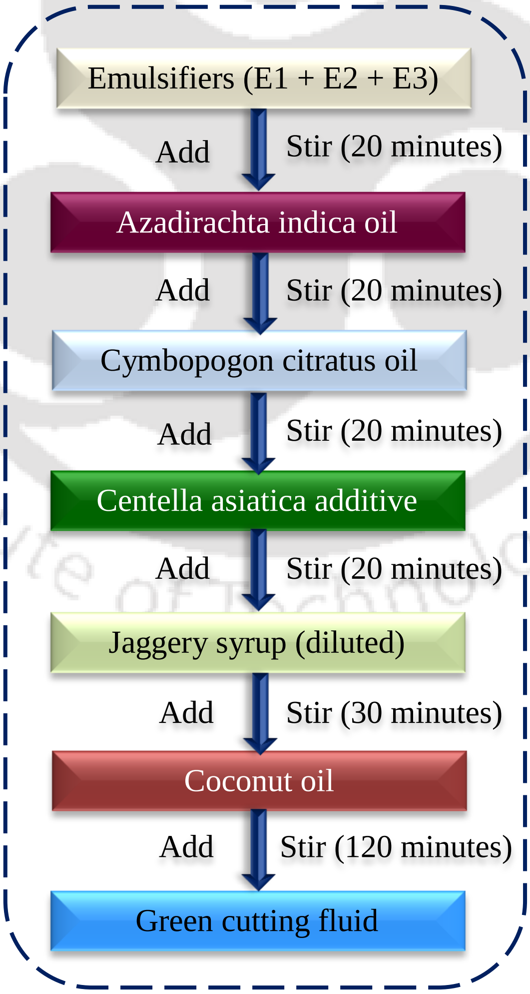

Figure 5.1. Flow chart for the synthesis of green cutting fluid

5.2.2 Materials

The cutting fluids used in this study are in-house synthesised GCF, commercial environmental friendly BCF and petroleum-based MO. The BCF used in this study was supplied by CORTEC Corporation, India and MO by Servo Lubricants and Greases, Indian Oil Corporation Limited, India.

5.2.3 Physical and chemical properties of the cutting fluids

Various physical and chemical properties of cutting fluids are measured. The kinematic viscosity of cutting fluids are measured using a rheometer (Make: ANTON Paar®, Model: MCR 101) equipped with a concentric cylinder tool master at 40 °C. Varian digital pH meter was used to measure pH of cutting fluid. Flash point of cutting fluid was measured using Pensky-Martens closed cup flash point setup following EN ISO 2719 (ECS, 2003) standard. Pensky-Martens closed-cup method applies to cutting fluids, highly viscous liquids, liquids that tend to form a surface film under the test conditions, liquids with suspended solids, combustible liquids, etc. The only requirement is that liquid must have a flash point higher than 30 ºC.

5.2.4 Biodegradation study

The chemical breakdown or transformation of any substance by micro-organisms like bacteria, enzymes, fungi, etc. is known as biodegradation. **The ability of a substance or matter to biodegrade is known as biodegradability.** Biodegradation has two significant extents:

- Primary biodegradation: Change in chemical and physical properties of the substance caused by micro-organism activity.
- Ultimate biodegradation: Complete utilisation of substance resulted in its conversion into methane (CH_4), carbon dioxide (CO_2), water (H_2O), biomass (microbial cellular constituents) and mineral salts.

The primary objective of biodegradation studies is to measure ultimate biodegradability. Generally, oil or cutting fluid biodegradability tests are performed in a free environment with ample amounts of oxygen and water (aerobic aquatic biodegradation). Dissolved oxygen in any liquid substance is an essential element for measuring its life cycle. Biological oxygen demand (BOD) tests measure only the biodegradable portion of the organic matter in cutting fluid, whereas chemical oxygen demand (COD) tests measure the oxygen demand for both biodegradable substances/matter and non-biodegradable oxidisable substances/matter. Therefore, the BOD/COD ratio is the quantitative measure of the degree of biodegradation.

Standard Methods 2005 (American Public Health Association) [178] are followed to conduct BOD and COD tests with BCF and MO using 1:100000 (lubricant: aerated water) diluted samples.

5.2.5 Thermal gravimetric analysis study

Twenty mg of each cutting fluids in alumina crucible are tested for thermal degradation studies using thermal gravimetric analysis setup (Make: NETZCH Instruments, Model: STA F4913). Samples are tested in the range of 50–700ºC with the heating rate of 10ºC min^{-1}. Tests are carried out under argon atmosphere (argon flow rate = 60 mL min^{-1}).

5.2.6 Rheological study

The flow and lubricant behaviour of cutting fluid depends on its shear stress and viscosity. Therefore, shear stress and viscosities of cutting fluids are measured as a function of shear rate using a rheometer (Make: ANTON PAAR®, Model: MCR-101) with coaxial cylinder tool master (Figure 5.2). To obtain shear flow conditions, measurement were carried out under steady flow state. Measurements were carried out by the linear increase in shear rate from 1−1000 s^{-1} at four different temperatures of 20 ºC, 50 ºC, 80 ºC and 100 ºC. Average values of three tests are reported.

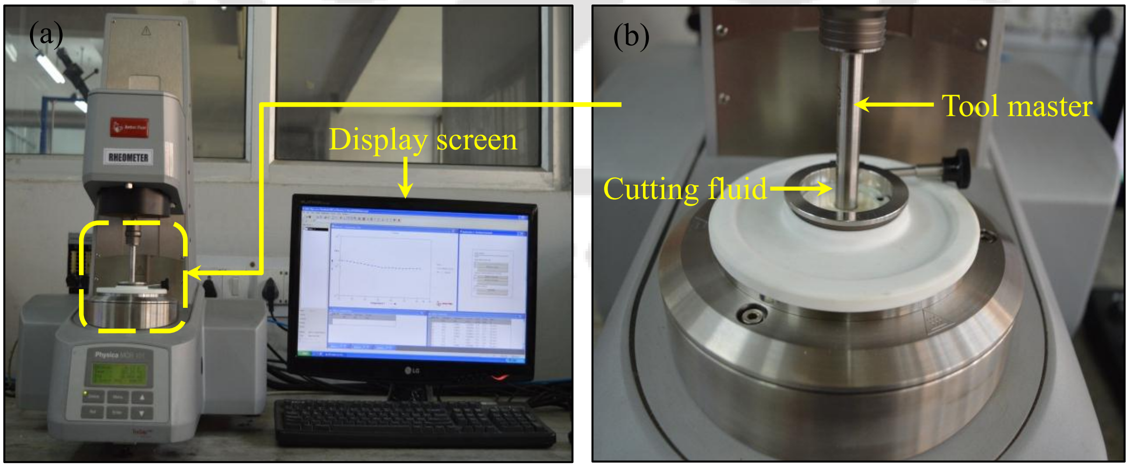

Figure 5.2. (a) Overview of the rheometer setup and (b) close view of nano-green cutting fluid along with tool master

5.2.7 Determination of apparent activation energy

The term activation energy is defined as the minimum necessary energy required for the occurrence of a specific chemical reaction. Arrhenius type equation relates the viscosity (μ) and the activation energy (E_a) as follows:

$$\mu = A\exp^{\left(\frac{E_a}{RT}\right)} \tag{5.1}$$

where T is the absolute temperature, R refers to real gas constant and A is a constant. Activation energy is determined using the temperature dependence of viscosity with the help of Eq. 5.1 [179, 180]. Eq. (5.1) can be rewritten as:

$$\ln(\mu) = \ln(A) + \left(\frac{E_a}{R}\right)\frac{1}{T} \tag{5.2}$$

5.2.8 Corrosion study of the cutting fluids

Cutting fluids corrosion tests are performed in accordance with ASTM D 4627 standard [181]. Figure 5.3 (a) illustrates 47 mm diameter filter paper made of glass fiber (1.5 µm particle retention) placed inside the petri dish. Cutting fluid with ten different oil concentration (0.5, 1, 1.5, 2, 2.5, 3, 4, 5, 7 and 10 %) of each BCF and MO were mixed with synthetic hard water (calcium chloride dehydrate in distilled water). As per the standard, grey cast iron chips are selected for corrosion tests. Chips were sieved using a 18 mesh screen. Figure 5.3 (b) illustrates 4 g of chips sprinkled on the top of glass fiber filter paper. Afterwards, different petri dishes were filled with 25 mL of ten different oil concentration of BCF and MO each.

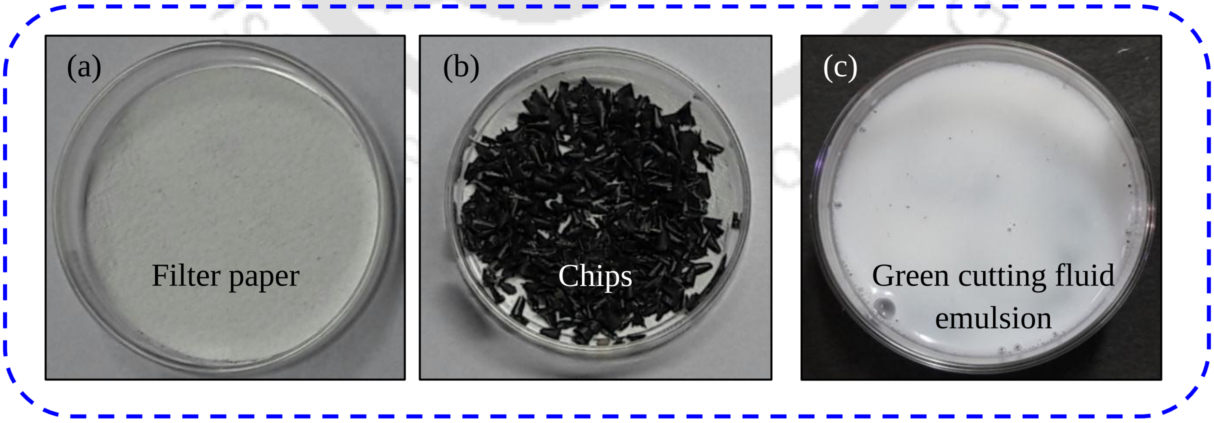

Figure 5.3. Overview of corrosion test method setup (a) filter paper with the petri dish, (b) grey cast iron chips on the filter paper and (c) cutting fluid poured into the petri dish submerging chips

Figure 5.3 (c) shows chips submerged in cutting fluids. All petri dishes were covered with the top lid. After an incubation time of 24 h, cutting fluids were drained from petri dish. Afterwards, corroded chips were collected separately. Chips were cleaned by sonication using acetone for 20 minutes and dried. Weight loss of chip because of its corrosion was also calculated. Moreover, glass fiber filter paper was rinsed. The amount of rust stain over the filter paper gives the measure of cutting fluid anti-corrosion properties that helps in identifying breakpoint. ASTM D4627 defined breakpoint as the weakest concentration of cutting fluid tested, which shows no rust stain on the glass fiber filter paper.

5.2.9 Storage stability of the cutting fluids

Cutting fluids are used in the form of an emulsion to reduce generated heat and friction during machining. Ten different compositions (1:2−1:20, 1 part of oil for 2 to 20 part of water) of cutting fluid emulsions were tested for storage stability. ASTM D 3707 standard was followed to perform a storage stability test for cutting fluid emulsions [182]. As per the guidelines, emulsions were prepared and 50 ml of each sample was kept in glass graduated cylinder as shown in Figure 5.4 (a). Test samples were kept inside convection oven for 48 h at 85±1 ºC. Afterwards, samples were withdrawn from the oven and allowed to stand at room temperature for one hour. After incubation, the samples were measured for the amount of separated oil, water and the remaining emulsion (Figure 5.4 b).

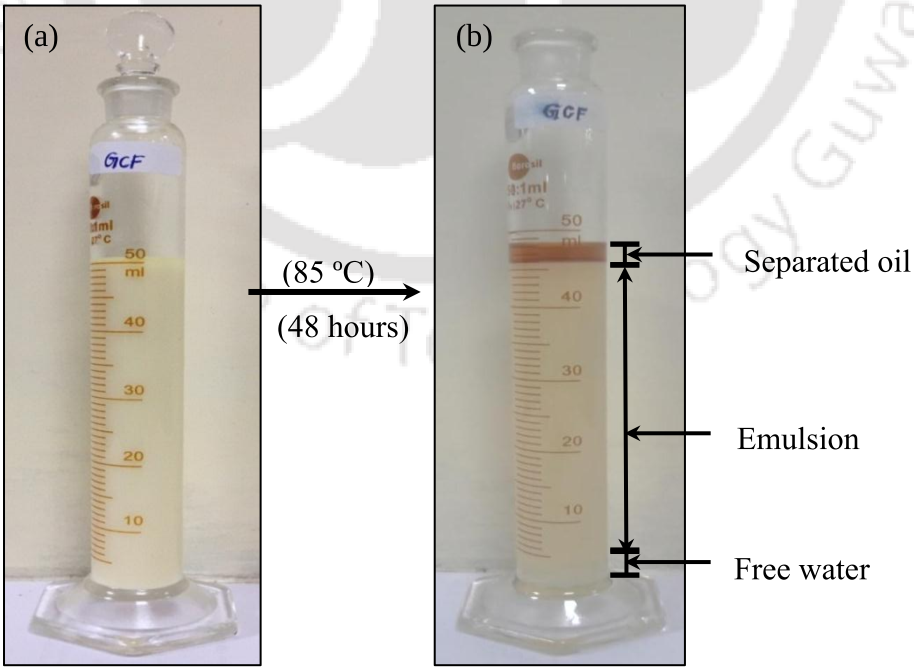

Figure 5.4. Cutting fluid emulsion (1:16) for the storage stability test (a) before (b) after 48 h @85ºC

5.3 Results and discussion

The properties of GCF, BCF and MO are presented in Table 5.1. GCF has more density and less pH as compared to BCF and MO that suggest that GCF is less basic among them. GCF has a higher viscosity and flash point than BCF and MO, which suggests that GCF possesses better lubrication ability. Additionally, these properties suggest that GCF is safer, even for the higher temperatures that occur during the hard machining of hardened AISI H-13 steel.

Table 5.1. Properties of various cutting fluids

Metal cutting fluid	pH	Density (g/mL)	Viscosity 40 °C (mm^2/s)	Flash point (°C)
Green cutting fluid	8.55±0.05	0.953±0.05	82.154±1.04	325–340
Bio-cutting fluid	8.65±0.06	0.942±0.04	64.721±0.74	310–320
Mineral oil	9.05±0.08	0.890±0.07	33.082±0.52	206–214

5.3.1 Biodegradability of the cutting fluids

The biodegradation of cutting fluids were assessed using BOD/COD ratio measurements taken at varying times. BOD tests were measured for a period of only five days. The BOD/COD ratio indicates the degradation percentage (%) of biodegradable substances (Figure 5.5).

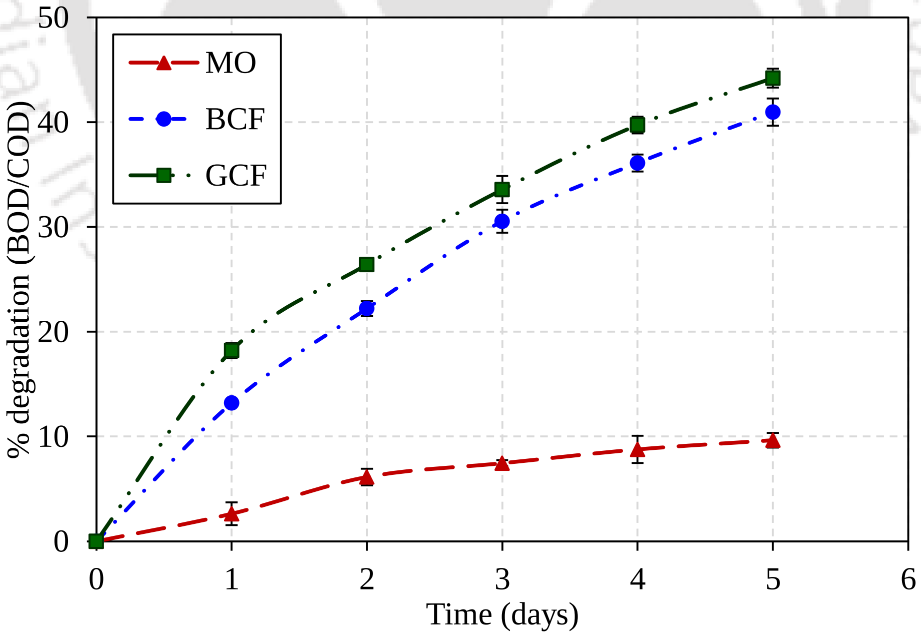

Figure 5.5. Biodegradability of various cutting fluids over five days

The results show that the biodegradability of cutting fluids is primarily determined by the chemical structure of the organic matter. Within five days of biodegradation, GCF and

BCF were degraded by 44% and 41%; however, MO is degraded by only 10%. This occurs because the GCF and BCF contain readily degradable organic matter, while MO contains primarily non-degradable volatile or fixed solids. Substances such as wastewater or chemicals with a BOD_5/COD ratio of 40% or more are considered to be completely degradable [183]. However, substances with values lower than 20% contain a higher amount of un-oxidisable organic matter, which may be toxic. BOD_5 does not provide complete information about total biodegradation. For complete biodegradation information, ultimate BOD (BOD_u) is calculated using the least square method, per *Standard Methods 2005* [184]. Thus, BOD_u and COD for GCF, BCF and MO are shown in Table 5.2.

Table 5.2. Ultimate aerobic biodegradability of various cutting fluids

Metal cutting fluid	BOD_u ultimate (g/L) (least square method)	COD (g/L)	BOD_u/COD	Final degradation (%)
GCF	1238.3	1260	0.9827	98.27
BCF	1392.0	1440	0.9667	96.67
MO	417.8	2280	0.1832	18.32

Over the five-day test period, the degree of degradation may seem low. However, Table 5.2 indicates that the GCF and BCF has a higher BOD_u value, while the MO has a higher COD value. Organic matter with a BOD_u/COD ratio over 0.5 is considered to be biodegradable; if the ratio is higher than 0.8, the organic matter is considered to be highly and readily biodegradable, as reported in [183]. Cutting fluids containing organic matter and exhibiting higher BOD values are easily oxidised by natural bacteria present in the atmosphere.

MO is not susceptible to high biodegradation. With the passage of time, these fluids become much more susceptible to metallic cations, which are harmful to sewage organisms and further reduce the efficiency of disposal plants.

Ultimate biodegradability tests show that sewage micro-organisms and organisms present in natural water bodies possess the capacity to degrade GCF and BCF on their own. However, MO was not degraded satisfactorily during the incubation time. Thus, a few components of MO may appear in the environment as pollutants.

5.3.2 Thermal stability of the cutting fluids

Thermal stability of the cutting fluids is determined in terms of the mass loss with respect to thermal degradation temperature (T). Figure 5.6 shows the mass loss of the MO, BCF and

GCF which have different behaviour in terms of starting the degradation temperature of the mass loss. Mass loss of the GCF and BCF started at 161 and 118 ºC respectively, indicating their higher thermal stability with respect to MO whose mass loss started at 51 ºC.

In the case of GCF, there was no mass loss until 100 ºC. This result indicates the absence of water in GCF. Up to 200 ºC mass loss was under 2 % and it increased to 63 ± 3 % at 400 ºC. Above 540 ºC, the mass loss rate leveled off, probably because of the previous degradation of its components with higher molecular mass. The final mass loss reached 97 ± 3 %. It is not possible to define whether the components of the GCF volatilized or degraded, but both phenomena could have happened. It can also be noted that no residues were observed after 580 ºC, indicating there was no significant content of inorganic compounds during heating.

In the case of BCF, up to 100 ºC no mass loss was observed, which shows the absence of water in it. BCF degrades 13.33± 1 % of its mass up to 200 ºC, which is much less than MO mass degradation (28.54± 2 %). After 466 ºC, mass almost become constant. It is attributed to decompose higher molecular mass components of BCF. Maximum mass loss of 91.2 ± 2 %) was observed for BCF. Mass loss with temperature is due to the combination of both degradation and vitalization.

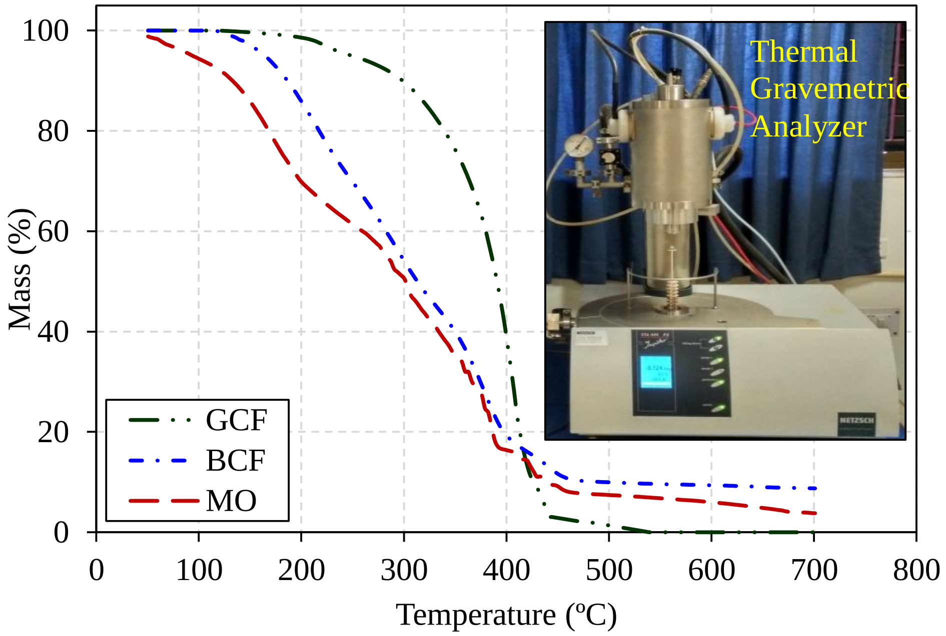

Figure 5.6. Variation of cutting fluids mass with respect to temperature

MO is least thermally stable, with mass losses over 10 % before 100 ºC indicating the presence of moisture and small carbon chain groups. Up to 460 ºC, continuous mass loss observed around 90 ± 3 %. The mass loss then levelled off after 460 ºC. The total mass loss at the end was around 4 ± 3 %, indicating the presence of inorganic material or formation of coke (carbon derived from pyrolysis of organic material). MO had lower thermal stability than the other fluids. Therefore, it is not recommended for use at high temperatures. The greater thermal resistance of the GCF and BCF should reduce the risk of machine operators due to the lesser generation of toxic vapours.

5.3.3 Shear stress and viscosity of the cutting fluids

It is evident that GCF cannot follow the same mechanism for lubrication as MO. Lubrication depends on various properties such as viscosity, density, composition, etc. However, cutting fluid viscosity is the most important among them. Cutting fluids having higher viscosity are believed to have better lubricating properties.

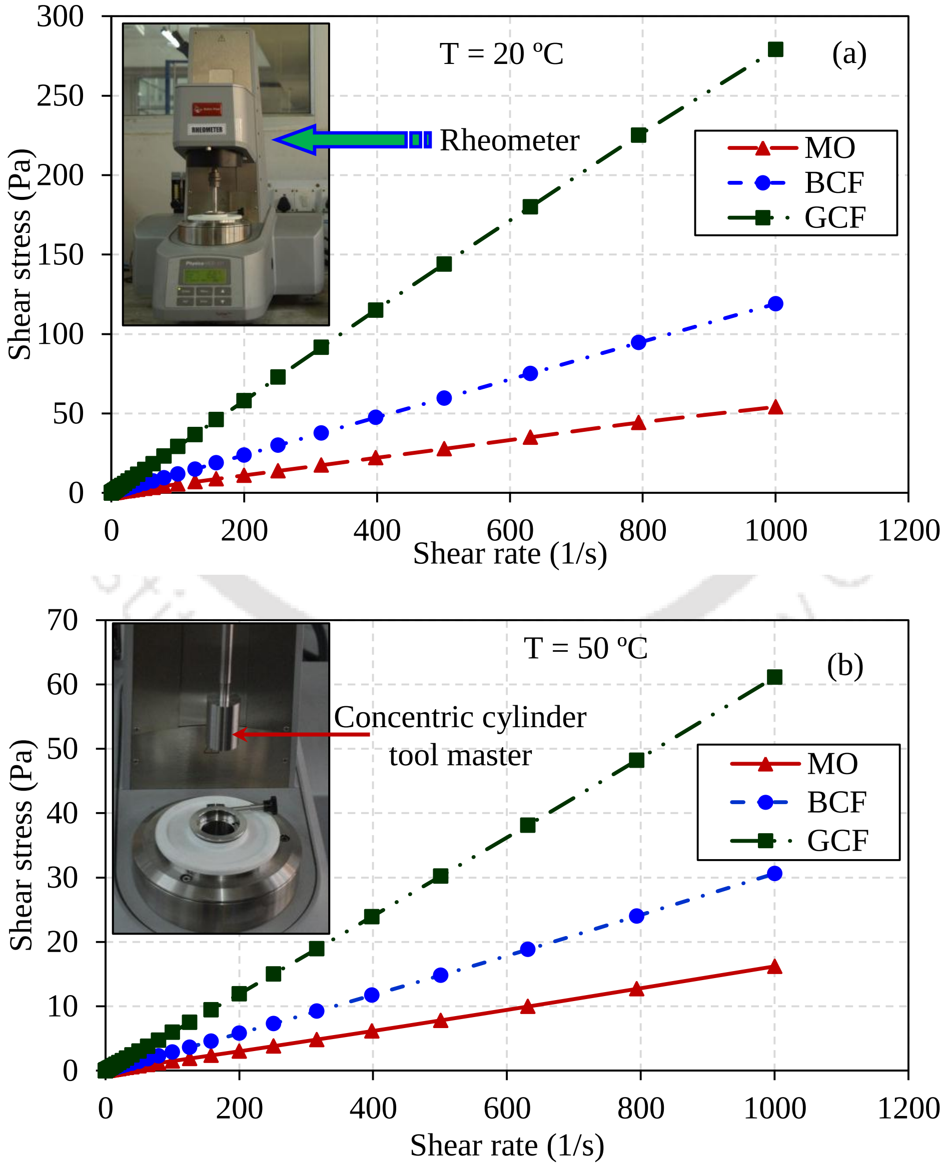

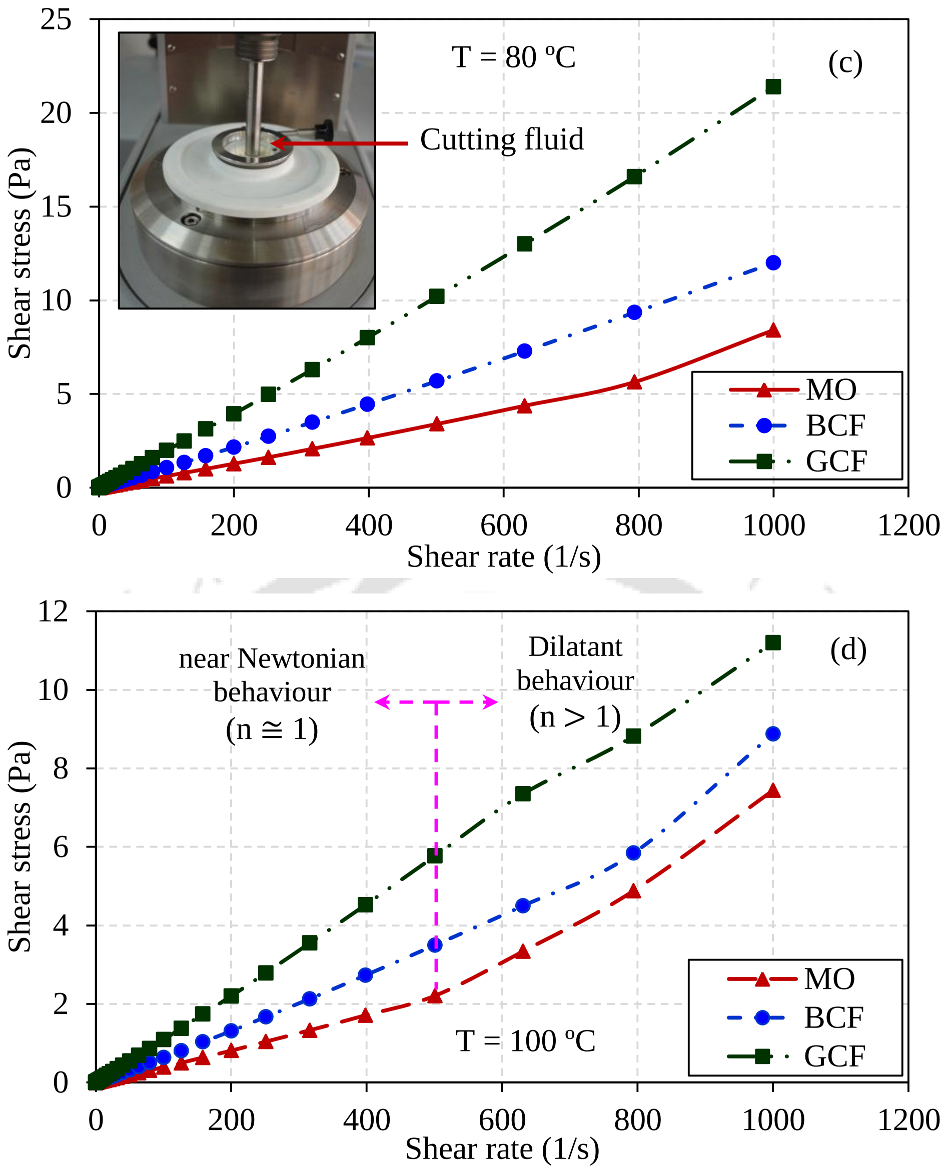

Figure 5.7. Effect of shear rate on the shear stress of various cutting fluids at (a) 20 ºC, (b) 50 ºC, (c) 80 ºC and (d) 100 ºC

Apparent viscosity can decrease, remain unchanged or increase with respect to shear rate for time-dependent fluids. These fluids are known as pseudoplastic (n<1), Newtonian (n=1) and dilatant (n>1), respectively. It is essential to know the behaviour of cutting fluid because various metalworking processes involve different operating range of temperature and shear rate.

Figure 5.7 (a−d) shows the effect of shear rate on the shear stress of GCF, BCF and MO at 20 ºC, 50 ºC, 80 ºC and 100 ºC, respectively. Even though the chemical composition of GCF, BCF and MO are different, their rheological behaviour is similar. All cutting fluids show near Newtonian behaviour (n = 1) at 20 ºC (Figure 5.7 a) and 50 ºC (Figure 5.7 b). Newtonian behaviour can be confirmed by the linear variation of shear stress with shear rate.

However, at the higher temperature of 80 ºC (Figure 5.7 c), only GCF shows Newtonian behaviour. At the higher shear rate, BCF shows near Newtonian behaviour while MO exhibits the dilatant behaviour. With the further increase in temperature at 100 ºC (Figure 5.7 d) both BCF and MO exhibits dilatant behaviour. Therefore, it can be said that GCF is able to maintain Newtonian behaviour at the higher temperature even at the higher shear rate as compared to BCF and MO.

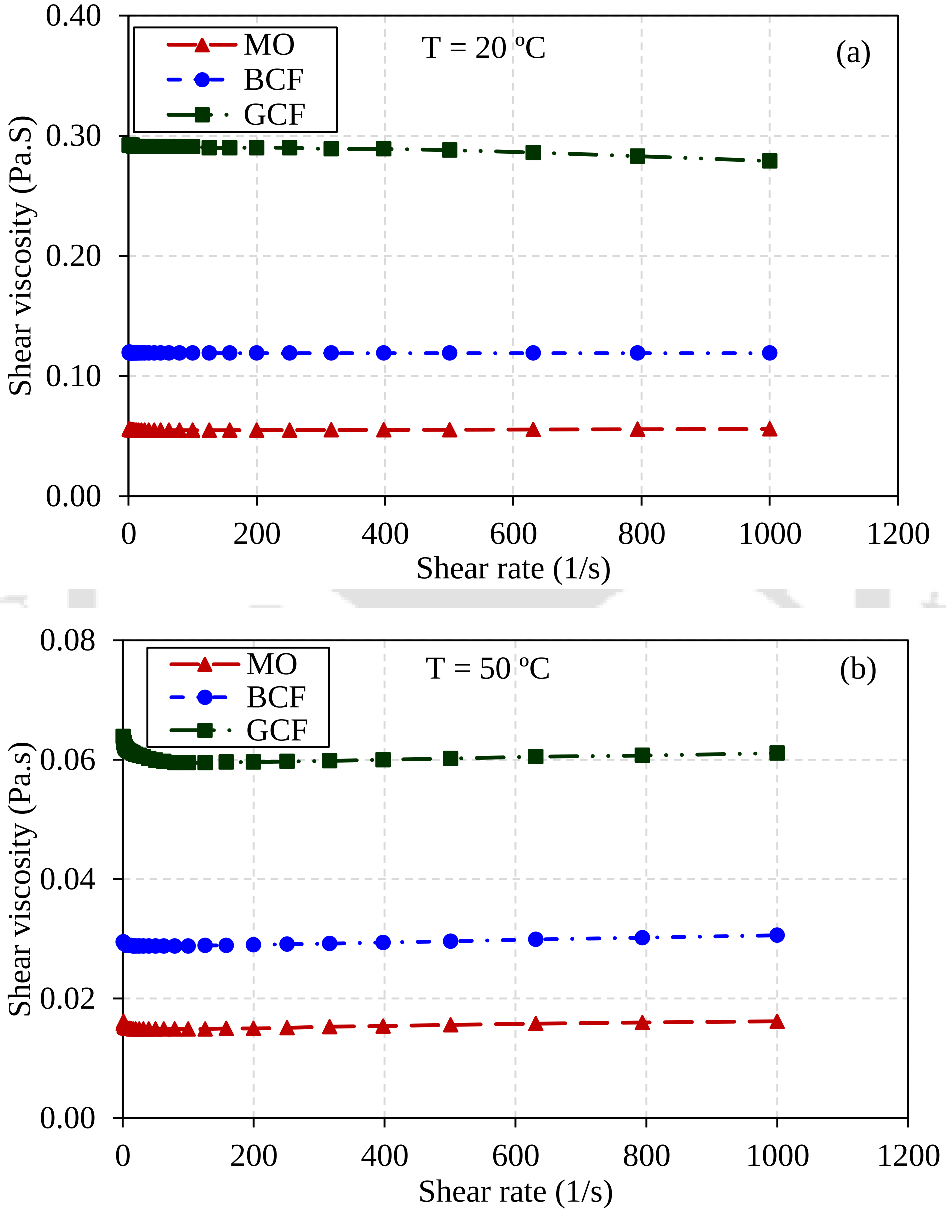

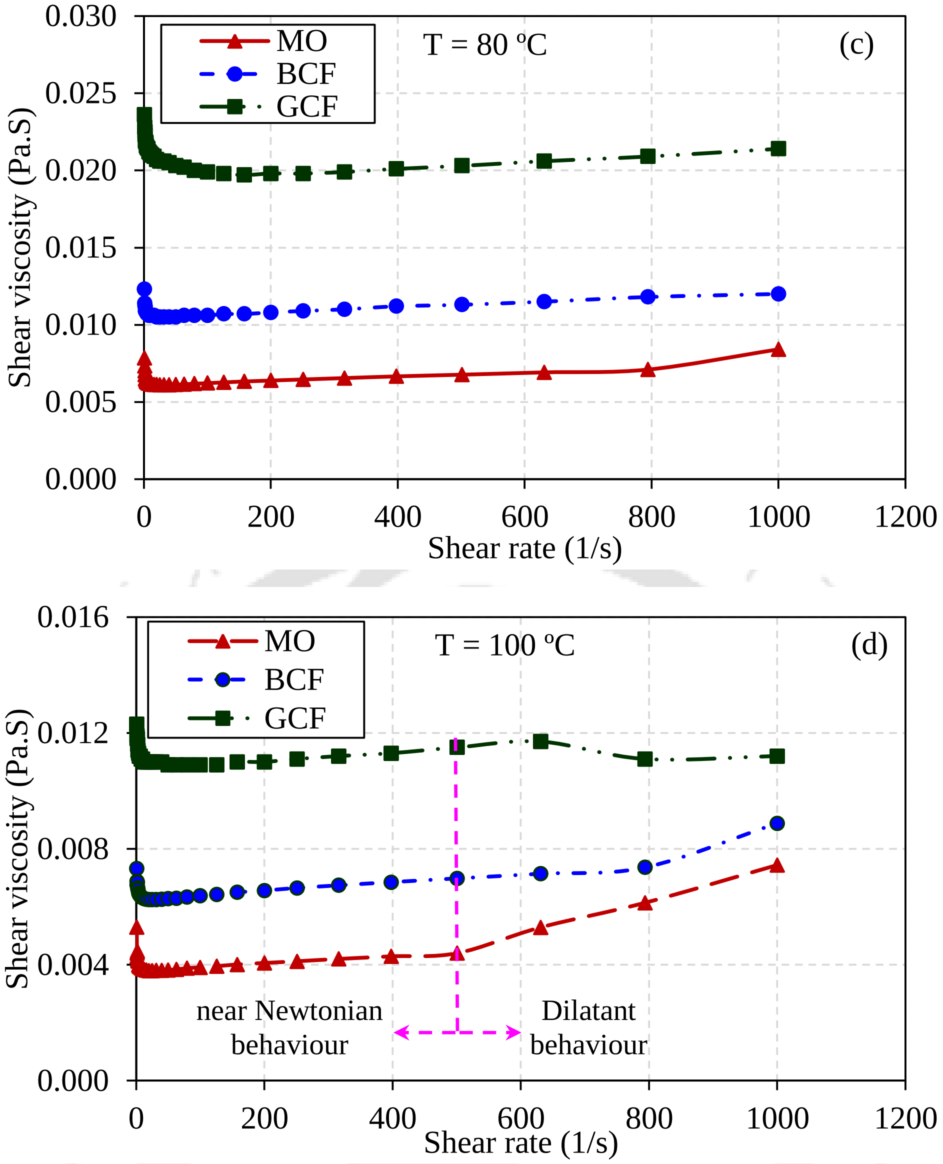

Figure 5.8. Effect of shear rate on shear viscosity of the mineral oil, bio-cutting fluid and green cutting fluid at (a) 20 °C, (b) 50 °C, (c) 80 °C and (d) 100 °C

Figure 5.8 (a–d) illustrates the effect of shear rate on viscosities of BCF and MO at 20 °C, 50 °C, 80 °C and 100 °C, respectively. At 20 °C, viscosities of GCF, BCF and MO are 0.28 Pa.s, 0.12 Pa.s and 0.05 Pa.s, respectively. However, due to high heat and temperature during machining operations, mostly cutting fluids operate much above 20 °C. Therefore, viscosities of GCF, BCF and MO at higher temperature are also reported. At 50 °C, viscosities of GCF, BCF and MO are 0.06 Pa.s, 0.03 Pa.s and 0.015 Pa.s, respectively. Furthermore, with increase in temperature, the viscosities of GCF, BCF and MO are 0.020 Pa.s, 0.011 Pa.s and 0.007 Pa.s, respectively at 80 °C as well as 0.011 Pa.s, 0.007 Pa.s and 0.004 Pa.s, respectively at 100 °C. At higher temperature, the viscosity of all cutting fluids reduces. It is attributed to molecules that overcome a threshold energy barrier and occupy the adjacent vacant site due to thermal activation. For varying temperature range, GCF has more viscosity as compared to both BCF and MO that enables it to lubricate better as compared to others.

5.3.4 Apparent activation energy of the cutting fluids

The flow of molecules is a thermally activated process. In any liquid, molecules need to overcome an energy barrier to flow to the nearby vacant site. With the increase in temperature, the number of vacant sites in the liquid as well as molecules thermal energy increases. The dependence of the reaction rate on the temperature indicates the apparent activation energy. Figure 5.9 shows the variation of viscosities with respect to temperature for BCF and MO. Using equation 5.2 and data from Figure 5.9, a relation between ln(μ) against T^{-1} is plotted as shown in Figure 5.10. From the slopes of ln(μ) against T^{-1}, apparent activation energy is calculated and reported in Table 5.3. GCF has high activation energy that means GCF is less sensitive and more stable with increasing temperature as compared to BCF and MO.

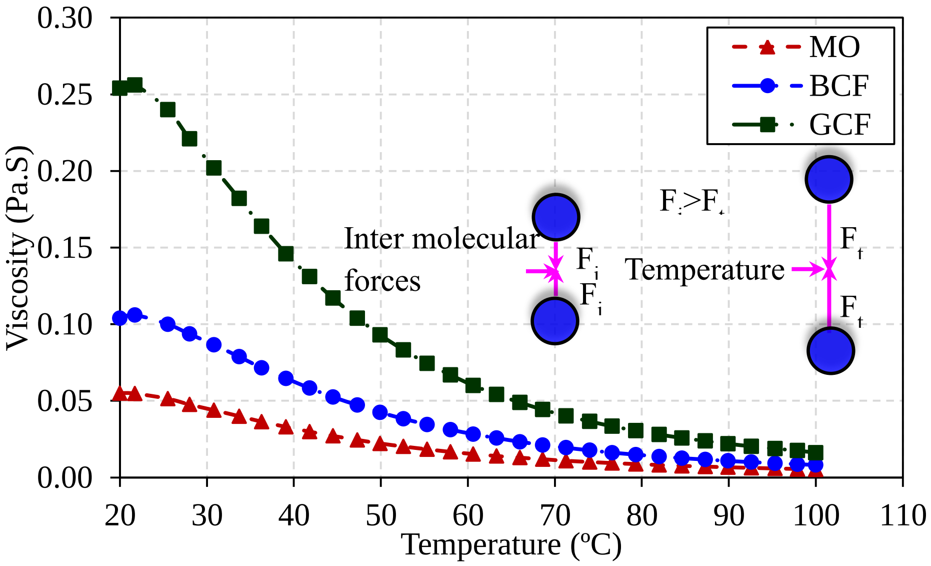

Figure 5.9. Effect of temperature on the viscosity of various cutting fluids

Table 5.3. Apparent activation energies of various cutting fluids

Cutting fluid	Apparent activation energy E_a (kJ/mol)
Green cutting fluid	33.43 ± 0.6
Bio-cutting fluid	31.23 ± 0.5
Mineral oil	28.50 ± 0.8

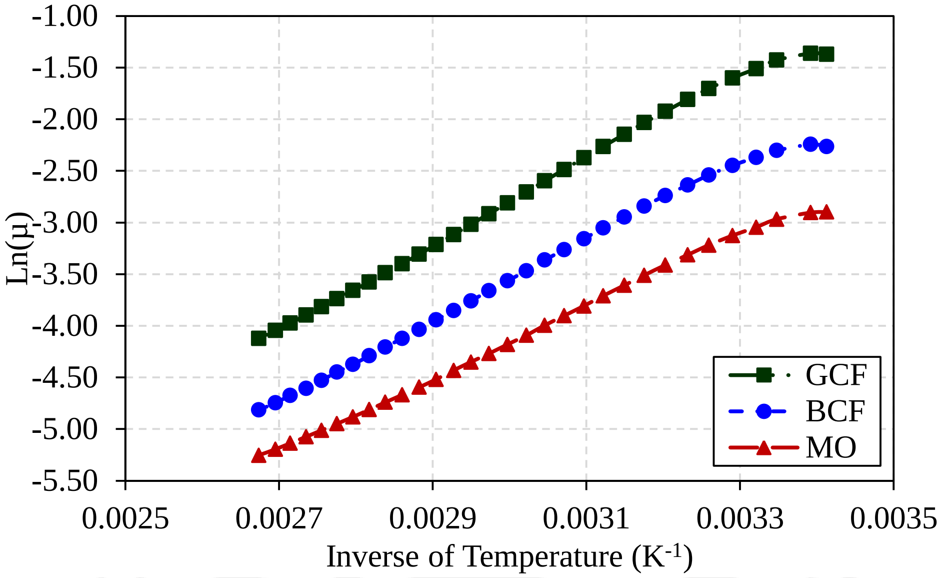

Figure 5.10. Variation of ln(μ) with respect to the variation of temperature for apparent activation energies of various cutting fluids

5.3.5 Anti-corrosion properties of the cutting fluids

The anti-corrosion properties of cutting fluids were evaluated in accordance with ASTM D 4627 standard. The rate of corrosion is graded from 1 to 10, where ten is highly corrosive, five represent medium corrosion, and one stands for non-corrosive cutting fluids [181]. After the corrosion test, rusted filter paper with several concentrations of GCF, BCF and MO is shown in Figure 5.11 (a-c). Results show that the amount of rusting reduces with the increase in the concentration of cutting fluids. For GCF less rusting was observed as compared to filter paper of BCF and MO for all concentrations. Breakeven point of 4, 8 and 9 exhibit by GCF, BCF and MO, respectively, where naked eyes observe no further rust. It confirms that the GCF has better anti-corrosion properties with respect to BCF and MO-based cutting fluids.

Moreover, the chips weight loss was also measured and reported as shown in Figure 5.12. It is observed that chips weight loss and the rate of corrosion reduces with the increase in the concentration of cutting fluids. It is attributed to anti-corrosion properties of cutting fluids that slow the reaction of oxygen and iron in its presence. Even though GCF, BCF and MO have the different composition, they follow similar behaviour in case of chips weight loss after corrosion tests. GCF contains Triethanolamine (TEA) and jaggery which are corrosion inhibitors. The inhibition efficiency of TEA is due to the presence of a terminal amine with higher electron density that binds more strongly to the metal surface. Moreover, jaggery contains 50−60 % sucrose which helps in inhibition. The lone pair of electrons present in oxygen helps the sucrose adsorption to the metal surface.

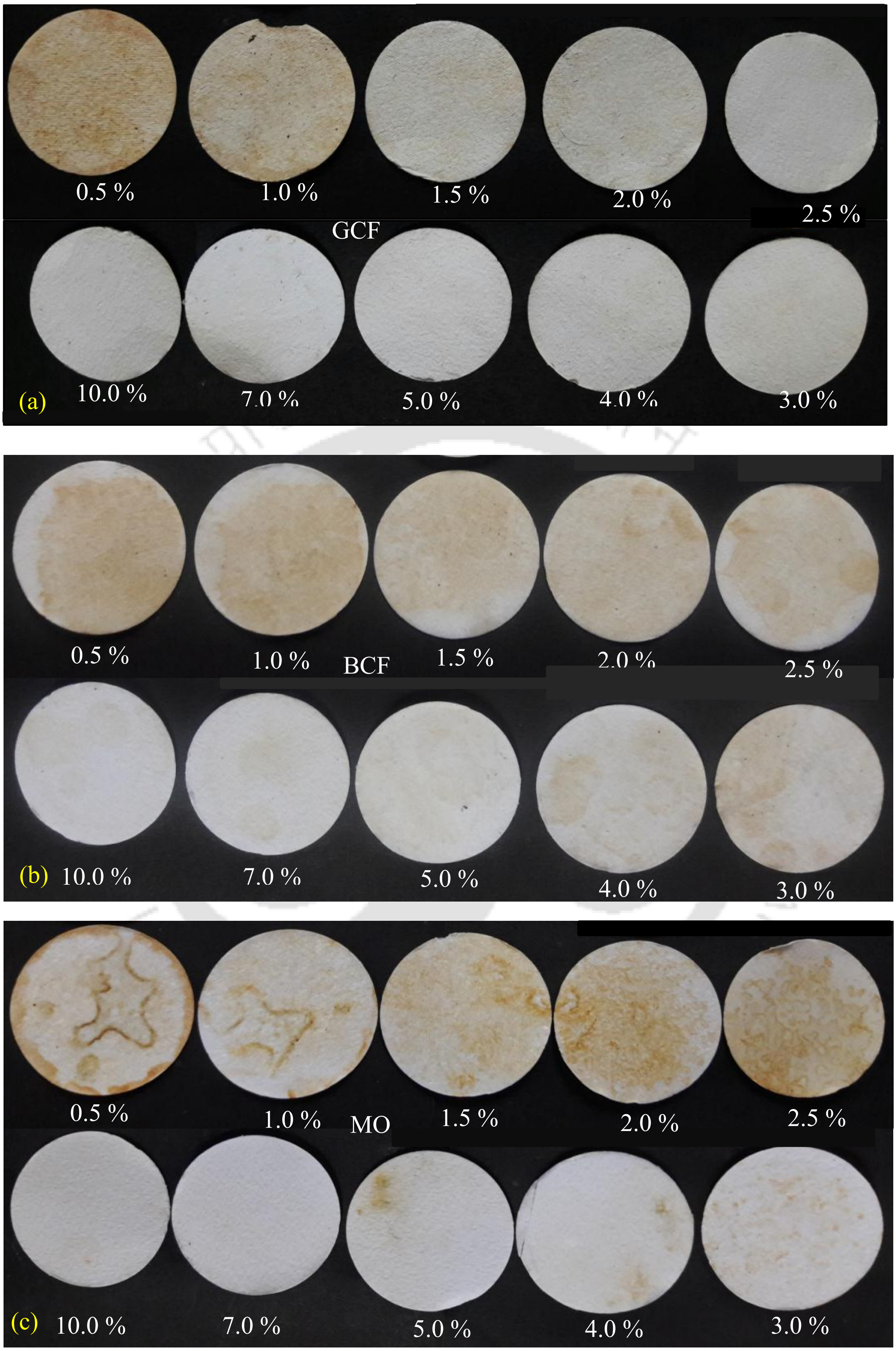

Figure 5.11. Rusted filter paper after corrosion test with various concentration of (a) green cutting fluid, (b) bio-cutting fluid and (c) mineral oil

Therefore, the vacant adsorption site is filled by sucrose instead of oxygen. Thus, GCF shows better anti-corrosion properties. Tested chips and corresponding filter paper with 0.5 % concentration of BCF and MO are shown in Figure 5.13 (a-c).

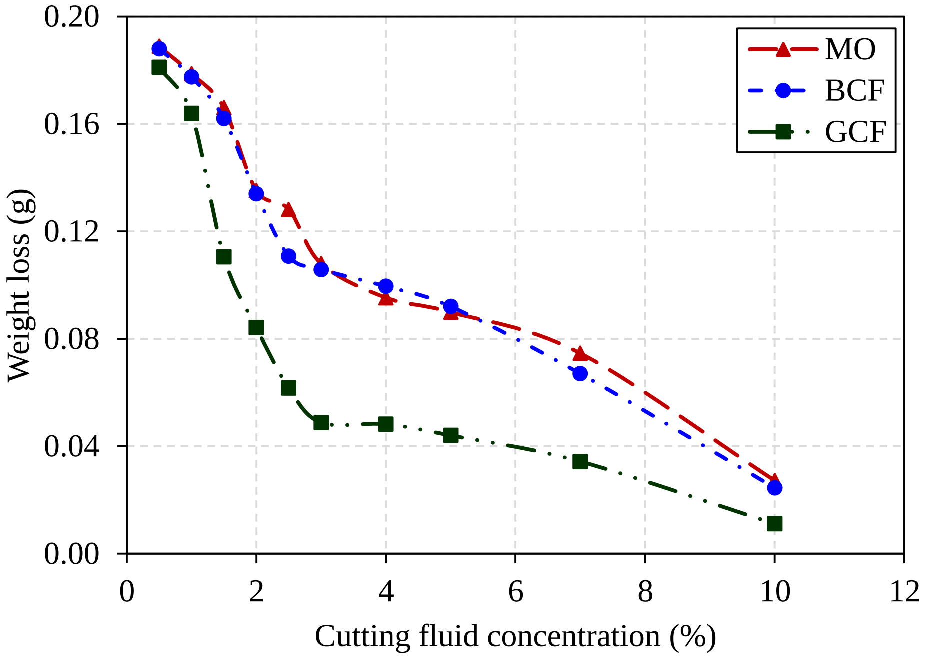

Figure 5.12. Effect of bio-cutting fluid and mineral oil on weight loss of chips due to corrosion at varying concentration

Figure 5.13. Tested chips with 2.5 % concentration of (a) mineral oil, (b) bio-cutting fluid and (c) green cutting fluid

5.3.6 Storage stability of the cutting fluids

In accordance with ASTM D3707 standard, cutting fluids emulsion stability was tested [182]. Storage stability of the emulsion was assessed by measuring separated oil and water from intact emulsion after tests. Tests were carried out in a thermostatically controlled oven for 48 h at 85±1°C. After tests, the samples were cooled for one hour at room temperature.

Afterwards, separated oil and separated water were measured in the sample. Amount of sample evaporated was considered as separated water. Amount of initial sample minus measured separated oil and separated water was considered as an intact emulsion after tests.

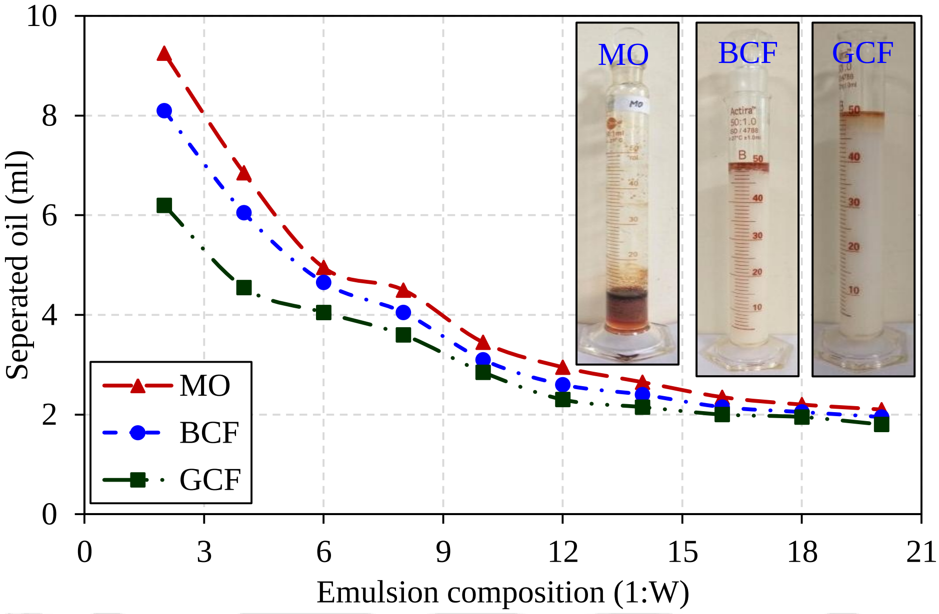

Figure 5.14. Assessment of separated oil from the emulsion after oven test with respect to emulsion concentration (1:W represents 1 part of the oil in W part of water)

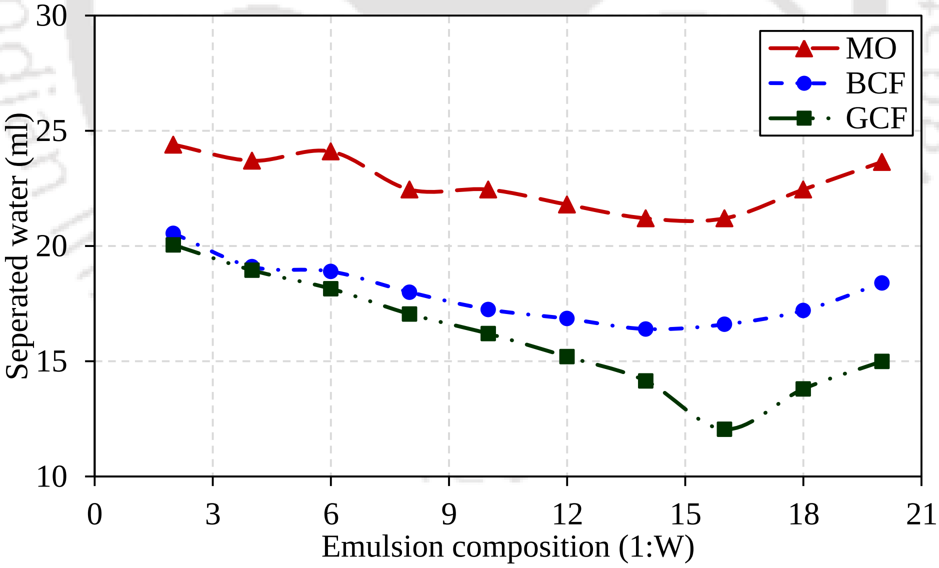

Figure 5.15. Assessment of separated water from the emulsion after oven test with respect to emulsion concentration (1:W represents 1 part of the oil in W part of water)

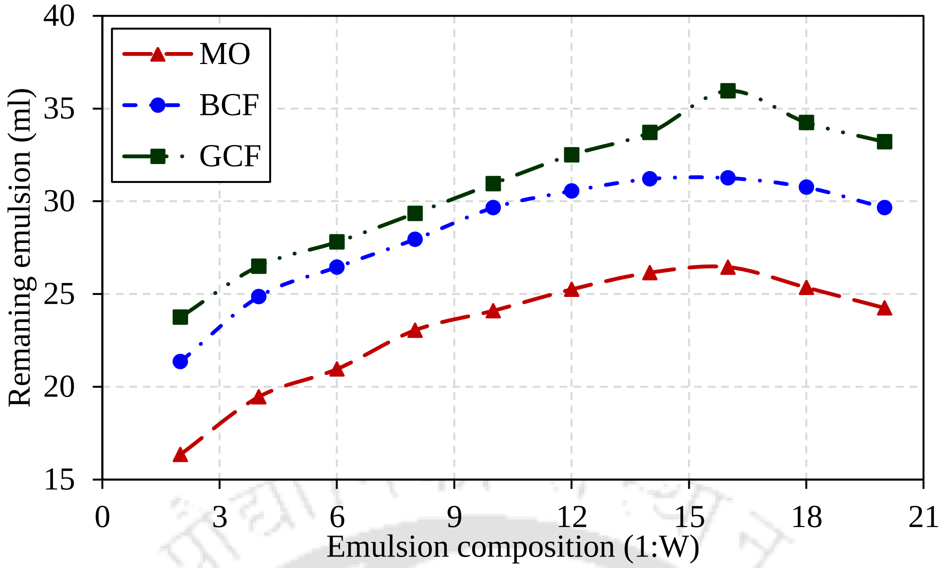

Figure 5.16. Assessment of remaining emulsion after oven test with respect to emulsion concentration (1:W represents 1 part of the oil in W part of water)

Figures (5.14–5.16) illustrates the effect of emulsion concentration on separated oil, separated water and remaining emulsions, respectively for GCF, BCF and MO after oven tests. The result shows that separation of oil increases with the increase in the concentration of water in emulsions (Figure 5.14) for all cutting fluids. However, in the case of GCF, the amount of separated oil is less as compared to BCF and MO. Moreover, the amount of separated water reduces up to 1:16 emulsion concentration while afterwards, it starts increasing for all cutting fluids (Figure 5.15). Similarly, the amount of remaining emulsion increases up to 1:16 emulsion concentration while afterwards, it starts increasing for all cutting fluids (Figure 5.16). However, in all cases, the amount of separated oil and separated water is less for GCF as well as the amount of remaining emulsion is high for GCF as compared to BCF and MO. The emulsion type and composition showing the least separation (most remaining emulsion) after oven test is considered as the most stable composition. Therefore, based on the measured parameters, the storage stability of 1:16 GCF emulsion composition is proved to be better among others.

5.4 Findings from the research work

Environmental friendly green cutting fluid was synthesised. The physical, thermal, rheological, biodegradation, anti-corrosion and storage stability properties of GCF, BCF and MO are assessed and compared. The salient findings are as follows:

- The flash point of GCF is higher as compared to BCF and MO that allows its use for high-temperature hard machining.
- As per *Standard methods 2005*, ultimate biodegradability of GCF, BCF and MO are found to be 98.27%, 96.67% and 18.32%, respectively.
- GCF exhibits less variation from Newtonian behaviour even at the higher temperature. Also, its sensitivity to temperature is lower as compared to BCF and MO.
- GCF showed corrosion breakpoint of 4; whereas BCF and MO exhibit corrosion breakpoint of 8 and 9 as per ASTM D 4627 standard.
- As per ASTM D 3707 standard, GCF shows more remaining emulsion as compared to BCF and MO after storage stability test.

Chapter 6

MINIMUM QUANTITY ENVIRONMENTAL FRIENDLY CUTTING FLUIDS IN HARD MACHINING

Chapter 6 discusses the development of minimum quantity cutting fluid setup. The MQCF input parameters such as emulsion composition, stand-off distance between the nozzle and machining zone as well as nozzle spraying angle are optimised experimentally. Afterwards using experimental optimised input parameters, hard machining performance of MO, BCF and GCF with MQCF technique are compared.

6.1 Introduction to minimum quantity cutting fluids

Hard machining of difficult-to-cut material generates significant heat, which results in high temperatures. In manufacturing processes using conventional fluid application methods, 15−17% of product cost is associated with cutting fluid cost [99]. Research has shown that the costs associated with cutting fluids are frequently higher than those for cutting tools [13]. Therefore, the elimination or minimisation of cutting fluids is desirable from both economic and environmental perspectives. Therefore, for these applications, the concept of near-dry machining came into existence [100].

Near-dry machining (NDM) or MQL or micro-lubrication, also known as minimum quantity cutting fluid (MQCF), is an alternative solution for reducing detrimental environmental effects and improving machining performance [101−103]. In MQCF applications, a minute amount of cutting fluid is used at a flow rate of 5–600 mL/h. A cutting fluid with a high convective heat transfer coefficient is mixed with compressed air to form a uniform atomised mist. This generated mist is injected directly into the tool-chip interface in the machining region [104, 105]. MQCF reduces occupational hazards, addresses environmental issues, and produces economic benefits by reducing cutting fluid costs. MQCF is an accepted eco-friendly machining method that can improve workpiece surface finish, and reduce tool wear and cutting forces relative to dry machining [106, 107].

MQCF provides several benefits during machining. MQCF techniques have existed since the past decade; however, the effectiveness of its input parameters has not been discussed. The efficiency of an MQCF system depends upon mist (the mixture of pressurised air and cutting fluid) formation and quality, which are controlled by the MQCF input parameters, namely, emulsion composition, stand-off distance between the nozzle and machining zone, nozzle spraying angle, and air pressure. No clear guidelines have been created by researchers for selecting or optimising these parameters.

In this Chapter, the MQCF input parameters are experimentally optimised. Hard turning experiments are conducted to investigate the relative influences of three different cutting fluids using MQCF on cutting force, feed force, coefficient of friction and workpiece surface roughness. This Chapter also compares the effectiveness of GCF, BCF and MO using MQCF with dry machining (DM).

6.2 Experimental details

6.2.1 Materials

Three cutting fluids were analysed for this study: vegetable-based in-house synthesised GCF, commercial BCF and petroleum-based MO. The MO was supplied by Servo Lubricants and Greases, Indian Oil Corporation Limited, Bandra (East) Mumbai, India and BCF were supplied by CORTEC Corporation, Bangalore, India. Details of workpiece material and cutting tool insert are mentioned in Chapter 4. Figure 6.1 shows a workflow diagram for this Chapter.

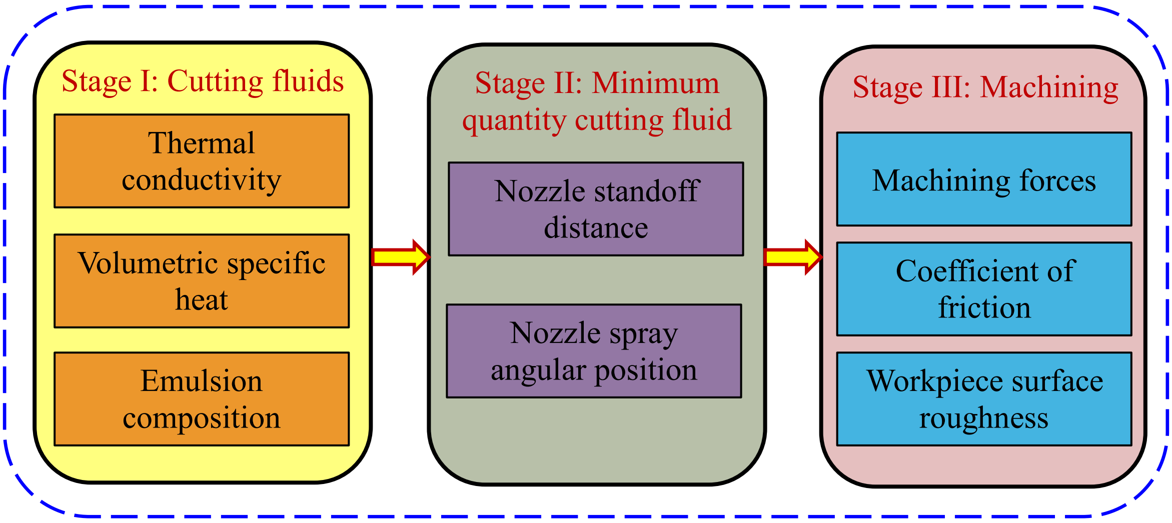

Figure 6.1. Schematic representation of proposed work

6.2.2 Selection of optimum cutting fluid emulsion concentration, nozzle standoff distance and nozzle spray angle position

Cutting fluids are primarily used in machining to reduce generated heat (cooling) and friction (lubrication). Water is known to be the best coolant. Thus, emulsions (mixtures of cutting fluid and water) with higher water content provide better cooling and partial lubrication. However, higher oil content in an emulsion provides better lubrication and partial cooling. To obtain better cooling and lubricating performance from a cutting fluid emulsion, the optimum quantity of the cutting fluid and water are mixed.

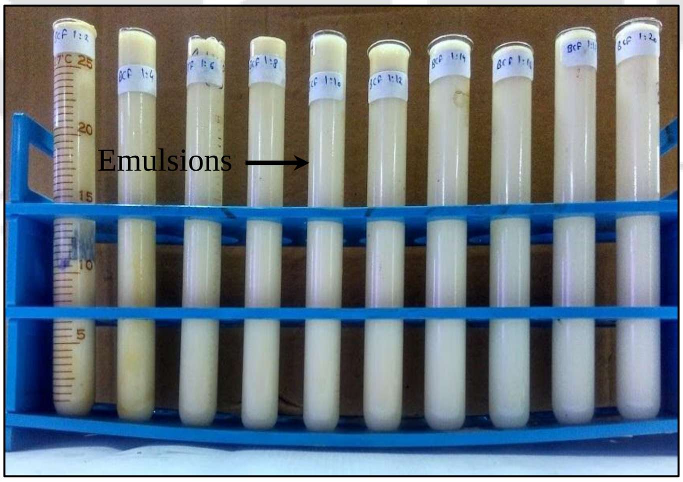

Figure 6.2. Cutting fluid emulsions with varying compositions in test tubes

Experiments are carried out in three stages to successively determine the optimum emulsion composition, standoff distance, and nozzle position. First, preliminary experiments are carried out to estimate the optimum emulsion composition (Figure 6.2). The heat extraction capacity of a particular cutting fluid emulsion typically depends on its thermal conductivity and specific heat. Therefore, the thermal conductivity and specific heat of all cutting fluid emulsions (cutting fluid to water ratio varied from 1:2 to 1:20) are measured using the KD2 Pro thermal properties analyser.

In an MQCF system, the distance between the machining zone and nozzle position is known as the standoff distance. This distance governs mist formation. If the standoff distance is too large, MQCF jet flaring may occur. It leads to mist divergence, resulting in the lesser force being applied by the cutting fluid emulsion mist in the machining region. Therefore, the MQCF mist experiences difficulty penetrating the air boundary layer created by workpiece rotation, resulting in reduced effectiveness in cooling and lubrication. In contrast, for smaller standoff distances, the MQCF mist may not completely cover the high-temperature machining region. Therefore, experimental optimisation of the standoff distance to maximise the effectiveness of the MQCF system is carried out.

An indigenously developed MQCF system is used to spray the cutting fluid emulsion. A Kistler piezoelectric quartz dynamometer is used to measure the force exerted by the MQCF spray. The standoff distances are varied from 10 to 100 mm, with an interval of 10 mm. At each standoff distance, the forces exerted by the MQCF spray are recorded multiple times, and the average force values are considered. Apart from the force exerted by spray, it is also important that the spray completely cover the high-temperature machining region.

`Brinksmeier et al. [184] discuss in detail about types and nozzle positions in grinding with MQL technique. The systematic study of various types of cutting fluid and nozzle positions in FC and MQL are carried out. Among all, shoe nozzle is best from the useful flow rate point of view.

Ebbrell et al. [185] conducted surface grinding experiments using different nozzle positions and measured the resulting grinding forces. The minimum grinding forces were found when the nozzle was placed at an angular position. Therefore, optimising the nozzle spray angle position is vital for maximising the effectiveness of the MQCF system and minimising machining forces. In the present experimental study, the nozzle spray angle was varied from 15° to 90° (at 15° intervals), and the machining forces were measured.

6.2.3 Experimental design

The experiments were planned and designed in such a way that useful inferences could be obtained by performing a minimum number of experiments. The total number of experiments in a central composite rotatable design (CCRD) technique = 2^k + rotatable + central runs. Therefore, for this study, experiments were planned for different variables (k=2): speed and feed. The total number of experiments required to be performed for one type of cutting fluid application system is $2^k + 2k + 5$ ($4 + 4 + 5 = 13$ (with each technique)). The depth of cut is kept constant at 0.5 mm. All experiments are carried out with FC and MQCF using MO and BCF cutting fluid emulsions (Total experiments = 13×4= 52 (each experiment repeated thrice)). The effects of control variables on the output responses are also determined. The CCRD coded values are presented in Table 4.2 (Chapter 4), and the machining control parameters are presented in Table 6.1.

Table 6.1. Machining conditions

Parameter	**Values**
Cutting speed	55−125 m/min
Feed	0.04−0.28 mm/rev
Depth of cut	0.5 mm
Environments	Dry, MQCF
Cutting fluid	Green cutting fluid, bio-cutting fluid and mineral oil
Air pressure	5 bar (0.5 MPa)

6.2.4 Machining experiments

Machining experiments are carried out on a lathe (Make: HMT, Model: NH26) equipped with a commercial tool holder PTGNR 2525 M22. The experiments are performed for an MQCF spray environment with GCF, BCF and MO. Tests are conducted at optimised machining input parameters. For comparison purposes, dry machining experiments are also performed. A compressed air pressure of 0.5 MPa (5 bar) and oil flow rate of 35 mL/h are maintained for MQCF experiments. Figure 6.3 shows an overview of the MQCF experimental setup. An infrared thermography camera (Make: Infratech®, Model: Variocam hr-400) measures the average cutting temperature of the tool-chip interface. Cutting and feed forces are measured using a piezoelectric quartz dynamometer (Make: Kistler®, Model: 9272B). The surface roughness of the workpiece is measured at five different positions using a contact-type surface profilometer (Make: Mahr®, Model: FEDERAL), and the average values are plotted. The morphology of cutting tool wear regions are examined by an optical microscope (Make: Zeiss®, Model: AxioCam MRc) and field emission scanning electron microscope (FESEM; Make: Zeiss®, Model: Sigma).

Figure 6.3. (a) Overview of MQCF experiment setup, (b) magnified view of the infrared camera, emulsion-air hoses, tooling, etc. and (c) magnified view of the tool-workpiece-mist interaction

6.3 Results and discussion

6.3.1 Selection of cutting fluid concentration in the emulsion

The thermal conductivity and specific heat of various emulsions are measured by the KD2 Pro thermal properties analyser. Figure 6.4 shows variations in thermal conductivity and specific heat with respect to the concentration of cutting fluid in the emulsion. With increasing emulsion water content, the thermal conductivity of all cutting fluids increases up to the saturation point (0.55 ± 0.03 W/(m °C)). Thermal conductivity saturation levels for all cutting fluids are reached because the thermal conductivity of water falls in the range of 0.6 ± 0.05 W/(m °C). For BCF and MO, the saturation point is reached at a 1:8 composition for thermal conductivity; however, for GCF the saturation point is reached at 1:16 composition (Figure 6.4).

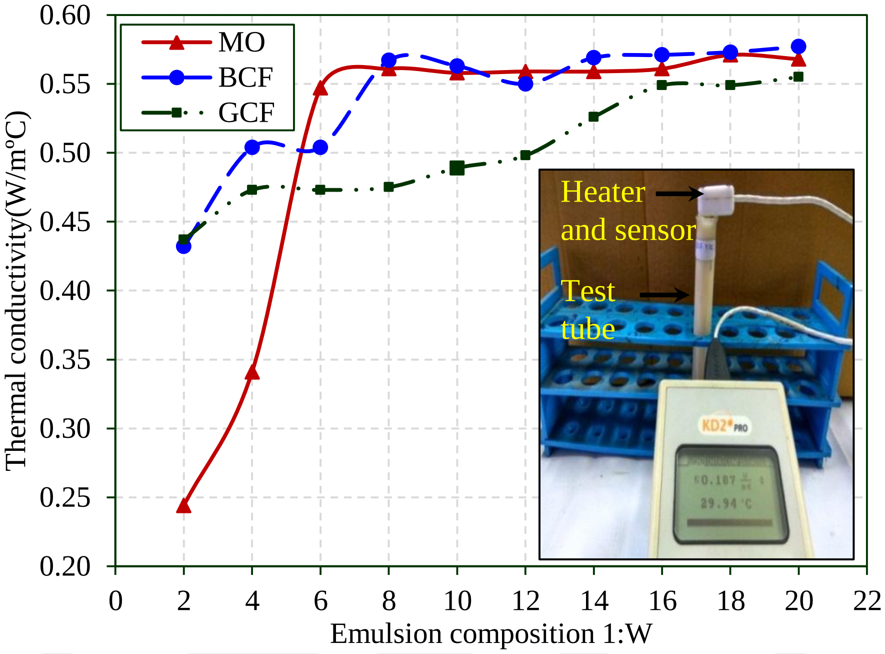

Figure 6.4. Variation in thermal conductivity with varying cutting fluid emulsion compositions

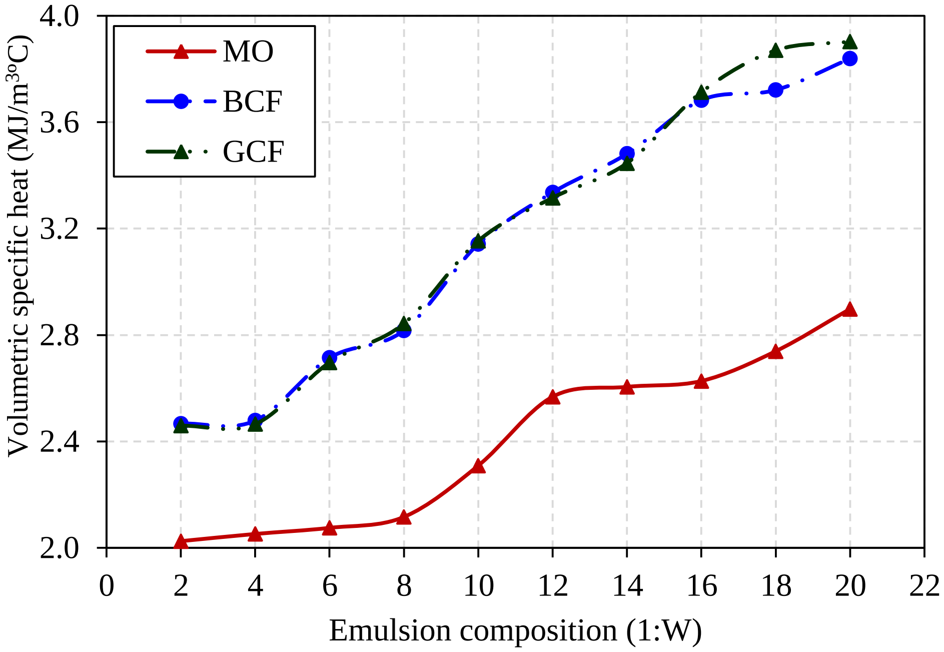

Figure 6.5. Variation of volumetric specific heat with varying cutting fluid emulsion compositions

Figure 6.5 shows the specific heat for the varying cutting fluid concentrations in the emulsion. It can be observed that with increasing emulsion water content, the specific heat of both cutting fluids continues to increase, up to 1:20. GCF and BCF can extract more heat than MO because of its higher specific heat. Therefore, from Figure 6.4 and 6.5, it can be observed that emulsion compositions ranging from 1:16 to 1:20 produce better heat extraction. However, considering the lubrication properties and storage stability (Chapter 5) of the cutting fluid, a 1:16 emulsion composition is selected to attain a better surface finish.

6.3.2 Selection of nozzle standoff distance

A dynamometer is used to record the forces exerted by MQCF sprays with respect to different standoff distances, as shown in Figure 6.6. It is observed that at a distance of 10 mm, the MQCF system can exert maximum force, whereas force gradually decreases as standoff distance increases for both cutting fluids. With increasing standoff distance, the cutting fluid mist/spray begins to diverge, and the velocity decreases. Thus, spray exerting forces gradually decrease.

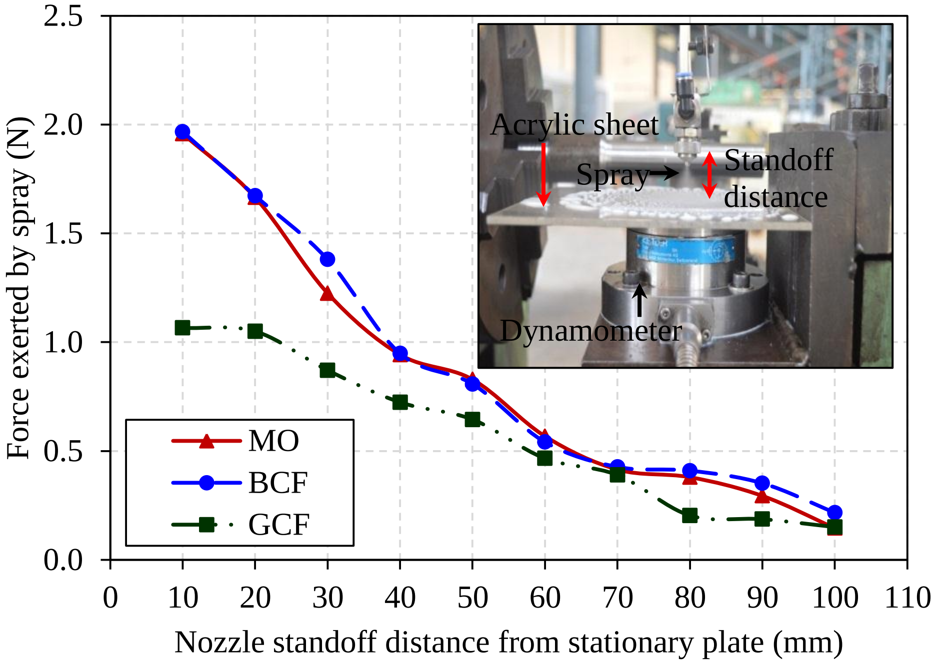

Figure 6.6. Variation in the radial force exerted by a spray for varying standoff distances

In addition to the force exerted by spray, the area covered by the spray is also important. The spray should cover the complete machining region, where temperatures are high**.** Figure 6.7 shows an infrared micrograph of the machining region, highlighting the length of the high-temperature zone during dry machining (L = 27.15 mm). The shape of the high-temperature zone in machining is approximately elliptical. Therefore, in the present study, an MQCF nozzle with a rectangular slit (1×5 mm^2) outlet is selected for generating an elliptical mist. The minor axis of the ellipses is considered to cover the machining region with spray in all directions during machining. To select the optimum standoff distance, the minor axis lengths covered by the MQCF spray nozzle for both cutting fluids are recorded at varying standoff distances, using an indigenously developed experimental setup (Figure 6.8).

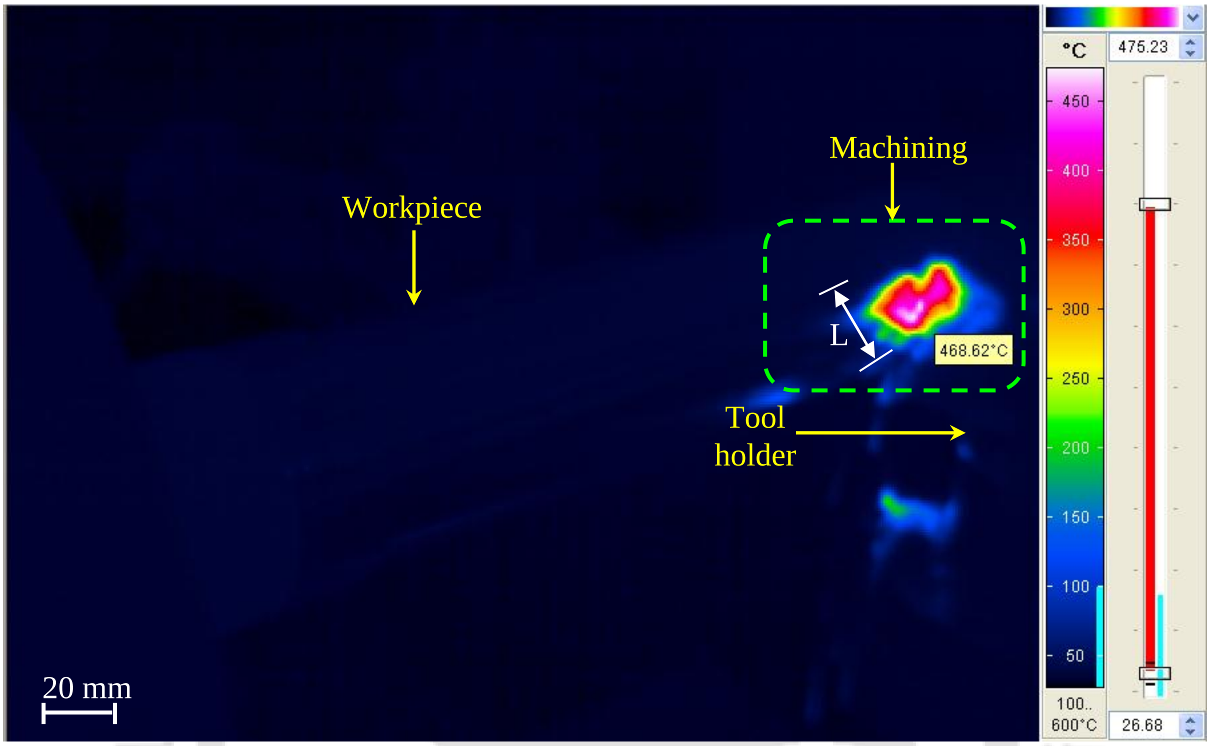

Figure 6.7. Infrared micrograph of machining zone with the maximum length of high-temperature zone

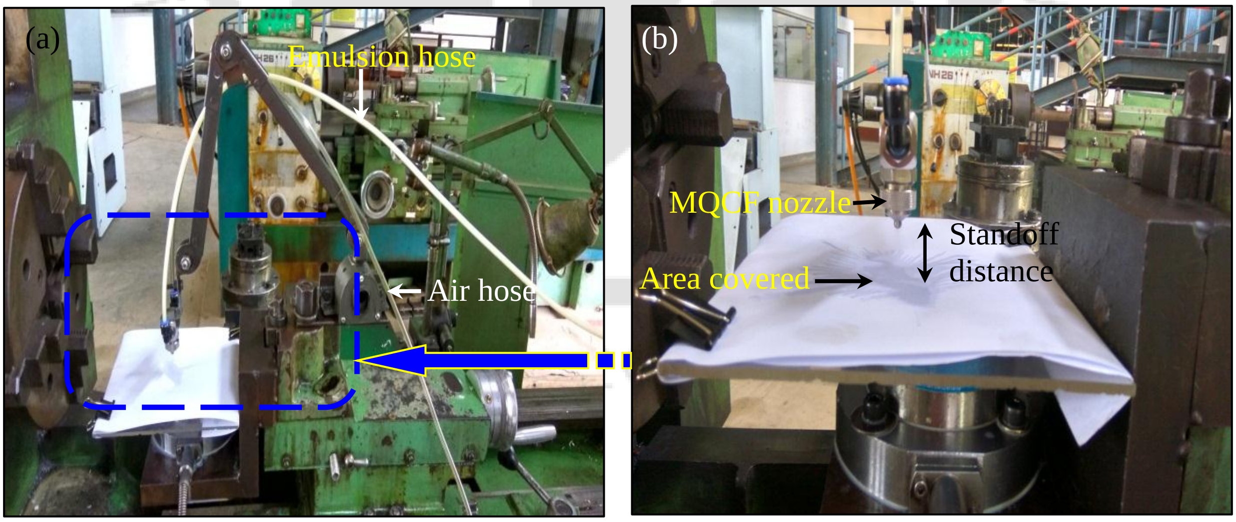

Figure 6.8. (a) Experimental setup for spray area measurement at varying standoff distances and (b) area covered by mist using MQCF technique

An MQCF atomised mist is sprayed onto an acrylic sheet that is fixed adequately over the dynamometer. Figure 6.9 shows the minor axis lengths covered by the MQCF spray nozzle using both cutting fluids at varying standoff distances. From Figure 6.7, it is evident that the minor elliptical axis of the spray should be longer than the minor axis of the machining region (27.15 mm). However, from Figure 6.9, it is observed that at a 30 mm standoff distance, the minor axis covered by all cutting fluids mist is longer than 27.15 mm. Beyond a standoff distance of 30 mm, the exerted spray force gradually decreases. Thus, the optimum standoff distance is 30 mm standoff from the perspective of spray exerted force and corresponding covered area. Figure 6.10 shows images of the area covered by the MQCF spray for both cutting fluids.

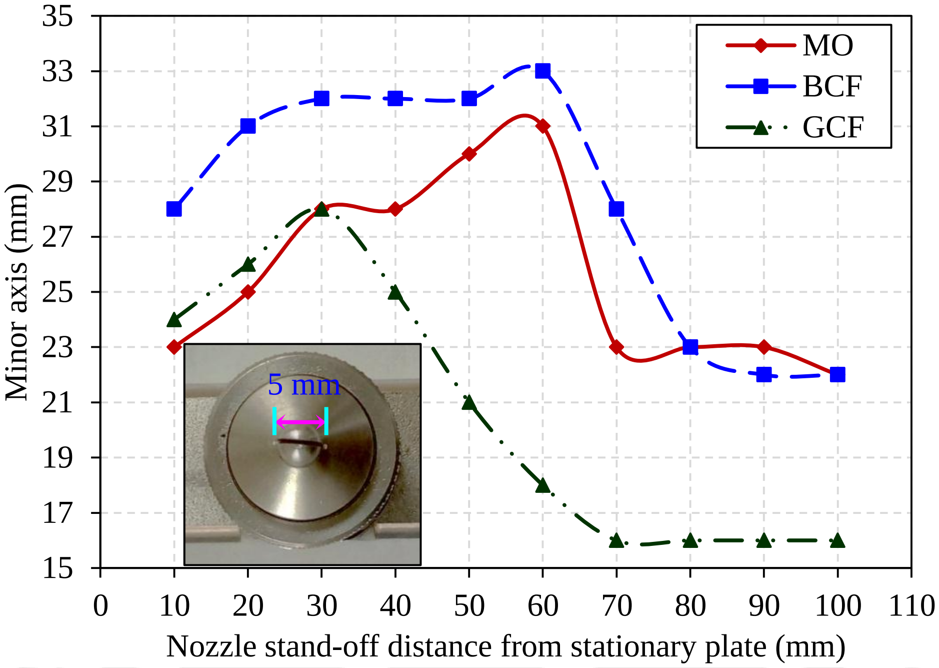

Figure 6.9. Minor axis length covered by spray using minimum quantities of both cutting fluids

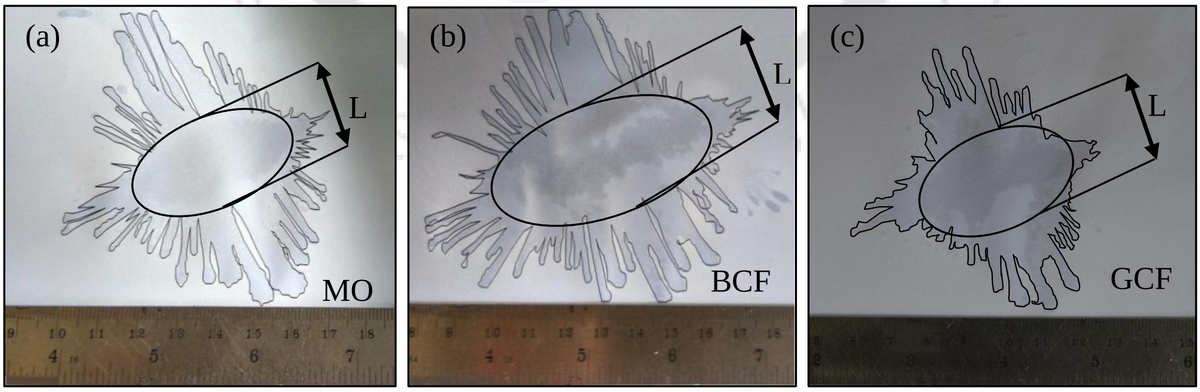

Figure 6.10. Minor axis length (L) covered by MQCF spray nozzle at 10 mm standoff distance for (a) mineral oil, (b) bio-cutting fluid and (b) green cutting fluid

6.3.3 Selection of nozzle spray angular position

Nozzle placement must ensure the easy injection of spray into the machining zone through the penetration of a stiff peripheral air boundary layer, formed on the rotating workpiece. To overcome the influence of surrounding air boundaries on the cutting fluid, researchers have suggested that angular nozzle positions are better than horizontal or vertical positions [185].

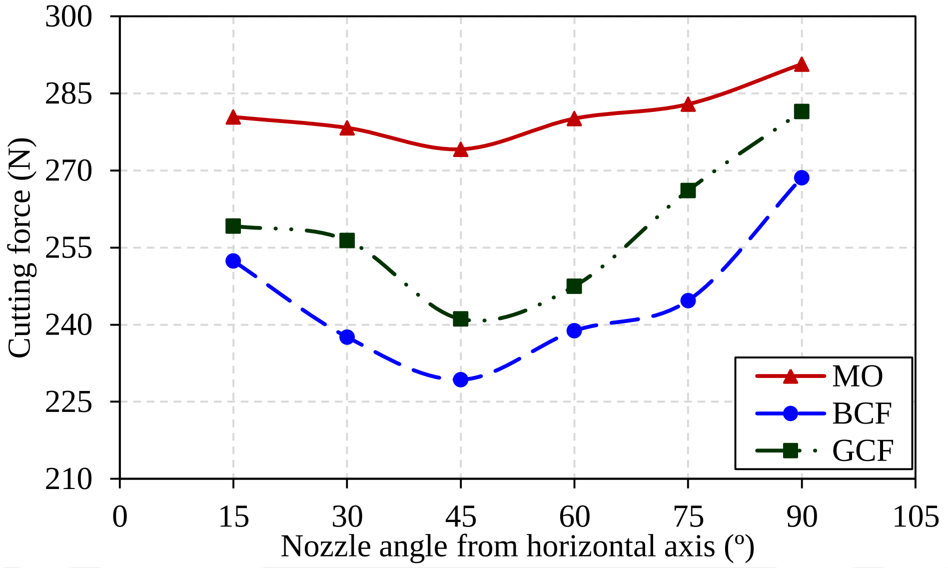

Figure 6.11. Variation of cutting force with nozzle angular position

Figure 6.11 shows the cutting forces for MQCF spray machining using both cutting fluids (1:16 oil to water emulsion concentration ratio) at a standoff distance of 30 mm. Nozzle angular position is varied from 15–90° from the horizontal axis (at 15° intervals). Machining experiments are carried out (*v* = 90 m/min, *f* = 0.16 mm/rev and *d* = 0.5 mm) in order to evaluate the effect of nozzle angle on cutting forces. Initially, with an increase in angle from the horizontal axis, cutting forces are reduced by up to 45°, and begin increasing after 45° (Figure 6.11). At a 15° nozzle angle, spray passes directly over the chip, pushing the chip towards the cutting tool and resulting in an increase in machining forces (Figure 6.12 a). With an increase in nozzle angle position, the MQCF spray can penetrate the stiff peripheral air boundary layer formed on the rotating workpiece, which results in the reduction of cutting forces until an angle of 45°. With further increases in nozzle angle position, cutting forces increases (Figure 6.12 b-e). Figure 6.13 shows a schematic of the MQCF mist and nozzle angle position.

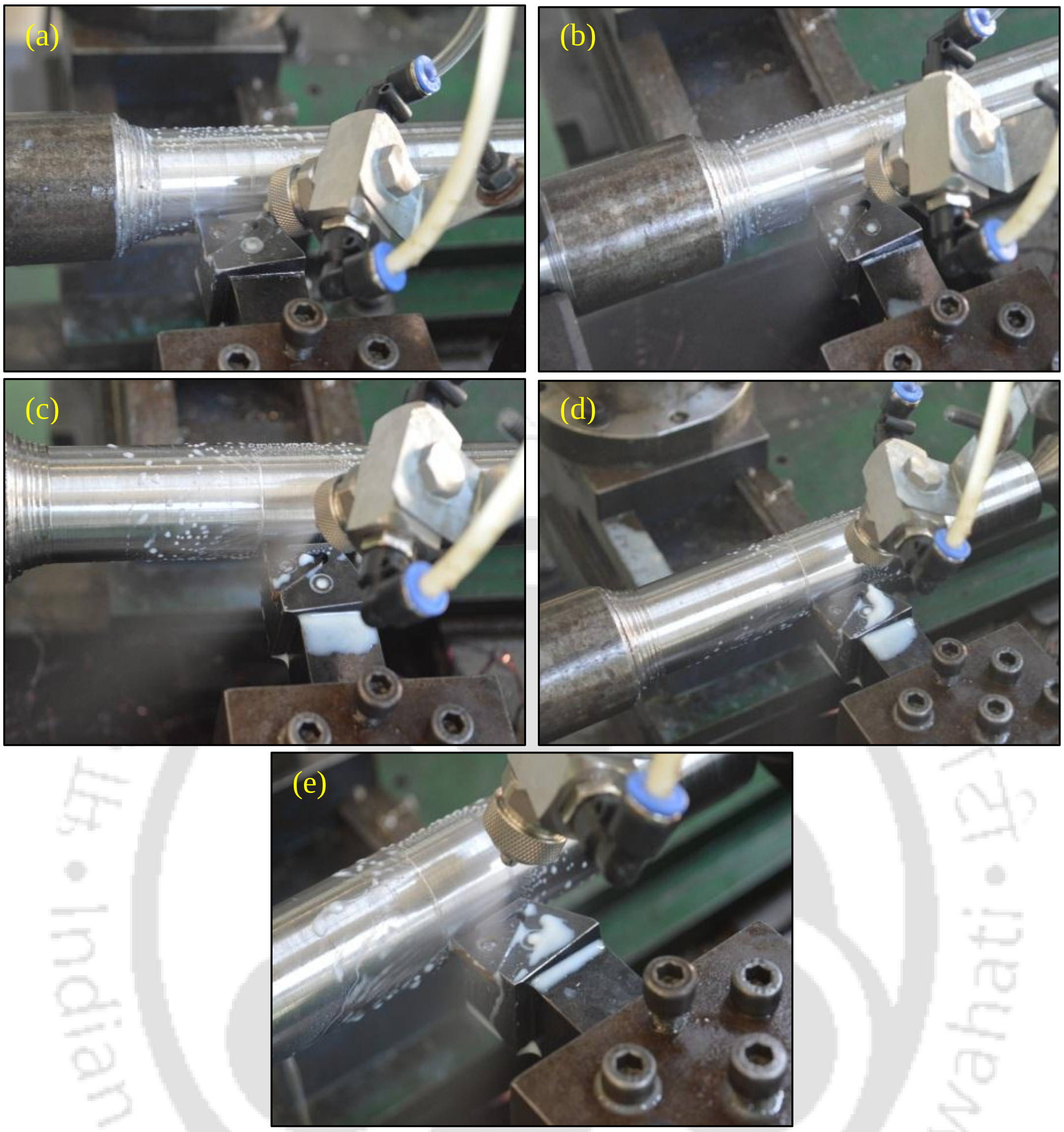

Figure 6.12. Variation of nozzle angle from horizontal axis (a) 15º, (b) 30º, (c) 45º, (d) 60º and (e) 75º

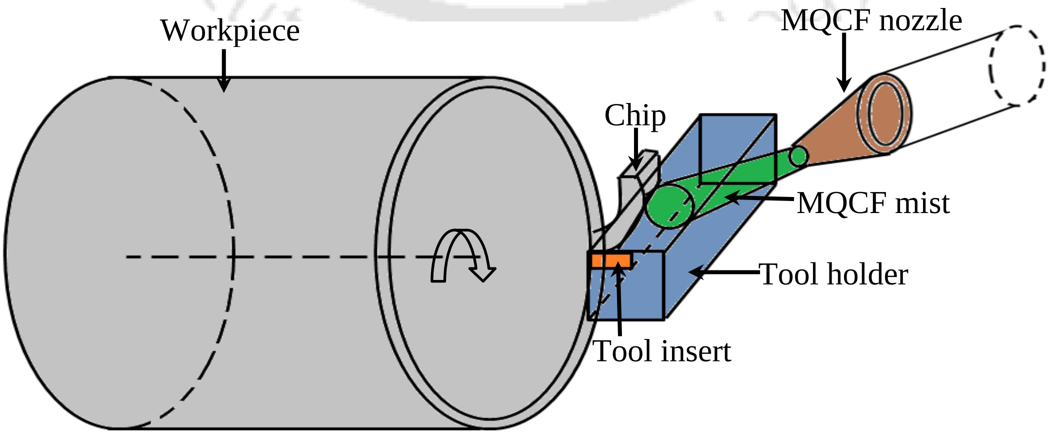

Figure 6.13. Schematic of MQCF mist and nozzle direction

6.3.4 Machining performance

6.3.4.1 Cutting forces

The experiments are carried out according to the central composite rotatable design (CCRD), and the results are analysed using response surface methodology (RSM). Input parameters (feed, cutting speed) and output responses (cutting force) for all types of cutting fluids and application techniques are presented in Table 6.2. Equation models for cutting force per CCRD are given below (Eq. 6.1−6.4).

$$F_{c-DM} = 529.18 + 1302.57f - 7.45v - 2.48vf + 644.81f^2 + 0.03v^2 \quad (6.1)$$

$$F_{c-MO} = -173.37 + 2501.81f + 3.61v - 4.507vf - 2907.17f^2 - 0.016v^2 \quad (6.2)$$

$$F_{c-BCF} = -33.88 + 1415.003f + 1.27v - 0.4125vf - 1116.49f^2 - 0.005v^2 \quad (6.3)$$

$$F_{c-GCF} = -22.79 + 1727.219f + 0.73v - 3.41vf - 975.044f^2 - 0.0003v^2 \quad (6.4)$$

where v, f and F_c represent the cutting speed (m/min), feed (mm/rev) and cutting force (N), respectively, and the subscript of F_c denotes machining environment.

Table 6.2. Complete CCRD table showing input parameters and output responses for hard machining using minimum quantity cutting fluid with three cutting fluids and dry machining

Exp. No	**Feed (mm/rev)**	**Speed (m/min)**	**$F_{c\text{-}DM}$ (N)**	**$F_{c\text{-}MO}$ (N)**	**$F_{c\text{-}BCF}$ (N)**	**$F_{c\text{-}GCF}$ (N)**
1	0.24	115.00	421.73	339.03	302.30	316.13
2	0.16	90.00	324.79	282.60	230.56	243.73
3	0.16	90.00	324.61	280.19	233.78	241.17
4	0.16	125.00	303.72	257.43	241.40	251.03
5	0.28	90.00	464.28	377.17	343.15	366.10
6	0.08	115.00	204.57	172.36	146.80	158.07
7	0.24	65.00	526.83	359.83	295.30	327.51
8	0.16	90.00	322.48	282.73	228.94	240.95
9	0.04	90.00	184.31	94.89	90.01	92.89
10	0.16	55.00	407.31	257.43	211.80	235.47
11	0.16	90.00	323.97	280.13	232.43	245.67
12	0.08	65.00	289.81	157.10	136.50	142.12
13	0.16	90.00	324.82	281.76	232.79	243.56

Table 6.3. ANOVA for cutting force ($F_{c\text{-}BCF}$) for machining using minimum quantity cutting fluid with bio-cutting fluid

Source	*F*-Value	*p*-value Prob>*F*	Percentage contribution
Model	7.14	0.0007	
A-Feed	35.42	0.0081	35.80
B-Speed	15.88	0.0033	16.05
AB	0.11	0.7411	0.11
A^2	34.24	0.0003	34.61
B^2	13.28	0.0041	13.43
Lack of Fit	1.07	0.4366	

Table 6.3 shows the ANOVA for cutting force using MQCF and BCF; the feed is found to have the highest contribution (70.41%), followed by cutting speed (29.48%). The coefficient of determination (R^2) is found to be 0.9763. All CCRD terms are considered in the regression models to improve prediction accuracy. R^2 values for DM and MQCF using all three cutting fluids are also found to be higher than 0.95 for all output responses. This shows good agreement between input parameters and output responses.

Figure 6.14 (a-b) illustrate cutting force components at different feed as well as cutting speeds at a constant cut depth of 0.5 mm. As can be observed from the experimental results, the feed has a profound effect on cutting force. As feed increases, the shear angle decreases, and chip thickness increases. The increase in chip thickness increases the chip load and friction on the tool rake surface. Therefore, the cutting force increases with feed (Figure 6.14 a).

With increasing cutting speed, the tool-workpiece interaction time during machining decreases, but the material removal rate (MRR) increases. Therefore, the temperatures in the primary and secondary shear zones increase. Because of the good thermal conductivity of the workpiece, the probability of preheating adjacent to the machining region increases. Thus, thermal softening of the workpiece surface occurs. Rising temperatures in the secondary shear zone cause the decrease of flow stress in the workpiece material, thereby reducing cutting force with increasing cutting speed (Figure 6.14 b).

After the uniform mixing of the cutting fluid and compressed air in MQCF, the pressurised mist is forcibly injected into the tool-chip interface. The results show that the performance of the MQCF spray is superior to that of DM. As the MQCF method uses a mist, micro-cutting fluid droplets have a better chance of reaching between the tool-chip interface. An MQCF spray containing cutting fluid can penetrate the sliding zone and probably small areas of the sticking zone, because of the high force exerted by the pressurised mist in the tool-chip interface. The penetration force of the MQCF spray is an important parameter affecting machining performance. In machining with MQCF, the mist penetration force, specific heat carrying capacity of the cutting fluid, and coverage area for the BCF mist is higher compared to these properties for the MO and GCF mist. From cutting force results, the cutting fluid mist supplied at the tool-chip interface is considered to prevent chip adhesion. Thus, an MQCF mist with a BCF emulsion shows the smallest cutting force of all investigated systems.

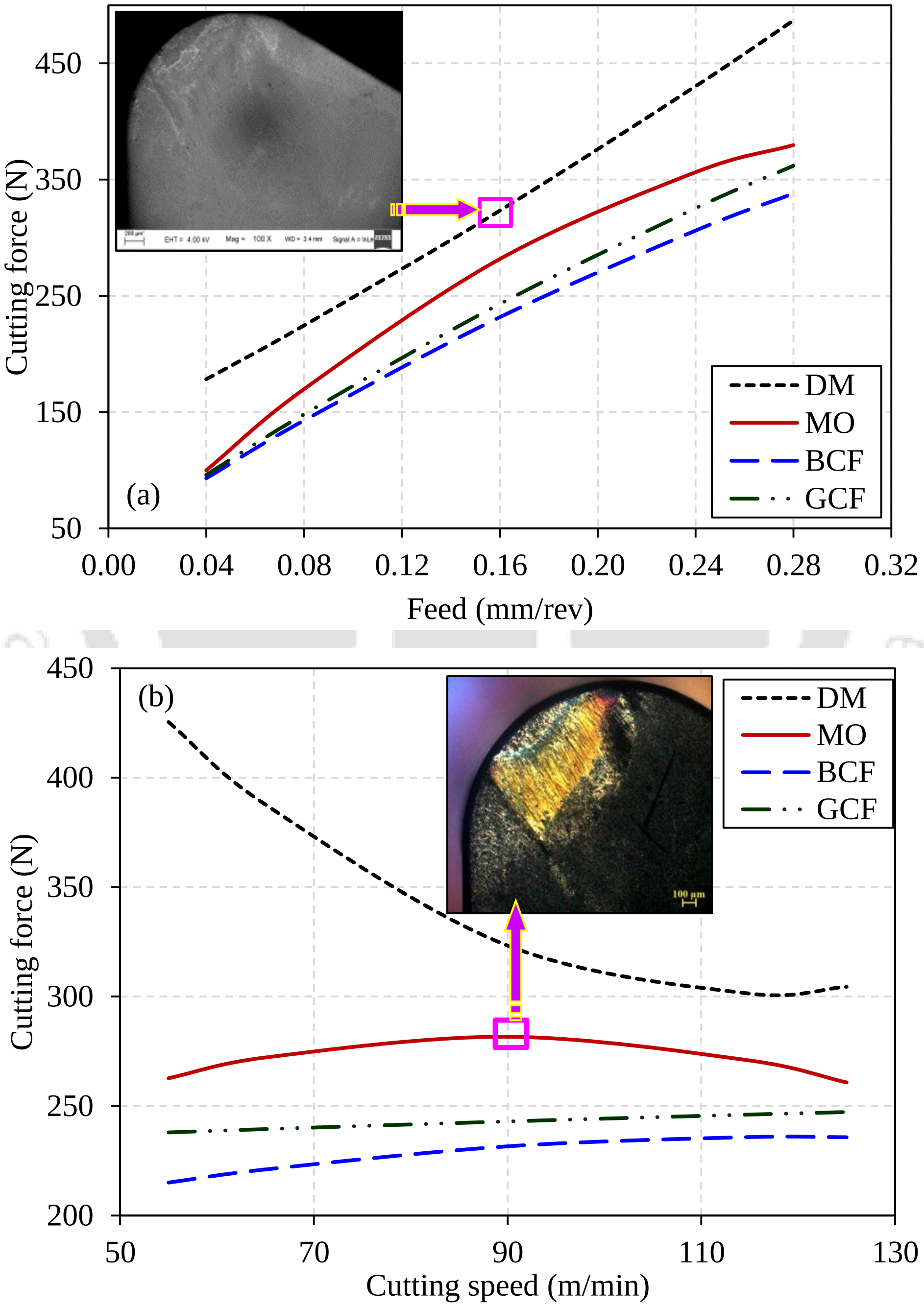

Figure 6.14. Variation of cutting force with (a) feed and (b) cutting speed for various machining environments

6.3.4.2 Feed forces

Response surface methodology models for feed force per CCRD are given below (Eq. 6.5−6.8).

$$F_{f-DM} = 18.61 + 637.72f + 0.55v - 0.695vf - 643.79f^2 - 0.004v^2 \tag{6.5}$$

$$\mathrm{F}_{f-MO} = 3.86 + 357.98f + 0.625v - 0.412vf - 103.05f^2 - 0.0035v^2 \tag{6.6}$$

$$\mathrm{F}_{f-BCF} = 27.98 + 315.97f + 0.27v - 0.655vf - 18.12f^2 - 0.00209v^2 \tag{6.7}$$

$$F_{f-GCF} = 30.31 + 296.28f + 0.408v - 0.307\upsilon f - 4.426f^2 - 0.00315v^2 \tag{6.8}$$

Figure 6.15 (a) shows the variation of feed force with feed for a constant depth of cut (0.5 mm) during machining using MQCF with MO, BCF and GCF emulsions as well as dry machining. As feed increases, the advancement per revolution by the cutting tool increases, i.e. the amount of workpiece material that comes into contact with the cutting tool per unit time increases. Therefore, the load on the tool and thus the feed force increase, irrespective of the cooling technique.

For a constant feed and depth of cut, with increasing cutting speed, feed force reduces as MRR increases (Figure 6.15 b). Increases in MRR leads to increases in temperature, resulting in the thermal softening of the workpiece and reducing the feed force.

Optical micrographs of the cutting tool rake surface after machining using MQCF with MO, BCF and GCF emulsions as well as DM are characterised for a cutting speed of 90 m/min, feed of 0.24 mm/rev, and depth of cut of 0.5 mm, for 15 minutes of machining. Figure 6.16 shows the sticking and sliding zone for various machining environment. The sticking region exhibits full metal to metal contact, and the overall surface has a similar morphology. In contrast, the sliding region exhibits abrasion marks. The sticking and sliding regions are separated by an interface, which is highlighted in Figure 6.16 (a-b). The contact length was measured and tabulated as presented in Table 6.4. It was observed that the sticking and sliding widths for DM were much larger relative to the widths during machining using MQCF.

In MQCF machining, the BCF emulsion performs better than the MO and GCF emulsion; this is confirmed by the least tool-chip contact length (sticking and sliding zone widths) among all four types of machining environment. The average tool-chip contact length on the cutting tool rake surface with MQCF machining using BCF is 843.47 µm, GCF is 874.13 µm, MO is 911.35 µm, whereas that length for DM is 1699.78 µm. A shorter tool-chip contact length results in less contact area, which leads to a reduction in the coefficient of friction. Reductions in coefficient of friction are directly related to lower machining forces and surface roughnesses, because of better cooling and lubrication. Thus, MQCF machining with BCF performs better relative to other combinations.

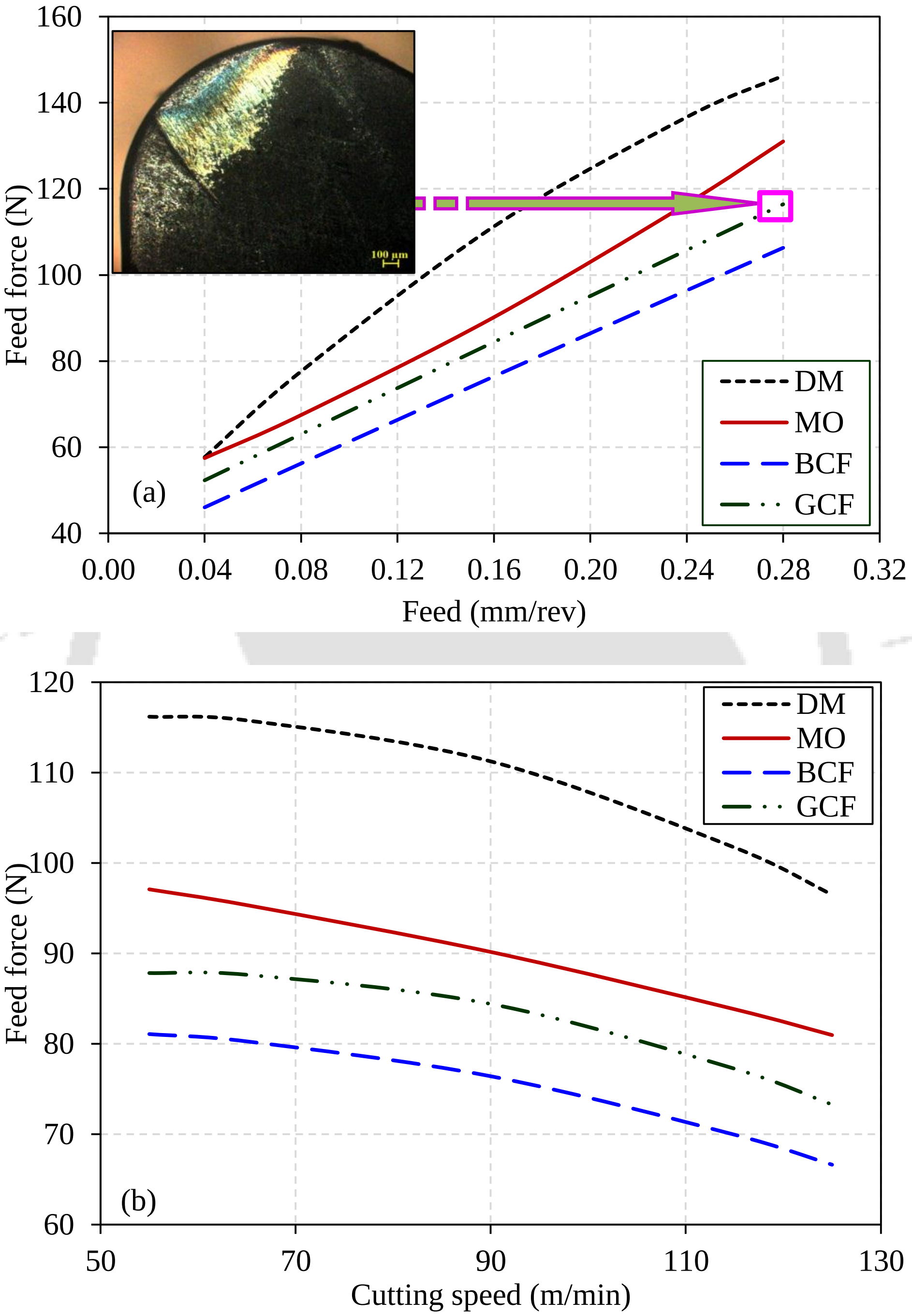

Figure 6.15. Variation of feed force with (a) feed and (b) cutting speed for various machining environments

Table 6.4. Sticking and sliding regions for various machining conditions

Machining condition	Sticking region width (μm)	Sliding region width (μm)
DM	217.4±1.4	1482.4±3.1
MQCF with MO emulsion	179.0±0.4	732.4±1.9
MQCF with BCF emulsion	162.5±0.6	681.0±1.1
MQCF with GCF emulsion	169.9±0.8	704.2±1.6

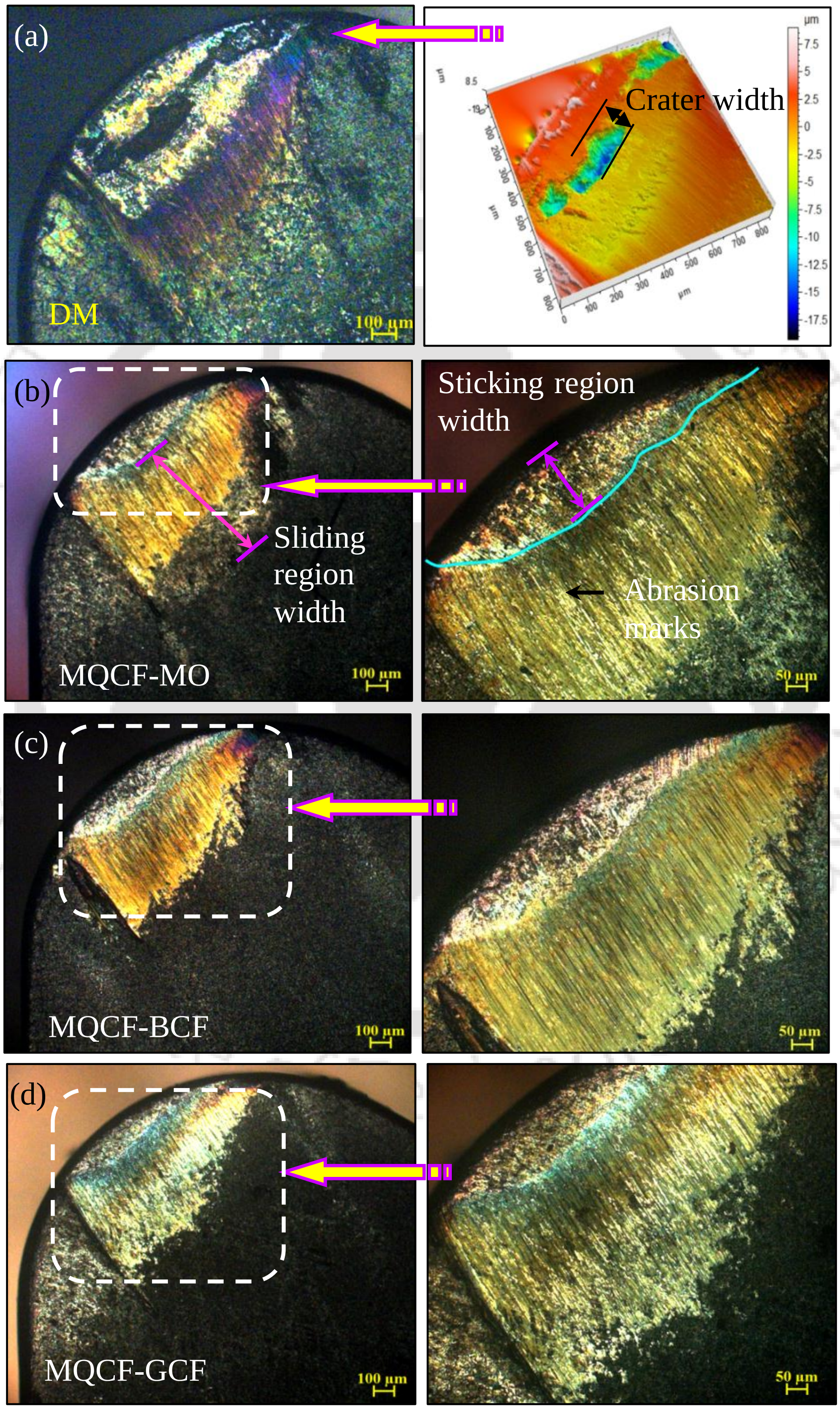

Figure 6.16: Sticking and sliding regions of the tool-chip interface during (a) dry machining, machining using (b) mineral oil, (c) bio-cutting fluid and (d) green cutting fluid

6.3.4.3 Tool-chip interface coefficient of friction

The average coefficient of friction at the tool-chip interface is calculated by:

$$\mu = \tan\left(\alpha\right) = \tan(\lambda + \tan^{-1}(F_f / F_c)) \tag{6.9}$$

where α is the rake angle, λ is the friction angle, F_f is the feed force, and F_c is the cutting force. Figure 6.17 illustrates the average coefficient of friction at the tool-chip interface for DM and MQCF (using MO and BCF). The frictional force at the tool-chip interface depends on the tool-chip contact length. MQCF spray penetrates the tool-chip interface and reduces the contact area by providing both lubrication and cooling, resulting in the reduction of friction coefficients.

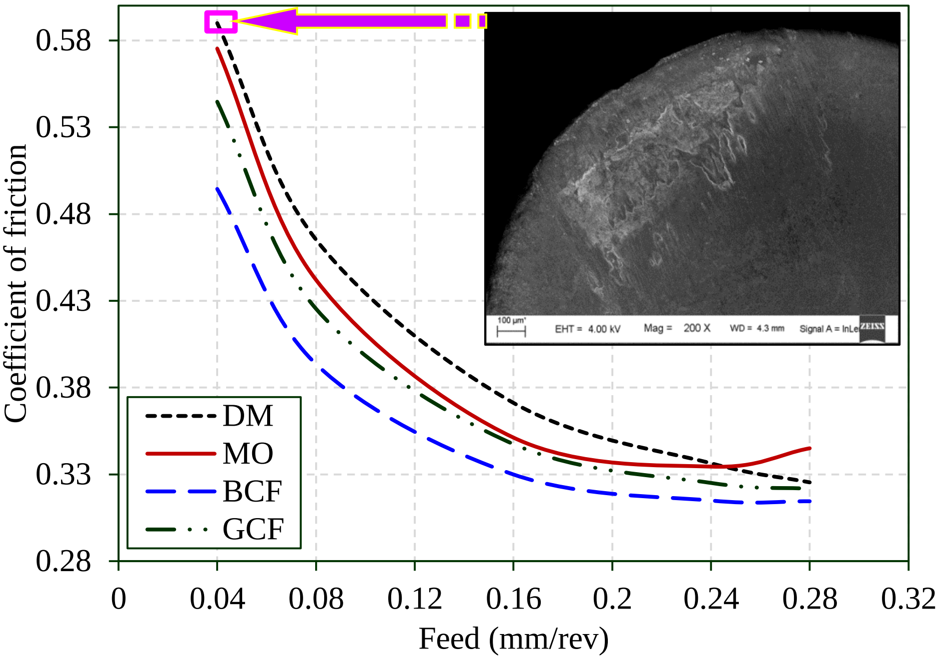

Figure 6.17. Variation of the coefficient of friction with feed for various machining environments

For MQCF using a BCF emulsion, a minimum coefficient of friction is observed, resulting from the maximum penetration force, higher specific heat, and larger spray coverage area. Figure 6.18 shows the tool rake surface morphology after 15 minutes of MQCF machining using three cutting fluids and DM (cutting speed = 90 m/min, feed = 0.16 mm/rev and depth of cut = 0.5 mm).

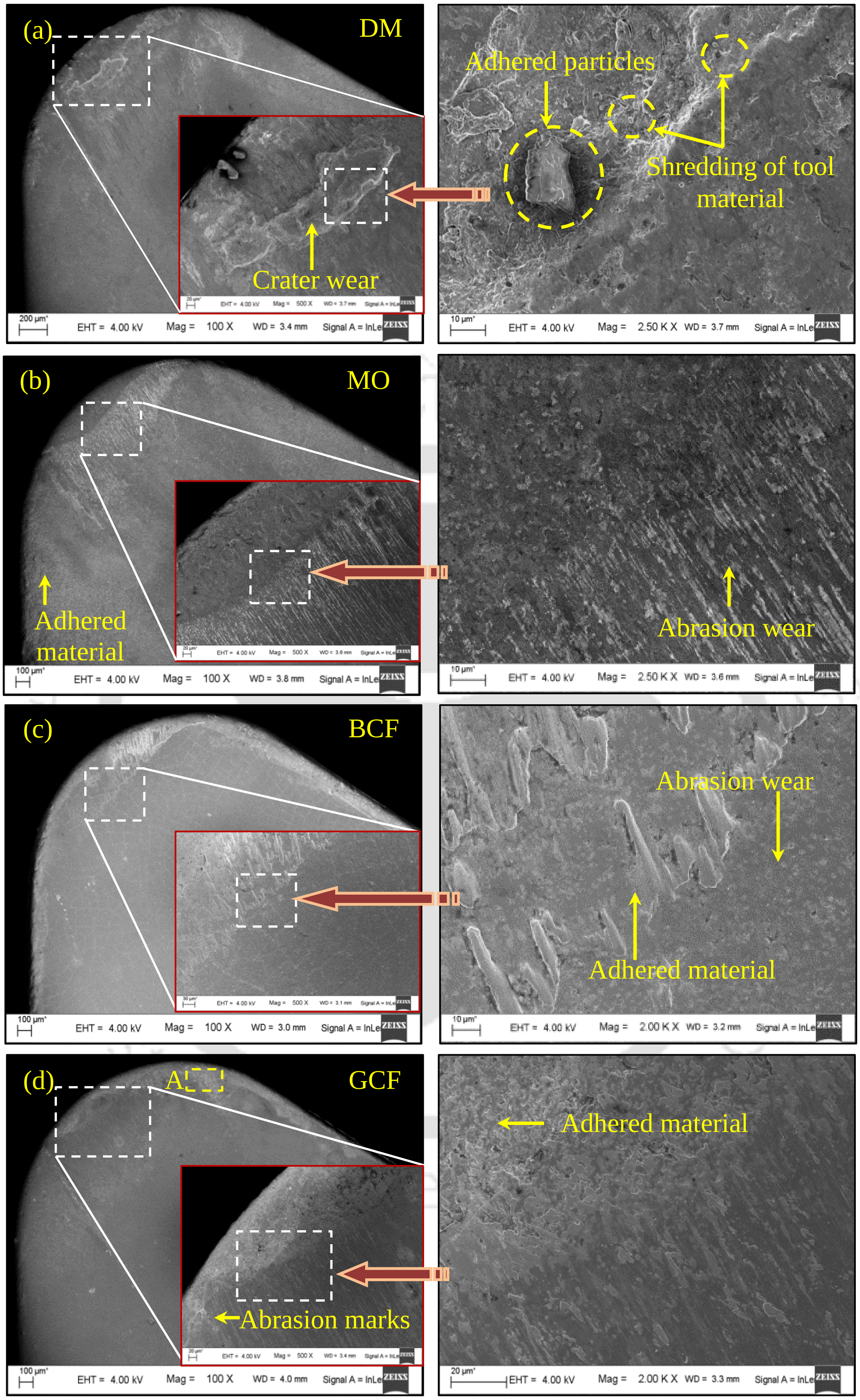

Figure 6.18. Cutting tool rake surface morphology showing tool-chip interface during (a) dry machining, machining using (b) mineral oil, (c) bio-cutting fluid and (d) green cutting fluid showing crater, adhesion and abrasion wear

In the case DM, more severe crater wear to the cutting tool rake surface is observed (Figure 6.18 a). Also, adhered particles and shredding to tool material are also witnessed. However, for machining with MQCF, only adhesion and abrasion wear to the tool rake surface occurs (Figure 6.18 b-d). It occurs because of the high-pressure MQCF mist, which easily flushes away chip debris particles and does not allow the material to stick to the cutting tool rake surface. MQCF sprays provide proper cutting tool cooling that reduces adhesion due to rising temperatures. It also lubricates the tool-chip interface, thereby avoiding any built-up edge formation.

Among cutting tool rake surface after machining using MQCF with three different cutting fluids, the maximum abrasion wear is observed in the case of MO, which is a symptom of high coefficient of friction (Figure 6.18 b). However, less abrasion wear is seen with MQCF using BCF and GCF (Figure 6.18 c-d). MQCF machining with BCF and GCF also shows lower machining forces and less tool-chip contact length. Reductions in the tool-chip contact length reduce the tool-chip contact area, which in turn leads to less heat generation and lower friction coefficients.

Figure 6.19 shows the elemental composition of the adhered material (Area A; Figure 6.18 d), which is similar to the composition of the workpiece material. This evidence supports the adhesion of workpiece material to the cutting tool rake surface.

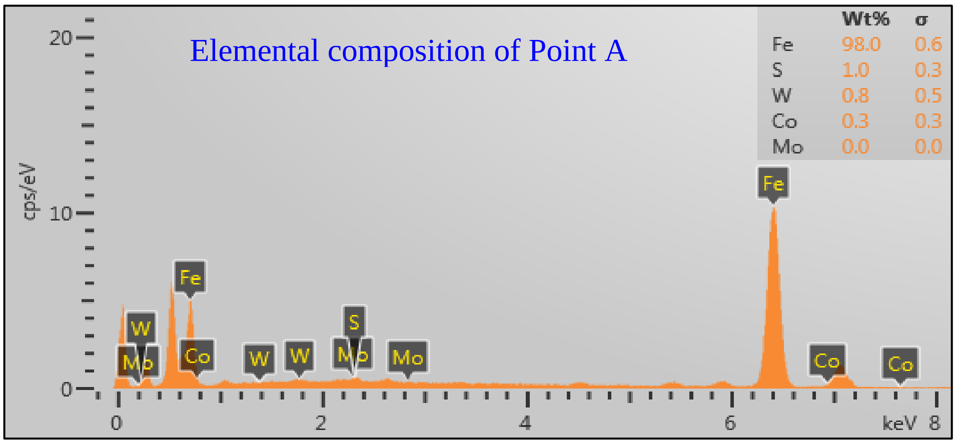

. **Figure 6.19.** Elemental composition of cutting tool rake surface at adhered material location (corresponding to Point A; Figure 6.19 d)

6.3.4.4 Workpiece surface roughness

The surface roughness of a machined product is an important machinability index. Equation models for workpiece surface roughness (per RSM of CCRD) are as follows (Eq. 6.10−6.13):

$$R_{a-DM} = 1.3231 + 4.439\,f - 0.00291v + 0.055vf + 30.39\,f^2 + 0.000076v^2 \tag{6.10}$$

$$R_{a-MO} = 1.247 + 3.27\,f - 0.0142v - 0.0078vf + 33.87\,f^2 + 0.0000763v^2 \tag{6.11}$$

$$R_{a-BCF} = 1.09 + 2.402\,f - 0.013v - 0.0032vf - 26.05\,f^2 + 0.0000715v^2 \tag{6.12}$$

$$R_{a-GCF} = 1.22 + 2.69\,f - 0.015v - 0.0036vf + 29.28\,f^2 + 0.00008v^2 \tag{6.13}$$

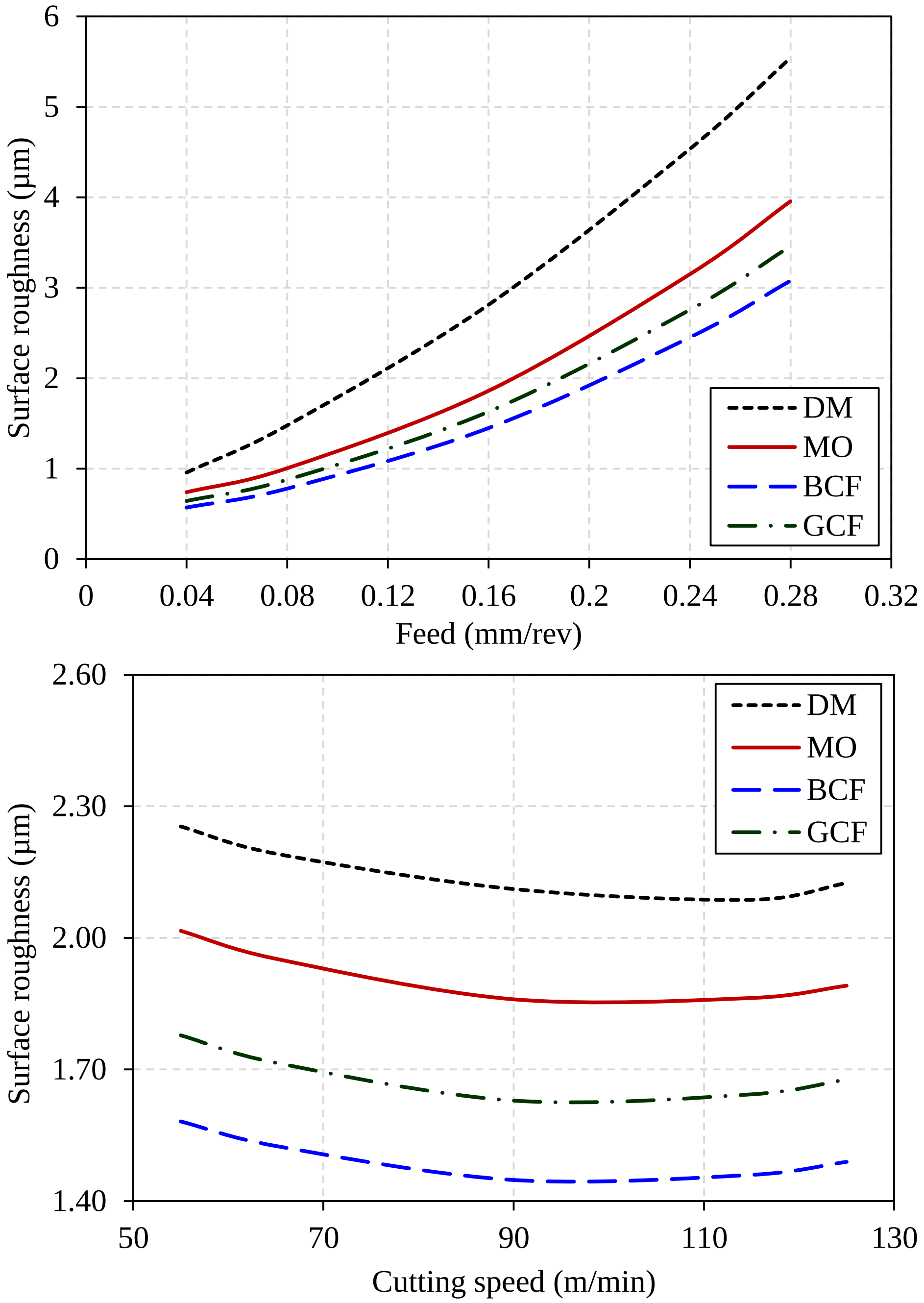

Figure 6.20. Variation of workpiece surface roughness with (a) feed and (b) cutting speed for various machining environments

Figure 6.20 (a-b) shows variations in workpiece surface roughness with feed and cutting speed. Workpiece surface roughness is observed to increase with increasing feed, irrespective of the cutting fluid application technique. In the case of DM, because of tool crater wear and high friction at the tool-chip interface, the workpiece has a higher surface roughness. Workpiece surface roughness is lower when machined with MQCF, because of lower cutting and feed forces. It may cause comparatively less tool chatter, leading to better surface finishes, i.e. low surface roughness. From the experimental results, cutting force, feed force, coefficients of friction and workpiece surface roughnesses are reduced with MQCF (for all three cutting fluids) relative to DM due to cooling and lubrication properties. Among three cutting fluids, BCF produces better results than MO and GCF.

6.4 Findings from the research work

In this Chapter, an indigenous MQCF setup was developed. MQCF input parameters were optimised. Machining experiments were carried out with DM and MQCF using three cutting fluids (MO, BCF and GCF). The salient findings are as follows:

- 1:16 emulsion composition was found to be optimum in terms of its better thermal conductivity, specific heat as well as its storage stability as per ASTM D 3707 standard.
- 30 mm MQCF nozzle stand-off distance was found to be optimum by considering mist coverage region and cutting forces exerted by mist at tool-chip interface.
- With 45° nozzle angle, MQCF mist could penetrate better into the air boundary periphery that is generated by the rotating workpiece.
- Relative to DM, machining with MQCF (using all three cutting fluid emulsions) produced better results in terms of the cutting force, feed force, coefficient of friction, and workpiece surface roughness.
- The BCF emulsion performed better than MO and GCF, in terms of its higher thermal conductivity, high specific heat, and better ability to penetrate the tool-chip interface.
- Sticking and sliding zones were reduced in the case of MQCF machining. The BCF emulsion performed better than the MO and GCF emulsion in this regard.

Chapter 7

Performance of Molybdenum Disulphide and Calcium Fluoride based Nano-Green Cutting Fluids

- **7.1 Introduction to nano-cutting fluids**
- **7.2 Nano-solid lubricant enhanced green cutting fluids**
  - 7.2.1 Preparation of nano-green cutting fluids
  - 7.2.2 Characterization of nano-green cutting fluids
    - 7.2.2.1 Dispersion test
    - 7.2.2.2 Thermal conductivity and specific heat capacity test
    - 7.2.2.3 Rheological study
  - 7.2.3 Wetting angle measurements
  - 7.2.4 Materials and machining experiments
- **7.3 Results and discussion**
  - 7.3.1 Dispersion stability of the nano-green cutting fluids
  - 7.3.2 Thermal conductivity and specific volumetric heat capacity of the nano-green cutting fluids
  - 7.3.3 Viscosity of the nano-green cutting fluids
  - 7.3.4 Surface wettability by water and cutting fluids
  - 7.3.5 Machining experiments
    - 7.3.5.1 Effect of various cutting fluids on cutting force, feed force and coefficient of friction
    - 7.3.5.2 Workpiece surface roughness
- **7.4 Findings from the research work**

In **Chapter 7**, MoS_2 and CaF_2 based nano-green cutting fluids with varying concentration are prepared. The effect of the nano-solid lubricant (MoS_2 nanosheet and CaF_2 nanoparticles) enhanced cutting fluids are studied by conducting absorbance tests, dynamic viscosity tests, thermal conductivity tests, volumetric specific heat test and wettability test. Afterwards, hard machining experiments are carried out to evaluate the performance of nano-solid lubricant enhanced GCF using MQCF technique.

7.1 Introduction about nano-cutting fluid

In Chapter 6, minimum quantity cutting fluid (MQCF) machining using BCF showed lower cutting force, feed force, tool-chip interface coefficient of friction and workpiece surface roughness as compared to GCF and MO-based cutting fluids during machining of hardened AISI H-13 steel. However, due to very high heat generation during hard machining, the effectiveness of MQCF and GCF needs further improvement.

Solid lubricants such as molybdenum disulphide (MoS_2), calcium fluoride (CaF_2), tungsten disulphide (WS_2), etc. are previously used as coating materials or filling micro-reservoirs for reducing friction between sliding surfaces. Studies also reported the reduction of machined surface roughness and cutting forces in the machining tests [186]. Moreover, nano-sized solid lubricants have the ability to act as an additive for cutting fluids to reduce generated heat further and to improve the effectiveness of MQCF during hard machining. Furthermore, nano-sized lubricants can easily penetrate into the machining sliding region, and due to the small size, it can try to reach into the sticking region with the help of high pressurised aerosol (MQCF). Figure 7.1 illustrates the machining region with sticking and sliding zones on the cutting tool rake surface.

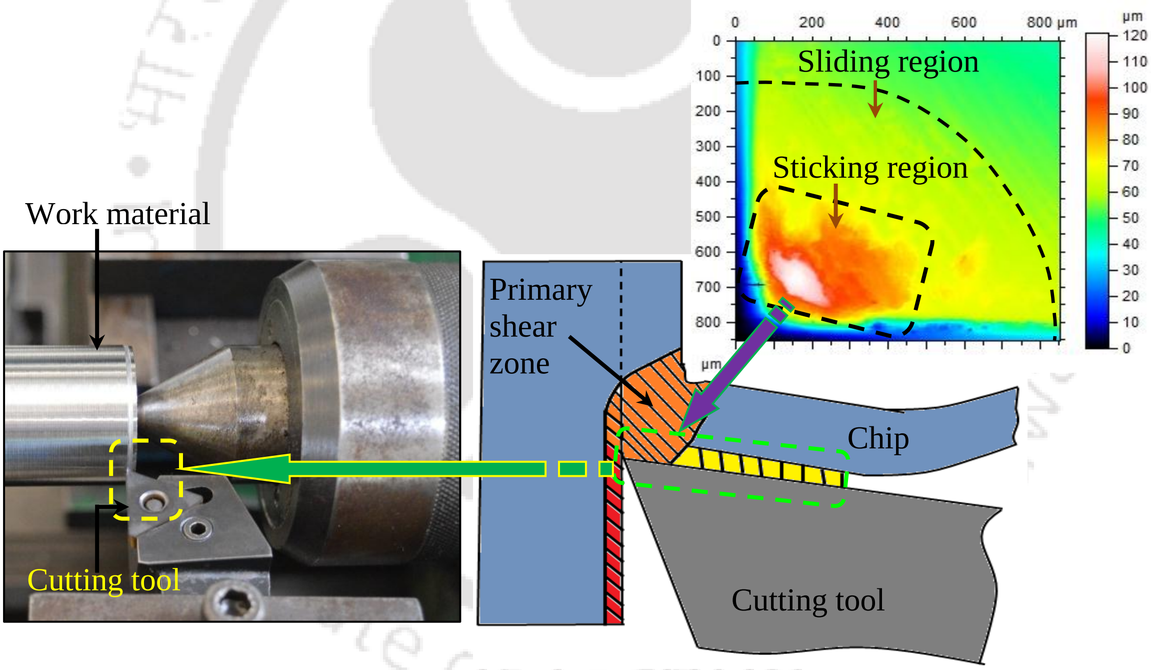

Figure 7.1. Overview of machining region showing sticking and sliding zones on the cutting tool rake surface

Nano-solid lubricants such as MoS_2 and CaF_2 can enhance thermal conductivity, specific heat and lubricating properties of cutting fluid. Also, nano-size solid lubricants are economical as compared to metal-based nanoparticles. In this work, the effect of the nano-solid lubricant (MoS_2 nanosheet and CaF_2 nanoparticles) enhanced cutting fluids was studied by conducting absorbance tests, dynamic viscosity tests, thermal conductivity tests, volumetric specific heat test, wettability test and hard machining tests during turning of hardened AISI H-13 steel. First, the absorbance test was conducted to ensure proper dispersion of various concentrations of solid lubricants in indigenous formulated green cutting fluid (GCF). Second, viscosity, thermal conductivity, and the volumetric specific heat of various nano-cutting fluids were measured to determine the optimum concentration of solid lubricants in GCF. Third, wetting angle with various cutting fluid on the cutting tool surface was measured to check wettability. Afterwards, hard machining experiments were carried out to evaluate the performance of nano-solid lubricant enhanced GCF using MQCF technique in terms of cutting force, feed force, tool-chip interface coefficient of friction and machined workpiece surface roughness. For comparison, machining tests are also carried out using GCF, BCF and MO-based cutting fluid. The evaluating responses are cutting force, feed force, tool-chip interface coefficient of friction and workpiece surface roughness.

7.2 Nano-solid lubricant enhanced green cutting fluids

MoS_2 nanosheets and CaF_2 nanoparticles, supplied by Loba Chemie, were mixed with GCF to develop nano-enhanced cutting fluid. Highly biodegradable eco-friendly vegetable-based GCF was developed indigenously (Chapter 5).

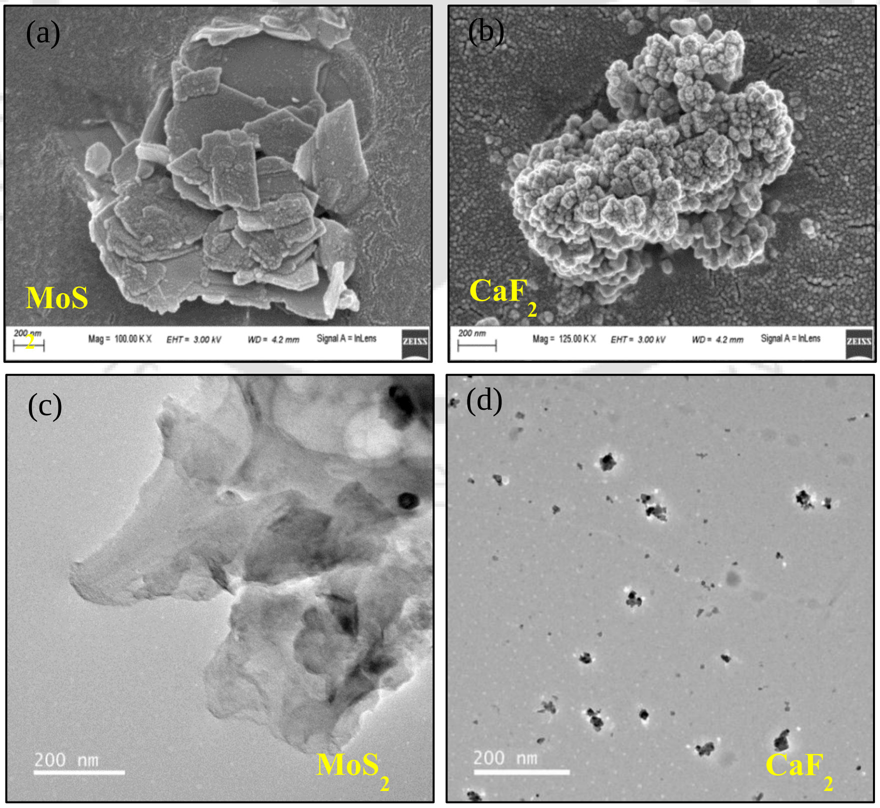

Figure 7.2. Surface micrograph of (a) MoS_2, (b) CaF_2 and transmission electron micrograph of (c) MoS_2, (d) CaF_2

Figure 7.2 illustrates the surface morphology of commercial MoS_2 nanosheets and CaF_2 nanoparticles used in this work. In procured specimen, most of the particles were found to be in the agglomerated condition that is a common phenomenon with nanopowders. It is due to the high surface tension of nanoparticles. Therefore, high-frequency ultra-sonication is required while preparing nano-GCFs. The diameters of MoS_2 nanosheets are in the range of 50−300 nm (Figure 7.2 a). The average particle size of CaF_2 is 15−40 nm (Figure 7.2 b). The transmission electron micrograph of nano-size MoS_2 and CaF_2 are shown in Figure 7.2 (c-d).

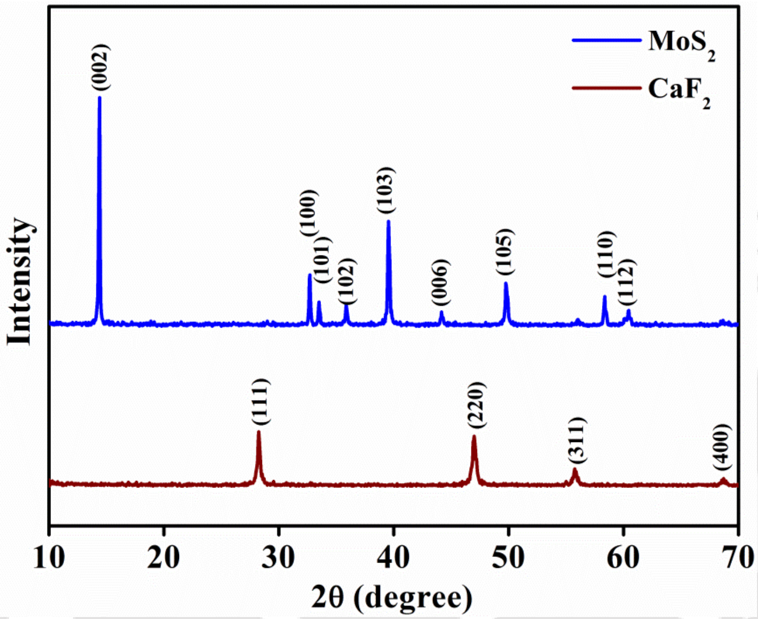

Figure 7.3. X-ray diffraction pattern of MoS_2 and CaF_2 solid lubricants

Figure 7.3 illustrates the phase composition of commercial MoS_2 nanosheets and CaF_2 nanoparticles which were characterised using X-ray diffractometry (XRD, Make: Bruker, Model: D8 Advance). The phase analysis of the CaF_2 reveals peaks at 28.3º (111), 47.1º (220), 55.9º (311) and 68.9º (400). Peaks at similar 2θ were also observed by Toulemonde et al. (2012) for the XRD pattern of virgin CaF_2 [187]. The phase analysis of the MoS_2 reveals peaks at 14.35º (002), 32.7º (100), 33.5º (101), 35.85º (102), 39.55º (103), 44.15º (006), 49.75º (105), 58.35º (110) and 60.45º (112). Peaks at similar 2θ were also observed by Hu et al. (2012) [188].

7.2.1 Preparation of nano-green cutting fluids

Green cutting fluid with 1:16 (1 part oil and 16 part water) emulsion composition was selected based on the previous results (Chapter 6) due to its superior thermal conductivity and specific volumetric heat.

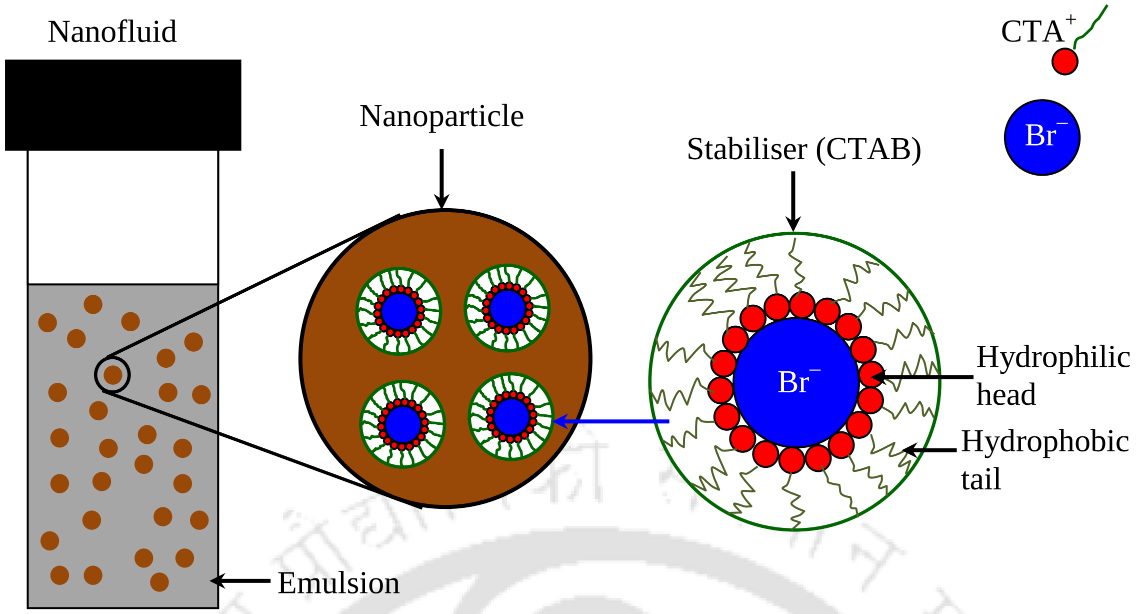

Figure 7.4. Schematic of nano-fluids and stabiliser

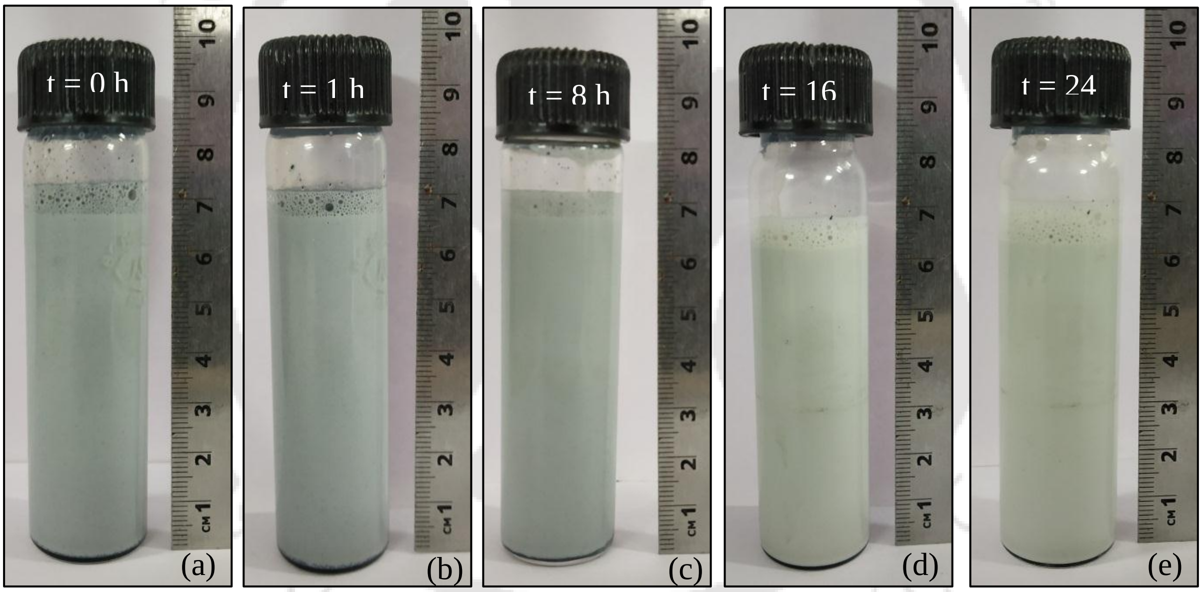

Figure 7.5. MoS_2 nano-fluid with 0.3 % volume fraction after (a) 0h, (b) 1h, (c) 8h, (d) 16h and (e) 24h after sonication

Five different concentration (0.1−0.5 %, with 0.1 % increment) of both MoS_2 and CaF_2 solid lubricants were used to developed nano-fluids. Two steps method was used for developing nano-fluids. First, a mixture of nanoparticles and GCF was ultra-sonicated in a sonicator (Make: Buehler®, Model: 75-2003-220) for 60 minutes. Afterwards, it was stirred using a magnetic stirrer (Make: Abdos®, Model: MS-H280-Pro) at 600 rpm for 45 minutes. Both steps were repeated multiple times until consistent dispersion of nanoparticles in the

GCF was observed. The appearance of MoS_2 and CaF_2 based developed nano-fluid is greyish and whitish, respectively. Figure 7.4 illustrates schematic of nano-fluid as well as a stabiliser. Figure 7.5 shows MoS_2 based developed nano-fluid with 0.3 % volume fraction after 0h (just after sonication), 1h, 8h, 16h and 24h after sonication.

7.2.2 Characterization of nano-green cutting fluids

7.2.2.1 Dispersion test

Monochromatic light of fixed wavelength absorbance in the UV range with respect to reference beam relates the absorbance magnitude. Spectral UV rays absorbance indicates the amount of light absorbed by the sample (cutting fluid) of a fixed length. Absorbance is directly proportional to the concentration of matter in the sample. In this study, different concentrations of nanoparticles in GCF were tested for absorbance to ensure its suspension stability. Proper dispersion of nanoparticles in cutting fluid is one of the foremost requisite for the development of nano-fluid. Each nano-green cutting fluid (nano-GCF) was tested for dispersion of nanoparticles with varying concentration using UV spectroscopy (Make: Varian® Model: Cary 50). Initially, 1:250 dilution samples for each nano-GCF was prepared and filled in a cuvette to find out the wavelength for dispersion test using UV spectroscopy. Further, absorbance at that particular wavelength of UV rays was used for dispersion test of nano-fluids to check suspension stability of nanoparticles.

7.2.2.2 Thermal conductivity and specific heat capacity test

The nano-GCFs heat extraction capacity usually depends upon its thermal conductivity and specific heat capacity. Therefore, nano-GCFs were also tested for its thermal conductivity and specific heat. KD2 Pro thermal properties analyser was used to determine these properties. Analyser works on the principle of the transient line heat source (transient hot wire) for measurement of thermal conductivity. The analyser has a needle attached to a heater and temperature sensor. The needle was fully immersed in nano-fluid (30 ml, each sample). Heater passes the current and the sensor monitor the temperature of nano-fluid through which the analyser obtained thermal conductivity as well as specific heat capacity. The thermal conductivity of nano-GCF is shown as follow:

$$k = \left[\frac{q}{4\pi(\Delta \mathrm{T}_2 - \Delta \mathrm{T}_1)}\right] \ln\left(\frac{t_2}{t_1}\right) \tag{7.1}$$

where k represents the thermal conductivity, q represents the heat flux, t_1 and t_2 represent the initial and final temperature.

7.2.2.3 Rheological study

The lubrication property of nano-GCFs depends upon its viscosity. Therefore, shear viscosity of nano-fluids as a function of temperature was measured using a rheometer (Make: Anton Paar®, Model: MCR-101) with coaxial cylindrical tool master (Figure 5.2, Chapter 5). 7 ml sample volume was tested for each nano-GCF. Measurements were carried out by the linear increase in temperature from 20−100ºC at the constant shear rate of 100 s^{-1}.

7.2.3 Wetting angle measurement

When a droplet of liquid (cutting fluid) resting on the solid surface create an interface, the angle between a droplet and the contact surface outline is known as wetting (contact) angle. Its wetting angle evaluates the wetting ability of the cutting fluids on the cutting tool surface. A liquid droplet with low surface tension on high energy solid forms a spherical shape gives a low wetting angle, which is considered to have better wettability. Wetting angle measurements were carried out for five different fluids such as water, MO emulsion, GCF emulsion, nano-GCF emulsion with 0.3 % concentration of CaF_2 (GCF-0.3C) and nano-GCF emulsion with 0.3 % concentration of MoS_2 (GCF-0.3M) using contact angle goniometer (Make: Holmarc®, India, Model: HO-IAD-CAM-01B). Cutting fluid droplets of 2 µl volume were kept for the residence time of 15 s on the cleaned cutting tool surface, and the contact angle was measured from the optical image.

7.2.4 Materials and machining experiments

Experiments are carried out using the same workpiece and cutting tool materials with same experimental setup as shown in Chapter 6. However, machining experiments were performed for an MQCF environment with nano-fluids (GCF-0.3C and GCF-0.3M). For comparison, experiments were also carried out using GCF, BCF and MO. Machining conditions are shown in Table 7.1.

Table 7.1. Machining conditions

Input	Value
Cutting speed	90 m/min
Feed	0.28 mm/rev
Depth of cut	0.5 mm
Machining environment	MQCF, MQCF with nano fluids
Cutting fluids	MO, BCF, GCF, GCF-0.3C, GCF-0.3M
Oil flow rate	35 mL/hr
Air pressure	0.5 MPa (5 bar)
MQCF nozzle standoff distance	30 mm
MQCF nozzle angle	45°

7.3 Results and discussion

In this section, dispersion, thermal conductivity, specific heat, viscosity and wettability of nano-cutting fluids are discussed. Experimentally optimised MoS_2 and CaF_2 based nano-GCFs were selected. Hard machining performance using cutting fluids under MQCF environment was carried out during machining of hardened AISI H-13 steel. For comparison, experiments were also performed using GCF, BCF and MO. All tests are replicated thrice, and average values are discussed.

7.3.1 Dispersion stability of the nano-green cutting fluids

Proper dispersion of nanoparticles in cutting fluids is a challenging task. Nano-scale size of particles tends to suspend and agglomerate. Therefore, surfactants are generally used to break down the agglomerated particles as well as dispersed it properly by hydrophobic surface forces and electrostatic repulsive forces because of the physical adsorption of surfactants in nano-fluids [189]. 0.01−0.02 % (by volume) of cetyltrimethylammonium bromide (CTAB) was used as surfactants to achieve uniform dispersion and better stability of nano-fluids [190]. Figure 7.6 (a) shows the variation of absorbance with respect to wavelength for nano-fluids. At 254 nm a sharp peak is observed, which indicates the wavelength for dispersion test. Figure 7.6 (b) illustrates the effect of concentration of solid lubricants on absorbance, which indicates the dispersion of nanoparticles in GCF for this study. Absorbance for clear-cutting fluids without any nanoparticles is 0.0852 (Figure 7.6 b). However, with the increase in the concentration of nanoparticles the absorbance value also increases until saturation point (0.3 %). It indicates the proper dispersion of nanoparticles up to saturation point in the cutting fluids. Saturation of absorbance with the increase in nanoparticle concentration possibly has two reasons. First is due to the addition of limited surfactant (only 0.01−0.02 %), which is not enough for full dispersion of nanoparticles, if present in the higher amount. The quantity of surfactant cannot be increased further because it affects properties of nano-GCFs [190]. Another reason is due to sedimentation of nanoparticles with the increase in its concentration. Sedimentation of nanoparticles was also observed during experimentation for 0.4 % and 0.5 % concentration of nano-fluids. Therefore, 0.3 % concentration of solid lubricant nanoparticles can be successfully dispersed in the GCF.

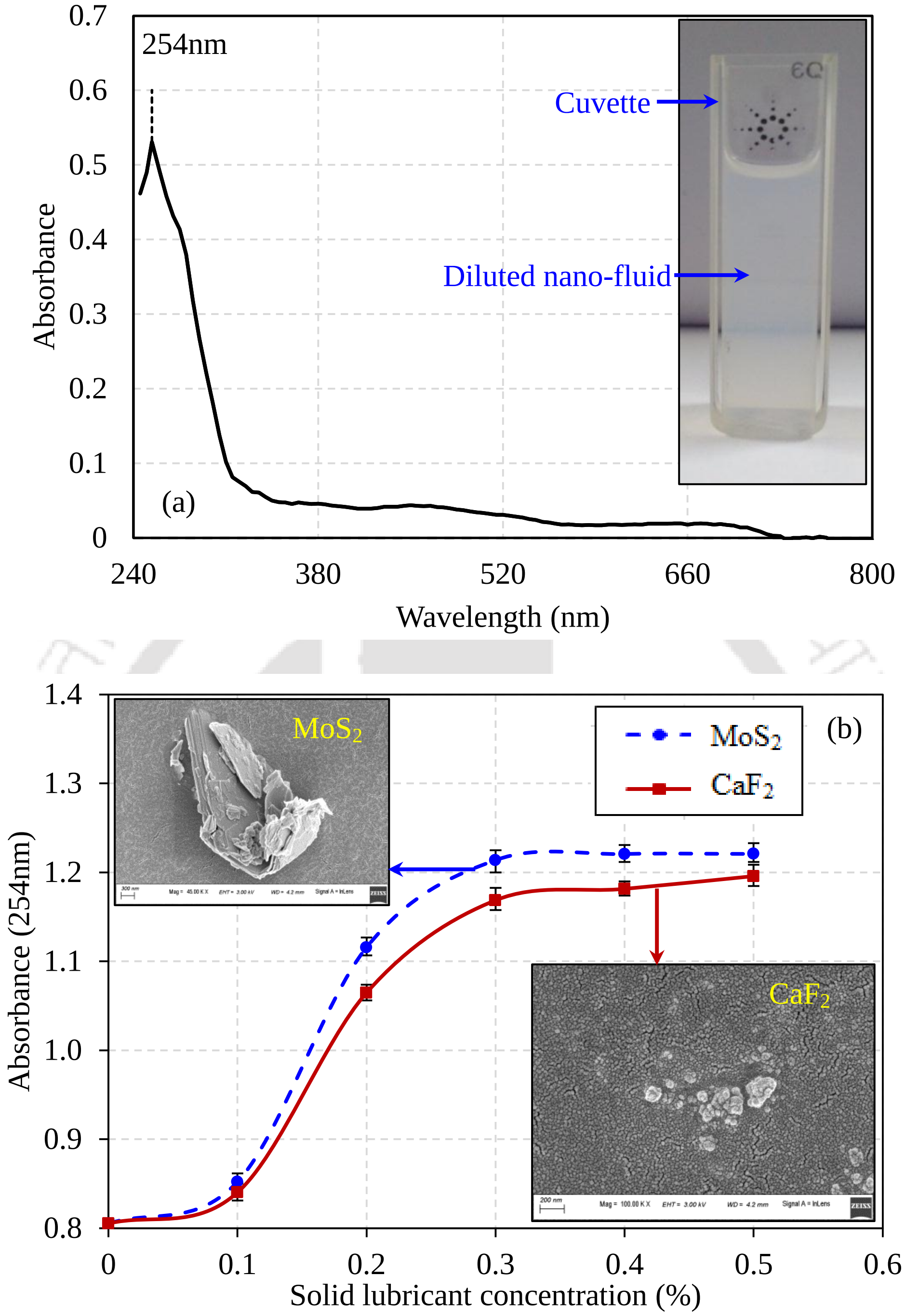

Figure 7.6. Variation of absorbance with (a) wavelength and (b) solid lubricant concentration for dispersion stability test

7.3.2 Thermal conductivity and specific volumetric heat capacity of the nano-green cutting fluids

Thermal conductivity and specific volumetric heat of nano-GCFs with varying nanoparticles concentration (0.1–0.5 %) were measured. Effect of nanoparticles concentration on thermal conductivity and specific volumetric heat of nano-GCFs are illustrated in Figure 7.7 (a-b). It was observed that thermal conductivity and specific volumetric heat of nano-GCFs increases with nanoparticles volume fraction till saturation point is reached (0.3%). Afterwards, an increase in thermal conductivity, and specific volumetric heat is very less. Increase in thermal conductivity of nano-GCF is due to the higher thermal conductivity of present nanoparticles. Similar behaviour of thermal conductivity enhancement with the increase of nanoparticles concentration in nano-fluids was observed by other researchers [190].

Results also showed that the thermal conductivity and volumetric specific heat of MoS_2 based nano-fluids are higher as compared to CaF_2 based nano-fluids. Two main reasons explain this behaviour. First, the thermal conductivity of MoS_2 is 34.5 W/m°K [191] that is much higher than CaF_2 6.04 W/m°K [192]. Secondly, due to the hexagonal shape (nanosheet) and larger size of MoS_2 as compared to CaF_2. Effect of shape of the nanoparticle can be seen by Hamilton and Crosser model [193]. The effective thermal conductivity of two-phase mixture as per the model is as follows:

$$k_{eff} / k_f = \left[\frac{k_p + (\mathrm{n}-1)k_f - (\mathrm{n}-1)\phi(k_f - k_p)}{k_p + (\mathrm{n}-1)k_f + \phi(k_f - k_p)} \right] \tag{7.2}$$

where n is the empirical shape factor given by n = 3/ψ and ψ is the sphericity. For the hexagonal (MoS_2) and spherical (CaF_2) shape particle, ψ is 0.5 and 1, respectively. The shape factor (n) is higher for hexagonal (6) particles as compared to spherical particles (3). Hamilton and Crosser's model validate that the MoS_2 based nano-GCFs have higher thermal conductivity as compared to CaF_2 based nano-GCFs. From Figure 7.7, 0.3 % concentration of MoS_2 and CaF_2 nanoparticles shows thermal conductivity enhancement of 16.93 % and 6.01 %, respectively and specific volumetric heat enhancement of 9.67 % and 5.46 %, respectively with respect to GCF.

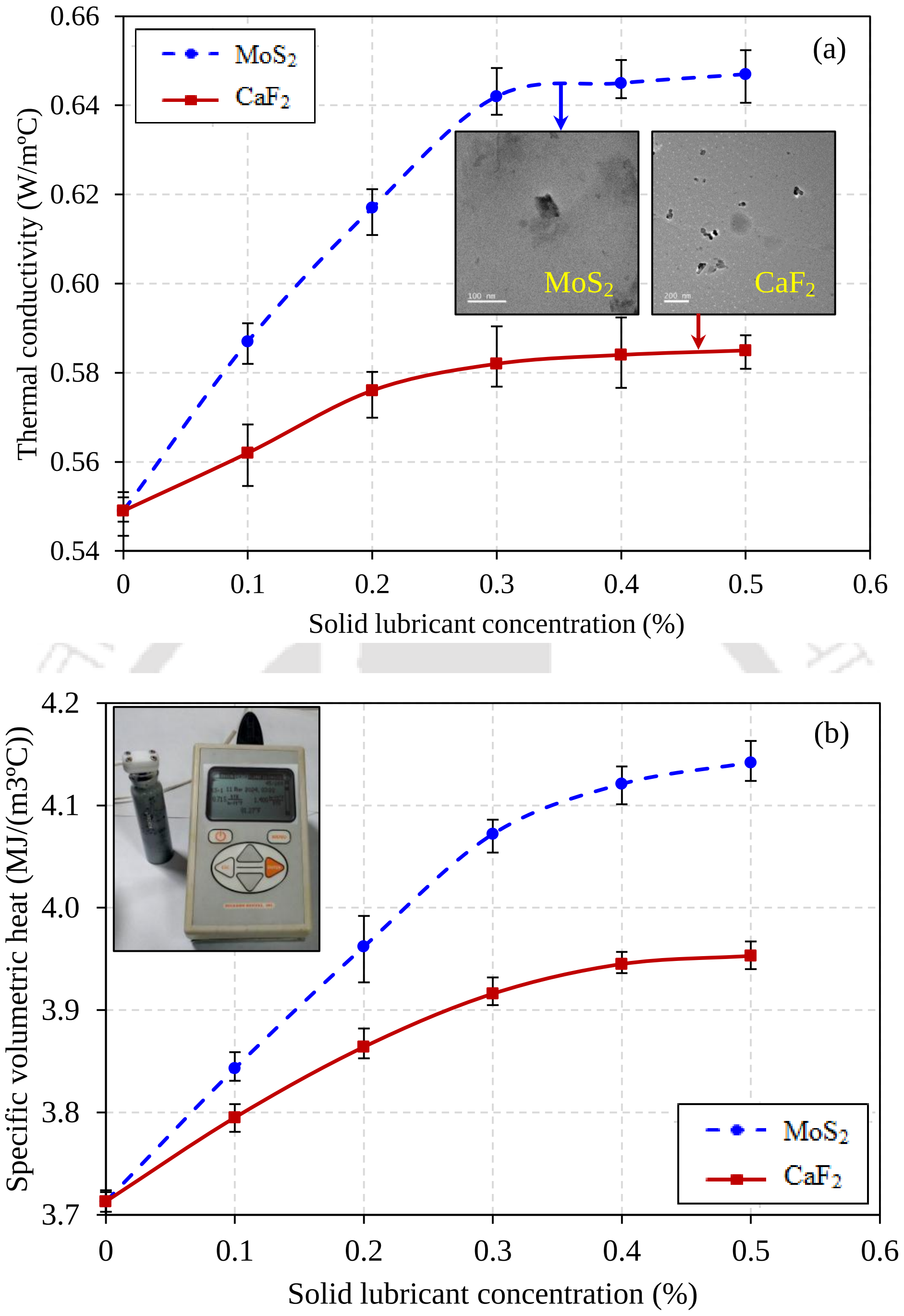

Figure 7.7. Effect of concentration of solid lubricants based nano-green cutting fluids on its (a) thermal conductivity and (b) specific volumetric heat capacity

Nanofluid specific heat can be calculated using the first law of thermodynamics. Assuming that base fluid and nanoparticles are in thermal equilibrium, the energy conservation infers that:

$$c_{pnf} = \omega c_{pnf} + (1-\omega) c_{pbf} \qquad (7.3)$$

where C_{pnf} is specific heat of nanofluid, C_p is the specific heat, ω is the nanoparticles mass fraction and c_{pbf} is specific heat of base fluid. Above equation can also be expressed as mass in density and volume function of the two-phase mixture is as follows [194]:

$$C_{pnf} = \frac{(1-\phi)(\rho C_p)_{bf} + \phi(\rho C_p)_p}{(1-\phi)_{bf} + \phi\rho_p} \tag{7.4}$$

where ϕ is volume fraction which depends upon size on nanoparticles, ρ is density and subscripts p, bf and nf represents corresponding to nanoparticles, base fluid and nanofluid. From Figure 7.7 (b), it is observed that the volumetric specific heats of GCF-0.3M are higher as compared to GCF-0.3C. It is attributed to the larger size of MoS_2 as compared to CaF_2 as well as due to much higher specific heat of MoS_2 than CaF_2. Specific heat enhancement of GCF-0.3M and GCF-0.3C is 9.67 % and 5.46 % higher as compared to GCF.

7.3.3 Viscosity of the nano-green cutting fluids

Variation of the dynamic viscosity of nano-GCFs having different nanoparticles concentration with varying temperature is illustrated in Figure 7.8 (a-b). With the increase in temperature, the dynamic viscosity of nano-GCFs reduces as expected. It is due to thermal energy, which moves apart from the molecules of cutting fluids by reducing intermolecular forces. However, with the increase in the nanoparticle, the dynamic viscosity of nano-GCFs increases till 0.3 % concentration of solid lubricants. This increase in viscosity is due to the inclusion of nanoparticles, which offers additional resistance to flow. Therefore, required torqued to rotate spindle also increases. Beyond 0.3 % concentration, the reduction in viscosity is observed with further increase in solid lubricant. Excess concentration of nanoparticles in GCF results in improper dispersion and sedimentation of particles. Therefore, with the higher concentration of nanoparticles, viscosity reduces after reaching a saturation point. The dynamic viscosity of 0.3 % concentration MoS_2 and CaF_2 based nano-GCFs at 20°C increases by 48.27 % and 39.24 %, respectively. MoS_2 based nano-GCFs shows higher viscosity as compared to CaF_2 based nano-GCFs. It is attributed to the larger average size of MoS_2 nanosheet as compared to CaF_2 nanoparticles. A similar trend for the viscosity of nano-cutting fluids was observed with increase in particle size of TiO_2 by [195]. This is due to stronger interactions in-between larger nanoparticles used in this work.

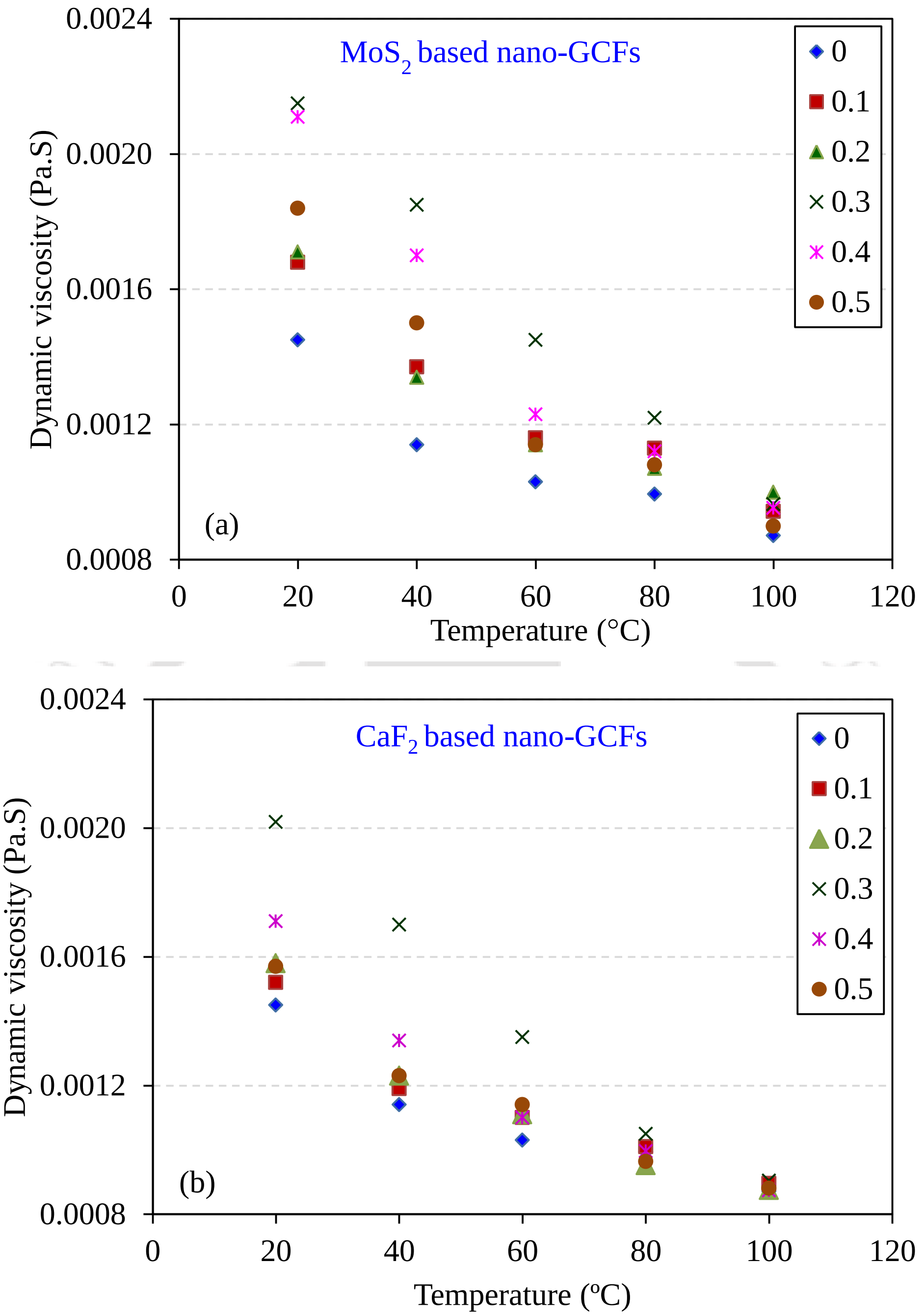

Figure 7.8. Effect of concentration of nanoparticles on the dynamic viscosity of nano-green cutting fluids with (a) MoS_2 and (b) CaF_2

7.3.4 Surface wettability by water and cutting fluids

The wettability of cutting fluids on the cutting tool surface is one of the vital factors because it has the substantial effect on its lubrication capability. The wettability of the cutting fluids is mainly influenced by cutting fluid chemistry with cutting tool surface, which affects interactive surface tension. Figure 7.9 illustrates the wetting angle with various cutting fluids on the cutting tool surface.

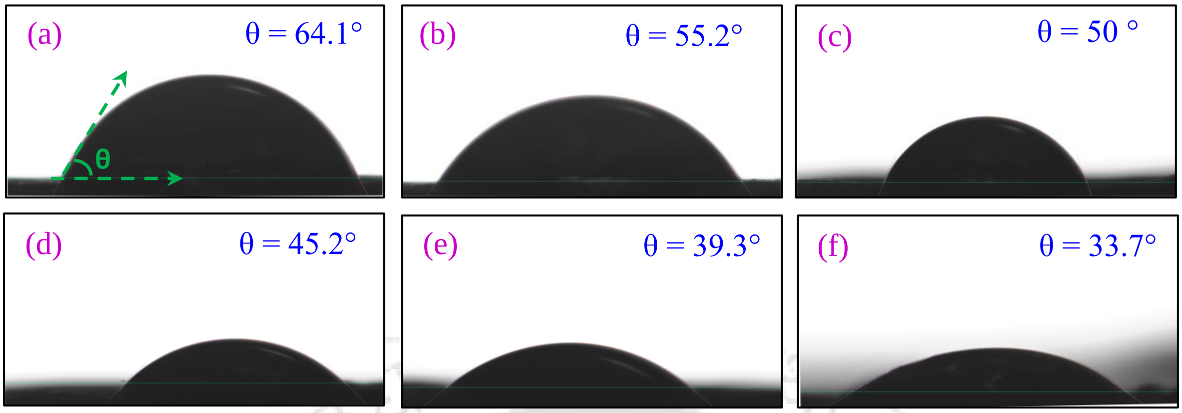

Figure 7.9. Contact angle between workpiece and droplet of (a) water, (b) mineral oil emulsion, (c) bio-cutting fluid emulsion, (d) green cutting fluid emulsion, (e) nano-green cutting fluid with 0.3 % concentration of CaF_2 and (f) nano-green cutting fluid with 0.3 % concentration of MoS_2

It was observed that wetting angle with water is highest (64.1°±2°) among all, whereas wetting angle decreased with the addition of MO, BCF and GCF in water. Wetting angle with MO, BCF and GCF emulsions were 55°±0.9°, 50°±1.2° and 45.2°±2°, respectively. Furthermore, with the addition of nano-size solid lubricant in GCF emulsion, wetting angle further decreased having 39.3°±0.9° for nano-GCF emulsion with 0.3 % concentration of CaF_2 nanoparticles and 33.7°±1.8° for nano-GCF emulsion with 0.3 % concentration of MoS_2 nanosheets. A similar trend for the wettability of nano-cutting fluids was observed with increase in the concentration of multi-walled carbon nanotubes [196]. It is attributed to the overall lower surface tension of nano-GCFs as compared to GCF, MO and water. Therefore, the nano-GCF emulsion with 0.3 % concentration of MoS_2 droplet tends to spread more that causes better lubrication in-between tool-chip interface as compared to others.

7.3.5 Machining experiments

7.3.5.1 Effect of various cutting fluid on cutting force, feed force and coefficient of friction

To evaluate the lubricating and cooling properties of the cutting fluids, hard machining experiments were carried out, and responses were evaluated concerning cutting forces, feed forces, tool-workpiece interface coefficient of friction and workpiece surface roughness. Effect of MQCF using different cutting fluids on the cutting forces and feed forces are illustrated in Figure 7.10 (a-b). Machining using MO has the highest cutting and feed force, followed by the GCF and BCF, whereas nano-cutting fluids (GCF-0.3C and GCF0.3M) performed best among all. The presence of the nano-size solid lubricant in the cutting fluids causes an increase in its viscosity and wettability.

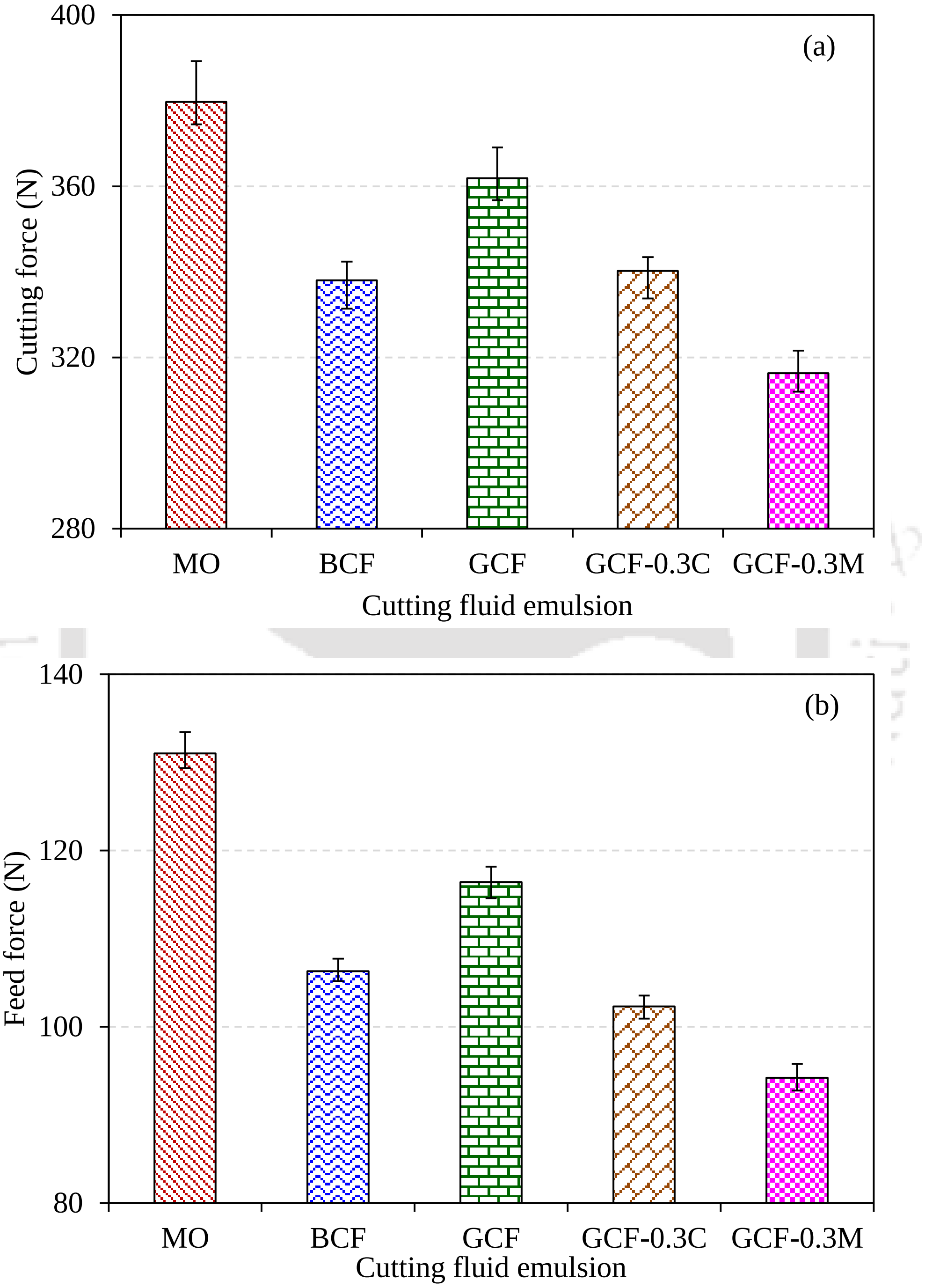

Figure 7.10. Effect of various cutting fluids on the (a) cutting force and (b) feed force

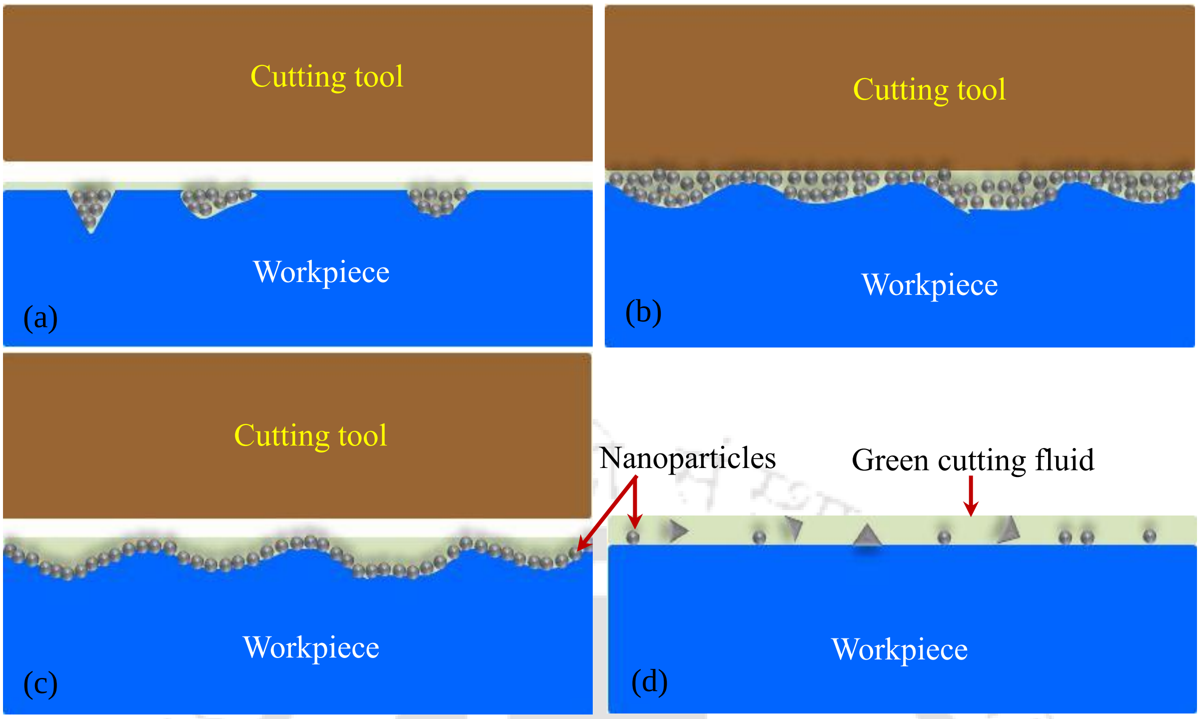

Figure 7.11. Presence of nanoparticles in-between tool-chip interface (a) mending effect, (b) rolling effect, (c) lubricating film and (d) polishing effect

In this case, nanoparticles mixed with GCF are forced with MQCF technique in between the tool-chip interface, which assists particles to get embedded into the workpiece surfaces during machining. Nano-size solid lubricant embedded in-between the tool-chip surface compensates for the loss of mass (Figure 7.11 a). This phenomenon is known as mending effect [197]. Some nanoparticles show a rolling effect (Figure 7.11 b). However, if machining pressure is very high nanoparticles show shearing effect. The particles having a rolling effect can role and fill the surface. Furthermore, few nanoparticles are released from the nozzle and delivered in-between tool-chip interface without being sheared. These nanoparticles fill the workpiece surface cavities that were sheared off by previous nanoparticles. Due to this a protective lubricating film (Figure 7.11 c) was formed, and the workpiece surface was polished (Figure 7.11 d) [198].

Figure 7.12 (a-e) illustrates the surface morphology of the cutting tool rake surface after 900 s of machining with different cutting fluids at the cutting speed of 90 m/min, feed of 0.28 mm/rev and depth of cut of 0.5 mm. Figure 7.12 (a-c) show the tool-chip contact length on the cutting tool rake surface in case of machining using MO, BCF and GCF, respectively. Tool-chip contact length is subdivided into two parts, i.e., sticking and sliding zone. Zoom in version of Figure 7.12 (a-c) illustrates the interface of sticking and sliding zone. In both cases, severe abrasion marks are observed. In case of machining with MO, length of sticking and sliding zone is large as compared to machining with BCF and GCF. Furthermore, tool-chip contact length reduces when machining with nano-GCFs (Figure 7.12 d-e). Also, abrasion marks are not observed when machining with nano-GCFs (Zoomed in Figure 7.12 d-e). Reduction in tool-chip contact length is attributed to better lubrication and cooling that it results in lower machining forces.

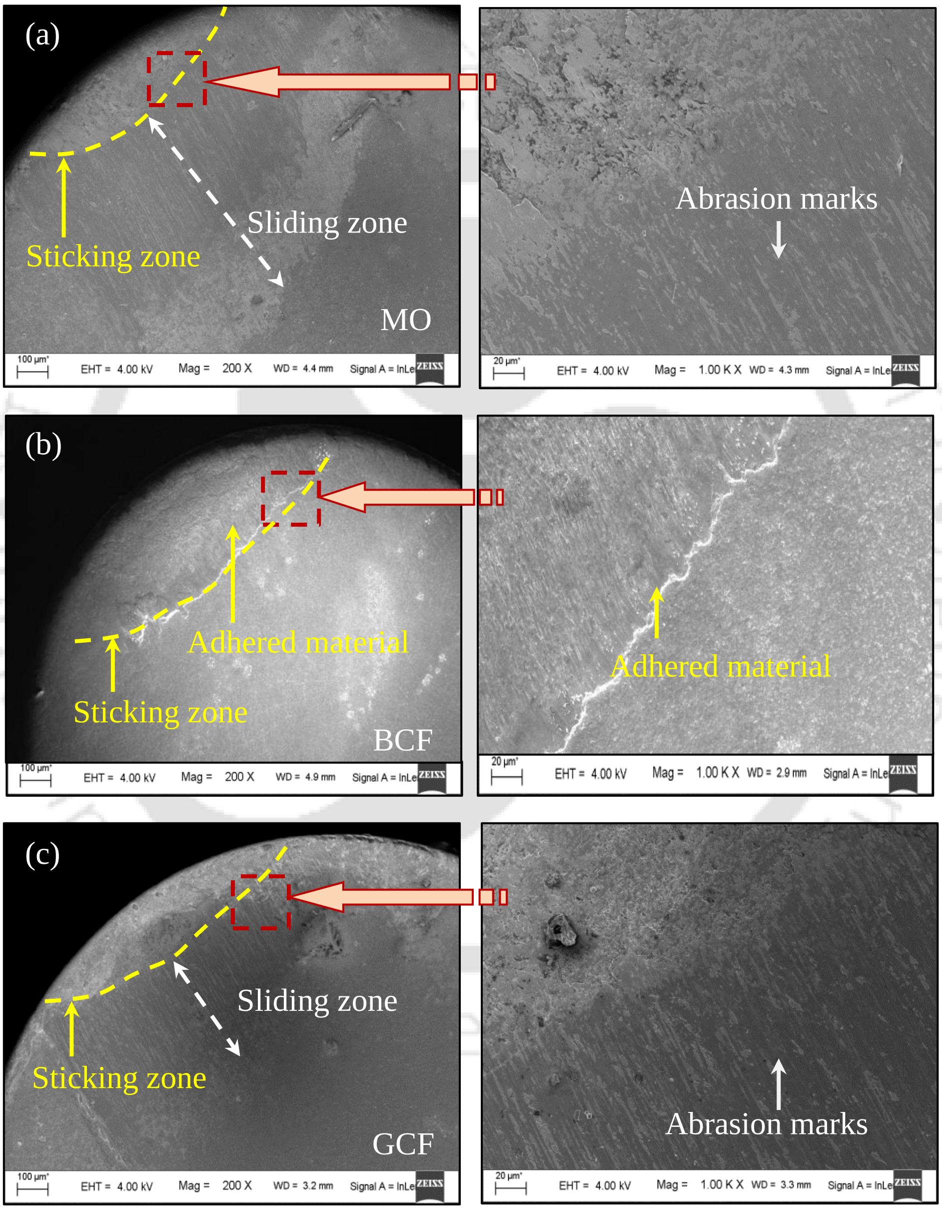

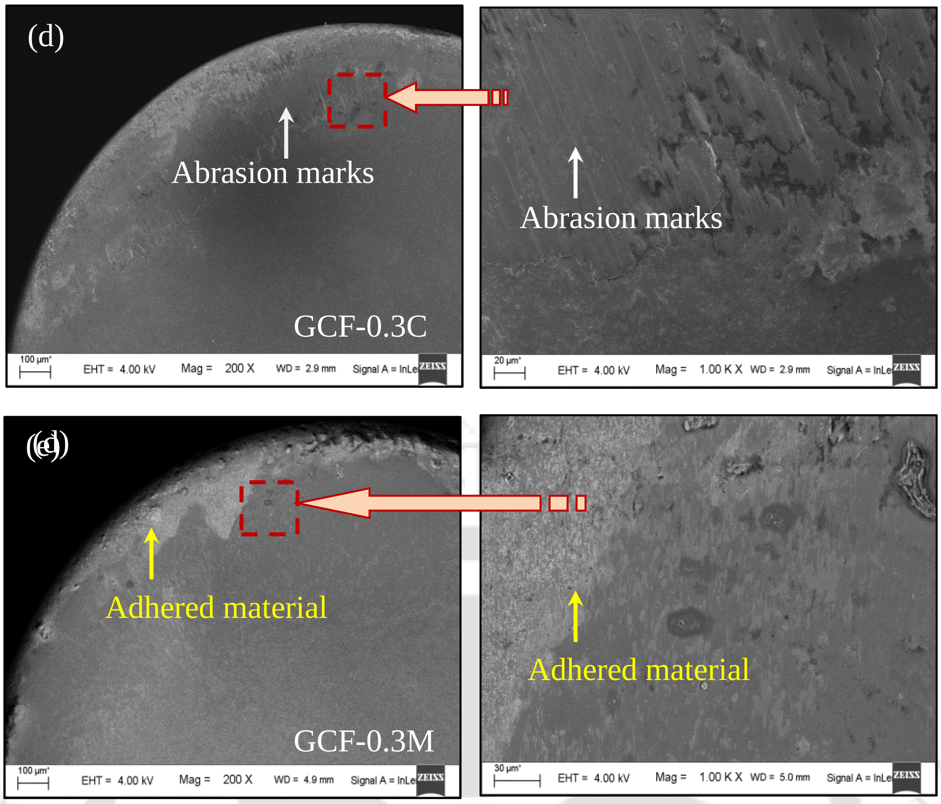

Figure 7.12. Surface morphology of the cutting tool rake surface after machining with MQCF using (a) mineral oil, (b) bio-cutting fluid, (c) green cutting fluid, (d) 0.3 % concentration of CaF_2 based hybrid nano-green cutting fluid (GCF-0.3C) and (e) 0.3 % concentration of MoS_2 based hybrid nano-green cutting fluid (GCF-0.3M)

Figure 7.13 (a-b) illustrated the surface morphology and corresponding elemental micrograph of the cutting tool rake surface after machining with MQCF using GCF and GCF-0.3C. Area A and B were chosen such that area A lies above sticking zone on the cutting tool rake surface, and area B lies above parent cutting tool material. Elemental composition of area A shows the presence of iron (Fe) in abundant that confirm the workpiece material adhesion on the cutting tool rake surface (elemental micrograph of Figure 7.13 a). However, area B has tungsten (W) in abundant (elemental micrograph of Figure 7.13 b).

Consequently, nano-GCFs reduce cutting and feed forces as compared to GCF, BCF and MO. Overall due to enhanced viscosity, thermal conductivity, specific heat and wettability, nano-GCFs were able to perform better concerning cutting forces and feed forces as compared to MO, BCF and GCF. The machining of hardened AISI H-13 steel with GCF-0.3M reduced the cutting forces by 17 %, 7 %, 13 % and 7 % as compared with MO, BCF, GCF and GCF-0.3C, respectively in MQCF machining process.

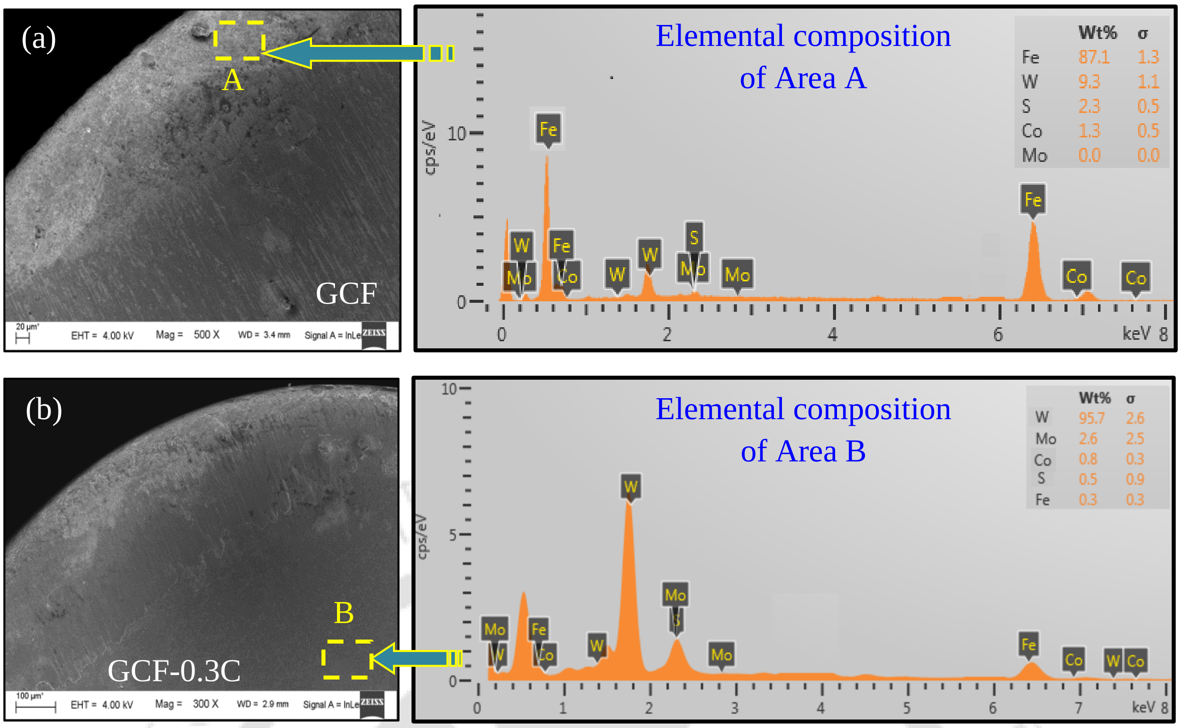

Figure 7.13. Surface morphology and corresponding elemental micrograph of the cutting tool rake surface after machining with MQCF using (a) green cutting fluid and (b) 0.3 % concentration of CaF_2 based hybrid nano-green cutting fluid (GCF-0.3C)

The tool-chip interface coefficient of friction was calculated. The coefficient of friction (μ) is given as [174]:

$$\mu = \frac{F_c \sin\alpha + F_f \cos\alpha}{F_c \cos\alpha - F_f \sin\alpha} \tag{7.5}$$

where α is the rake angle, μ denotes the coefficient of friction, F_f represents the feed force and, F_c is the cutting force. Figure 7.14 shows the effect of MQCF using various cutting fluids on the tool-workpiece interface coefficient of friction. It was observed that GCF-0.3M performed better as compared to GCF-0.3C in terms of cutting force, feed force and coefficient of friction. It is attributed to higher thermal conductivity, specific heat, viscosity and wettability of GCF-0.3M as compared to GCF-0.3C and others that lead to better lubrication and cooling at the tool-chip interface during machining. Furthermore, MoS_2 nanosheets are porous, and it has a hexagonal shape and larger size in this study. In a specific loading range, MoS_2 porous nanosheets impart high elasticity that enhances their flexibility and enlarges the gap between the tool-chip interfaces that leads to the reduction of the coefficient of friction [199]. Moreover, MoS_2 nanosheets are more effective because of its larger size, which enables it to make higher contact area in between tool-chip interface [200]. Also, MoS_2 nanosheets are more flexible, which allows it to buckle, bend and even roll freely in between tool-chip interface that affects the coefficient of friction. The machining of hardened AISI H-13 steel with GCF-0.3M reduced the tool-chip interface coefficient of friction by 11 %, 4 %, 5 % and 2 % as compared with MO, BCF, GCF and GCF-0.3C, respectively in MQCF machining process.

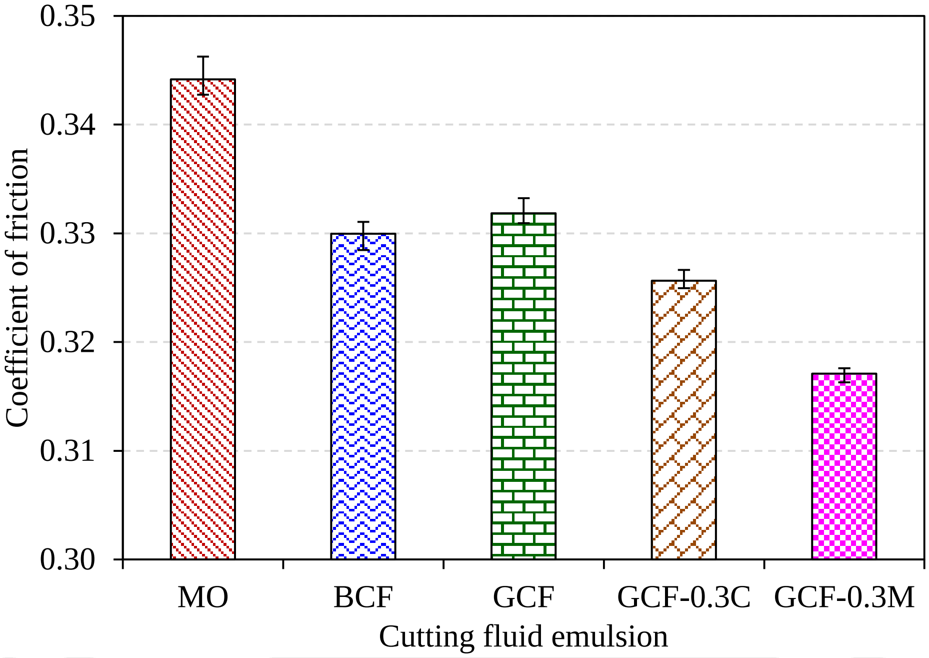

Figure 7.14. Effect of various cutting fluids on the tool-chip interface coefficient of friction

Figure 7.15 (a-b) shows the surface micrograph of the MO and GCF-0.3M tested cutting tool rake surface at 110X magnification, respectively after 15 minutes of MQCF machining (v = 90 m/min, f = 0.28 mm/rev and d = 0.5mm). Figures 7.15 (c-f) shows energy dispersive X-ray spectroscopy (EDS) maps of tungsten (W) and iron (Fe) on the MO and GCF-0.3M tested cutting tool rake surface, respectively. On the cutting tool rake surface, more adhered workpiece material was observed after machining with MO (Figure 7.15 a) as compared to GCF-0.3M (Figure 7.15 b). Presence of adhered workpiece material (Fe abundant) can be confirmed by an elemental map of the cutting tool rake surface (W abundant) as illustrated in Figure 7.15 (c-f). Also, abrasion marks were observed on the cutting tool rake surface after machining with MO, which was not seen after machining with GCF-0.3M. Reduction in workpiece material adhesion on the rake surface of the cutting tool is due to better lubrication, cooling and lesser machining forces. It confirms that GCF-0.3M performed better as compared to other cutting fluids used for this study.

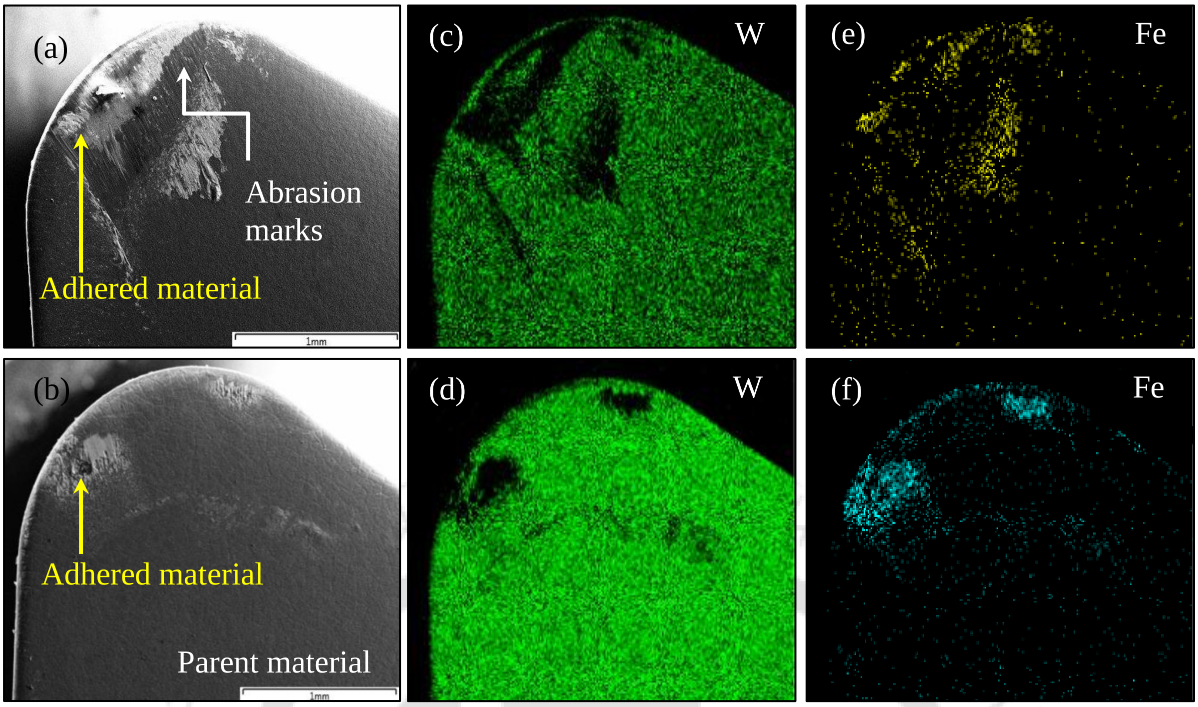

Figure 7.15. Surface morphology of the cutting tool rake surface after machining with MQCF using (a) mineral oil (MO), (b) 0.3 % concentration of MoS_2 based hybrid nano-green cutting fluid (GCF-0.3M), (c) elemental map of tungsten (W) for tested cutting tool rake surface with MO, (d) elemental map of tungsten (W) for tested cutting tool rake surface with GCF-0.3M, (e) elemental map of iron (Fe) for tested cutting tool rake surface with MO and (f) elemental map of iron (Fe) for tested cutting tool rake surface with GCF-0.3M

7.3.5.2 Workpiece surface roughness

Machined product surface roughness is a vital machining parameter. The effect of various cutting fluids on the workpiece surface roughness is illustrated in Figure 7.16. The surface roughness of the workpiece machined with MQCF using MO was highest among all, followed by GCF-0.3C and GCF, respectively. However, workpiece surface roughness was least after machining with MQCF using GCF-0.3M as compared to other cutting fluids. It is attributed to higher viscosity, thermal conductivity, specific heat and wettability of GCF-0.3M that leads to better cooling and lubrication in-between tool-chip interface. Furthermore, because of the low adhesion of workpiece and tool-chip interface coefficient of friction, workpiece surface finish is better (lower surface roughness) when machined with MQCF using GCF-0.3M. Figure 7.17 illustrates the 3D and 2D surface profile of the machined workpiece, respectively using various cutting fluids.

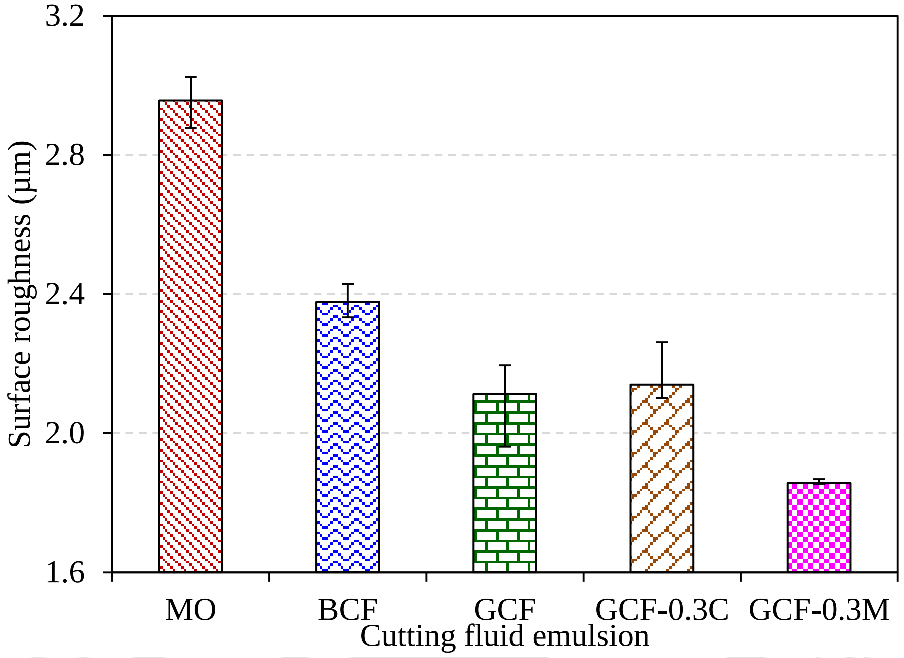

Figure 7.16. Effect of various cutting fluids on the workpiece surface roughness

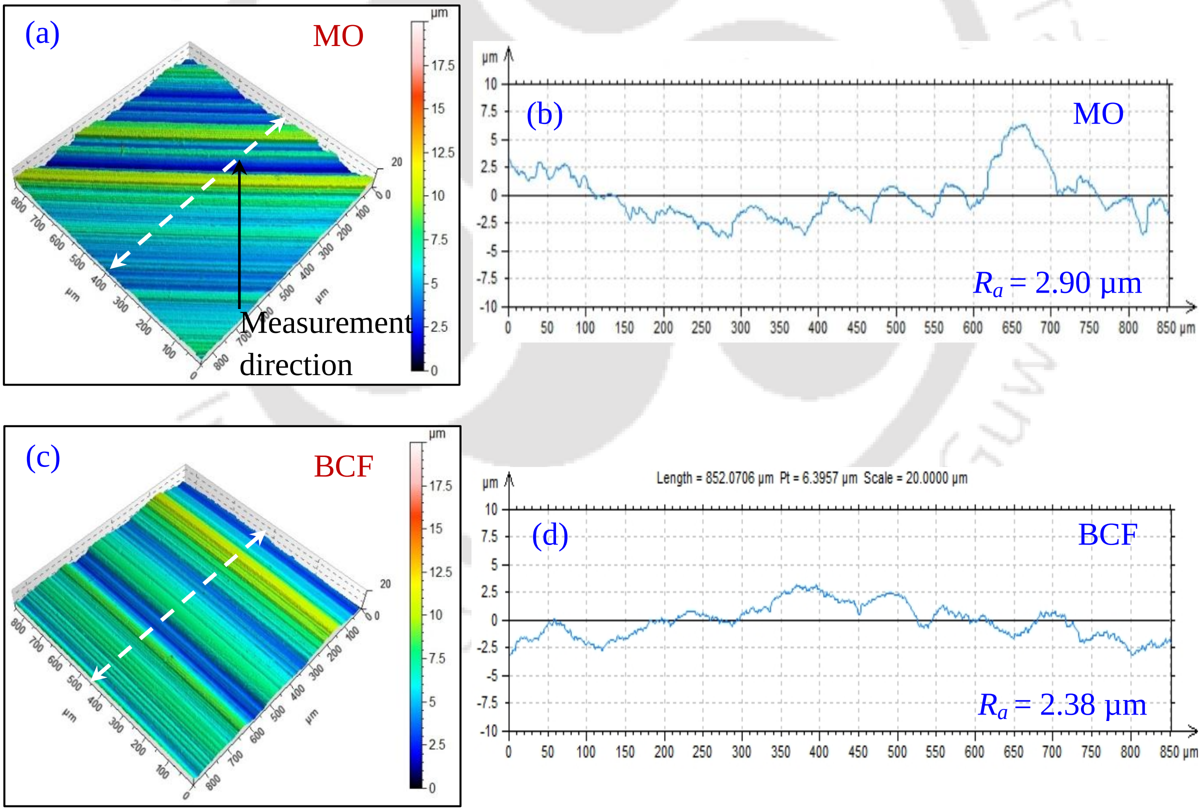

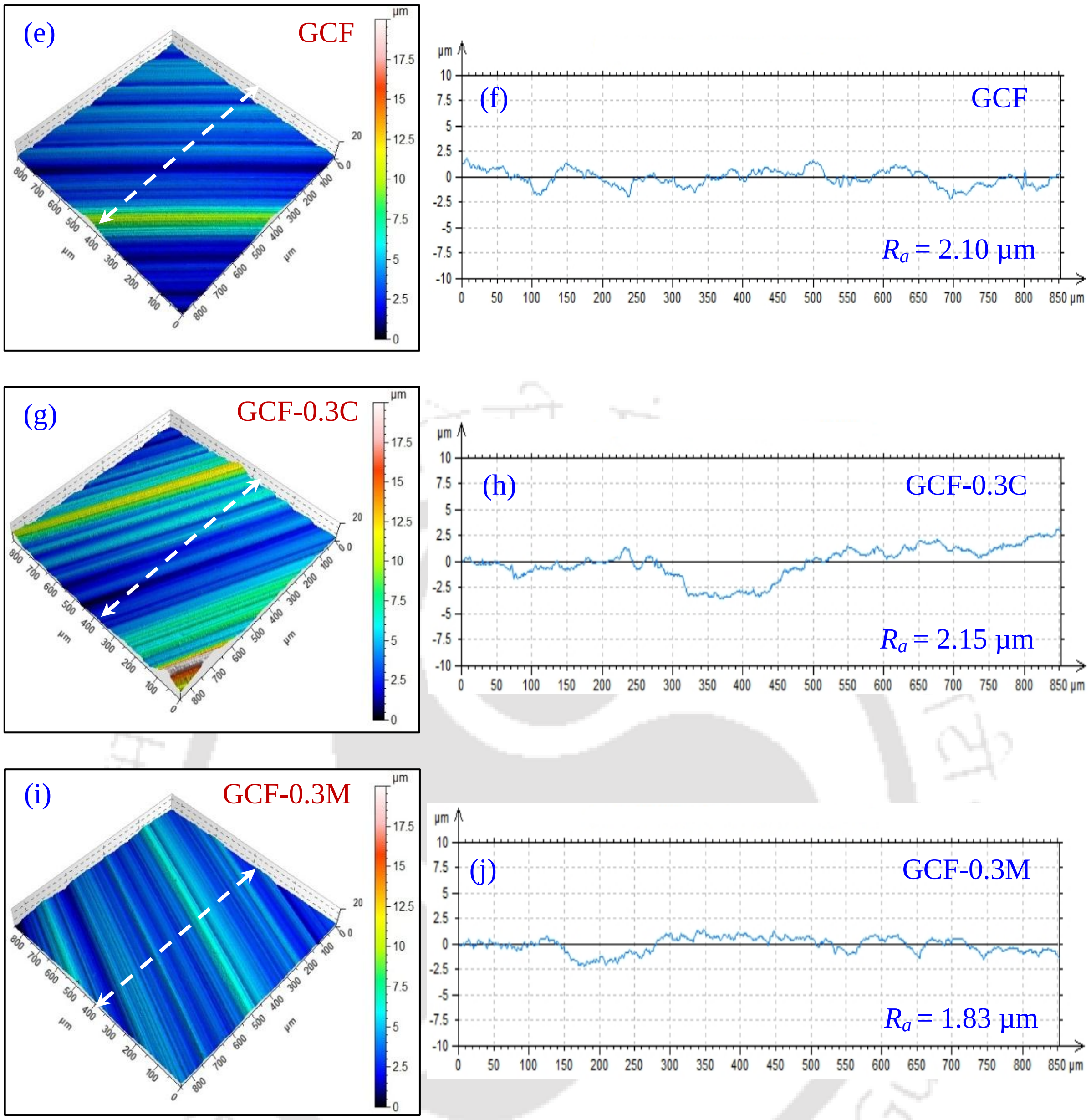

Figure 7.17. 3D and 2D surface profile of machined workpiece after machining with MQCF using (a-b) mineral oil, (c-d) bio-cutting fluid, (e-f) green cutting fluid, (g-h) 0.3 % concentration of CaF_2 based hybrid nano-green cutting fluid and (i-j) 0.3 % concentration of MoS_2 based hybrid nano-green cutting fluid

To correctly understand the surface morphology, obtained machined surface were observed under FESEM and EDS. Figure 7.18 (a-e) shows the surface micrograph of the machined workpiece with MQCF using MO, BCF, GCF, GCF-0.3C and GCF-0.3M, respectively. Figure 7.19 (a-b) shows the elemental composition analysis of point C and D, respectively that are highlighted on the surface of Figure 7.18 (d-e). Point C and D are selected over the nanoparticles present on the workpiece surface after machining. Deep feed marks are observed on the workpiece surface machined with MO, followed by BCF, GCF-

0.3C and GCF, respectively. However, in the case of machining using GCF-0.3M, mild feed marks are observed. CaF_2 nanoparticles and MoS_2 nanosheets are observed on the machined workpiece surface. Elemental composition of point A shows the higher percentage of calcium (Ca) and fluoride (F) elements (Figure 7.19 a), whereas point B has more molybdenum (Mo) and sulphur (S) elements (Figure 7.19 b). It confirms the presence of CaF_2 nanoparticles and MoS_2 nanosheets on the workpiece surface roughness after machining. In the case of machining with GCF-0.3C, it was observed that the workpiece surface roughness was higher as compared to workpiece surface machined with GCF (Figure 7.16). It is attributed to the smaller size of CaF_2 nanoparticles.

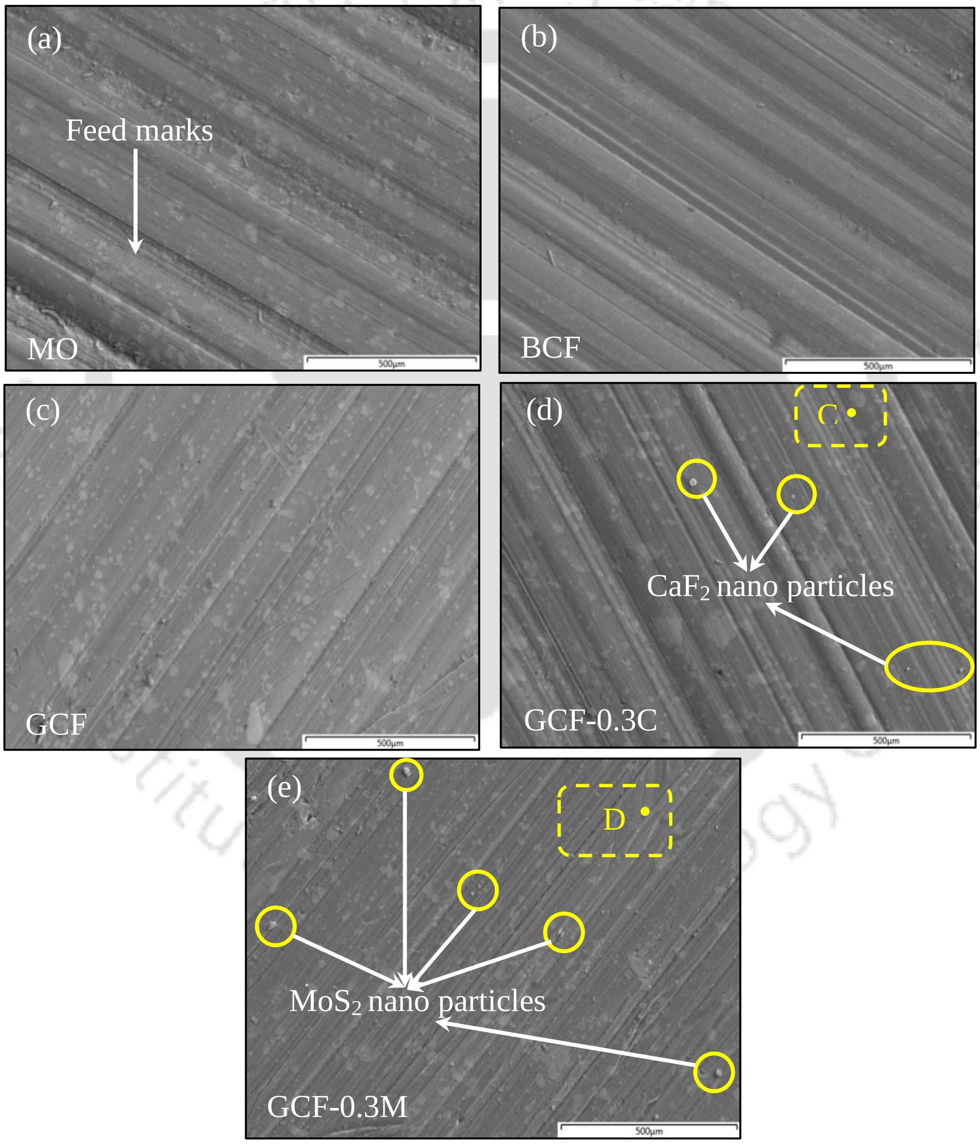

Figure 7.18. Surface morphology of the workpiece after machining with MQCF using (a) mineral oil, (b) bio-cutting fluid, (c) green cutting fluid, (d) 0.3 % concentration of CaF_2 based hybrid nano-green cutting fluid (GCF-0.3C) and (e) 0.3 % concentration of MoS_2 based hybrid nano-green cutting fluid (GCF-0.3M)

Smaller nanoparticles can shear off easily by other incoming particles. These ploughed-off particles remain in-between tool-chip interface that can cause 3D abrasion between tool-chip (Figure 7.18 d) [198]. Therefore, the surface roughness of the workpiece machined with GCF is better as compared with workpiece machined with GCF-0.3C. However, GCF-0.3M produces best surface finish among all. It is due to the larger size of nanoparticles, which are difficult to shear off. The machining of hardened AISI H-13 steel with GCF-0.3M improved the workpiece surface finish by 37 %, 22 %, 12 % and 13 % as compared with MO, BCF, GCF and GCF-0.3C, respectively in MQCF machining process.

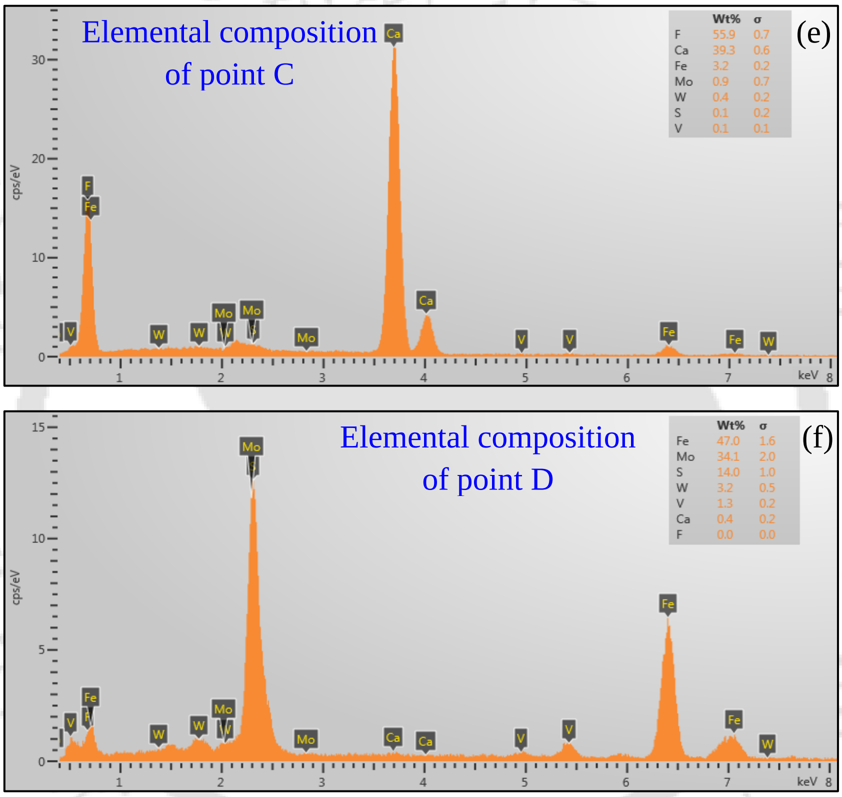

Figure 7.19. Elemental composition of (a) point C and (b) point D (Point C and D in Figure 7.18 d-e)

7.4 Findings from the research work

In the present Chapter, MoS_2 and CaF_2 based nano-GCFs with varying concentration were developed and characterised. Concentrations of developed nano-GCFs were optimised on the basis of its absorbance, thermal conductivity, specific heat, viscosities and wettability. Hard machining experiments were conducted using an in-house fabricated MQCF setup with in-house developed eco-friendly nano-GCFs, GCF, BCF and MO. The findings are as follows:

- The thermal conductivity, specific heat and viscosities are higher for MoS_2 based nano-GCFs as compared to others.

- The 0.3 % concentration of CaF_2 and MoS_2 based eco-friendly nano-GCFs were found to have optimised thermal conductivity, specific heat and viscosities.
- GCF-0.3M had 47 %, 39 %, 33 %, 25% and 14 % better wettability as compared to other MO, BCF, GCF and GCF-0.3C, respectively.
- Eco-friendly nano-GCFs performed better as compared to GCF, BCF and MO concerning cutting forces, feed forces, tool-chip interface coefficient of friction and workpiece surface roughness.
- Hard machining performance of MoS_2 based nano-GCFs was best among all.
- GCF-0.3M reduced the tool-chip interface coefficient of friction by 11 %, 4 %, 5 % and 2 % as compared with MO, BCF, GCF and GCF-0.3C, respectively.
- GCF-0.3M improved the workpiece surface finish by 37 %, 22 %, 12 % and 13 % as compared with MO, GCF and GCF-0.3C, respectively.
- Cutting tool wear and adhesion of workpiece material were lower for GCF-0.3M tested cutting tool rake surface after machining as compared to all others tested cutting fluids.

Chapter 8

HARD MACHINING PERFORMANCE WITH HYBRID MECHANICAL MICRO-TEXTURED CUTTING TOOLS AND MINIMUM QUANTITY NANO-GREEN CUTTING FLUIDS

Chapter 8 deals with the hybridisation of four individual sustainable machining processes. For hard machining, a combination of the mechanical-micro-textured cutting tool with in-house fabricated minimum quantity cutting fluid using in-house developed nano-green cutting fluid is used. Hard machining experiments are carried out, and the results are compared with DM, GCF and Nano-GCF.

8.1 Introduction

In previous Chapters, the area density of mechanical micro-textures was experimentally optimised (10 %), and perpendicular mechanical micro-textured (PDT) cutting tool performs best among all textured and untextured cutting tools. Also, 0.3 % MoS_2 based nano-GCF showed least machining forces, coefficient of friction and workpiece surface roughness. Therefore, in this Chapter, to make machining more sustainable, four individual sustainable machining techniques are combined. Hard machining experiments were carried out using PDT MμT cutting tool with experimentally optimised minimum quantity MoS_2 based nano-GCF which is named as PDT-NGCF. For comparison, experiments were also carried out with DM, GCF and NGCF (i.e. GCF-0.3M).

8.2 Experimental details

The experiments were planned and designed using CCRD as explained in Chapter 6. Experiments were conducted at the same input process parameters. However, the type of cutting tools and machining environment is different.

8.2.1 Materials and equipment

Experiments are carried out using the same workpiece and cutting tool materials with the same experimental setup as explained in Chapter 6. However, machining experiments were performed with 10 % area density perpendicular mechanical micro texture cutting tool (Figure 1 a) for an MQCF environment using 0.3 % MoS_2 based nano-GCF (PDT-NGCF). For comparison, experiments were also carried out using an un-textured tool (Figure 1 b) at the dry environment (DM), un-textured tool for an MQCF environment using GCF (GCF) and with an un-textured tool for an MQCF environment using nano-GCF (NGCF). Machining conditions are shown in Table 8.1. Figure 8.2 (a-b) illustrates the green cutting fluid and 0.3 % MoS_2 based nano-GCF.

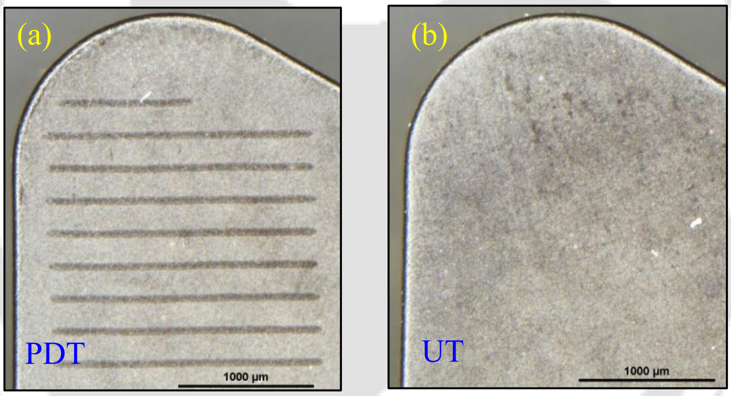

Figure 8.1. Rake surface of mechanical micro-textured cutting tools: (a) perpendicular textured tool and (b) untextured tool

Table 8.1. Machining conditions and environments

Input	Value
Cutting speed	55−125 m/min
Feed	0.04−0.28 mm/rev
Depth of cut	0.5 mm
Machining environment	Dry, MQCF, MQCF with nano fluids
Cutting fluids	DM, GCF, NGCF, PDT-NGCF
Oil flow rate	35 mL/hr
Air pressure	0.5 MPa (5 bar)
MQCF nozzle standoff distance	30 mm
MQCF nozzle angle	45°

Figure 8.2. (a) Green cutting fluid and (b) 0.3% MoS_2 based nano-green cutting fluid

8.3 Results and discussion

In this section, experimentally obtained results during hard machining in terms of cutting force, feed force, coefficient of friction, workpiece surface roughness, tool wear and chip morphology are discussed. All tests are replicated thrice, and average values are considered for discussion.

8.3.1 Cutting force

The experiments are carried out according to the central composite rotatable design (CCRD), and the results are analysed using response surface methodology (RSM). Input parameters (feed, cutting speed) and output responses (cutting force) for all different machining environment and types of cutting tools are presented in Table 8.2. Equation models for cutting force per CCRD are given as follows (Eq. 8.1−8.4):

$$F_{c-DM} = 529.18 + 1302.57f - 7.45v - 2.48vf + 644.81f^2 + 0.03v^2 \tag{8.1}$$

$$F_{c-GCF} = -22.79 + 1727.219f + 0.73v - 3.41vf - 975.044f^2 - 0.0003v^2 \tag{8.2}$$

$$F_{c-NGCF} = 51.20 + 1071.632f + 1.9375v - 0.221vf - 891.82f^2 - 0.0007v^2 \tag{8.3}$$

$$F_{c-PDT-NGCF} = 41.48 + 809.139f + 2.6625v + 0.0456vf - 552.319f^2 - 0.0017v^2 \tag{8.4}$$

where v, f and F_c represent the cutting speed (m/min), feed (mm/rev) and cutting force (N), respectively, and the subscript of F_c denotes machining environment.

Table 8.2. Complete CCRD table showing input parameters and output responses for hard machining for different machining environment with untextured and perpendicular mechanical micro-textured cutting tool

Exp. No	Feed (mm/rev)	Speed (m/min)	$F_{c\text{-}DM}$ (N)	$F_{c\text{-}GCF}$ (N)	$F_{c\text{-}NGCF}$ (N)	$F_{c\text{-}PDT\text{-}NGCF}$ (N)
1	0.24	115.00	421.73	316.13	292.64	259.42
2	0.16	90.00	324.79	243.73	212.31	184.06
3	0.16	90.00	324.61	241.17	213.41	185.25
4	0.16	125.00	303.72	251.03	223.94	189.37
5	0.28	90.00	464.28	366.1	316.42	280.49
6	0.08	115.00	204.57	158.07	131.37	106.67
7	0.24	65.00	526.83	327.51	276.41	241.9
8	0.16	90.00	322.48	240.95	216.64	185.64
9	0.04	90.00	184.31	92.89	85.63	74.64
10	0.16	55.00	407.31	235.47	205.64	177.51
11	0.16	90.00	323.97	245.67	212.45	185.36
12	0.08	65.00	289.81	142.12	130.64	110.45
13	0.16	90.00	324.82	243.56	212.64	184.42

Table 8.3. ANOVA for cutting force ($F_{c\text{-}PDT\text{-}NGCF}$) for machining with the perpendicular mechanical micro-textured cutting tool using minimum quantity cutting fluid with 0.3 % MoS_2 based nano-green cutting fluid

Source	*F*-Value	*p*-value Prob>*F*	Percentage contribution
Model	11.24	0.0012	
A-Feed	29.38	0.0072	30.10
B-Speed	19.17	0.0047	19.64
AB	0.84	0. 8124	0.008
A^2	28.74	0.0032	29.45
B^2	19.45	0.0026	19.93
Lack of Fit	2.42	0..4721	

Table 8.3 shows the ANOVA for cutting force for machining using PDT-NGCF. Feed is found to have the highest contribution (59.55%), followed by cutting speed (39.57%). The coefficient of determination (R^2) is found to be 0.9512. All CCRD terms are considered in the regression models to improve prediction accuracy. R^2 values for machining at DM, GCF and NGCF environments are also found to be higher than 0.95 for all output responses. This shows good agreement between input parameters and output responses.

Figure 8.3 (a-b) illustrates the variation of cutting force with respect to feed and cutting speed, respectively at the constant depth of cut (0.5 mm). Feed and cutting speeds have a profound effect on cutting force. Figure 8.3 (a) illustrates the increase in cutting force with increasing feed, which is a well-known phenomenon in machining. It was also observed that GCF with MQCF shows the lower cutting forces as compared to DM. Moreover, NGCF with PDT cutting fluid shows the lowest cutting force among all (Figure 8. 3 a-b).

In this case, nanoparticles mixed with GCF are forced with MQCF technique in between the tool-chip interface, which assists particles to get embedded into the workpiece surfaces during machining. Nano-size solid lubricant embedded in-between the tool-chip surface compensates for the loss of mass. Some nanoparticles shows a rolling effect. However, if machining pressure is very high nanoparticles show shearing effect. The particles having a rolling effect can role and fill the surface. Furthermore, few nanoparticles are released from the nozzle and delivered in-between tool-chip interface without being sheared. These nanoparticles fill the workpiece surface cavities that were sheared off by previous nanoparticles. Due to this, a protective lubricating film was formed, and the workpiece surface was polished. All above reasons cause the reduction in machining forces with NGCF. In case of machining with PDT using NGCF, a relative lower cutting force was observed due to the ability of micro-channels to carry cutting fluids which has better lubricating and cooling properties.

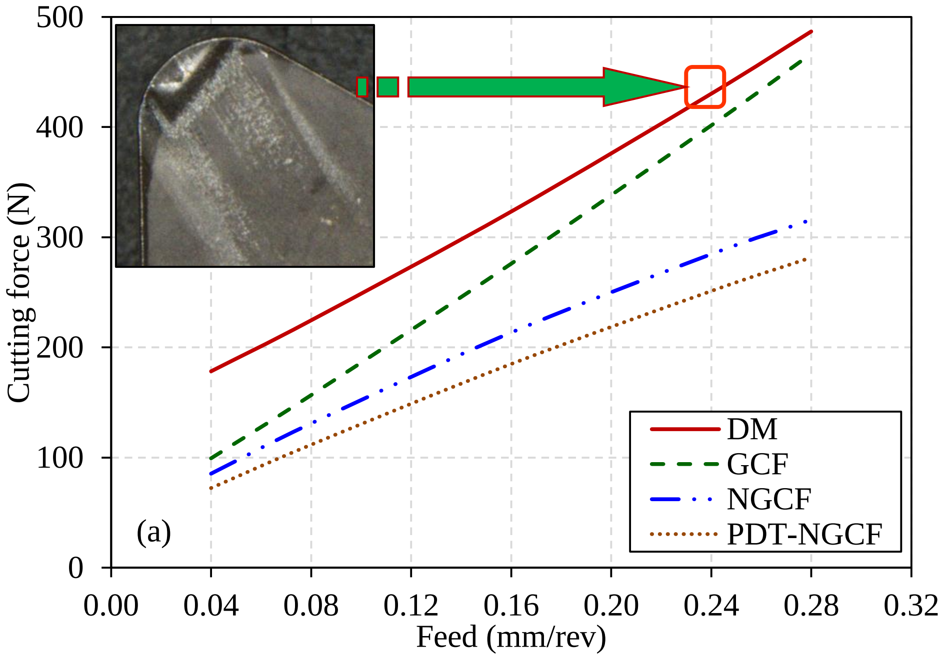

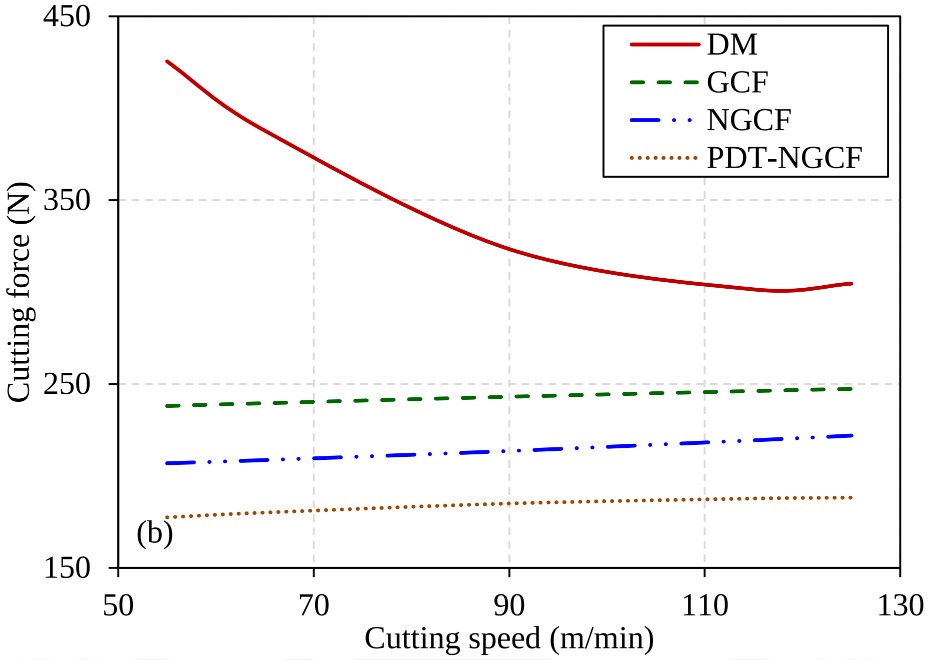

Figure 8.3. Variation of cutting force with (a) feed and (b) cutting speed for various cutting tools and machining environments

8.3.2 Feed force

Response surface methodology models for feed force per CCRD are given below (Eq. 8.5−8.8):

$$F_{f-DM} = 18.61 + 637.72f + 0.55v - 0.695vf - 643.79f^2 - 0.004v^2 \quad (8.5)$$

$$F_{f-GCF} = 30.31 + 296.28f + 0.408v - 0.307\upsilon f - 4.426f^2 - 0.00315v^2 \quad (8.6)$$

$$F_{f-NGCF} = 23.71 + 306.33f - 0.755v + 0.257\upsilon f - 28.098f^2 - 0.00175v^2 \quad (8.7)$$

$$F_{f-PDT-NGCF} = 10.88 + 280.60f - 0.4075v + 0.4799\upsilon f - 104.506f^2 - 0.00315v^2 \quad (8.8)$$

where v, f and F_f represent the cutting speed (m/min), feed (mm/rev) and feed force (N), respectively, and the subscript of F_f denotes the machining environment.

Figure 8.4 (a) shows the variation of feed force with feed for a constant depth of cut (0.5 mm) during machining using UT cutting tool with GCF and NGCF emulsions as well as dry machining. Also, machining was carried out with PDT cutting tool with NGCF emulsion. As feed increases, the advancement per revolution by the cutting tool increases, i.e. the amount of workpiece material that comes into contact with the cutting tool per unit time increases. Therefore, the load on the tool and thus the feed force increase, irrespective of cooling technique. For a constant feed and depth of cut, with increasing cutting speed, feed force reduces as MRR increases (Figure 8.4 b). Increases in MRR leads to increases in temperature, resulting in the thermal softening of the workpiece and reducing the feed force.

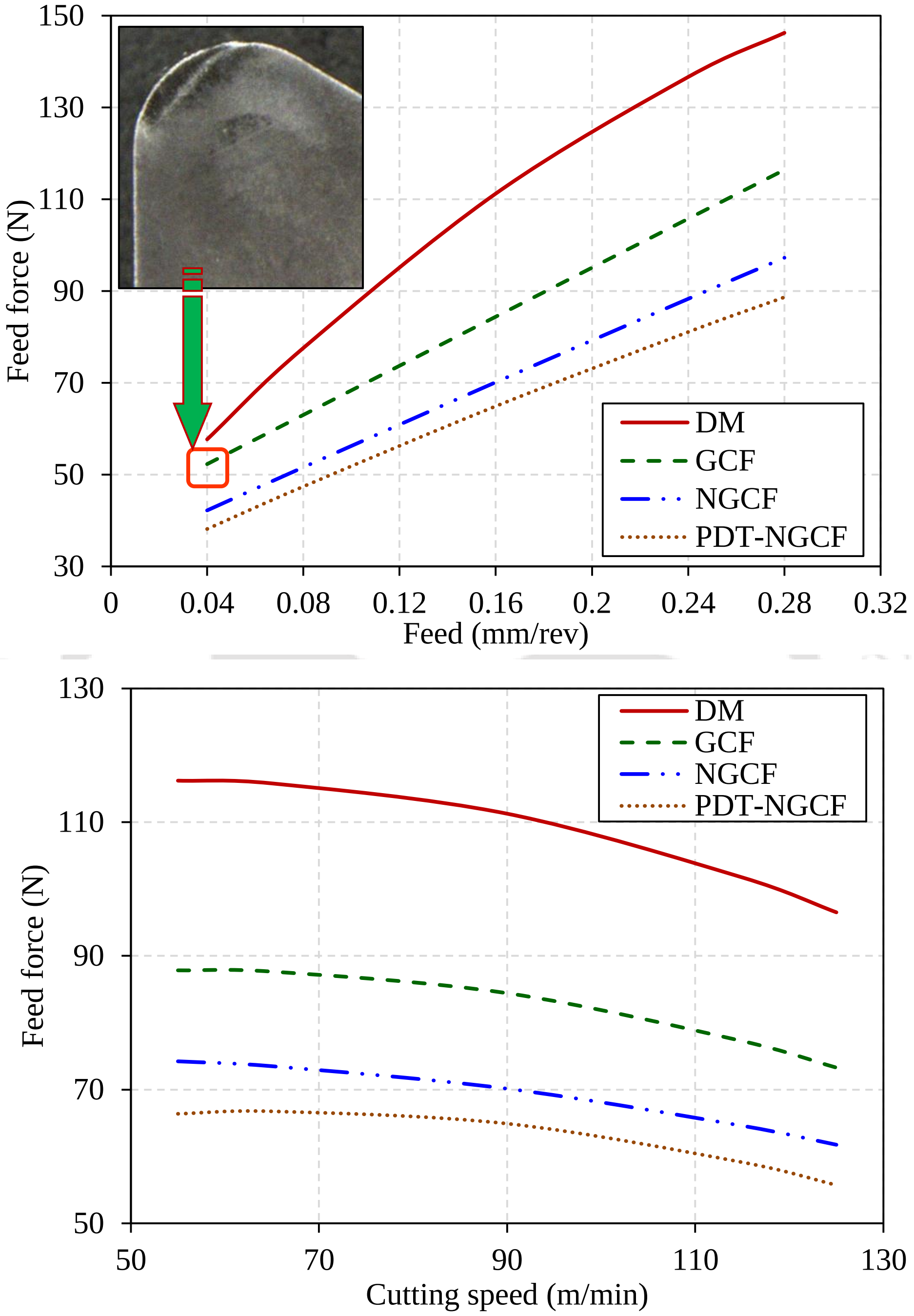

Figure 8.4. Variation of feed force with (a) feed and (b) cutting speed for various cutting tools and machining environments

Stereoscopic micrographs of the cutting tool rake surface after machining at DM, GCF, NGCF and PDT-NGCF environments are characterised for a cutting speed of 90 m/min, feed of 0.16 mm/rev and depth of cut of 0.5 mm, for 15 minutes of machining. Figure 8.5 illustrates the sticking and sliding zone for the different cutting tool with various machining environment. The sticking region exhibits full metal to metal contact, and the overall surface has a similar morphology. In contrast, the sliding region exhibits abrasion marks. The sticking and sliding regions are separated by an interface, which is highlighted in Figure 8.5 (a). The contact length was measured and tabulated as presented in Table 8.4. It was observed that the sticking and sliding widths for dry machining with DM were much larger relative to the widths during machining using various cutting fluids.

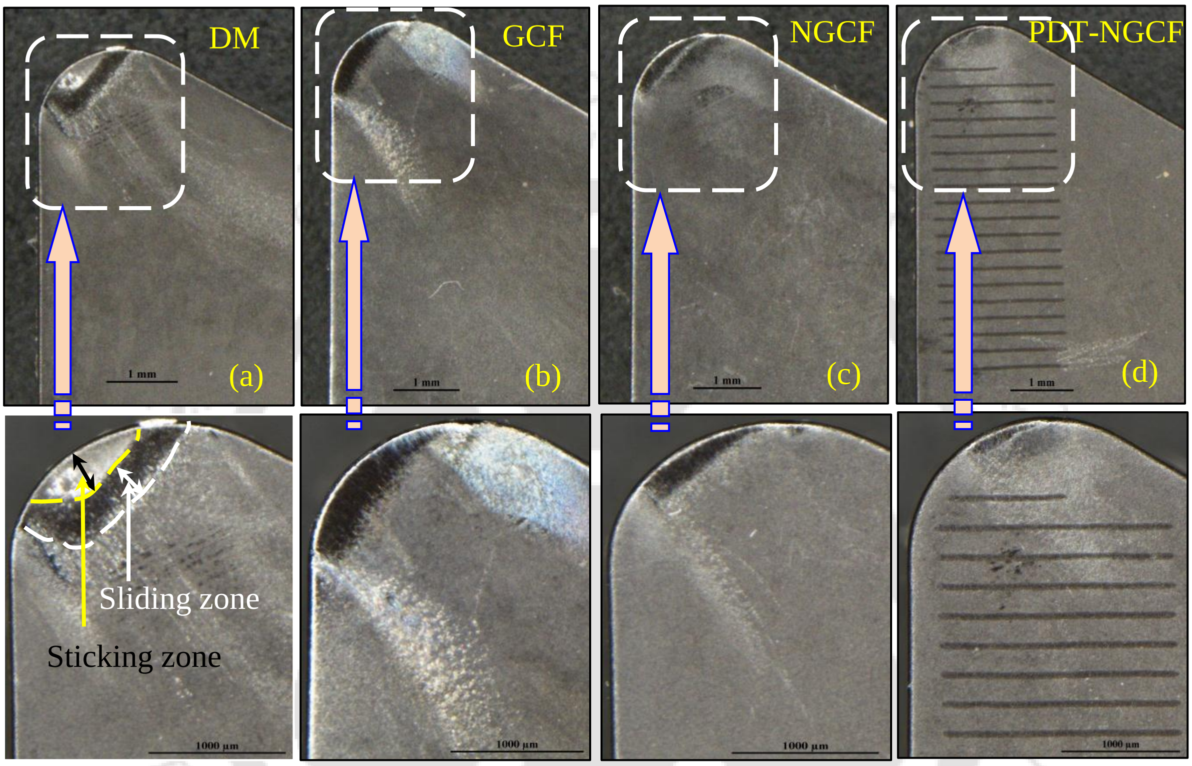

Figure 8.5: Sticking and sliding regions of the tool-chip interface during machining at (a) dry environment, (b) green cutting fluid environment, (c) nano-green cutting fluid environment and (d) perpendicular textured tool with nano-green cutting fluid environment

Least tool-chip contact length (sticking and sliding zone widths) among all four types of machining environment is observed during machining with the combination of PDT tool using NGCF. The average tool-chip contact length on the cutting tool rake surface with machining using PDT-NGCF is 371.85 µm, NGCF is 503 µm, GCF is 728.13 µm, whereas that length for DM is 1170.15 µm. A shorter tool-chip contact length results in less contact area, which leads to a reduction in the coefficient of friction. Reductions in coefficient of friction are directly related to lower machining forces and workpiece surface roughnesses. Thus, PDT-NGCF performs better relative to other combinations due to the ability of micro-channels to carry cutting fluids as well as due to better cooling and lubrication properties of NGCF.

Table 8.4. Sticking and sliding regions for the combination of various cutting tools and machining environments (v = 90m/min, f = 0.28 mm/rev and d = 0. 5 mm)

Cutting tool and machining environment	**Sticking region width (μm)**	**Sliding region width (μm)**
UT tool with DM	180.9±1.4	989.2±3.1
UT tool with GCF emulsion	149.9±0.8	578.2±1.6
UT tool with NGCF emulsion	118.9±0.4	384.1±0.9
PDT tool with NGCF emulsion	84.4±0.7	287.4±2.4

8.3.3 Tool-chip interface coefficient of friction

Tool-chip interface COF is calculated using experimental values of cutting and feed forces. The COF is given as follows [170]:

$$\mu = \frac{F_c \sin\alpha + F_f \cos\alpha}{F_c \cos\alpha - F_f \sin\alpha} \tag{8.9}$$

where F_f is the feed force, F_c is the cutting force, α is the rake angle and μ is the COF.

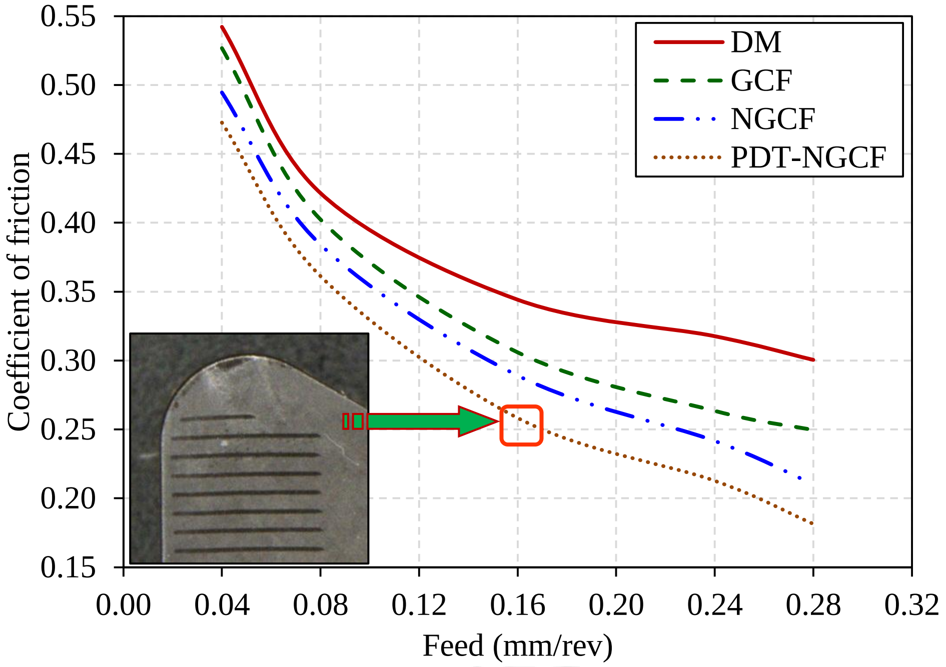

Figure 8.6. Variation of coefficient of friction with feed (v = 90 m/min, d = 0.5 mm, for 15 minutes of machining)

Figure 8.6 illustrates the average coefficient of friction at the tool-chip interface for machining using DM, GCF, NGCF and PDT-NGCF. The frictional force at the tool-chip interface depends on the tool-chip contact length. MQCF spray penetrates the tool-chip interface and reduces the contact area by providing both lubrication and cooling, resulting in the reduction of friction coefficients.

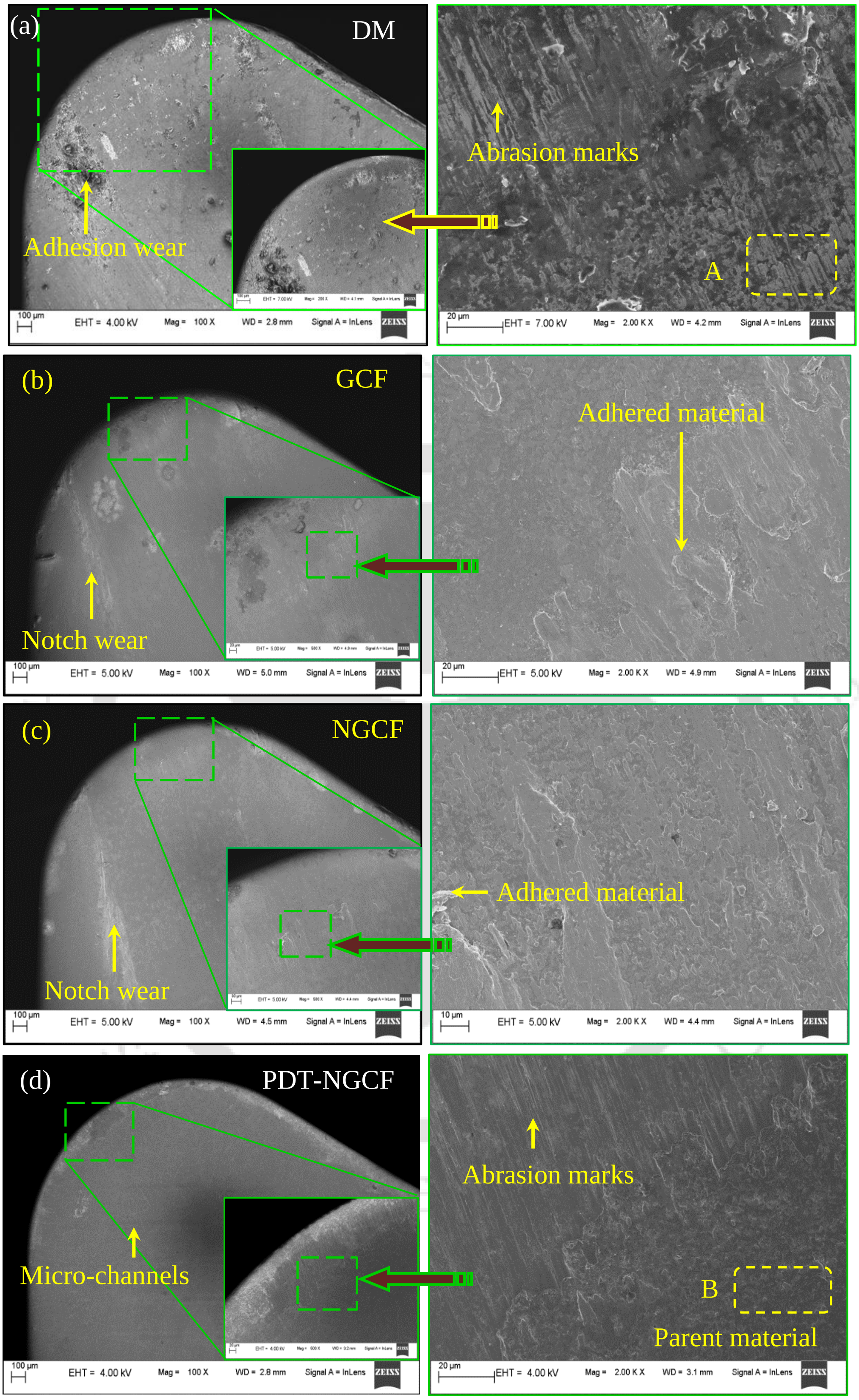

Figure 8.7. Cutting tool rake surface morphology showing tool-chip interface during (a) dry machining, machining using (b) green cutting fluid, (c) nano-green cutting fluid and (d) perpendicular texture cutting tool with nano-green cutting fluid

Moreover, NGCF reduces COF even further due to rolling, mending, lubricating and polishing effect as discussed in Chapter 7. PDT-NGCF shows even lower COF due to the ability of micro-channels to carry cutting fluids as well as due to better cooling and lubrication properties of NGCF.

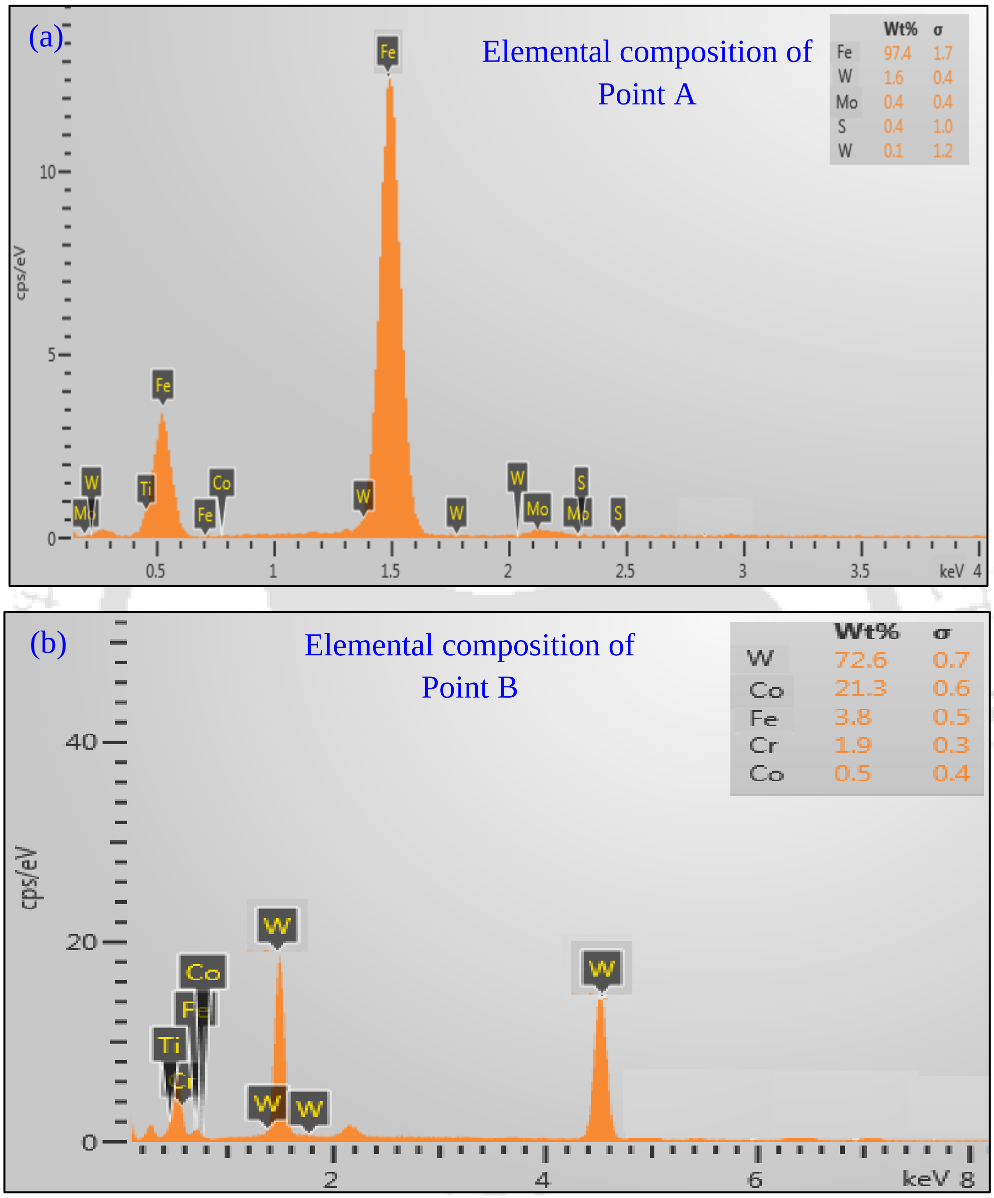

Figure 8.8. Elemental composition of cutting tool rake face at (a) adhered material location (corresponding to Point A; Figure 8.7 a) and (b) parent material location (corresponding to Point B; Figure 8.7 d)

Figure 8.7 (a-d) illustrates the surface morphology of the cutting tool rake surface after 15 minutes of machining under various machining environment. In the case DM, more severe abrasion marks on the cutting tool rake surface are observed (Figure 8.7 a). Also, adhered particles on the cutting tool rake surface are also witnessed. However, for machining with GCF, adhesion and notch wear are more predominant on the cutting tool rake surface (Figure 8.7 b). This occurs because of the high-pressure MQCF mist, which easily flushes away chip debris particles and does not allow the material to stick to the cutting tool rake surface. MQCF sprays provide proper cutting tool cooling that reduces adhesion due to rising temperatures. It also lubricates the tool-chip interface, thereby avoiding any built-up edge formation. Similar cutting tool rake surface morphology was observed in case of machining using NGCF (Figure 8.7 c). However, adhesion wear is even less as compared to the former.

Among all cutting tool rake surface after machining using MQCF with the combination of PDT tool and NGCF, the minimum abrasion wear is observed, which is a symptom of lower COF (Figure 8.7 d). MQCF machining with PDT tool using NGCF also shows lower machining forces and less tool-chip contact length. Reductions in the tool-chip contact length reduce the tool-chip contact area, which in turn leads to less heat generation and lower friction coefficients.

Figure 8.8 (a) shows the elemental composition of the adhered material (Area A; Figure 8.7 a), which is similar to the composition of the workpiece material. However, at similar position of the cutting tool when machined using PGT-NGCF, elemental composition (Area B; Figure 8.7 d) shows composition similar to the tool material. This evidence supports the adhesion of workpiece material to the cutting tool rake surface is high in the case of DM as compared to PDT-NGCF.

8.3.4 Workpiece surface roughness

The surface roughness of a machined product is an important machinability index. Equation models for workpiece surface roughness (per RSM of CCRD) are as follows (Eq. 8.10−8.13):

$$R_{a-DM} = 1.3231 + 4.439f - 0.00291v + 0.055vf + 30.39f^2 + 0.000076v^2 \qquad (8.10)$$

$$R_{a-GCF} = 1.22 + 2.69f - 0.015v - 0.0036vf + 29.28f^2 + 0.00008v^2 \qquad (8.11)$$

$$R_{a-NGCF} = 0.70 + 0.811f - 0.0036v + 0.0137vf + 23.29f^2 + 0.000006v^2 \qquad (8.12)$$

$$R_{a-PDT-NGCF} = 0.81 - 1.499f - 0.00536v + 0.0125vf + 28.77f^2 + 0.000018v^2 \qquad (8.13)$$

where v, f and R_a represent the cutting speed (m/min), feed (mm/rev) and surface roughness (µm), respectively, and the subscript of R_a denotes the machining environment.

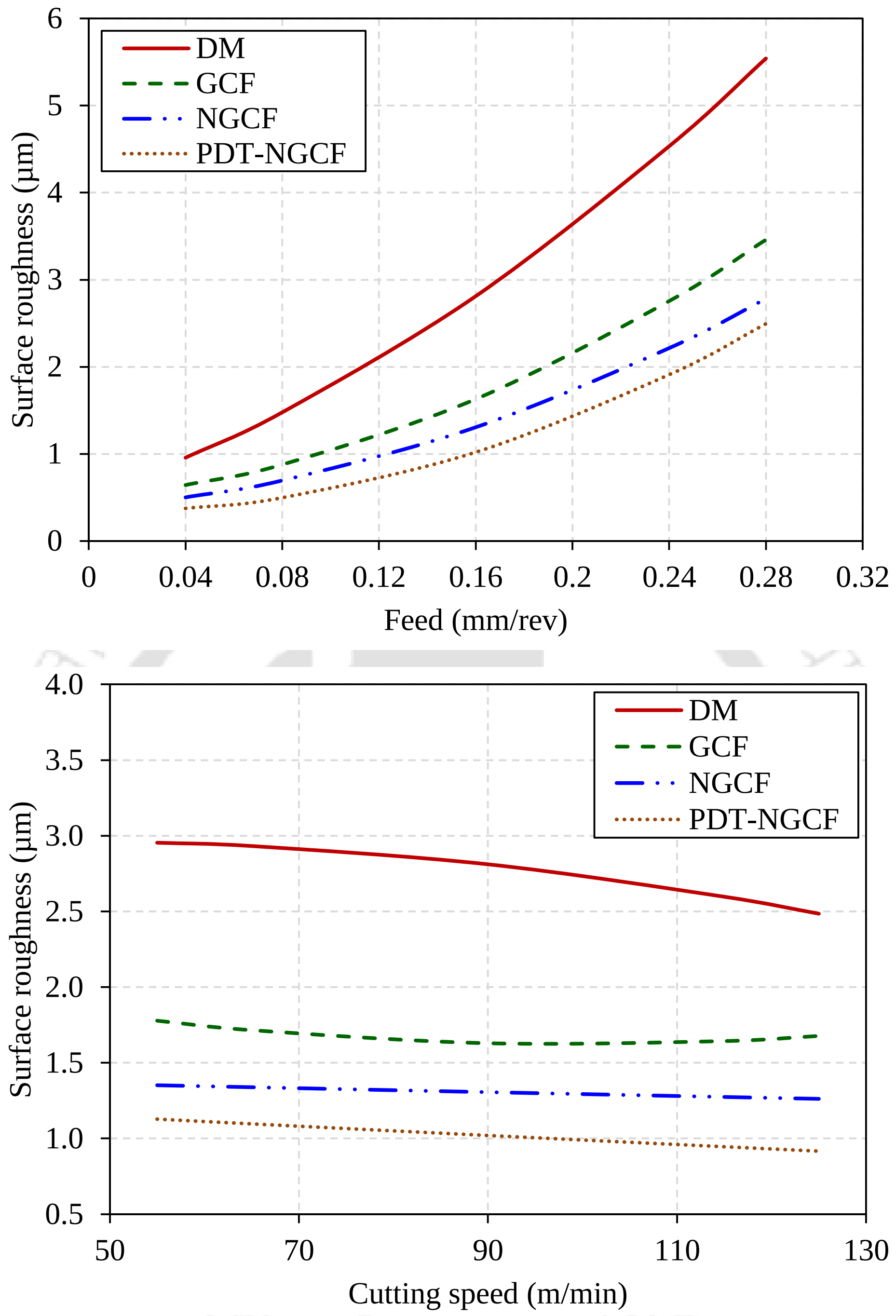

Figure 8.9. Variation of workpiece surface roughness with (a) feed and (b) cutting speed for various machining environments

Figure 8.9 (a-b) shows variations in workpiece surface roughness with feed and cutting speed. Workpiece surface roughness is observed to increase with increasing feed, irrespective of the cutting fluid application technique. In the case of DM, because of tool crater wear and high friction at the tool-chip interface, the workpiece has a higher surface roughness. Workpiece surface roughness is lower when machined at various cutting fluid environments, because of lower cutting and feed forces. This may cause comparatively less tool chatter, leading to better surface finishes, i.e. low surface roughness. From the experimental results, cutting force, feed force, coefficients of friction and workpiece surface roughnesses are reduced with GCF, NCGF and PDT-NGCF relative to DM due to cooling and lubrication properties. Among all machining environments, PDT-NGCF produces better results than DM, GCF and NGCF due to the combination of mechanical micro-textures and nano-GCF. Individually both have the ability to reduce surface roughness, and their combination improves surface finish even better due to ease in the flow of nano-GCF because of the presence of the micro-textures on the cutting tool rake surface.

8.3.5 Chip morphology

After machining, chips produced from all experiments were collected. Surface micrographs of chips were obtained using an optical microscope as well as FESEM, and average chip-thickness was measured. Experimentally obtained average values of chip thickness for various experimental runs are plotted. The average is taken for minimum three readings. Chip reduction ratio (ξ) is also plotted which is defined as the ratio of average chip thickness to uncut chip thickness.

The variation of chip thickness and chip reduction ratio (ξ) with varying feed at constant cutting speed (v = 90 m/min) and depth of cut (d = 0.5 mm) are shown in Figure 8.10 (a-b). It is observed that chip thickness and chip reduction ratio has a significant effect with respect to feed. As the feed increases, chip thickness and chip reduction ratio are also increasing trend irrespective of the type of machining environment whereas it is also observed that at the constant feed, chip thickness and chip reduction ratio are showing a downward trend with the machining with DM, GCF, NGCF and PDT-NGCF. Out of all, PDT-NGCF chip thickness was least among all.

Collected chip micrographs of machined hardened AISI H-13 tool steel at cutting speed v = 90 m/min, depth of cut d = 0.5 mm with two different feed = 0.08 and 0.24 mm /rev and four different machining environment are illustrated in Figure 8.11. For the lower feed, metallic colour continuous chips were observed. Chip morphologies with different machining environment at lower feed are almost similar to the DM cutting tool chips apart from chip thickness.

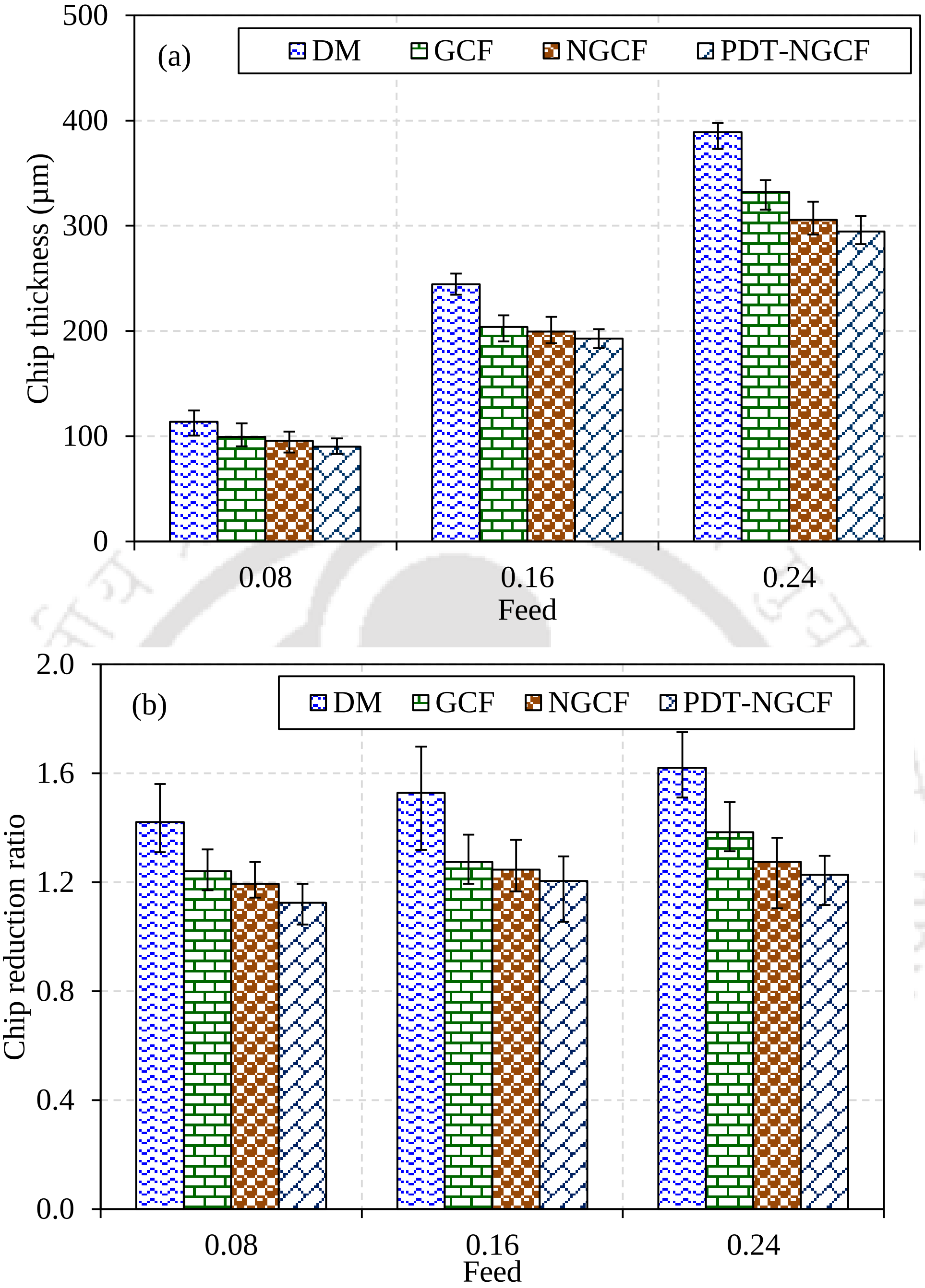

Figure 8.10. Effect of feed on (a) chip thickness and (b) chip reduction ratio for different machining environment

With the increase in feed, dark blue colour continuous chips were formed with DM cutting tools. However, metallic colour chips were observed with machining using NGCF and PDT-NGCF. With PDT-NGCF machining, chip thickness and chip reduction ratio were reduced much more that indicates better machinability of hardened AISI H-13 tool steel.

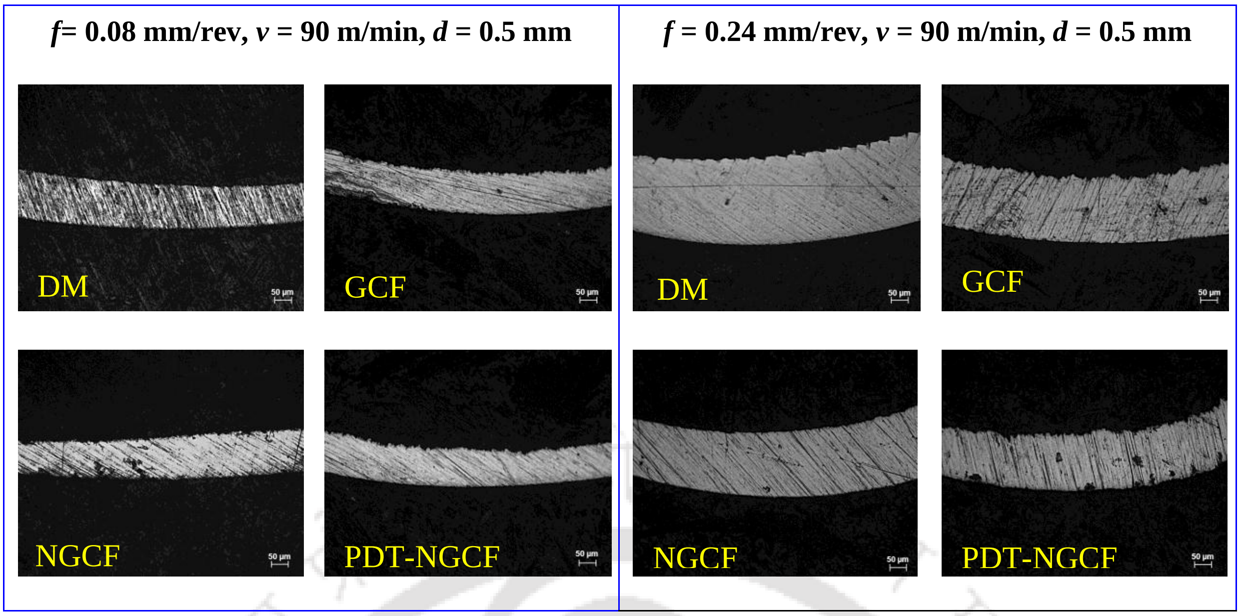

Figure 8.11. Chip morphologies of hardened AISI H-13 tool steel machined at different environments (*v* = 90m/min, *d* = 0. 5 mm with two different feed *f* = 0.08 and 0.24 mm/rev)

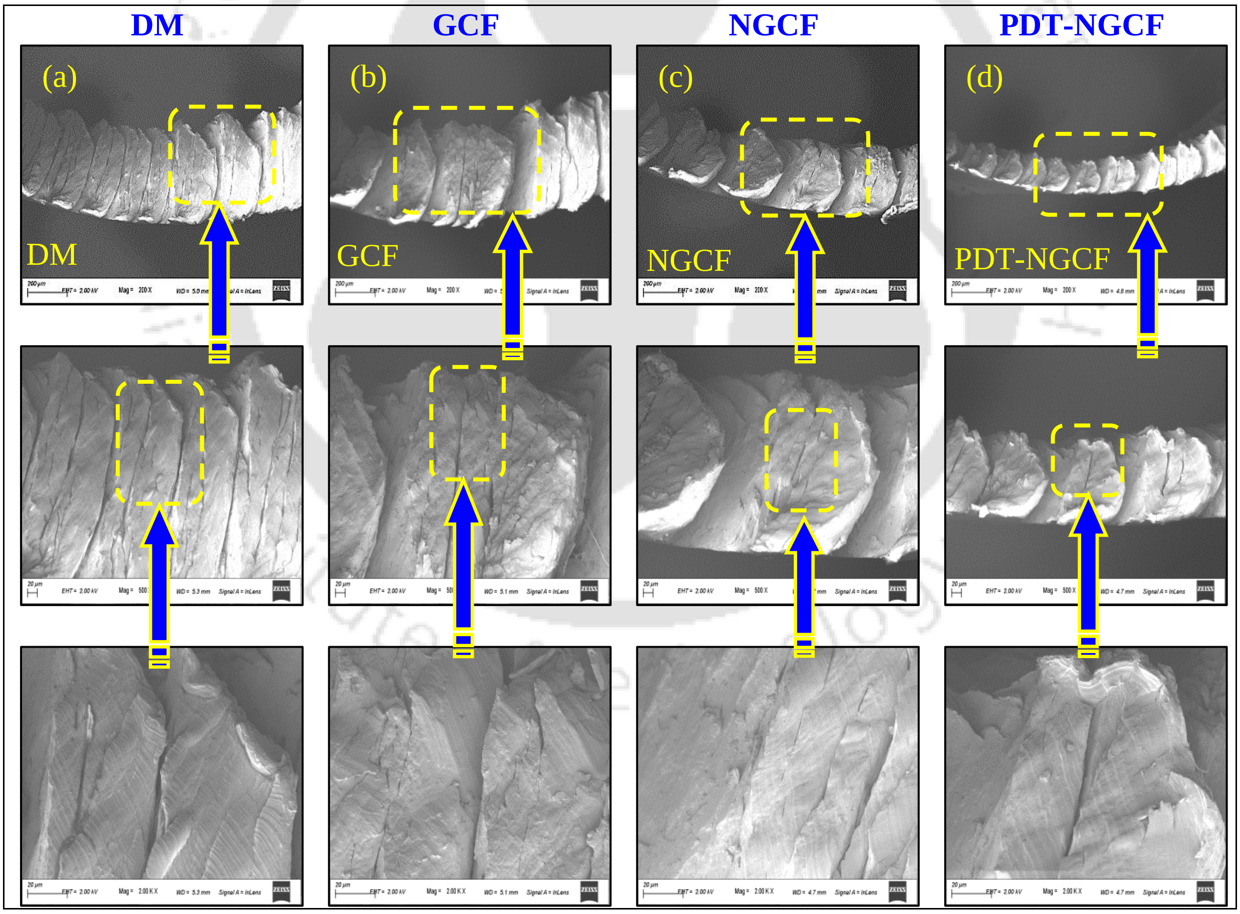

Figure 8.12. Surface micrograph of the top surface of chips machined at at (a) dry environment, (b) green cutting fluid environment, (c) nano-green cutting fluid environment and (d) perpendicular textured tool with nano-green cutting fluid environment (*v* = 90m/min, *f* = 0.16 mm/rev and *d* = 0. 5 mm)

Figure 8.12 illustrates the chip surface morphology for DM, GCF, NGCF and PDT-NGCF machining environments. It was observed that severe chip serrations occur in the top (free) surface of the chip, which is caused due to periodic crack propagation and severe plastic deformation of chips. Due to the large angle of the cutting tool, high compressive stresses are experienced, which results in plasticization.

In the case of PDT-NGCF machining environments, the longitudinal strain is low as compared to NGCF, GCF and DM. Cut chip thickness is the least for chip during machining at PDT-NGCF machining environments as compared to NGCF, GCF and DM. This suggests that less chip thickening occurs and redundant plastic deformation work is the least in the case of machining at PDT-NGCF environment. It is due to the less friction between tool-chip interfaces at PDT-NGCF machining environment, which provide less resistance to flow to chip in width direction.

8.4 Findings from the research work

In this Chapter, the hybridisation of four individual sustainable machining processes was carried out. For hard machining, a combination of the mechanical-micro-textured cutting tool with in-house fabricated minimum quantity cutting fluid using in-house developed nano-green cutting fluid is used. Hard machining experiments are carried out, and the results are compared with DM, GCF and Nano-GCF. The salient findings are as follows:

- Cutting force, feed force and workpiece surface roughness were reduced in the range of 38−59.5 %, 15.9−39.2 % and 15.9−61 %, respectively, as compared to DM with UT cutting tools.
- Amongst all, PDT-NGCF machining environment is best in terms of reducing tool-chip interface temperature, machining forces and tool-chip interface COF.
- In the case of machining with PDT-NGCF, at cutting speed of 90 m/min, feed of 0.28 mm/rev and depth of cut of 0.5 mm, 37.5 % COF was reduced. Also, workpiece surface roughness was reduced by 66.5% as compared to DM.
- In the case of machining with PDT-NGCF, the improvement is attributed to lower tool-chip contact length, better thermal conductivity of NGCF, reduced tool-chip interface contact length and due to passage provided by micro-textures for ease in flow of cutting fluid emulsion.
- Reduced chip thickness and least redundant plastic deformation work were observed in the case of machining at PDT-NGCF environment.

Chapter 9

CONCLUSION AND SCOPE FOR FUTURE WORK

9.1. Summary of the thesis work

Tribological studies revealed that 10 % area density mechanical micro textured (MµT) pins showed lower coefficient of frivtion (COF) and wear among all tested pins (0−14 % area density MμT pins). Afterwards, 10 % area density textures were fabricated on the rake surface of HSS cutting tool using Vickers hardness tested. Feasibility studies were carried out that confirms the reduction of cutting temperature, machining forces, COF and workpiece surface roughness using uncoated and MoS_2 coated MμT cutting tool as compared to the untextured (UT) cutting tool. The better machining performance of MoS_2 coated MμT cutting tool is attributed to the reduction of the real contact area, formation of the self-lubricating film and entrapment of wear debris inside MμT.

Furthermore, in Chapter 4, three different geometric MμT cutting tools were fabricated and coated with MoS_2. Hard machining performance revealed that uncoated and coated perpendicular textured (PDT and PDTM) cutting tools were able to perform better in terms of machining forces, COF and workpiece surface roughness. The better machining performance of PDTM cutting tool is due to the perpendicular inclination of micro-textures, which reduces the maximum real contact length. Table 8.5 tabulates the quantitative reduction of machining forces, COF and workpiece surface roughness with various cutting tools and machining environment (v = 90m/min, f = 0.28 mm/rev and α = 0. 5 mm). PDT cutting tool shows 8.38 % reduction in COF and 10.41 % reduction in workpiece surface roughness as compared to UT cutting tool (Table 8.5).

In Chapter 5, green cutting fluid (GCF) was synthesised, and its thermal, rheological, biodegradation, anti-corrosion as well as storage stability studies were compared with commercial mineral oil (MO) and eco-friendly bio-cutting fluid (BCF). Among all three, GCF shows better-tested properties with more than 98 % biodegradation.

Afterwards, in Chapter 6, minimum quantity cutting fluid (MQCF) experimental setup was fabricated, and hard machining was performed with three different cutting fluids. Results were also compared with dry machining (DM). It was observed that MQCF machining was better than DM. As the MQCF method uses a mist, micro-cutting fluid droplets have a better chance of reaching between the tool-chip interface. An MQCF spray containing cutting fluid can penetrate the sliding zone and probably small areas of the sticking zone, because of the high force exerted by the pressurised mist in the tool-chip interface. Also, BCF and GCF shows lower COF as compared to MQCF machining using MO as well as DM. It is attributed to better thermal properties and penetrating ability of BCF and GCF mist. MQCF with GCF shows 16.67 % reduction in COF and 37.55 % reduction in workpiece surface roughness as compared to DM (Table 9.1).

Table 9.1. Quantitative comparison of reduction of machining forces, coefficient of friction and workpiece surface roughness with various cutting tools and machining environment (v = 90 m/min, f = 0.28 mm/rev and α = 0. 5 mm)

Tool type	**Machini-ng environ-ment**	**Cutting fluid**	**Reduction in cutting force (%)**	**Reduction in feed force (%)**	**Reduction in coefficient of friction (%)**	**Reduction in workpiece roughness (%)**
UT	DM	Datum Reference				
PDT	DM	---------	4.10	12.07	8.38	10.41
PDTM	DM	---------	8.27	14.53	9.94	14.02
UT	MQCF	MO	22.00	17.61	10.71	28.58
UT	MQCF	BCF	30.57	27.32	18.47	44.46
UT	MQCF	GCF	25.67	20.41	16.67	37.55
UT	MQCF	NGCF	35.02	35.59	20.05	55.00
PDT	**MQCF**	**NGCF**	**42.17**	**39.38**	**37.52**	**66.48**

To further improve the performance of GCF, solid lubricant (CaF_2 and MoS_2) based nanoparticles (0.1 % to 0.5 %) were dispersed in GCF. Their thermal, rheological as well as wettability test, were carried out. Machining experiments were conducted, and it was revealed that NGCF (GCF-0.3M) with MQCF were able to reduce 20.05 % COF and 55 % workpiece surface roughness as compared to DM (Table 8.5). Better performance of nano-green cutting fluid (NGCF) is attributed to four different mechanisms namely mending effect, rolling effect, lubricating film and polishing effect.

Finally, in this Chapter, PDT MμT cutting tool was used for hard machining with MQCF experimental setup using NGCF. The main aim was to perform hybrid machining to enhance overall machining performance. Hybridization of PDT cutting tool with MQCF using NGCF was able to reduce 37.52 % COF and 66.48 % workpiece surface roughness. Also, cutting and feed forces were reduced by 42.17 % and 39.38 %, respectively as compared to dry machining using UT tools. It was attributed due to the combined effect of PDT toom, MQCF and NGCF.

9.2. Conclusion

In the current work, tribological and machining performance of micro-textured cutting tool is carried out. Also, environmental friendly GCF is developed. The physical, thermal, rheological, biodegradation, anti-corrosion and storage stability properties of GCF, BCF as well as MO are compared. The MQCF experimental setup is developed and hard machining experiments are carried out with DM as well as MQCF using three cutting fluids (MO, BCF, GCF). Further, nano-GCFs are prepared using varying concentration (0.1%−0.5%, at interval of 0.1%) of MoS_2 and CaF_2. These nano-GCFs are characterised and used during hard machining experiments. Later, hard machining experiments are carried out with the combination of mechanical-micro-textured cutting tool using in-house fabricated MQCF with indigenously developed nano-GCFs. On the basis of work reported (mechanical micro-textured cutting tool, environmental friendly GCF and nano-GCFs), the following conclusions are drawn:-

9.2.1. Tribological and machining performance of mechanical micro-textured cutting tools

9.2.1.1. Tribological performance of mechanical micro-textured pins

i. Mechanical texture was fabricated on the sliding surface of plasma nitrided HSS cutting tool with a Vickers hardness tester. MoS_2 solid lubricant along with graphite-based grease was filled in the micro-indents.

ii. The coefficient of friction (COF) between MoS_2 filled textured 10 % texture area density pin was reduced by 51.37% and 53.33% as compared to UT pins under 19.6 N and 49 N loads, respectively.

iii. MoS_2 filling of textured tools reduced the pin surface temperature, wear, weight loss of pin and wear rate.

iv. MoS_2 filled pins with 10% texture area density showed the best tribological performance amongst all investigated samples.

v. Surface morphology and elemental mapping analysis confirmed the formation of the self-lubricating film between sliding surfaces for MoS_2 filled micro-textured pin.

9.2.1.2. Machining performance of mechanical micro-textured cutting tools

For preliminary experiments, the Vicker hardness tester was used to fabricate mechanical micro-textures (MμT, 10% area density) over the rake face of PN-HSS cutting tools, and molybdenum disulphide solid lubricant was coated over mechanical micro-textures. Machining tests were performed using un-textured (UT), MμT, and MoS_2 coated-MμT (C-MμT) and the obtained conclusions are detailed as follows:

i. Finite element analysis shows that von-Mises stress generation at the cutting edge of UT and MµT cutting tool are within safe limits. Also, the presence of the mechanical micro-textures on the tool rake surface had very less influence on the mechanical strength of the cutting tool.
ii. Tool-chip interface temperature and COF along with machining forces and tool-chip interface were reduced significantly for MµT and C-MµT as compared to UT cutting tools.
iii. Workpiece surface roughness reduces with MµT and C-MµT cutting tools as compared to UT cutting tool.
iv. In C-MµT cutting tool, formation of the self-lubricating film during machining reduces friction, which is the prime reason for the improvement in its cutting performance.

9.2.1.3. Comparative hard machining performance of various mechanical micro-textured tungsten carbide cutting tools

i. Tool-chip interface temperature, machining forces and tool-chip interface COF are reduced significantly for Vickers texture (VT), parallel texture (PT), perpendicular texture (PDT), MoS_2 coated Vickers texture (VT-M), MoS_2 coated parallel texture (PT-M) and MoS_2 coated perpendicular texture (PDT-M) as compared to UT cutting tools.
ii. The improvements in machining performance of uncoated MµT cutting tools are due to reduced contact length and air flow cooling through micro-textures.
iii. During machining with MoS_2 coated MµT cutting tools, the formation of a self-lubricating film reduces friction and thus enhancing its machining performance.
iv. Cutting force was reduced in the range of 4.23−10.82 % and 7.31−17.41 %, respectively, with PDT and PDT-M as compared to UT cutting tools.
v. Amongst all, PDT-M cutting tool machining performance is best in terms of reducing tool-chip interface temperature, machining forces and tool-chip interface COF.
vi. Reduced chip thickness and least redundant plastic deformation work were observed in the case of machining using PDT-M cutting tool.

9.2.2. Synthesis and characterisation of environmental friendly cutting fluids

i. Green cutting fluid (GCF) was synthesised using various environmental friendly vegetable based oils, emulsifiers and additives.

ii. The flash point of GCF is higher as compared to bio-cutting fluid (BCF) and mineral oil (MO) that allows its use for high-temperature hard machining.

iii. As per *Standard methods 2005*, the ultimate biodegradability of GCF, BCF and MO are found to be 98.27%, 96.67% and 18.32%, respectively.

iv. GCF exhibits less variation from Newtonian behaviour even at the higher temperature. Also, its sensitivity to temperature is lower as compared to BCF and MO.

v. GCF showed corrosion breakpoint of 4; whereas BCF and MO exhibit corrosion breakpoint of 8 and 9 as per ASTM D 4627 standard.

vi. As per ASTM D 3707 standard, GCF shows more remaining emulsion as compared to BCF and MO after storage stability test.

9.2.3. Hard machining performance of various cutting fluids

9.2.3.1 Comparative performance of various cutting fluids using minimum quantity cutting fluids

i. An indigenous minimum quantity cutting fluid (MQCF) setup was fabricated.

ii. 1:16 emulsion composition was found to be optimum in terms of its better thermal conductivity, volumetric specific heat as well as its storage stability as per ASTM D 3707 standard.

iii. Optimum MQCF nozzle stand-off distance was found to be 30 mm by considering mist coverage region and cutting forces exerted by mist at tool-chip interface.

iv. With 45° nozzle angle, MQCF mist could penetrate better into the air boundary periphery that is generated by the rotating workpiece.

v. Relative to DM, machining with MQCF (using all three cutting fluid emulsions) produced better results in terms of the cutting force, feed force, coefficient of friction, and workpiece surface roughness.

vi. The BCF emulsion performed better than MO and GCF, in terms of its higher thermal conductivity, high specific heat, and reduced tool-chip interface contact length.

vii. Sticking and sliding zones were reduced in the case of MQCF machining. The BCF emulsion performed better than the MO and GCF emulsion in this regard.

9.2.3.2 Performance of MoS_2 and CaF_2 based minimum quantity nano-green cutting fluids

i. MoS_2 and CaF_2 based nano-GCFs with varying concentration (0.1%–0.5%, at interval of 0.1%) were developed and characterised.

ii. The thermal conductivity, specific heat and viscosities are higher for MoS_2 based eco-friendly nano-cutting fluids as compared to others.
iii. The 0.3 % concentration of CaF_2 and MoS_2 based eco-friendly nano-GCFs were found to have optimised thermal conductivity, specific heat and viscosities.
iv. GCF-0.3M had 47 %, 39 %, 33 %, 25% and 14 % better wettability as compared to other MO, BCF, GCF and GCF-0.3C, respectively.
v. Eco-friendly nano-GCFs performed better as compared to GCF, BCF and MO concerning cutting forces, feed forces, tool-chip interface coefficient of friction and workpiece surface roughness.
vi. Hard machining performance of MoS_2 based nano-GCFs performed better among all.
vii. GCF-0.3M reduced the tool-chip interface coefficient of friction by 11 %, 4 %, 5 % and 2 % as compared with MO, BCF, GCF and GCF-0.3C, respectively.
viii. GCF-0.3M reduced the workpiece surface roughness by 37 %, 22 %, 12 % and 13 % as compared with MO, GCF and GCF-0.3C, respectively.
ix. Cutting tool wear and adhesion of workpiece material to tool rake surface was lower for GCF-0.3M as compared to all others tested cutting fluids.

9.2.4. Hard machining performance with hybrid mechanical micro-textured cutting tools and minimum quantity nano-green cutting fluids

i. Cutting force, feed force and workpiece surface roughness were reduced in the range of 38−59.5 %, 15.9−39.2 % and 15.9−61 %, respectively, as compared to DM with UT cutting tools.
ii. Amongst all, PDT-NGCF machining environment is best in terms of reducing tool-chip interface temperature, machining forces and tool-chip interface COF.
iii. In the case of machining with PDT-NGCF, at cutting speed of 90 m/min, feed of 0.28 mm/rev and depth of cut of 0.5 mm, 37.5 % COF was reduced. Also, workpiece surface roughness was reduced by 66.5% as compared to DM.
iv. In the case of machining with PDT-NGCF, the improvement is attributed to lower tool-chip contact length, better thermal conductivity of NGCF, reduced tool-chip interface contact length and due to passage provided by micro-textures for ease in flow of cutting fluid emulsion.
v. Reduced chip thickness and least redundant plastic deformation work were observed in the case of machining at PDT-NGCF environment.

9.3. Scope for future work

There is a lot of scope for further sustainable machining research work as briefly stated in the following section.

9.3.1. Micro-textured cutting tools

- Inclined and curvilinear micro-textured cutting inserts performance needs to be explored and compared machining performance as well as tool life with existing parallel and perpendicular micro-groove textured cutting tools.
- Comparative study of various solid lubricants such as MoS_2, CaF_2, WS_2, graphite, etc. needs to be carried out with combination of mechanical micro-textured cutting tools.
- Machining performance comparison of mechanical micro-textured cutting tools with laser textured, focus ion beam textured as well as micro-EDM textured cutting tools can be done to emphasis more on its effect on workpiece surface roughness and tool life.
- The research can also be focused on bio-mimicking some natural textures on tool rake face to make it more hydrophilic and different possibilities of texture patterns can also be studied to improve the hydrodynamic lubrications on the cutting tool surface. The texture dimension (depth and width) optimization needs to be explored in the future to make the machining more environment-friendly while machining difficult to cut materials.

9.3.2. Minimum quantity nano-cutting fluid

- Chip evacuation ability and initial equipment cost are two significant challenges, which will require attention in full MQCF implementations. Tool-chip interface temperature studies can also be performed to correlate with machining forces and coefficient of friction.
- In addition, not all cutting fluid compositions are suitable for MQCF. The optimisation of cutting fluid compositions requires more detailed investigations.
- New MQCF setup designs using controlled air-entrapped cutting fluids may have good potential in achieving better machining. Investigations into MQCF should also emphasise reducing power consumption, enhancing lubrication, and improving cooling capability, in order to create a sustainable and clean manufacturing environment. Further investigation can also be focused on the application of MQCF with hybrid nanofluids in machining of different materials.
- New GCF with custom ingredients as per requirement of applications can be prepared. Refrigeration of cutting fluid while its application can be explored for better cooling.

Multiple MQCF jets with varying emulsion concentration at rake surface and flank surface can be explored to get better cooling and lubricating properties for lesser tool wear and better surface finish.

9.4. Publications

9.4.1. International Journals: Published

1. **Kishor Kumar Gajrani**, P. S. Suvin, Satish Vasu Kailas, Mamilla Ravi Sankar, 2019, **"Thermal, rheological, wettability and hard machining performance of MoS$_2$ and CaF$_2$ based minimum quantity hybrid nano-green cutting fluids"**, Journal of Materials Processing Technology, Vol. 266, pp. 125−139. (**DOI**: 10.1016/j.jmatprotec.2018.10.036).
2. **Kishor Kumar Gajrani**, P. S. Suvin, Satish Vasu Kailas, Mamilla Ravi Sankar, 2019, **"Hard machining performance of indigenously developed green cutting fluid using flood cooling and minimum quantity cutting fluid"**, Journal of Cleaner Production, Vol. 206, pp. 108−123. (**DOI:** 10.1016/j.jclepro.2018.09.178)**.**
3. **Kishor Kumar Gajrani,** Somapalli Suresh, Mamilla Ravi Sankar, 2018, **"Environmental friendly hard machining performance of uncoated and MoS$_2$ coated mechanical micro-textured tungsten carbide cutting tools"**, Tribology International, Vol. 125, pp. 141−155. (**DOI**: 10.1016/j.triboint.2018.04.031).
4. **Kishor Kumar Gajrani**, Mamilla Ravi Sankar, Uday Shanker Dixit, 2018, "**Tribological performance of MoS$_2$-filled microtextured cutting tools during dry sliding test",** ASME Journal of Tribology, Vol. 140(2), 2018, pp. 021301 (1−11). (**DOI**: 10.15/1.4037354).
5. **Kishor Kumar Gajrani**, Rokkham Pavan Kumar Reddy, Mamilla Ravi Sankar, 2018, **"Tribo-mechanical, surface morphological comparison of un-textured, mechanical micro-textured (MμT) and coated-MμT cutting tools during machining",** Proceedings of the Institution of Mechanical Engineers, Part J: Journal of Engineering Tribology, 2018. **(DOI:** 10.1177/1350650118764975).
6. **Kishor Kumar Gajrani**, Mamilla Ravi Sankar, Uday Shanker Dixit, 2018, "**Environmentally friendly machining with MOS$_2$ filled mechanically micro-textured cutting tools",** Journal of Mechanical Science and Technology, Vol. 32(8), pp. 3797−3805. (**DOI:** 10.1007/s12206-018-0732-5).
7. **Kishor Kumar Gajrani**, Dhanna Ram, Mamilla Ravi Sankar, 2017, "**Biodegradation and hard machining performance comparison of eco-friendly cutting fluid and mineral oil using flood cooling and minimum quantity cutting fluid techniques",** Journal of Cleaner Production, Vol. 165(C), 2017, pp. 1420−1435. (**DOI**: 10.1016/j.jclepro.2017.07.217).

8. **Kishor Kumar Gajrani**, Dhanna Ram, Mamilla Ravi Sankar, Uday Shanker Dixit, P. S. Suvin, Satish Vasu Kailas, 2017, **"Machining of hardened AISI H-13 steel using minimum quantity eco-friendly cutting fluid",** International Journal of Additive and Subtractive Materials Manufacturing, Vol. 1 (3/4), 2017, pp. 240−256. (**DOI**: 10.1504/IJASMM.2017.10010905).
9. **Kishor Kumar Gajrani**, Rokkham Pavan Kumar Reddy, Mamilla Ravi Sankar, 2016, **"Experimental comparative study of conventional, micro-textured and coated micro-textured tools during machining of hardened AISI 1040 alloy steel",** International Journal of Machining and Machinability of Materials, Vol. 18(5/6), 2016, pp. 522−539. (**DOI**: 10.1504/IJMMM.2016.078982).

9.4.2. International Journals: Under preparation

10. **Kishor Kumar Gajrani**, P. S. Suvin, Satish Vasu Kailas, Mamilla Ravi Sankar, 2018, **"Environmentally friendly hard machining performance using hybridization of mechanical micro-textured cutting tool with minimum quantity nano-green cutting fluids "** (Under preparation).

9.4.3. International Procedia Journals: Published

11. **Kishor Kumar Gajrani**, Mamilla Ravi Sankar, 2017, **"State of the art on micro to nano textured cutting tools",** Materials Today: Proceedings, Vol. 4(2A), pp. 3776−3785. (**DOI**: 10.1016/j.matpr.2017.02.274).
12. **Kishor Kumar Gajrani**, Mamilla Ravi Sankar, 2017, **"Past and current status of eco-friendly vegetable oil based metal cutting fluids",** Materials Today: Proceedings, Vol. 4(2A), pp. 3786−3795. (**DOI**: 10.1016/j.matpr.2017.02.275).

9.4.4. Book chapter: Published and Accepted

1. **Kishor Kumar Gajrani**, Mamilla Ravi Sankar, 2018, **"Sustainable cutting fluids: Thermal, rheological, biodegradation, anti-corrosion, storage stability studies and its machining performance",** Reference Module in Materials Science and Materials Engineering, Elsevier. (**DOI:** 10.1016/B978-0-12-813195-4.11152-X).
2. **Kishor Kumar Gajrani**, Mamilla Ravi Sankar, 2018, **"Sustainable machining with self-lubricating coated mechanical micro-textured cutting tools",** Reference Module in Materials Science and Materials Engineering, Elsevier. (**DOI:** 10.1016/B978-0-12-803581-8.11325-6).

3. **Kishor Kumar Gajrani**, Y. Bishal Singha, Mamilla Ravi Sankar, Uday Shanker Dixit, 2018, **"Tribological and machining performance of graphite, CaF_2 and MoS_2 coated mechanical micro-textured self-lubricating cutting tool material"**, Manufacturing Engineering, Springer. **(Accepted)**.

9.4.5. Conferences

1. **Kishor Kumar Gajrani**, Y. Bishal Singha, Mamilla Ravi Sankar, Uday Shankar Dixit, **"Tribological performance of graphite, CaF_2 and MoS_2 coated mechanical micro-textured self-lubricating cutting tool material"** Vth International Conference on Production & Industrial Engineering (CPIE), 26−29 June, 2018, Urbana Sathorn, Bangkok, Thailand.
2. **Kishor Kumar Gajrani,** Mamilla Ravi Sankar **"Cutting fluid emissions in mechanical machining and its adverse effects on biodiversity"** 21ST ADNAT Convention and International Symposium on Biodiversity and Biobanking (BIODIVERSE 2018), 27−29 January, 2018, IIT Guwahati, India.
3. **Kishor Kumar Gajrani**, Subrat Kumar Mallick, Mamilla Ravi Sankar, **"Comparative studies on mineral oil, eco-friendly bio-cutting fluids treatment and their machining performance"** Proceedings of the National Conference on Sustainable Mechanical Engineering: Today and Beyond (SMETB), March 25−26, 2017 at Tezpur University, India, pp. 111−116, 2017 **(BEST PAPER AWARD)**.
4. Mamilla Ravi Sankar, **Kishor Kumar Gajrani**, **"Cutting fluid emissions and eco-friendly cutting fluid for sustainable machining"** Proceedings of the National Conference on Sustainable Mechanical Engineering: Today and Beyond (SMETB), March 25−26, 2017 at Tezpur University, India, pp. 157−162, 2017.
5. **Kishor Kumar Gajrani**, Dhanna Ram, Mamilla Ravi Sankar, Uday Shankar Dixit, P. S. Suvin, Satish Vasu Kailash, **"Machining of hardened AISI H-13 steel using minimum quantity indigenously developed eco-friendly cutting fluid"**, IVth International Conference on Production & Industrial Engineering (CPIE), 19−21 December, 2016, NIT Jalandhar, pp. 179 (1−10). . [Extended version of this paper is published as Journal #6]
6. **Kishor Kumar Gajrani**, Mamilla Ravi Sankar, Divyansh Bhatnagar, M. Manohar, **"Influence of mechanical micro-textured cutting tool on chip formation during machining of hardened AISI H-13 steel"**, 6th International and 27th All India Manufacturing Technology Design and Research (AIMTDR) Conference, 16−18 December, 2016, COEP Pune, pp. 1284−1288, 2016.

7. **Kishor Kumar Gajrani**, P. S. Suvin, Satish Vasu Kailash, Mamilla Ravi Sankar, **"Comparative studies on thermal, rheological behaviour of eco-friendly cutting fluids and their machining performance"**, 6th International and 27th All India Manufacturing Technology Design and Research (AIMTDR) Conference, 16−18 December, 2016, COEP Pune, pp. 674−678, 2016.
8. **Kishor Kumar Gajrani**, Subrat Kumar Mallick, Praveen Verma, Mamilla Ravi Sankar, **"Bio-degradability and machining performance comparison of mineral oil and bio-cutting fluids"**, Recycle – 2016, International Conference on Waste Management, 1−2 April, 2016, IIT Guwahati, pp. 107, 2016.
9. **Kishor Kumar Gajrani**, Mamilla Ravi Sankar, **"State of the art on micro to nano textured cutting tools"**, 5th International Conference of Materials Processing and Characterization (ICMPC), 12−13 March, 2016, GRIET Hyderadbad, India, 2016. [Also published as Procedia Journal #11]
10. **Kishor Kumar Gajrani**, Mamilla Ravi Sankar, **"Past and current status of eco-friendly vegetable oil based metal cutting fluids"**, 5th International Conference of Materials Processing and Characterization (ICMPC), 12−13 March, 2016, GRIET Hyderadbad, India, 2016. [Also published as Procedia Journal #12]
11. Rokkham Pavan Kumar Reddy, **Kishor Kumar Gajrani**, Mamilla Ravi Sankar, **"Experimental comparative study of conventional and micro-textured tools during machining of AISI 1040 alloy steel"**, 5th International and 26th National All India Manufacturing Technology Design and Research Conference (AIMTDR), 12−14 December, 2014, IIT Guwahati, Guwahati, India, pp. 51 (1−6), 2014. [Extended version of this paper is published as Journal #7]
12. **Kishor Kumar Gajrani**, Sumit Shekhar, Mamilla Ravi Sankar, **"Experimental comparative study of conventional, micro-textured and coated micro-textured cutting tools in machining"**, Proceedings of the International Colloquium on Materials Manufacturing and Metrology (ICMMM), 8−9 August, 2014, IIT Madras, Chennai, India, pp. 866−869, 2014.

9.4.6. Posters

1. **Kishor Kumar Gajrani,** Y. Bishal Singha, Mamilla Ravi Sankar, "**Comparative tribological performance of graphite, CaF_2 and MoS_2 coated mechanical micro-textured cutting tool material during dry sliding test**" Research Conclave'18, 09−11

March 2018, IIT Guwahati, Guwahati, India. **(BEST POSTER AWARD)**.

2. **Kishor Kumar Gajrani**, Mamilla Ravi Sankar, "**Numerical and experimental investigation of effect of offset distance mechanical micro-textured cutting tools in dry machining**", Research Conclave'17, 16−19 March 2017, IIT Guwahati, Guwahati, India.
3. **Kishor Kumar Gajrani**, Mamilla Ravi Sankar, **"Fabrication and performance of the self-lubricating mechanical micro-textured tools in dry cutting of H-13 steel",** Research Conclave'16, 17−20 March 2016, IIT Guwahati, Guwahati, India.
4. **Kishor Kumar Gajrani**, Mamilla Ravi Sankar, **"Dynamic analysis of micro-textured tools: An experimental and numerical approach",** Tech-Expo, Techniche, 3−6 September 2015, IIT Guwahati, Guwahati, India.

References

[1] Huddle, D., (2001), New hard turning tools and techniques offer a cost-effective alternate to grinding, Tooling and Production Magazine.

[2] Gosh, A., Mallik, A.K., (1985), Manufacturing science, Affiliated East West Press Limited, New Delhi.

[3] Buddinski, G.K., (2007), Guide to friction, Wear and Erosion Testing, ASTM International, West Conshohocken.

[4] Burge, H., (2006), Machining coolants, The Environmental Reporter, Technical Newsletter, EMLab P&K **4**.

[5] Shokrani, A., Dhokia, V., Newman, S.T., (2012), Environmentally conscious machining of difficult-to-machine materials with regard to cutting fluids. International Journal of Machine Tools and Manufacture, **57**, 83−87.

[6] Sharma, V., Pandey, P.M., (2016), Recent advances in turning with textured cutting tools: A review, Journal of Cleaner Production, **137**, 701−715.

[7] Varadarajan, A.S., Philip, P.K., Ramamoorthy, B., (2002), Investigations on hard turning with minimal cutting fluid applications (HTMF) and its comparison with dry and wet turning, International Journal of Machine Tools and Manufacture, **42**, 193−200.

[8] Sharma, A.K., Tiwari, A.K., Dixit, A.R., (2015), Progress of nanofluid application in machining: A review, Materials and Manufacturing Processes, **30**, 813−828.

[9] Finkelstein, E., Lazarov, A., Cagnano, M., Halevy, S. (1994), Oil acne: successful treatment with isotretinoin, Journal of the American Academy of Dermatology, **30(3),** 491−492.

[10] Decoufle, P. (1978). Further analysis of cancer mortality patterns among workers exposed to cutting oil mists, Journal of the National Cancer Institute, **61(4),** 1025−1030.

[11] Sagel, S.D., Davis, S.D, Campisi, P., Dell, S.D. (2011), Update of respiratory tract disease in children with primary ciliary dyskinesia, Proceedings of the American Thoracic Society, **8(5),** 438−443.

[12] Goh, C. L., Gan, S. L. (1994). Efficacies of a barrier cream and an afterwork emollient cream against cutting fluid dermatitis in metalworkers: a prospective study, Contact Dermatitis, **31(3),** 176−180.

[13] Byrne, G., Scholta, E., (1993), Environmentally clean machining processes – A strategic approach, **42(1),** 471−474.

[14] Komanduri, R., Desai, J., (1983), Tool materials, Encyclopedia of Chemical Technology, **23**, 273−309.

[15] Goindi, G.S., Sarkar P., (2017), Dry machining: A step towards sustainable machining - Challenges and future directions, Journal of Cleaner Production, **165,** 1557–1571.

[16] Howes, T.D., Tonshoff, H.K., Heuer. W., (1991), Environmental aspects of grinding fluids, CIRP Annals – Manufacturing Technology, **42(2)**, 623−630.

[17] Narutaki, N., Yamane, Y., Tashima, S., Kuroki, H., (1997), A new advanced ceramic for dry machining, CIRP Annals – Manufacturing Technology, 46(1), 43−48.

[18] Lenz, E., Katz, K., Ber, A., (1976), Investigations on the flank wear of cemented carbide tools, ASME Journal of Manufacturing Science and Engineering, **98(1)**, 246−250.

[19] Ber, A., Goldblatt, M., (1989), The influence of temperature gradient on cutting tool's life, CIRP Annals – Manufacturing Technology, **38**, 63−73.

[20] Jen, T.C., Gutierrez, G., Eapen, S., Barber, G., Zhao, H., Szuba, P.S., Labataille, J., Manjunathaiah, J., (2002), Investigation of heat pipe cooling in drilling applications, International Journal of Machine Tools and Manufacture, **42**, 643−652.

[21] Hollis, W.S., (1961), The application and effect of controlled atmospheres in the machining of metals, International Journal of Machine Tool Design and Research, **1**, 59−78.

[22] Syed, I., Sarangi, M., (2014), Hydrodynamic lubrication with deterministic micro textures considering fluid inertia effect, Tribology International, **69**, 30−38.

[23] Teleginski, V., Cristina, D., Claudia, A., Oliveira, C., De Cesar, J., Santos, J., Fernanda, R., Riva, R., Vasconcelos, G., (2014), Yb: fiber laser surface texturing of stainless steel substrate, with MCrAlY deposition and CO_2 laser treatment, Surface and Coatings Technology, **260**, 251−259.

[24] Costil, S., Lamraoui, A., Langlade, C., Heintz, O., Oltra, R., (2014), Surface modifications induced by pulsed-laser texturing — Influence of laser impact on the surface properties, Applied Surface Science, **288**, 542−549.

[25] Demir, A.G., Maressa, P., Previtali, B., (2013), Fiber laser texturing for surface functionalization, Physics Procedia, **41**, 759−768.

[26] Bruzzone, A., Costa, H.L., Lonardo, P.M., Lucca, D.A., (2008), Advances in engineered surfaces for functional performance, CIRP Annals – Manufacturing Technology, **57**, 750−769.

[27] Evans, C.J., Bryan, J., (1999), Structured, textured or engineered surfaces, CIRP Annals – Manufacturing Technology, **48**, 541−556.

[28] Grabon, W., Koszela, W., Pawlus, P., Ochwat, S., (2013), Improving tribological behaviour of piston ring – cylinder liner frictional pair by liner surface texturing, Tribology International, **61**, 102−108.

[29] Borghi, A., Gualtieir, E., Marchetto, D., (2008), Tribological effects of surface texturing on nitriding steel for high-performance engine applications, Wear, **265**, 1046−1051.

[30] Xing, Y., Deng, J., Feng, X., Yu, S., (2013), Effect of laser surface texturing on Si3N4/TiC ceramic sliding against steel under dry friction, Materials and Design, **52**, 234−245.

[31] Wan, Y., Xiong, D.S., The effect of laser surface texturing on frictional performance of face seal, Journal of Materials Processing Technology, **197,** 96−100.

[32] Renevier, N.M., Hampshire, J., Fox, V.C., Witts, J., Allen, T., Teer, (2001), D.G., Advantages of using self-lubricating, hard, wear-resistant MoS_2-based coatings, Surface and Coatings Technology, **142,** 67−77.

[33] Renevier, N.M., Oosterling, H., König, U., Dautzenberg, H., Kim, B.J., Geppert, L., Koopmans, F.G.M., Leopold, J., (2003), Performance and limitations of MoS_2/Ti composite coated inserts, Surface and Coatings Technology, **172,** 13−23.

[34] Ezugwu, E.O., Bonney, J., Yamane, Y., (2003), An overview of the machinability of aeroengine alloys, Journal of Materials Processing Technology, **134**, 233−253.

[35] Aizawa, T., Mitusuo, A., Yamamoto, S., Sumitomo, T., Muraishi, S., (2005), Self-lubrication mechanism via the in situ formed lubricious oxide tribofilm, Wear, **259,** 708−718.

[36] Jianxin, D., Wenlong, S., Hui, Z., Pei, Y., Aihua, L., (2011), Friction and wear behaviours of the carbide tools embedded with solid lubricants in sliding wear tests and in dry cutting processes, Wear, **270**, 666−674.

[37] Koshy, P., Tovey, J., (2011), Performance of electrical discharge textured cutting tools, CIRP Annals – Manufacturing Technology, **60**, 153−156.

[38] Xie, J., Zhuo, Y.W., Tan, T.W., (2011), Experimental study on fabrication and evaluation of micro pyramid-structured silicon surface using a V-tip of diamond grinding wheel, Precision Engineering, **35,** 173−182.

[39] Obikawa, T., Kamio, A., Takaota, H., Osada, A., (2011), Micro-texture at the coated tool face for high performance cutting, International Journal of Machine Tools and Manufacture, 51, 966−972.

[40] Wakuda, M., Yamauchi, Y., Kanzaki, S., Yasuda, Y., (2003), Effect of surface texturing on friction reduction between ceramic and steel materials under lubricated sliding contact, Wear, **254,** 356−363.

[41] Kovalchenko, A., Ajayi, O., Erdemir, A. Fenske, G., (2011), Friction and wear behavior of laser textured surface under lubricated initial point contact, Wear, **271,** 1719−1725.

[42] Sun, J., Zhou, Y., Deng, J., Zhao, J., (2016), Effect of hybrid texture combining micro-pits and micro-grooves on cutting performance of WC/Co-based tools, International Journal of Advanced Manufacturing Technology, **86**, 3383−3394.

[43] Bouzakis, K.D., Michailidis, N., Vidakis, N., Eftathiou, K., Kompogiannisl, S., Erkens, G., (2000), Interpretation of PVD coated inserts wear phenomena in turning, CIRP Annals – Manufacturing Technology, **49**, 65−68.

[44] Brinksmeier, E., Riemer, O., Twardy, S., (2010), Tribological behavior of micro structured surfaces for micro forming tools, International Journal of Machine Tools and Manufacture, **50**, 425−430.

[45] Fatima, A., Mativenga, P.T., (2013), Assessment of tool rake surface structure geometry for enhanced contact phenomena, International Journal of Advanced Manufacturing Technology, **69,** 771−776.

[46] Jianxin, D., Wenlong, S., Hui, Z., (2009), Design, fabrication and properties of a self-lubricated tool in dry cutting, International Journal of Machine Tools and Manufacture, **49**, 66−72.

[47] Ibatan, T., Uddin, M.S., Chowdhury, M.A.K., Recent development on surface texturing in enhancing tribological performance of bearing sliders, Surface and Coatings Technologies, **272**, 102−120.

[48] Kümmel, J., Braun, D., Gibmeier, J., Schneider, J., Greiner, C., Schulze, V., Wanner, A., (2015), Study on micro texturing of uncoated cemented carbide cutting tools for wear improvement and built-up edge stabilisation, Journal of Materials Processing Technology, **215,** 62−70.

[49] Tang, W., Zhou, Y., Zhu, H., Yang H., (2013), The effect of surface texturing on reducing the friction and wear of steel under lubricated sliding contact, Applied Surface Science, **273,** 199−204.

[50] Shaw, M.C., (2005), Metal cutting principles, Oxford University Press, New York.

[51] Jianxin, D., Ze, W., Yunsong, L., Ting, Q., Jie, C., (2012), Performance of carbide tools with textured rake-face filled with solid lubricants in dry cutting processes, International Journal of Refractory Metals and Hard Materials, **30,** 164−172.

[52] Xie, J., Luo, M.J., Wu, K.K., Yang, L.F., Li, D.H., (2013), Experimental study on cutting temperature and cutting force in dry turning of titanium alloy using a non-coated micro-grooved tool, International Journal of Machine Tools and Manufacture, **73**, 25−36.

[53] Xing, Y., Deng, J., Zhao, J., Zhang, G., Zhang, K., (2014), Cutting performance and wear mechanism of nanoscale and microscale textured Al_2O_3/TiC ceramic tools in dry cutting of hardened steel, International Journal of Refractory Metals and Hard Materials, **43,** 46−58.

[54] Lian, Y., Deng, J., Yan, G., Cheng, H., Zhao, J., (2013), Preparation of tungsten disulfide (WS_2) soft-coated nano-textured self-lubricating tool and its cutting performance, International Journal of Advanced Manufacturing Technology, **68,** 2033−2042.

[55] Kawasegi, N., Sugimori, H., Morimoto, H., Morita, N., Hori, I., (2009), Development of cutting tools with microscale and nanoscale textures to improve frictional behavior, Precision Engineering, **33,** 248−254.

[56] Ze, D., Jianxin, D., Yang, C., Youqiang, X., Jun, Z., (2012), Performance of the self-lubricated textured tools in dry cutting of Ti-6Al-4V, International Journal of Advanced Manufacturing Technology, **62,** 943−951.

[57] Wenlong, S., Jianxin, D., Ze, W., Hui, Z., Pei, Y., Jun, Z., Xing, A., (2010), Cutting performance of cemented-carbides-based self-lubricated tool embedded with different solid lubricants, International Journal of Advanced Manufacturing Technology, **52,** 477−485.

[58] Bruzzone, A., Costa, H.L., Lonardo, P.M., Lucca, D.A., (2008), Advances in engineered surfaces for functional performance, CIRP Annals – Manufacturing Technology, **57**, 750−769.

[59] Sugihara, T., Enomoto, T., (2009), Development of a cutting tool with a nano/micro-textured surface-Improvement of anti-adhesive effect by considering the texture patterns, Precision Engineering, **33(4),** 425−429.

[60] Suh, M., Chae, Y., Kim, S., Hinoki, T., Kohyama, A., (2010), Effect of geometrical parameters in micro-grooved crosshatch pattern under lubricated sliding friction, Tribology International, **43,** 1508−1517.

[61] Xie, J., Luo, M.J., He, J.L., Liu, X.R., Tan, T.W., (2012), Micro-grinding of micro-groove array on tool rake surface for dry cutting of titanium alloy, International Journal of Precision Engineering and Manufacturing, **13(10),** 1845−1852.

[62] Xing, Y., Deng, J., Zhang, K., Zhang, G., Gao, H., (2014), Effect of femtosecond laser pretreatment on wear resistance of Al_2O_3/TiC ceramic tools in dry cutting, International Journal of Refractory Metals and Hard Materials, **43,** 291−301.

[63] Jiang, W., (2014), Bio-inspired self-sharpening cutting tool surface for finish hard turning of steel**,** CIRP Annals – Manufacturing Technology, **63**, 517−520.

[64] Zhang, K., Deng, J., Xing, Y., Li, S., Gao, H., (2015), Effect of microscale texture on cutting performance of WC/Co-based TiAlN coated tools under different lubrication conditions, Applied Surface Science, **326,** 107−118.

[65] Lie, S., Devarajan, S., Chang, Z., (2009), A study of micropool lubricated cutting tool in machining of mild steel, Journal of Materials Processing Technology, **209(3),** 1612−1620.

[66] Moksin, V., Vekteris, V., (2011), Effectiveness of twisted nematic liquid crystals as water based cutting fluid additive and tap lubricant, Mechanika, **17(5),** 570–575.

[67] Bennett, E.O., (1983), Water based cutting fluids and human health, Tribology International, **16(3),** 133–136.

[68] Hasib, M.A., Al-Faruk, A., Ahmed, N., (2010), Mist application of cutting fluid, International Journal of Mechanical and Mechatronics Engineering, **10(4),** 10–14.

[69] Bienkowski, K., (1993), Coolants and lubricants-The truth, Manufacturing Engineering, **19,** 90–96.

[70] Sluhan, C.A., (1986), Considerations in selection of coolants used in flexible machining cells, Society of Manufacturing Engineers Technical papers, **25,** 1–5.

[71] Flores, J., Health hazards in Industry, Public Health 4310, Metal Fabrication.

[72] Shihab, S.K., Khan, Z.A., Aasmohammad, Siddiquee, A.N., (2013), Application of response surface methodology for determining cutting forces in hard turning using

Castrol coolant. International Journal of Advanced Materials Manufacturing and Characterization, **3(1),** 27–36.

[73] Occupational Safety and Health Administration, (2001), Metal working fluids safety and health best practices manual, U. S. department labor.

[74] Kuram, E., Ozcelik, B., Demirbas, E., Şık, E., (2010), Effects of the cutting fluid types and cutting parameters on surface roughness and thrust force, World Congress on Engineering, **2,** 1.

[75] John, J., Bhattacharya, M., Raynor, P., (2004), Emulsions containing vegetable oils for cutting fluid application, Colloids and Surfaces A: Physicochemical Engineering Aspects Abbreviation, **237,** 141−150.

[76] Adler, D.P., Hii, W.W.S., Michalek, D.J., Sutherland, J.W., (2006), Examining the role of cutting fluids in machining and efforts to address associated environmental/health concerns, Machining Science and Technology, **10,** 23–58.

[77] Bennett, E.O., Bennett, D.L., (1985), Occupational airway diseases in the metalworking industries, Tribology International, **18(3),** 169–176.

[78] Fox, N.J., Stachowiak, G.W., (2007), Vegetable oil based lubricants–A review of oxidation, Tribology International, **40,** 1035–1046.

[79] Mongkolwongrojn, M., Arunmetta, P., (2002), Theoretical characteristics of hydrodynamic journal bearings lubricated with soyabean-based oil, Journal of Synthetic Lubrication, **19(3),** 213−228.

[80] Krahenbuhl, U., (2002), Vegetable oil-based coolants improve cutting performance (Cutting Fluids), Tooling and Production, Nelson Publishing.

[81] Woods, S., (2005), Going green, Cutting Tool Engineering, **57(2),** 48–51.

[82] Khan, M.M.A., Dhar, N.R., (2006), Performance evaluation of minimum quantity lubrication by vegetable oil in terms of cutting force, cutting zone temperature, tool wear, job dimension and surface finish in turning AISI-1060 steel, Journal of Zhejiang University Science A, **7(11),** 1790–1799.

[83] Shashidhara, Y.M., Jayaram, S.R., (2010), Vegetable oils as a potential cutting fluid—An evolution, Tribology International, **43,** 1073–1081.

[84] Adhvaryu, A., Erhan, S.Z., (2002), Epoxidized soyabean oil as a potential source of high temperature lubricants, Industrial Crops and Products, **15,** 247–254.

[85] Svajus, A., (2001), Thin film test to investigate liquid oxypolymerization of nonvolatile analyses: assessment of vegetable oils and biodegradable lubricants, Journal of the American Oil Chemists' Society, **78,** 1029–1035.

[86] Matthew, T.S., Nader, S., Bigyan, A., Lambert, A.D., (2007), Influence of fatty acid composition on the tribological performance of two vegetable-based lubricants, Journal of Synthetic Lubrication, **24,** 101–110.

[87] Joseph, P.V., (2007), Study of some non-edible vegetable oils of Indian origin for lubricant application, Journal of Synthetic Lubrication, **24,** 181–197.

[88] Sivasankaran, G.A., (1988), Jojoba-oil-based two stroke gasoline engine lubricant, Tribology International, **21,** 327–333.

[89] Jacob, J., (2004), Emulsions containing vegetable oils for cutting fluid application, Colloids and Surfaces A: Physicochemical Engineering Aspects Abbreviation, **237,** 141–150.

[90] Bhatnagar, A.H., (2006), HFRR studies on methyl ester of non-edible vegetable oils, Energy Fuels, **20,** 1341–1344.

[91] Singh, A.K., (2006), Metal working fluids from vegetable fluids, Journal of Synthetic Lubrication, **123,** 167–176.

[92] Loredana, P., (2008), Base stock oils for lubricants from mixtures of corn oil and synthetic diesters, Journal of the American Oil Chemists' Sociecty, **85,** 71–76.

[93] Mercurio, P., Burns, K.A., Negri, A., (2004), Testing the ecotoxicology of vegetable versus mineral based lubricating oils—1. Degradation rates using tropical marine microbes, Environmental Pollution, 129(2), 165–173.

[94] Iowa Soyabean Promotion Board and Center for Agricultural and Rural Development, (1993), The future of the Iowa soyabean industry. Iowa State University.

[95] Paul, I.D., Bhole, G.P., Chaudhari, J.R., (2014), A review on green manufacturing: It's important, methodology and its application, Procedia Materials Science, **6,** 1644-1649.

[96] Bondiloli, P., (2003), Crambeabyssinica oil and its derivatives as renewable lubricants: synthesis and characterisation of different esters based on crambe fatty acids, Journal of Synthetic Lubrication, **15,** 271–283.

[97] Ojolo, S.J., Amuda, M.O.H., Ogunmola, O.Y., Ononiwu, C.U., (2008), Experimental determination of the effect of some straight biological oils on cutting force during cylindrical turning, Revista Matéria, **13(4),** 650–663.

[98] Ozcelik, B., Kuram, E., Cetin, M.H., Demirbas, E., (2011), Experimental investigations of vegetable based cutting fluids with extreme pressure during of AISI 304L, Tribology International, **44,** 1864–1871.

[99] Klocke, F., Eisennblatter, G., (1997), Dry cutting, CIRP Annals − Manufacturing Technology, **46(2),** 519–526.

[100] Sharma, V.S., Singh, G., Sorby, K., (2015), A review on minimum quantity lubrication for machining processes, Materials and Manufacturing Processes, **30(8),** 935−953.

[101] Sharma, A.K., Tiwari, A.K., Dixit, A.R., (2016), Effects of minimum quantity lubrication (MQL) in machining processes using conventional and nanofluid based cutting fluids: A comprehensive review, Journal of Cleaner Production, **127,** 1–18.

[102] Dixit, U.S., Sarma, D.K., Davim, J.P., (2012), Environmentally friendly machining, Springer, NewYork.

[103] Shaikh, V., Boubekri, N., Scharf T.W., (2014), Analyzing the effectiveness of microlubrication using a vegetable oil-based metal working fluid during end milling AISI 1018 steel, International Journal of Manufacturing Engineering, 261349(1−13).

[104] Giasin, K., Ayvar-Soberanis, S., Hodzic, A., (2016), Evaluation of cryogenic cooling and minimum quantity lubrication effects on machining GLARE laminates using design of experiments, Journal of Cleaner Production, **135,** 533–548.

[105] Khandekar, S., Sankar, M.R., Agnihotri, V., Ramkumar J., (2012), Nano cutting fluid for enhancement of metal cutting performance, Materials and Manufacturing Processes, **27,** 963–967.

[106] Sutherland, J.W., Kulur, V.N., King, N.C., Turkovich, B.F.V., (2006), An experimental investigation of air quality in wet and dry turning, CIRP Annals − Manufacturing Technology, **49(1)**, 61–64.

[107] Lugscheider, E., Knotek, O., Barimani, C., Leyendecker, T., Lemmer, O., Wenke, R., (1997), Investigations on hard coated reamers in different lubricant free cutting operations, Surface Coatings Technology, **90,** 172–177.

[108] Gunter, K.L., Sutherland, J.W., (1999), An experimental investigation into the effect of process conditions on the mass concentration of cutting fluid mist in turning. Journal of Cleaner Production, **7(5),** 341–350.

[109] Sohrabpoor, H., Khanghah, S., Teimouri, R., (2015), Investigation of lubricant condition and machining parameters while turning of AISI 4340, International Journal of Advanced Manufacturing Technology, **76(9−12),** 2099–2116.

[110] Dhar, N.R., Ahmed, M.T., Islam, S., (2007), An experimental investigation on effect of minimum quantity lubrication in machining AISI 1040 steel, International Journal of Machine Tools and Manufacture, **47(5),** 748–753.

[111] Park, K.H., Yang, G.D., Lee, M.G., Jeong, H., Lee, S.W., Lee, D., (2014), Eco-friendly face milling of titanium alloy, International Journal of Precision Engineering and Manufacturing, **15(6),** 1159–1164.

[112] Park, K.H., Suhaimi, M.A., Yang, G.D., Lee, D.Y., Lee, S.W., Kwon, P., (2017), Milling of titanium alloy with cryogenic cooling and minimum quantity lubrication (MQL), International Journal of Precision Engineering and Manufacturing, **18(1),** 5–14.

[113] Beatrice, B.A., Kirubakaran, E., Jeba Thangaiah, P.R., Dev Wins, K.L., (2014), Surface roughness prediction using artificial neural network in hard turning of AISI H13 steel with minimal cutting fluid application, Procedia Engineering, **97,** 205−211.

[114] Sarıkaya, M., Gullu, A., (2015), Multi-response optimization of minimum quantity lubrication parameters using Taguchi-based grey relational analysis in turning of difficult-to-cut alloy Haynes 25, Journal of Cleaner Production, **91,** 347–357.

[115] Sarıkaya, M., Gullu, A., (2014), Taguchi design and response surface methodology based analysis of machining parameters in CNC turning under MQL, Journal of Cleaner Production, **65,** 604–616.

[116] Sharma, J., Sidhu, B.S., (2014), Investigation of effects of dry and near dry machining on AISI D2 steel using vegetable oil, Journal of Cleaner Production, **66,** 619–623.

[117] Heinemann, R., Hinduja, S., Barrow, G., Petuelli, G., (2006), Effect of MQL on the tool life of small twist drills in deep-hole drilling, International Journal of Machine Tools and Manufacture, **46(1),** 1–6.

[118] Itoigawa, F., Childs, T.H.C., Nakamura, T., Belluco, W., (2006), Effects and mechanisms in minimal quantity lubrication machining of aluminum alloys, Wear, **260(3),** 339–344.

[119] Yoshimura, H., Itoigawa, F., Nakamura, T., Niwa, K., (2005), Development of nozzle system for oil-on-water droplet metalworking fluid and its application to practical production line, JSME International Journal Series C Mechanical Systems, Machine Elements and Manufacturing, **48(4),** 723–729.

[120] Wakabayashi, T., Inasaki, I., Suda, S., (2006), Tribological action and optimal performance: research activities regarding MQL machining fluids, Machining Science and Technology, **10(1),** 59–85.

[121] Suda, S. Yokota, H. Inasaki, I., Wakabayashi, T., (2002), A synthetic ester as an optimal cutting fluid for minimal quantity lubrication machining, CIRP Annals − Manufacturing Technology, **51(1),** 95–98.

[122] Daungthongsuk, W., Wongwises, S, (2005), A critical review of convective heat transfer of nanofluids, Renewable and Sustainable Energy Reviews, **11(5),** 797−817.

[123] Saidur, R., Leong, K.Y., Mohammad, H.A., (2011), A review on applications and challenges of nanofluids, Renewable and Sustainable Energy Reviews, **15(3),** 1646–1668.

[124] Kakac¸, S., Pramuanjaroenkij, A, (2009), Review of convective heat transfer enhancement with nanofluids, International Journal of Heat and Mass Transfer, **52(13−14),** 3187–3196.

[125] Wen, D., Lin, G., Vafaei, S., Zhang, K., (2009), Review of nanofluids for heat transfer applications, Particuology, **7(2),** 141–150.

[126] Chen, H., Ding, Y., (2009), Heat transfer and rheological behaviour of nanofluids-A review, Advances in Transport Phenomena, **1,** 135–177.

[127] Srikant, R.R., Rao, D.N., Subrahmanyam, M.S., Vamsi, K.P., (2009), Applicability of cutting fluids with nanoparticle inclusion as coolants in machining. Proceedings of the Institution of Mechanical Engineers, Part J: Journal of Engineering Tribology, **223,** 221–225.

[128] Eastman, J.A., Choi, S.U.S., Li, S., Yu, W., Thompson, L.J., (2001), Anomalously increased effective thermal conductivities of ethylene glycol-based nanofluids containing copper nanoparticles, Applied Physics Letters, **78(6),** 718–720.

[129] Liu, M.S., Lin, M.C.C., Tsai, C.Y., Wang, C.C., (2006), Enhancement of thermal conductivity with Cu for nanofluids using chemical reduction method. International Journal of Heat and Mass Transfer, **49(17–18),** 3028–3033.

[130] Yoo, D.H., Hong, K.S., Yang, H.S., (2007), Study of thermal conductivity of nanofluids for the application of heat transfer fluids, Thermochimica Acta, **455(1–2),** 66–69.

[131] Chon, C.H., Kihm, K.D., Lee, S.P., Choi, S.U., (2005), Empirical correlation finding the role of temperature and particle size for nanofluid Al_2O_3 thermal conductivity, Applied Physics Letters, **87,** 152107 (1–3).

[132] Choi, S.U.S., Eastman, J.A., Enhancing thermal conductivity of fluids with nanoparticles, (1995), ASME International Mechanical Engineering Congress & Exposition, San Francisco, CA.

[133] Vajjha, R.S., Das, D.K., (2012), A review and analysis on influence of temperature and concentration of nanofluids on thermophysical properties, heat transfer and

pumping power, International Journal of Heat and Mass Transfer, **55(15−16),** 4063–4078.

[134] Qiang, L., Yimin, X., (2002), Convective heat transfer and flow characteristics of Cu-water nanofluids, Science in China Series E: Technological Science, **45(4),** 408–416.

[135] He, Y., Jin, Y., Chen, H., Ding, Y.; Cang, D., Lu, H., (2007), Heat transfer and flow behaviour of aqueous suspensions of TiO_2 nanoparticles (nanofluids) flowing upward through a vertical pipe, International Journal of Heat and Mass Transfer, **50(11−12),** 2272–2281.

[136] Choi, S.U.S., Zhang, Z.G., Yu, W., Lockwood, F.E., Grulke, E.A., (2001), Anomalous thermal conductivity enhancement in nanotube suspensions, Applied Physics Letters, **79(14),** 2252–2254.

[137] Lee, C.G., Hwang, Y.J. Choi, Y.M., Lee, J.K., Choi, C., Oh, J.M., (2009), A study on the tribological characteristics of graphite nano lubricants, International Journal of Precision Engineering and Manufacturing, **10(1)**, 85–90.

[138] Reddy, N.S.K., Rao, P.V., (2006), Experimental investigation to study the effect of solid lubricants on cutting forces and surface quality in end milling, International Journal of Machine Tools and Manufacture, **46,** 189–198.

[139] Rao, S.N., Satyanarayana, B., (2011), Experimental estimation of tool wear and cutting temperatures in MQL using cutting fluids with CNT inclusion, International Journal of Engineering Science and Technology, **3(4),** 928–931.

[140] Krishna, P.V., Srikant, R.R., Rao, D.N., (2010), Experimental investigation on the performance of nanoboric acid suspensions in SAE-40 and coconut oil during turning of AISI 1040 steel, International Journal of Machine Tools and Manufacture, **50,** 911–916.

[141] Yan, J., Zhang, Z., Kuriyagawa, T., (2011), Effect of nanoparticle lubrication in diamond turning of reaction-bonded SiC, International Journal of Automation Technology, **5(3),** 307–312.

[142] Sayuti, M., Sarhan, A.A.D., Salem, F., (2014), Novel uses of SiO_2 nano-lubrication system in hard turning process of hardened steel AISI4140 for less tool wear, surface roughness and oil consumption, Journal of Cleaner Production, **67,** 265–276.

[143] Prasad, M.M.S., Srikant, R.R., (2013), Performance evaluation of nano graphite inclusion in cutting fluids with MQL technique in turning of AISI 1040 steel, International Journal of Research in Engineering and Technology, **2(11),** 381–393.

[144] Nam, J.S., Lee, P.H., Lee, S.W., (2011), Experimental characterization of micro-drilling process using nanofluid minimum quantity lubrication, International Journal of Machine Tools and Manufacture, **51,** 649–652.

[145] Mao, C., Tang, X., Zou, H., Huang, X., Zhou, Z., (2012), Investigation of grinding characteristic using nanofluid minimum quantity lubrication, International Journal of Precision Engineering and Manufacturing, **13(10),** 1745–1752.

[146] Prabhu, S., Vinayagam, B.K., (2012), AFM investigation in grinding process with nanofluids using Taguchi analysis, International Journal of Advanced Manufacturing Technology, **60,** 149–160.

[147] Prabhu, S., Vinayagam, B.K., (2010), Nano surface generation of grinding process using carbon nano tubes. Sadhana, **35(6),** 747–760.

[148] Lee, P.H., Nam, T.S., Li, C., Lee, S.W., (2010), Environmentallyfriendly nano-fluid minimum quantity lubrication (MQL) meso-scale grinding process using nano-diamond particles, International Conference on Manufacturing Automation, Hong Kong, December 13–15, 44–49.

[149] Park, K.H., Ewald, B., Kwon, P.Y., (2011), Effect of nano-enhanced lubricant in minimum quantity lubrication balling milling, ASME Journal of Tribology, **133,** 031803(1–8).

[150] Sayuti, M., Sarhan, A.A.D., Tanaka, T., Hamdi, M., Saito, Y., (2013), Cutting force reduction and surface quality improvement in machining of aerospace duralumin AL-2017-T4 using carbon onion nanolubrication system, International Journal of Advanced Manufacturing Technology, **65,** 1493–1500.

[151] Rahmati, B., Sarhan, A.A.D., Sayuti, M., (2013), Morphology of surface generated by end milling AL6061-T6 using molybdenum disulfide (MoS_2) nanolubrication in end milling machining, Journal of Cleaner Production, **66,** 685–691.

[152] Etsion, I., (2005), State of the art in laser surface texturing, Journal of Tribology—Transactions of the ASME, **127(1)**, 248–253.

[153] Rapoport, L., Moshkovich, A., Perfilyev, V., Lapsker, I., Halperin, G., Itovich, Y., Etsion, I., (2008), Friction and wear of MoS_2 films on laser textured steel surfaces, Surface and Coatings Technology, **202(14),** 3332–3340.

[154] Etsion, I., Sher, E., (2009), Improving fuel efficiency with laser surface textured piston rings, Tribology International, **42(4),** 542–547.

[155] Brizmer, V., Kligerman, Y., Etsion, I., (2003), A laser textured parallel thrust bearing," Tribology Transactions, **46(3),** 397–403.

[156] Kawasegi, N., Ozaki, K., Morita, N., Nishimura, K., Yamaguchi, M., (2017), Development and machining performance of a textured diamond cutting tool fabricated with a focused ion beam and heat treatment, Precision Engineering, **47**, 311–320.

[157] Coblas, D.G., Fatu, A., Maoui, A., Hajjam, M., (2015), Manufacturing textured surfaces: State of art and recent developments, Proceedings of the Institution of Mechanical Engineers, Part J: Journal of Engineering Tribology, **229(1),** 3–29.

[158] Costa, H.L., Hutchings, I.M., (2015), Some innovative surface texturing techniques for tribological purposes, Proceedings of the Institution of Mechanical Engineers, Part J: Journal of Engineering Tribology, **229(4),** 429–448.

[159] Muthuraja, A., and Senthilvelan, S., (2015), Abrasive wear performance of tungsten carbide based self-lubricant cutting tool material, International Journal of Refractory Metals and Hard Materials, **51,** 91−101.

[160] Zhang, X., (2014), A review: The method for synthesis MoS_2 monolayer," International Journal of Machining and Machinability of Materials, **10(5−6),** 489–499.

[161] Jackson, R.L., Green, I., (2006), A statistical model of elasto-plastic asperity contact between rough surfaces, Tribology International, **39,** 906–914.

[162] Mao, M., Peng, L., Yi, P., Lai, X., (2016), Modeling of the friction behavior in metal forming process considering material hardening and junction growth, Journal of Tribology—Transactions of the ASME, **138(1),** 012202(1−18).

[163] Wu, Z., Deng, J., Zhang, H., Lian, Y., Zhao, J., (2012), Tribological behaviour of textured cemented carbide filled with solid lubricants in dry sliding with titanium alloys, Wear, **292–293,** 135–143.

[164] Logothetis, N., (1997), Managing for total quality: from deming to taguchi and SPC," Prentice Hall of India Private Limited, New Delhi.

[165] Rech, J., Claudin, C., Grzesik, W., Zalis, Z., (2008), Characterization of the friction properties of various coatings at the tool−chip−workpiece interfaces in dry machining of AISI 4140 steel, Proceedings of the Institution of Mechanical Engineers, Part J: Journal of Engineering Tribology, **222(4),** 617−627.

[166] Ksiazek, M., Tchorz, A., Boron, (2014), Mechanical properties and the microstructure of $Al_2O_3/Al/Al_2O_3$ joints with the surface modification of alumina by a thin layer of Ti + Nb, Journal of Materials Engineering and Performance, **23(5),** 1635−1640.

[167] Wu, T., Cheng, K., (2013), Micro milling performance assessment of diamond-like carbon coatings on a micro-end mill, Proceedings of the Institution of Mechanical Engineers, Part J: Journal of Engineering Tribology, **227(9),** 1038−1046.

[168] Jianxin, D., Tongkun, C., Zeliang, D., Jianhua, L., Junlong, S., Jinlong, Z., (2006), Tribological behaviors of hot-pressed Al_2O_3/TiC ceramic composites with the addition of CaF_2 solid lubricants, Journal of European Ceramic Society, **26(8),** 1317−1323.

[169] Jianxin, D., Tongkun, C., Xuefeng, Y., Jianhua, L., (2006), Self-lubrication of sintered ceramic tools with CaF_2 addition in dry cutting, International Journal of Machine Tools Manufacture, **46(9),** 957−963.

[170] Basnyat, P., Luster, B., Muratore, C., Voevodin, A.A., Haasch, R., Zakeri, R., Kohli, P., Aouadi, S.M., (2008), Surface texturing for solid adaptive lubrication, Surface and Coatings Technology, 203(1−2), 73−79.

[171] Sugihara, T., Enomoto, T., (2009), Development of cutting tool with nano/micro textured surface; improvement of anti-adhesive effect by considering the texture patterns, Precision Engineering, **33(4),** 425−429.

[172] Jianxin, D., Wenlong, S., Hui, Z., Pei, Y., Aihua, L., (2011), Friction and wear behaviors of the carbide tools embedded with solid lubricants in sliding wear tests and in dry cutting processes, Wear, **270(9–10),** 666–674.

[173] Cochran, W.G., Cox, G.M., (1968), Experimental Designs, Second Edition, John Wiley & Sons, Inc.

[174] Ernst, H., Merchant, M.E., (1941), Chip formation, friction and high quality machine surfaces in surface treatment of metals, Transaction of ASME, **29,** 299−378.

[175] Cheng, RY. Principle of Metal Cutting, China Machine Press, Beijing, 1992.

[176] Shi, MS. Solid Lubrication Materials, China Chemistry Press, Beijing, 2000.

[177] Dogra, M., Sharma, V.S., Sachdeva, A., Suri, N.M., Dureja, J.S., (2010), Tool wear, chip formation and workpiece surface issues in CBN hard turning: A review, International Journal of Precision Engineering and Manufacturing, **11(2),** 341–358.

[178] APHA, AWWA, WPCF, (2005), Standard methods for the examination of water and wastewater, 21st edition, American Public Health Association, Washington, DC.

[179] Moraes, I.C.F., Fasolin, L.H., Cunha, R.L., Menegalli, F.C., (2011), Dynamic and steady: shear rheological properties of xanthan and guar gums dispersed in yellow

passion fruit pulp (*Passiflora edulis* f. *flavicarpa*), Brazilian Journal of Chemical Engineering, **28,** 483–494.

[180] Qi-Wei, L., Hernandez-Hernandez, M.E., Macosko, C.W., (2003), Explaining the abnormally high flow activation energy of thermoplastic polyurethanes, Polymer, **44,** 3309–3318.

[181] ASTM D 4627, (2012), Test method for iron chip corrosion for water-dilutable metal working fluids, ASTM International.

[182] ASTM D 3707, (2010), Test method for storage stability of water-in-oil emulsions by the oven test method, ASTM International.

[183] Adams, M.C., Gannon, J.E., Bennett, E.O., (1979), BOD and COD studies of synthetic and semisynthetic cutting fluids, Water, Air, and Soil Pollution, **11(1)**, 105–113.

[184] Brinksmeier, E., Heinzel, C., Wittmann, M., (1999), Friction, cooling and lubrication in grinding, CIRP Annals: Manufacturing Technology, **48**, 581–598.

[185] Ebbrell, S., Woolley, N.H., Tridimas, Y.D., Allanson D.R., Rowe, W.B., (2000), The effects of cutting fluid application methods on the grinding process, International Journal of Machine Tools and Manufacture, **40**, 209–223.

[186] Braga, D.U., Diniz, A.E., Miranda, G.W.A., Coppini, N.L., (2002), Using a minimum quantity of lubricant (MQL) and a diamond coated tool in the drilling of aluminium-silicon alloys, Journal of Materials Processing Technology, **122**, 127–138.

[187] Toulemonde, M., Benyagoub, A., Trautmann, C., Khalfaoui, N., Boccanfuso, M., Dufour, C., Gourbilleau, F., Grob, J.J., Stoquert, J.P., Costantini, J.M., Haas, F., Jacquet, E., Voss, K.O., Meftah, A., (2012), Dense and nanometric electronic excitations induced by swift heavy ions in an ionic CaF_2 crystal: Evidence for two thresholds of damage creation, Physical Review B, **85**, 054112(1−16).

[188] Hu, K., Hu, X., Xu, Y., Sun, X., Jiang, Y., (2012), Tribology of MoS_2-based Nanocomposites, Tribology of Nanocomposites, 41–60. Springer, Berlin, Heidelberg, Germany.

[189] Sakamoto, M., Kanda, Y., Miyahara, M., Higashitani, K., (2002), Origin of long-range attractive force between surfaces hydrophobized by surfactant adsorption, Langmuir, **18(15)**, 5713–5719.

[190] Murshed, S.M.S., Leong, K.C., Yang, C., (2005), Enhanced thermal conductivity of TiO_2-water based nanofluids, International Journal of Thermal Sciences, **44(4)**, 367–373.

[191] Yan, R., Simpson, J.R., Bertolazzi, S., Brivio, J., Watson, M., Wu, X., Kis, A., Luo, T., Walker, A.R.H., Xing, H.G., (2014), Thermal conductivity of monolayer molybdenum disulfide obtained from temperature-dependent raman spectroscopy, ACS Nano, **8(1)**, 986–993.

[192] Andersson, S., Backstrom, G., (1987), Thermal conductivity and heat capacity of single-crystal LiF and CaF_2 under hydrostatic pressure, Journal of Physics C: Solid State Physics, **20**, 5951–5962.

[193] Hamilton, R.L., Crosser, O.K., (1962), Thermal conductivity of heterogeneous two component systems, Industrial and Engineering Chemistry Fundamentals, **1(3)**, 187–191.

[194] Zhou, L.P., Wang, B.X., Peng, X.F., Du, X.Z., Yang, Y.P., (2010), On the specific heat capacity of CuO nanofluid, Advances in Mechanical Engineering, **2010**, 172085 (1–4). DOI: 10.1155/2010/172085.

[195] He, Y., Jin, Y., Chen, H., Ding, Y., Cang, D., Lu, H., (2007), Heat transfer and flow behaviour of aqueous suspensions of TiO_2 nanoparticles (nanofluids) flowing upward through a vertical pipe, International Journal of Heat and Mass Transfer, **50(11)**, 2272–2281.

[196] ManojKumar, K., Ghosh, A., (2016), Assessment of cooling-lubrication and wettability characteristics of nano-engineered sunflower oil as cutting fluid and its impact on SQCL grinding performance, Journal of Materials Processing and Technology, **237**, 55–64.

[197] Liu, G., Li, X., Qin, B., Xing, D., Guo, Y., Fan, R., (2004), Investigation of the mending effect and mechanism of copper nano-particles on a tribologically stressed surface, Tribology Letters, **17(4)**, 961–966.

[198] Rapoport, L., Leshchinsky, V., Lvovsky, M., Nepomnyashchy, O., Volovik, Y., Tenne, R., (2002), Mechanism of friction of fullerenes, Industrial Lubrication and Tribology, **54(4)**, 171–176.

[199] Zhang, B.S., Xu, B.S., Xu, Y., Gao, F., Shi, P.J., Wu, Y.X., (2011), Cu nanoparticles effect on the tribological properties of hydrosilicate powders as lubricant additive for steel-steel contacts, Tribology International, **44(7–8)**, 878–886.

[200] Alberts, M., Kalaitzidou, K., Melkote, S., (2009), An investigation of graphite nanoplatelets as lubricant in grinding, International Journal of Machine Tools and Manufacture, **49(12−13)**, 966–970.

Appendix

Specification of field emission scanning electron microscope (FESEM)

Make	Zeiss
Model	Sigma
Chamber	330 mm inner diameter, 270 mm height
Specimen weight	up to 200 g
Movement	X = 125 mm, Y = 125 mm, Z = 50 mm
Stage	5-axis Motorized Cartesian
Detector	In lens, SE-2, BSD
Magnification range	100 X to 2000 kX

Specification of optical microscope

Make	Carl Zeiss
Model	Axiotech-100 HD, 3D
Chamber	330 mm inner diameter, 270 mm height
Specimen weight	up to 200g
Stage movement	3 axis measuring system, reflect light measuring X = 75 mm, Y = 50 mm, Z = 50 mm
Lens	Binocular photo tube
Magnification range	5 X to 200 X
Software	Axio-Cam and Axiovision 4.8.2 (in built)

Specification of non-contact profilometer

Make	Taylor Hobson
Model	CCI-Lite
Magnification range	20 X
Precision	1 megapixel
Power supply	220 V
Focal distance	4.7 mm
Field of view	0.825 mm × 0.825 mm

Specification of pin-on-disc tribometer

Make	DUCOM
Model	TR-201
Sensors	Proximity, load cell, LVDT
Track diameter	10 mm to 100 mm
Speed	10 to 1000 rpm
Load	10 N to 100 N

Specification of Infrared Camera

Make	Infratech
Model	Variocam-hr
Time duration	1 s to 7200 s
Frequency range	1 to 8 Hz
Emissivity range	0.01 to 1